Die approbierte Originalversion dieser Dissertation ist in der Hauptbibliothek der Technischen Universität Wien aufgestellt und zugänglich.
http://www.ub.tuwien.ac.at

The approved original version of this thesis is available at the main library of the Vienna University of Technology.
http://www.ub.tuwien.ac.at/eng

DOCTORAL THESIS

Continuum micromechanics of textured microstructures: bone, bone biomaterials, and paper

submitted in satisfaction of the requirements for the degree of
Doctor of Science in Civil Engineering
of the Vienna University of Technology, Faculty of Civil Engineering

---

DISSERTATION

Kontinuumsmikromechanik von texturierten Mikrostrukturen:
Knochen, Kochenersatz- oder Biomaterialien und Papier

ausgeführt zum Zwecke der Erlangung des akademischen Grades eines
Doktors der technischen Wissenschaft
eingereicht an der Technischen Universität Wien Fakultät für Bauingenieurwesen

von

Dipl.-Ing. Viktória Vass
Matrikelnummer: 1127214
Miesbachgasse 7/11, 1020 Wien

Gutachter:
Univ.-Prof. Dipl.Ing. Dr. techn. **Christian Hellmich**
Institut für Mechanik der Werkstoffe und Strukturen
Technische Universität Wien
Univ. Prof. DI Dr. mont. **Thomas Antretter**
Institut für Mechanik
Montanuniversität Leoben
Univ.-Prof. Dr. **Heinz Redl**
Ludwig Boltzmann Institut, Wien

Wien, im Mai 2017 ....

“Non est ad astra mollis e terris via”

Seneca

Acknowledgements

I would like to acknowledge financial support of the MICROBONE project (grant number 257032), granted by the European Research Council (ERC), which enabled my employment as a research assistant at the Vienna University of Technology.

Foremost, I would like to express my gratitude to my supervisor Christian Hellmich for taking me on board, for supporting me throughout my Ph.D. research, and for setting an example with his immense knowledge and his dedication to science. I am truly grateful to Claire Morin for always being helpful in scientific discussions, and for her guidance and hospitality during my stay in Saint-Étienne.

I would like to thank my colleagues for the delightful work environment we shared over the past years. My special thanks goes to Markus Lukacevic, who supported me in many scientific and real life matters. I would like to thank the Wood-Group for sharing their coffee with me, the Bone-Group for providing a place for fruitful discussions, the Festigkeitslehre-Team, and Gabriele Ostrowski, Martina Pöll, and Astrid Schuh for always being kind and helpful with administrative issues.

My appreciation goes to my university professors who paved my way towards a scientific career: to Imre Bojtár for introducing the field of biomechanics, to György L. Balázs for the opportunity to participate in many conferences, and to Johann Kollegger for encouraging me to think outside the box and utilize my engineering skills in such interdisciplinary fields as computational biomechanics.

I am thankful to my father for teaching me that knowledge is a treasure, to my mother, who has always encouraged me, and provided me with emotional and financial support to reach my goals, to my family and friends for always being there for me.

Köszönöm.

Abstract

Recently, self-consistent continuum micromechanics formulations have turned out as particularly efficient and reliable tools to predict (poro-)elasticity and brittle strength of many natural and man-made materials characterized by textured microstructures. Thereby, materials are envisioned as porous polycrystals consisting of an infinite number of non-spherical crystal phases, interacting with a spherical pore phase.

In case of hydrated polycrystals, sliding events along very thin (liquid crystalline) water layers forming interfaces between or within the single crystal phases entail ideal plastic behavior of crystals (or clusters thereof). Its occurrence in the extrafibrillar space of bone ultrastructure, together with brittle rupture of collagen, could well explain the strength of different bone samples from different species, ages, and anatomical locations. This explanation, however, required major micromechanical developments, which we refine and extend in the present contribution: The sliding-related elastic-perfectly plastic constitutive law is elaborated for a non-associated Mohr-Coulomb plasticity. Upscaling this elastoplastic behavior from the single crystal to the polycrystal scale is achieved through derivation of concentration and influence tensors for eigenstressed microheterogeneous materials, which itself is a generalization of the well-known transformation field analysis. The resulting multiscale-multisurface elastoplasticity problema is solved through a new variant of the algorithmic strategy of return-mapping.

Then, we consider fluids as a source of plastic sliding events of hydrated polycrystals in (bio-)materials, comprising heterogeneous microstructures and fluid-filled interfaces at small length scales. By bridging liquid crystal physics with continuum micromechanics, homogenization schemes for eigenstressed heterogeneous materials specialized for the limit case of flat interfaces are used to upscale this interface behavior to the much larger composite comprising an isotropic, linear elastic solid matrix of hydroxyapatite, as well as interacting parallel interfaces representing the entity of all fluids in a so-called “liquid crystal” state.

Next, application examples underpin the relevance of continuum micromechanics tools in medical practice. Herein, chemical information is extracted from Computed Tomographic (CT) data, and converted, via micromechanics laws, into object-specific, inhomogeneous and anisotropic material properties. Such CT-to-micromechanics approaches provide a basis for Finite Element Models, and pave the way to patient-specific, medical image-based bone fracture risk assessment.

Finally, motivated by the success in adapting the polycrystal morphology for 3D (spatial) networks of solid crystal needles, the development of a similar theoretical concept for planar wood fiber networks is tackled. The model is confirmed by various experimental data and deemed as a new support tool in the design of paper production processes.

Kurzfassung

In der letzten Zeit haben sich selbstkonsistente Kontinuums-Mikromechanik-Formulierungen als besonders effiziente und zuverlässige Werkzeuge erwiesen, um die (Poro-)Elastizität und die spröde Festigkeit vieler natürlicher und künstlicher Materialien, die durch strukturierte Mikrostrukturen gekennzeichnet sind, vorherzusagen. Dabei stellt man sich Materialien als poröse Polykristalle vor, die aus einer unendlichen Anzahl von nichtkugelförmigen Kristallphasen bestehen und mit einer kugelförmigen Porenphase zusammenwirken.

Im Falle von hydratisierten Polykristallen führt das Gleiten entlang sehr dünner (flüssigkristalliner) Wasserschichten, die Grenzflächen zwischen oder innerhalb der Einkristallphasen bilden, zu einem ideal-plastischen Verhalten von Kristallen. Diese Effekt im extrafibrillaren Raum der Knochen-Ultrastruktur, zusammen mit dem spröden Bruch von Kollagen, könnte auch die Festigkeit der Knochen von verschiedenen Arten, Altersgruppen und anatomischen Orten erklären. Dieser Modellansatz erforderte jedoch gravierende mikromechanische Weiterentwicklungen: das auf das Gleiten bezogene, elastisch-ideal-plastische Grundgesetz wird für eine nicht assoziierte Mohr-Coulomb-Plastizität ausgearbeitet. Das Hochskalieren dieses elastoplastischen Verhaltens vom Einkristall zum polykristallinen Maßstab wird durch Ableitung von Konzentrations- und Einflusstensoren für die unter Eigenspannungen stehenden mikroheterogenen Materialien erreicht, welches selbst eine Verallgemeinerung der bekannten Transformationsfeldanalyse ist. Die resultierende Mehrskalen-Mehrflächen-Elastoplastizität wird durch eine neue Variante der algorithmischen Strategie des Return-Mappings gelöst.

Dann betrachten wir Flüssigkeiten als Quelle von plastischen Gleitungen von hydratisierten Polykristallen in (Bio-)Materialien, die heterogene Mikrostrukturen und füßigkeitsgefüllte Grenzflächen in kleinen Längenskalen umfassen. Durch die Überbrückung der Physik von Flüssigkristallen mit der Kontinuumsmikromechanik werden Homogenisierungsschemen für die unter Eigenspannungen stehenden heterogenen Materialien, die auf den Grenzfall von flachen Grenzflächen spezialisiert sind, verwendet. Damit kann dieses Grenzflächenverhalten auf den viel größeren Verbundwerkstoff mit einer isotropen, linearen elastischen festen Matrix aus Hydroxyapatit und interagierender, paralleler, flüssigkeitsgefüllter Grenzflächen hochskaliert werden.

Als nächstes zeigen Anwendungsbeispiele die Relevanz von Kontinuumsmikromechanik-Werkzeugen in der medizinischen Praxis. Hierbei werden

chemische Informationen aus Computertomographie-Daten extrahiert und über mikromechanische Gesetze in objektspezifische, inhomogene und anisotrope Materialeigenschaften umgewandelt. Solche CT-zu-Mikromechanik-Ansätze bilden eine Basis für Finite-Element-Modelle und ebnen den Weg zur patientenspezifischen, medizinisch-bildbasierten Knochenbruchrisikobewertung.

Schließlich wird die Entwicklung eines ähnlichen theoretischen Konzepts für ebene Holzfasernetze vorgestellt, die durch den Erfolg der Anpassung der polykristallinen Morphologie an 3D-Netzwerke von festen Kristallnadeln motiviert ist. Das Modell wird durch verschiedene experimentelle Daten bestätigt und kann als neues Unterstützungsinstrument bei der Gestaltung von Papierherstellungsprozessen benutzt werden.

Contents

Contents vii

List of Figures xi

List of Tables xix

1 Introduction **1**
- 1.1 Investigated materials . . . 2
  - 1.1.1 Bone . . . 2
  - 1.1.2 Bone biomaterials . . . 6
  - 1.1.3 Paper . . . 7
- 1.2 Theoretical framework: continuum micromechanics . . . 9
- 1.3 Beyond elasticity: Fundamentals of elastoplasticity . . . 15
- 1.4 Return-mapping . . . 16
- 1.5 Outline of the thesis . . . 19

2 Review of "universal" rules governing bone composition, organization, and elasticity across organizational hierarchies **22**
- 2.1 Introduction . . . 23
- 2.2 Morphological patterns of bone . . . 25
- 2.3 Mineral and collagen dosages in extracellular bone matrix . . . 27
  - 2.3.1 Dehydration-demineralization tests . . . 28
  - 2.3.2 Dehydration-deorganification tests . . . 31
  - 2.3.3 Dehydration-ashing tests . . . 32
  - 2.3.4 Determination of tissue-specific volume fractions . . . 33
  - 2.3.5 "Universal" rules in bone fibrillogenesis and mineralization . 36
  - 2.3.6 Cell biology aspects . . . 39
- 2.4 Mineral distribution in extracellular bone matrix . . . 41
  - 2.4.1 Experimental set II: Transmission electron microscopy . . . 44
  - 2.4.2 Comparison of independently derived values of the relative amount of extrafibrillar mineral . . . 45
- 2.5 Hydration-dependent evolution of unmineralized collagenous tissues 45
- 2.6 Bone tissue evolution during mineralization . . . 50

2.7 Nano- and microstructural patterns governing anisotropic tissue elasticity . . . 55
    2.7.1 Micromechanical representation of bone tissue by means of representative volume elements (RVEs) . . . 56
    2.7.2 Elasticity homogenization . . . 59
    2.7.3 Elasticity of elementary components . . . 62
    2.7.4 Model validation at the extravascular scale . . . 68
    2.7.5 Concluding remarks . . . 73

3 Micromechanics of elastoplastic porous polycrystals: theory, algorithm, and application to osteonal bone 79
3.1 Introduction . . . 80
3.2 Representative volume element (RVE) - momentum balance and kinematic compatibility - microstructural characteristics of porous polycrystals . . . 83
3.3 Elastoplasticity of solid phases - upscaling to porous polycrystal scale 86
3.4 Self-consistent estimation of concentration and influence tensors from eigenstressed Eshelby problems . . . 88
3.5 Algorithmic treatment of multiscale elastoplasticity . . . 92
    3.5.1 Spatial discretization of governing equations . . . 92
    3.5.2 Temporal discretization of governing equations . . . 95
    3.5.3 Iterative solution process I: macro-to-micro scale transitions 97
    3.5.4 Iterative process II: plastic flow - “return map” . . . 100
3.6 Exemplification of multiscale elastoplasticity through upscaling of Mohr-Coulomb criterion . . . 103
3.7 Application: Push-out test on osteonal bone . . . 109
3.8 Summary and conclusions . . . 113
3.9 Nomenclature . . . 121

4 Frictionally sliding micro-interfaces as source of kinematic hardening plasticity: a continuum micromechanics approach 125
4.1 Introduction . . . 126
4.2 Separation of scales, stress and strain average rules . . . 127
4.3 Behavior of material phases: linear elastic matrix and frictionally sliding interfaces . . . 130
4.4 Scale transition: concentration-influence relations . . . 132
4.5 Analytical solution of the problem . . . 133
    4.5.1 Elastic domain . . . 133
    4.5.2 Elasto-plastic domain . . . 135
        Plastic slope in pure shear . . . 136
        Plastic slope in case of combined loading . . . 137
4.6 Discussion, from a thermodynamics viewpoint . . . 140
4.7 Appendix A: Extension to multiple interface families . . . 141
    4.7.1 Elastic domain . . . 141
    4.7.2 Elasto-plastic domain . . . 143

4.8 Appendix B: Molecular dynamics simulations 146
4.9 Appendix: Derivation of homogenized stiffness tensor, of interface morphology tensor, as well as of the concentration and influence tensors 148
4.10 Nomenclature 150

5 Coupling multiscale X-ray physics and micromechanics for bone tissue composition and elasticity determination from micro-CT data, by example of femora from OVX and sham rats 152
5.1 Introduction 153
5.2 Materials and Methods 155
    5.2.1 Animal model and sample preparation 155
    5.2.2 Conversion of CT grey values to energy-dependent attenuation coefficients 156
    5.2.3 Identification of applied X-ray energy and of extracellular bone mass density 158
    5.2.4 Translation of voxel-specific composition into voxel-specific elastic properties 163
    5.2.5 Statistical Analysis 166
5.3 Results 166
5.4 Discussion 177
5.5 Appendix A. Derivation of the mineral volume fraction of Eq. $(5.15)_1$ 185
5.6 Appendix B. Derivation of fibrillar and extrafibrillar volume fractions, f_{fib}^{voxel} and f_{ef}^{voxel}, in the line of Morin and Hellmich [2013] . . 186
5.7 Nomenclature 188

6 X-ray physics-based CT-to-composition conversion applied to a tissue engineering scaffold, enabling multiscale simulation of its elastic behavior 191
6.1 Introduction 193
6.2 Material characterization and processing 195
6.3 Acquisition of the scaffold microstructure by means of micro-computed tomography 197
    6.3.1 Definition of imaging modality 197
    6.3.2 Analysis of microCT data for determination of the voxel-specific scaffold composition 197
6.4 Computation of strain and stress fields across the scaffold when subjected to uniaxial compression 201
    6.4.1 Finite Element model of scaffold structure 201
    6.4.2 Microstructure-based elastic constants by means of micromechanical homogenization 203
    6.4.3 Boundary and loading conditions 206
6.5 Numerical results 207
6.6 Discussion 207
6.7 Nomenclature 210

7 A continuum micromechanics approach to the elasticity of planar fiber networks and its application to paper 212
7.1 Introduction 213
7.2 Micromechanics model 216
    7.2.1 Representative volume element - stress and strain average rules 216
    7.2.2 Morphological representation of planar fiber networks: material phases 217
    7.2.3 Elastic concentration problem - Micro-macro transition - Homogenized stiffness tensor 219
    7.2.4 Matrix inclusion problem based self consistent estimate for the strain concentration tensors 220
7.3 Results and discussion 222
7.4 Nomenclature 228

8 Conclusions and outlook 230

Bibliography 233

List of Figures

1.1 Representative volume element of porous polycrystals: uniform orientation distribution of cylindrical (needle-like) inclusions and spherical pores 1
1.2 Needle-based micromechanics predictions for normalized Young's modulus E^{hom}/E_s, as a function of porosity, for a wide range of Young's modulus and Poisson's ratios of crystal solid phase; and comparison with experiments, see [Fritsch et al., 2013b] for experimental sources. 2
1.3 Hierarchical structure of bone: (a) photograph of a cross-section through a whole long bone, showing the macrostructure made up by cortical and trabecular bone; (b) scanning electron micrograph of an osteon, being composed of alternating collagen-rich and collagen-poor lamellae, and delineated by a collagen-free cement line [Ascenzi and Bonucci, 1972]; (c) trabecular struts making up trabecular bone; (d) bone ultrastructure [Prostak and Lees, 1996]; (e) scanning electron micrograph of the isolated cement line; (f) micromechanical representation of collagen-free compartment of bone ultrastructure [Davies, 2007]; (g) hydroxyapatite crystals, obtained by means of SEM [Weiner and Wagner, 1998]; (h) wet collagen, electron density map of [Orgel et al., 2006]. 3
1.4 (a) Cross-section of a fiber making up the three-phase composite scaffold; (b) TCP discs captured by means of SEM [Czenek et al., 2014]; (c) micromechanical representation of TCP crystals as disc-composed polycrystals 6
1.5 Hierarchical structure of paper: (a) paper fiber network, showing the non-uniformly distributed fibers; (b) micromechanical representation of planar fiber network; (c) cross-section across a single paper fiber, revealing its lamellar structure made up by the secondary walls [Chinga-Carrasco, 2011]; (d) microfibrils captured by means of FE-SEM [Chinga-Carrasco, 2011]; (e) elementary components making up the fibrils: cellulose, hemicellulose, and lignin. 8
1.6 Basic steps of continuum micromechanics 12

2.1 Hierarchical organization of bone: (a) photograph of a cross-section through and across a whole long bone (copyright Ralph Hutchings/Visuals Unlimited, Inc.), showing the macrostructure; microstructure featuring either (b) osteonal cortical bone, acquired by SEM [Hang and Barber, 2010], or (c) trabecular struts making up trabecular bone, visualized based on micro-computed tomography data [Metzger et al., 2015]; (d) osteocytic lacunae (brightfield light microscopy image taken by Tim Arnett); (e) ultrastructure, [Prostak and Lees, 1996]; (f) hydroxyapatite crystals, obtained by means of SEM [Weiner and Wagner, 1998]; (g) wet collagen, electron density map of [Orgel et al., 2006] [permission for reproduction requested from publisher: (b) The Royal Society; (c) ASME; (d) Annual Reviews; (e) Springer; (g) PNAS] 26

2.2 Relations between apparent mass densities in extracellular bone matrix in the line of Vuong and Hellmich [2011]: (a) hydroxyapatite versus organic matter, (b) water versus organic matter, and (c) water versus hydroxyapatite; across different species, organs, and ages 37

2.3 Apparent mass densities of water, hydroxyapatite, and organic matter, versus overall mass density of extracellular bone matrix, ρ^{excel}, across different species, organs, and ages 38

2.4 Working mode of pre-osteoblasts and osteoblasts: primary and secondary mineralization of an unmineralized osteoid; (a) pre-osteoblasts lay down an osteoid seam, reinforced by randomly oriented collagen fibrils; (b) primary mineralization: osteoblasts order the collagen fibrils through cell-driven stretch, and mediate, through budding of matrix vesicles from cell processes, the precipitation of hydroxyapatite; (c) secondary mineralization: crystals grow without control of local biological cells 40

2.5 Schematical sketch of spaces in the extracellular bone matrix or ultrastructure, (a) section through the ultrastructural representative volume element perpendicular to the direction of the fibrils, (b) and (c) close-ups 42

2.6 Transmission electron micrographs of cross sections through: (a) mineralized turkey leg tendon [Prostak and Lees, 1996]; (b) human tibia [Prostak and Lees, 1996] and (c) whale rostrum [Zylberberg et al., 1998] 43

2.7 Relative amount of extrafibrillar mineral, $\phi_{\mathrm{HA}}^{\mathrm{exfib}}$, as a function of extracellular mass density ρ^{excel}, according to Hellmich and Ulm [2003] 44

2.8 Scheme concerning hierarchical structure of collagen: (a) collagenous tissue, (b) wet collagen 46

2.9 Water-to-organic mass ratio: diffraction- and swelling rule-based predictions $\mathscr{R}^{\mathrm{pred}}$ versus direct experiments $\mathscr{R}^{\mathrm{exp}}$ 48

2.10 Tissue swelling (a) and evolution of tissue composition (b) during hydration: (a) water-to-organic mass ratio $\mathscr{R}$ over the fibrillar and extrafibrillar volumes making up the tissue; (b) water-to-organic mass ratio $\mathscr{R}$ over the fibrillar and extrafibrillar volume fractions at the tissue scale 49
2.11 Fibrillar swelling (a) and evolution of fibrillar composition (b) during hydration: (a) water-to-organic mass ratio $\mathscr{R}$ over the volumes of molecular collagen, water, and air making up the fibrils; (b) water-to-organic mass ratio $\mathscr{R}$ over the volume fractions of collagen, water, and air at the tissue scale 49
2.12 Predicted vs. experimental diffraction spacing for wet, dry, and partially dehydrated, mineralized tissues 53
2.13 Normalized tissue volume as function of the mineralization degree for different final tissue mass densities 54
2.14 Normalized tissue volume as function of the mineralization degree, for different final tissue mass densities 55
2.15 Micromechanical representation of bone material by means of a six-step homogenization scheme, according to Fritsch et al. [2009c] . . . 58
2.16 Comparison between model predictions and experiments of radial normal stiffness values at the extracellular scale (10 MHz experiments: Lees et al. [1979a, 1983, 1995], see also Table 2.7) 67
2.17 Comparison between model predictions and experiments of axial normal stiffness values at the extracellular scale (10 MHz experiments: Lees et al. [1979a, 1983], see also Table 2.8) 67
2.18 Comparison between model predictions and experiments of radial and axial normal stiffness values at the extravascular scale (2.25 MHz experiments: McCarthy et al. [1990], see also Table 2.9) . 71
2.19 Experimental data used for model validation: Macroscopic elastic stiffness constants of trabecular bone as a function of macroscopic mass density ρ^{μ}; T90...[Turner et al., 1990], K94... [Keaveny et al., 1994], R95... [Rho et al., 1995] 73
2.20 Comparison between model predicted and experimental macroscopic elastic stiffness constants of trabecular bone in transversal direction (50 kHz ultrasonic and mechanical experiments); T90...[Turner et al., 1990], K94... [Keaveny et al., 1994], R95... [Rho et al., 1995] 74
2.21 Comparison between model predicted and experimental macroscopic elastic stiffness constants of trabecular bone in longitudinal direction (50 kHz ultrasonic and mechanical experiments); T90...[Turner et al., 1990], K94... [Keaveny et al., 1994], R95... [Rho et al., 1995] 75

3.1 Representative Volume Element of the porous polycrystal 85
3.2 Orientation of solid needle by means of spherical coordinates θ and ϕ, and definition of corresponding spherical base frame 86

3.3 Quantifying RVE behavior through generalized Eshelby matrix-inclusion problems with eigenstresses 88
3.4 (a) Macroscopic stress-strain relation under pure shear, for different discretizations according to Stroud [1971] and Badel and Leblond [2004], IP... integration point; (b) distribution of the norm of the plastic microstrains over the solid needle phase orientations, at selected macroscopic stress levels 105
3.5 (a) Macroscopic stress-strain relation under uniaxial tension (depicted from the onset of plastic events), for different discretizations according to Stroud [1971] and Badel and Leblond [2004], IP... integration point; (b) distribution of the norm of the plastic microstrains over the solid needle phase orientations, at selected macroscopic stress levels 106
3.6 (a) Macroscopic stress-strain relation under uniaxial compression (depicted from the onset of plastic events), for different discretizations according to Stroud [1971] and Badel and Leblond [2004], IP... integration point; (b) distribution of the norm of the plastic microstrains over the solid needle phase orientations, at selected macroscopic stress levels 107
3.7 Hierarchical organization of bone: (a) photograph of a whole bone; (b) scanning electron micrograph of an osteon, being composed of alternating thick (dense, collagen-rich) and thin (loose, collagen-poor) lamellae, and delineated by a collagen-free cement line [Marotti, 1993], (c) scanning electron micrograph of the isolated cement line [Davies, 2007], (d) micromechanical representation of collagen-free compartment of bone ultrastructure, also referred to as "extrafibrillar space" [Prostak and Lees, 1996]; permission for image reproduction requested (a) from Paul Crompton, University of Wales College of Medicine, (b) from Springer-Verlag New York Inc. for Figures 1 of [Marotti, 1993], and (c) from Elsevier for Figure 2B of [Davies, 2007] 110
3.8 Apparent mass densities (per volume of extracellular space) of water, hydroxyapatite, and organic matter, versus overall mass density of extracellular bone matrix, across different species, organs, and ages; in the line of Vuong and Hellmich [2011] 112
3.9 Comparison of spherical and cylindrical pore shape representation in micromechanical model for porous polycrystal; and comparison with experiments, see [Fritsch et al., 2013b] for experimental sources. 115
3.10 Convergence behavior during return map of trial states onto Mohr-Coulomb surfaces related to 120 solid needle phases arising from Badel-Leblond discretization; residual vector **R** is defined through Eq. (3.84) 118

4.1 RVE of an isotropic solid matrix hosting $\mathcal{N}$ flat, parallel interfaces of identical shape and size, represented as one interface phase . . . 128

4.2 Macroscopic stress-interface displacement relation under pure shear, in dependency of the interface density d; for an elastic matrix with Young's modulus of $E_m = 114\,\text{GPa}$ and Poisson's ratio of $\nu_m = 0.27$; relating to hydroxyapatite [Gilmore and Katz, 1982, Katz and Ukraincik, 1971] 137
4.3 Macroscopic stress-strain relation under pure shear, in dependency of the interface density d; for an elastic matrix with Young's modulus of $E_m = 114\,\text{GPa}$ and Poisson's ratio of $\nu_m = 0.27$; relating to hydroxyapatite [Gilmore and Katz, 1982, Katz and Ukraincik, 1971] 137
4.4 Macroscopic stress-strain relation under pure shear showing kinematic hardening, for an interface density of $d = 0.5$, and an elastic matrix with Young's modulus of $E_m = 114\,\text{GPa}$ and Poisson's ratio of $\nu_m = 0.27$; relating to hydroxyapatite [Gilmore and Katz, 1982, Katz and Ukraincik, 1971] 138
4.5 Macroscopic stress-strain relation in dependency of the number of interfaces N, under pure shear loading (LC1), and under combined shear and tension (LC2), for interface densities $d_1 = 0.25$, $d_2 = 0.5$, $d_3 = 0.75$, $d_4 = 1$, $d_5 = 1.25$ 145
4.6 SMD force as a function of displacement 147

5.1 Probability density function of attenuation-related grey values of a sham rat femur 156
5.2 X-ray attenuation coefficients of hydroxyapatite, organics, water, and air as functions of the photon energy, according to NIST-database on http://physics.nist.gov/PhysRefData/XrayMassCoef/cover.html [Bolz and Tuve, 1973, Eastoe, 1955, Hubbell and Seltzer, 1996, Lees, 1987, Searle, 1934] 158
5.3 Averaging (a-b-c) or splitting up (c-b-a) X-ray attenuation coefficients or volume fractions within a bone tissue voxel: (a) elementary components with voxel-specific volume fractions (subvolumes), and with voxel-invariant attenuation coefficients and corresponding grey values, (b) water and "*solid* - ($HA + org$) compound" with voxel-specific volume fractions (subvolumes), and with voxel-invariant attenuation coefficients and corresponding grey values, (c) overall bone tissue with voxel-specific attenuation coefficient and corresponding grey value 161
5.4 Identification of the applied X-ray energy and of its role as argument in the concave function for the water volume fraction in the "average" bone tissue voxel, as given in (5.13) 162
5.5 Mechanical characterization of a bone tissue voxel by means of a four-step micromechanics model [Morin and Hellmich, 2014]: (a) bone tissue voxel with indication of volume fractions of mineral, organics, and water; (b) RVE of extracellular bone matrix – bone ultrastructure; (c) RVE of mineralized fibril; (d) RVE of extrafibrillar space; (e) RVE of wet collagen; (x_1, x_2: transverse material directions; x_3: axial material direction) 164

5.6 Probability density functions of attenuation-related grey values: (a) sham rats, (b) OVX rats 168
5.7 (a), (b) Line constants a and b relating grey values to attenuation coefficients, as functions of the photon energy, (c) Water volume fractions in the “average” bone voxel, as functions of the photon energy 169
5.8 Probability density functions of X-ray attenuation coefficients: (a) sham rats, (b) OVX rats 172
5.9 Grey value dependencies of composition and elasticity of bone tissue in sham rat #6: (a) volume fractions, (b) stiffness tensor components, (c) Young’s and shear moduli, (d) Poisson’s ratios 173
5.10 Grey value dependencies of composition and elasticity of bone tissue in OVX rat #6: (a) volume fractions, (b) stiffness tensor components, (c) Young’s and shear moduli, (d) Poisson’s ratios 174
5.11 Distribution of the mineral volume fraction, f_{HA}^{voxel}, and of the engineering constants – E_1^{voxel}, E_3^{voxel}, G_{12}^{voxel}, ν_{12}^{voxel}, ν_{13}^{voxel} – throughout the bone tissue compartment of the distal femur of sham rat #6; the color bars are labelled by extreme values, as well as by the most frequently occurring one 178
5.12 Distribution of the mineral volume fraction, f_{HA}^{voxel}, and of the engineering constants – E_1^{voxel}, E_3^{voxel}, G_{12}^{voxel}, ν_{12}^{voxel}, ν_{13}^{voxel} – throughout the bone tissue compartment of the distal femur of OVX rat #6; the color bars are labelled by extreme values, as well as by the most frequently occurring one 179
5.13 Example of a reconstructed micro-CT scan showing a cross section through the distal femur of sham rat #9 181

6.1 (a) Photograph of one of the produced scaffolds, obtained by means of stereomicroscopy; (b) cross section of one fiber, acquired by means of scanning electron microscopy, showing the distribution of PLGA and TCP inclusions, as well as large TCP agglomerations, within the PHBV matrix; and (c) one layer of the image stack obtained by means of microCT, relating to cross-section A-A indicated in (a) 196
6.2 Relative frequency distribution of the grey values obtained from microCT scanning of the scaffold depicted in Figure 6.1, together with the PHBV phantom; (b) relates to a zoom-out from (a) 199
6.3 (a) X-ray attenuation coefficients of PHBV, PLGA, TCP, and air, as functions of the photon energy, according to the NIST-database [Hubbel and Seitzer, 2004]; (b) $\mu_{\text{scaff}}^{\text{peak}}(\epsilon)$ according to both Eqs. (6.6) and (6.7), exhibiting an intersection at $\epsilon = 35.55\,\text{keV}$ 200

6.4 (a) Three-dimensional reconstruction of the scaffold structure based on the data obtained from microCT imaging, with indication of the rectangular prism cut out of the reconstructed scaffold structure serving as basis for the FE models; FE models with varying accuracy, i.e. consisting of (b) 59443 elements (with $7\times7\times7$ voxels combined into one element), and of (c) 2575100 elements (with $2\times2\times2$ voxels combined into one element) 202
6.5 Distribution of elastic Young's modulus and Poisson's ratio across the scaffold; (a) underlying CT-derived distribution of grey values in specific cross-section, and (b) corresponding distribution of Young's modulus and Poisson's ratio; (c) three-dimensional distribution of these elastic constants; one finite element follows from merging of $3\times3\times3$ voxels, with grey value averaging according to Eq. (6.10) . 206
6.6 Distributions of minimum principal strains (a) and (b), as well as minimum principal stresses (c) and (d) across the scaffold when subjected to uniaxial compression; based on a heterogeneously distributed scaffold composition (a) and (c), as well as on a homogeneous scaffold composition (b) and (d); the FE model has been built by merging $3\times3\times3$ voxels into one finite element, leading to 761631 elements 208

7.1 SEM micrograph of paper exhibiting a porous pulp fiber network predominantly oriented within the paper plane, permission for reproduction granted by Tryding [1996]. 215
7.2 (a) Planar sheet of length L, made of fibrous material (e.g. paper); $\mathbf{x}$ stands for the position vector labelling "material points", and $\mathbf{\Sigma}$ and $\mathbf{E}$ for (position-dependent, "macroscopic") stress and strain tensors prevailing at these material points; ($\mathbf{e}_1$, $\mathbf{e}_2$, $\mathbf{e}_3$) is an orthonormal base frame aligned with the sheet plane; (b) zooming out one material point, appearing as "representative volume element - RVE" at a length scale $\ell \ll \mathscr{L}$; the latter is made up of cylindrical fibers oriented in all planar directions, and of oblate spheroidal pores, which are aligned with the paper plane as well . . 216
7.3 Eshelby-Laws inclusion problem representation for (a) infinitely many fiber phases, and (b) one pore phase 220
7.4 Histogram of logarithmic sample of mean softwood pulp fiber Young's moduli in longitudinal direction 223
7.5 Relative approximation error concerning the pore stiffness approaching zero; according to Eq. (7.31), for selected values of the porosity 224
7.6 Micromechanically predicted in-plane Young's modulus of the planar network, as a function of the porosity of the latter 225
7.7 Micromechanically predicted in-plane Poisson's ratio of the planar network, as a function of the porosity of the latter 225
7.8 Homogenized in-plane Young's modulus of paper normalized with respect to fiber elastic modulus, for isotropic and transversely isotropic fiber phases; as function of porosity 226

7.9 Experimental validation of micromechanics model described in Section 2: prediction based on 5 % and 95 % quantiles of the pulp fiber stiffness satisfactorily frame experimental data on the paper level . 227

List of Tables

2.1 Bone composition from dehydration-demineralization experiments of Lees et al. (1979)[a] and Lees et al. (1995)[b] . . . 29

2.2 Mineralized tendon composition from dehydration-demineralization experiments of Lees et al. (1992) . . . 30

2.3 Bone composition from dehydration-demineralization experiments of Lees et al. (2003) . . . 31

2.4 Bone composition from dehydration-deorganification experiments of Gong et al. (1964) . . . 32

2.5 Bone composition from dehydration-ashing experiments of Biltz and Pellegrino (1969) . . . 33

2.6 Bone composition from dehydration-ashing experiments of Burns (1929)[a] and Hammett (1925)[b] . . . 34

2.7 Experimental characterization of various cortical bone samples by Lees et al. [1979a][a], Lees et al. [1983][b], and Lees et al. [1995][c]; Macroscopic and extracellular bone mass densities, ρ^{μ} and ρ^{excel}, longitudinal ultrasonic velocities in radial material directions, v_1, experimental and model-predicted normal stiffness values in radial direction, C_{1111}^{exp} and C_{1111}^{pred}, respectively . . . 65

2.8 Experimental characterization of various cortical bone samples by Lees et al. [1979a][a] and Lees et al. [1983][b]; Macroscopic and extracellular bone mass densities, ρ^{μ} and ρ^{excel}, longitudinal ultrasonic velocities in axial material directions, v_3, experimental and model-predicted normal stiffness values in axial direction, C_{3333}^{exp} and C_{3333}^{pred}, respectively . . . 66

2.9 Experimental characterization of equine cortical bone samples by McCarthy et al. [1990]; Macroscopic and extravascular bone mass densities, ρ^{μ} and ρ^{exvas}, longitudinal ultrasonic velocities in radial and axial material directions, v_1 and v_3, experimental and model-predicted normal stiffness values in radial and axial direction, C_{1111}^{exp}, C_{3333}^{exp}, C_{1111}^{pred}, C_{3333}^{pred}, respectively . . . 69

3.1 15 different needle orientations according to integration formulas of Stroud [1971] . . . 95

3.2 28 different needle orientations according to integration formulas of Stroud [1971] . . . 96

3.3 Properties of solid and pore material phases, for the case of porous hydroxyapatite polycrystals, see Section 3.7 for experimental details 106

3.4 Yield and ultimate macroscopic stresses [in MPa] computed for uniaxial tension, uniaxial compression, and pure shear: based on different discretization schemes and different numbers of integration points (#IP) . . . 107
3.5 Characterization of equine cortical bone samples of McCarthy et al. [1990]: experimentally determined macroscopic mass densities and vascular porosities; extravascular and extracellular mass densities according to Eq. (3.99) and (3.100); volume fractions of hydroxyapatite crystal needle phase and of pore phase according to "universal" composition rules reported in [Hellmich and Ulm, 2003, Morin and Hellmich, 2013, Morin et al., 2013, Vuong and Hellmich, 2011]; and shear strength values predicted by the micromechanics model from Section 3.6, based on the material properties of Table 3.3. . . . 114

5.1 Most frequently occurring grey values of air, fluid and bone tissue, and threshold grey values of the sham rats . . . 167
5.2 Most frequently occurring grey values of air, fluid and bone tissue, and threshold grey values of the OVX rats . . . 167
5.3 Line constants a and b, volume fractions, as well as attenuation coefficients and densities of the average bone tissue at $\overline{\varepsilon} = 14\,\mathrm{keV}$ of the sham rats . . . 170
5.4 Line constants a and b, volume fractions, as well as attenuation coefficients and densities of the average bone tissue at $\overline{\varepsilon} = 14\,\mathrm{keV}$ of the OVX rats . . . 170
5.5 Elasticity of extracellular bone tissue: Most frequent, minimum and maximum values for transverse and axial Young's moduli, isotropic shear moduli, and inplane and out-of-plane Poisson's ratios; E_1^{voxel}, E_3^{voxel} and G_{12}^{voxel} in [GPa], ν_{12}^{voxel} and ν_{12}^{voxel} in [–]; given for all 10 image stacks illustrating sham rat femurs . . . 175
5.6 Elasticity of extracellular bone tissue: Most frequent, minimum and maximum values for transverse and axial Young's moduli, isotropic shear moduli, and inplane and out-of-plane Poisson's ratios; E_1^{voxel}, E_3^{voxel} and G_{12}^{voxel} in [GPa], ν_{12}^{voxel} and ν_{12}^{voxel} in [–]; given for all 10 image stacks illustrating OVX rat femurs . . . 176

6.1 Young's moduli and Poisson's ratios of the constituents of the composite material studied in this paper . . . 205

Chapter 1

Introduction

Porous polycrystal-type microstructures built up by needle-like platelets or sheets are characteristic for numerous natural and man-made materials such as nacre, bone, metals, ceramics, polymers, rocks, and cement minerals [Wenk and Van Houtte, 2004]. Mechanical modeling of porous polycrystals may pose considerable challenges: classical two-phase self-consistent schemes [Hill, 1965a] can not capture the mechanical behavior of high-porosity materials, while discretization of each and every single crystal by finite elements may require disproportionate efforts in terms of CPU, or may be even impossible due to restricted access to the required microstructural details. As a recent remedy, continuum micromechanics formulations were extended as to involve an infinite number of non-spherical crystal phases, interacting with a spherical pore phase [Fritsch et al., 2006, 2009b], see Figure 1.1. Such formulations allow for satisfactory predictions of the (poro-)elasticity and brittle strength of vast classes of porous polycrystals, such as hydroxyapatite, bioactive glass-ceramics, gypsum, alumina, or zirconia (see Figure 1.2) [Fritsch et al., 2013b].

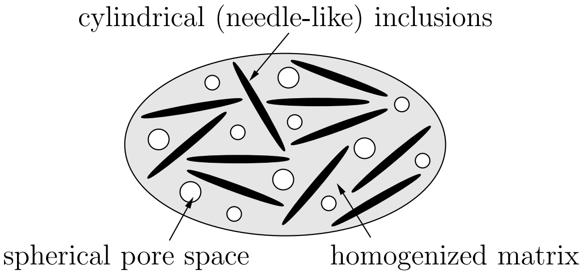

Figure 1.1: Representative volume element of porous polycrystals: uniform orientation distribution of cylindrical (needle-like) inclusions and spherical pores

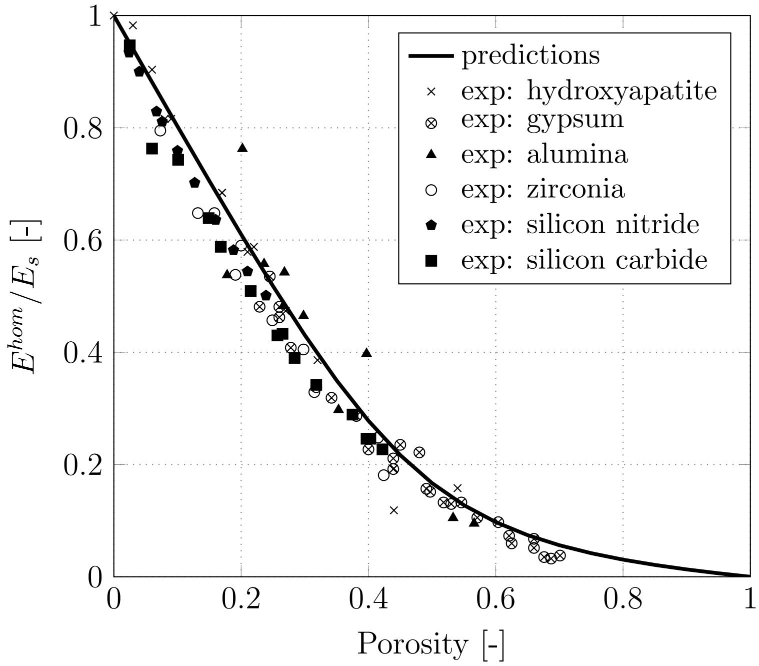

Figure 1.2: Needle-based micromechanics predictions for normalized Young's modulus E^{hom}/E_s, as a function of porosity, for a wide range of Young's modulus and Poisson's ratios of crystal solid phase; and comparison with experiments, see [Fritsch et al., 2013b] for experimental sources.

The central aim of this work is (i) to extend and refine the present contribution towards micro-elastoplasticity theory of porous polycrystals; (ii) to modify the precedent work towards uniform orientation distribution of needle-like phases in planar (2D) networks; and (iii) to strengthen the argument on the significant potential of such micromechanics models by showing further application examples relevant to medical practice.

1.1 Investigated materials

1.1.1 Bone

Bone has a hierarchical, highly complex structure characterized by a varied arrangement of different microstructures built up by its elementary components over a multitude of length scales. Understanding bone's mechanical properties is an ongoing research, in which, the key element is the profound understanding of the mechanical behavior of its elementary building blocks, as well as the structural relationships among them at various levels of the hierarchical organization:

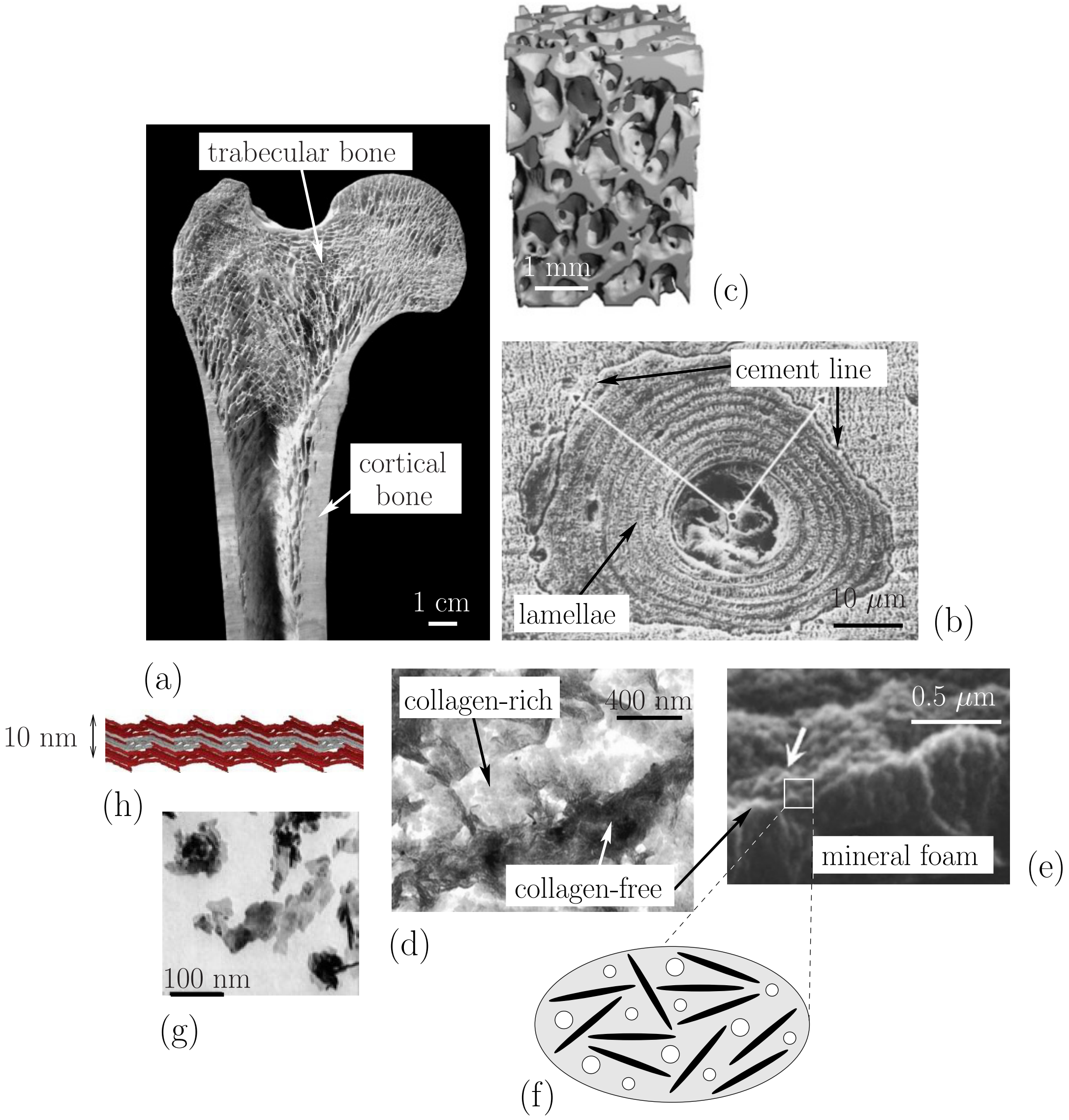
trabecular bone
cortical bone
1 cm
(a)
1 mm
(c)
cement line
lamellae
10 μm
(b)
10 nm
(h)
collagen-rich
400 nm
collagen-free
(d)
0.5 μm
mineral foam
(e)
100 nm
(g)
(f)

Figure 1.3: Hierarchical structure of bone: (a) photograph of a cross-section through a whole long bone, showing the macrostructure made up by cortical and trabecular bone [taken by Paul Crompton]; (b) scanning electron micrograph of an osteon, being composed of alternating collagen-rich and collagen-poor lamellae, and delineated by a collagen-free cement line [Ascenzi and Bonucci, 1972]; (c) trabecular struts making up trabecular bone; (d) bone ultrastructure [Prostak and Lees, 1996]; (e) scanning electron micrograph of the isolated cement line [Davies, 2007]; (f) micromechanical representation of collagen-free compartment of bone ultrastructure; (g) hydroxyapatite crystals, obtained by means of SEM [Weiner and Wagner, 1998]; (h) wet collagen, electron density map of [Orgel et al., 2006].

- *Macroscopically*, there are two types of bones: (i) the cortical or compact bone making up 80% of the skeleton and found in the shafts of long bones, and the outer surfaces of flat bones; and (ii) the trabecular or spongy bone, characterized by an interconnected rod-like and plate-like structure, occuring at the end of long bones, through the length of short bones, or in-between the compact bone shells of flat bones [Dempster et al., 2006], see Figure 1.3(a).

- At the *microstructural* observation scale of several hundred micrometers to millimeters, structural subunits called osteons build up the cortical bone, see Figure 1.3(b); while closer inspection of the trabecular bone reveals the flat planes of the spongy bone known as trabeculae, see Figure 1.3(c).

- At the *ultrastructural* level of few hundred nanometers, one can distinguish collagen-rich domains referred to as the mineralized collagen fibrils, and collagen-free domains, denoted as the extrafibrillar space, see Figure 1.3(d). These collagen-free domains (the so-called mineral foam) are also characteristic for the cement line (outer boundary of the osteons, see Figure 1.3(e)). Cement lines contain hydroxyapatite and water with noncollageneous organics making up a polycrystalline material as seen in Figure 1.3(f).

- Finally, at an observation scale of several nanometers, the *elementary building blocks* of bone can be distinguished: plate-shaped crystals consisting of impure hydroxyapatite (see Figure 1.3(g)); slender, helically round collagen molecules (see Figure 1.3(h)); different non-collagenous organic molecules; and water.

Theoretical modeling attempts have been mainly focused on macrostructural and microstructural length scales, where concepts of cellular solid mechanics [Gibson and Ashby, 1997] and of micro Finite Element models [Van Rietbergen et al., 1995] are well established and have become an integral part of bone biomechanics. Hereby, the reconstruction of bone microstructure entering such models is attained by means of different medical imaging techniques, such as Computed Tomography.

The theoretical understanding of the ultrastructural scales of bone and below required deeper interpretation of the material's composition, morphology, and mechanical properties. First of all, at this scale of observation, the exact composition of a bone sample under the microscope can not be captured "by the naked eye". A pioneering experimental campaign carried out by Lees and coworkers [Lees, 1987, 2003, Lees and Heeley, 1981, Lees and Page, 1992, Lees et al., 1979a, 1983, 1995] aimed at determining the chemical composition of bone tissues by means of dehydration-demineralization tests, dehydration-deorganification tests, and dehydration-ashing tests. Careful analysis of the data, so as to extract chemical concentrations of hydroxyapatite, water, and organic matter in the ultrastructural level of bone, revealed a unique bilinear relationship between organic and mineral concentrations across different species, different organs, and different age groups [Vuong and Hellmich, 2011].

As regards the contribution of the elementary constituents to the mechanical behavior of bone, Hellmich and Ulm [2002b] identified collagen and hydroxyapatite as the governing elements of the ultrastructural elastic stiffness. However, the organization of these elementary components within the ultrastructure of mineralized tissues had provoked some controversy concerning (i) the mineral-collagen distribution, and (ii) the mineral-collagen interaction within the ultrastructure. Hellmich and Ulm [2003] showed that the average mineral concentration in the non-collageneous space of the ultrastructure is the same inside and outside the fibrils (see Section 2.4 for further details). Concerning the mineral-collagen interaction, Hellmich et al. [2004a] developed three different collagen-mineral micromechanical representations, and validated these based on independent sets of experiments. It turned out that both concepts of "mineral-reinforced collagen matrix" [Currey, 1969] and "mineral matrix with collagen inclusions" [Cusack and Miller, 1979, Lees and Heeley, 1981, Lees et al., 1979b, 1990] dividing the scientific community are relevant, but at different observation scales. In line with the "mineral-reinforced collagen matrix" concept, we consider at an observation scale of some tens of nanometers, a "collagen matrix material", called wet collagen, built up by 1.2 nm thick collagen molecules and intermolecular water. At the scale of several hundred nanometers, the mineralized collagen fibril is formed by wet collagen and by mineralized crystal aggromerations, interpenetrating each other. At a scale of 5-10 micrometers, however, the mineralized collagen fibrils are embedded in an extrafibrillar mineral foam, in line with the concept of "mineral matrix with (mineralized) collagen inclusions" [Fritsch and Hellmich, 2007].

In Chapter 3, we target the micro-elastoplasticity theory of porous polycrystals, and experimentally validate it on push-out tests on pieces of Haversian lamellar bone [Bigley et al., 2006]. Such tests produce an almost pure shear (micro-)stress state at the outer boundaries (cement lines) of the osteons. These cement lines are collagen-free, so the RVE depicted on Figure 1.1 turns out as relevant for the extrafibrillar mineral foam making up the cement line material.

1.1.2 Bone biomaterials

Tissue engineering have advanced dramatically in the past three decades with the aim of restoring, replacing or regenerating defective tissues. Cells, scaffolds and growth-stimulating signals are generally referred to as the tissue engineering triad, the key components of engineered tissues [Chan and Leong, 2008]. Normal cells in human tissues reside achorage-dependent in a solid matrix called extracellular matrix (ECM), which provides the physical environment, biological signals, and growth factors enabling cell ingrowth; gives the tissue its structural and mechanical properties; and provides a degradable environment allowing for tissue remodeling. Intrinsically, the best scaffold for engineered tissues should be the extracellular matrix in its native state [Chan and Leong, 2008]. However, due the multitude of its functions, and to the unique coupling of its physical and mechanical properties making the exact reproduction of ECM difficult, the contemporary concept of tissue engineering is to mimic the functions of native extracellular matrix, at least partially [Chan and Leong, 2008]. Bone tissue engineering (BTE) has brought the advent of entirely new classes of hierarchically organized, multiporous materials [Bertrand and Hellmich, 2009] possessing features such as a suitable porous

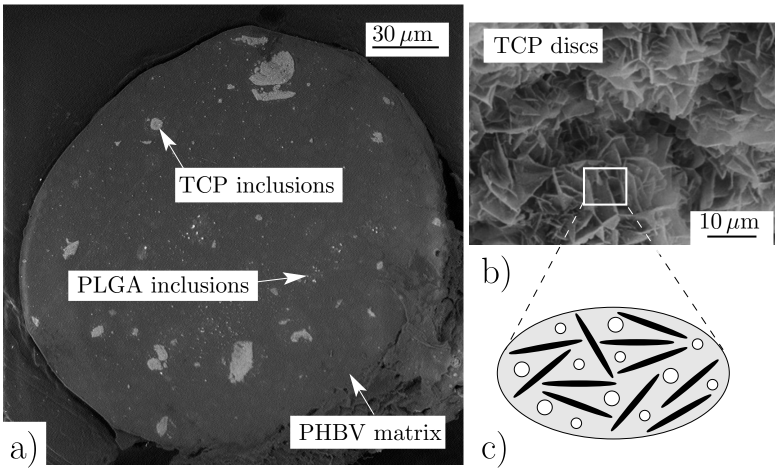

Figure 1.4: (a) Cross-section of a fiber making up the three-phase composite scaffold; (b) TCP discs captured by means of SEM [Czenek et al., 2014]; (c) micromechanical representation of TCP crystals as disc-composed polycrystals

structure (pore size and pore interconnectivity); good bioactivity, biodegradability, biocompatibility, and predictive rate of degradation; customized shape and matching mechanical properties to adapt the damaged bone tissue. Conventional materials often lack at least one of these features, which has emerged the blending of synthetic and natural polymers or the usage of composite materials in order to improve scaffold properties. Chapter 6 represents a three-phase composite material made up by PHBV (poly(3-hydroxybutyrate-co-3-hydroxyvalerate)), PLGA (poly(lactic-co-glycolide)), as well as TCP (tricalcium phosphate hydrate) uniting supreme characteristics: the high surface-to-volume ratio and the advantageous mechanical properties of PHBV are complemented by the high bioactivity of TCP, and the biodegradability of PLGA, see Figure 1.4. Herein, the elastic constants of the scaffold components are taken from experiments. However, a recent micromechanics study [Fritsch et al., 2013b] based on self-consistent estimates for infinitely many, spatially oriented crystal phases has revealed that the Young's modulus of disc-composed polycrystals (also characteristic for TCP) closely follow a power law relation with the (nano)porosity. This turns out helpful when modeling pure ceramic scaffolds.

1.1.3 Paper

Paper is an interesting engineering material most commonly utilised in every industry. Paper is formed by draining a suspension of fibers in a fluid through a filter screen to form a sheet of pulp fibers [Xia et al., 2002]. The final paper is a heterogeneous composition characterized by a hierarchical structure:

- At a scale of few hundred micrometers, paper consists of a network of non-uniformly distributed fibers and interfibrious porosity, see Figure 1.5(a). Here we are concerned with the arrangement of fibers, the properties of individual fibers, and the nature and frequency of the fiber-to-fiber bonds. The polycrystalline morphology for 3D (spacial) networks of solid fibers will be adapted at this scale to the planar fiber network of paper (Figure 1.5(b)).
- Closer observation of the fibers reveals that the fibers are actually filament wound composite systems [Baum, 1984]. The fiber wall is composed of different layers: the primary wall (P) and the secondary walls ($S1$, $S2$ and $S3$), see Figure 1.5(c). The cellulose fibrils building up these layers are arranged

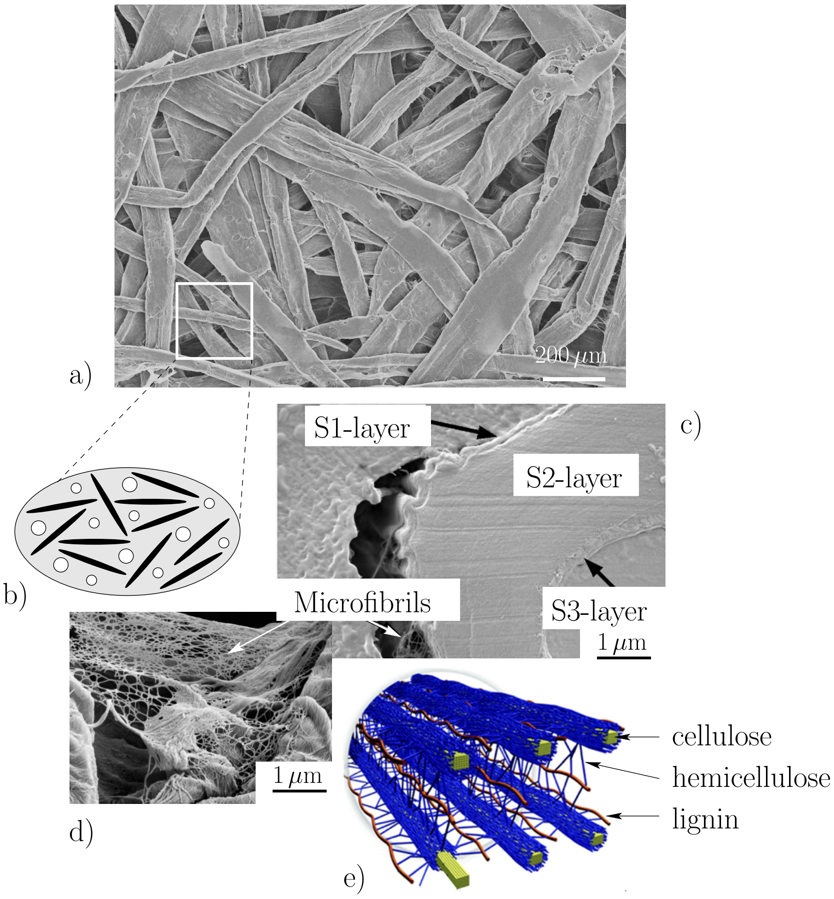

Figure 1.5: Hierarchical structure of paper: (a) paper fiber network, showing the non-uniformly distributed fibers; (b) micromechanical representation of planar fiber network; (c) cross-section across a single paper fiber, revealing its lamellar structure made up by the secondary walls [Chinga-Carrasco, 2011]; (d) microfibrils captured by means of FE-SEM [Chinga-Carrasco, 2011]; (e) elementary components making up the fibrils: cellulose, hemicellulose, and lignin.

in a regular fashion which differs in the various layers within the fiber wall (see Figure 1.5(d)), and are held together by a polymer matrix composed of hemicellulose, lignin, and extractives, see 1.5(e).

Various mathematical models have been proposed relating stresses and strains directly at the paper material level, neglecting the eminent role of the microstructural details (fiber arrangement, mechanical properties of fibers) governing the mechanical behavior of the overall paper-like materials.

Herein, our strategy for relating the aforementioned multiscale organizations of bone, bone biomaterials, and paper to effective elastic properties, relies on homogenization theory within the framework of continuum micromechanics [Hill, 1963, Suquet, 1997b, Zaoui, 2002], as described next.

1.2 Theoretical framework: continuum micromechanics

Bone, bone biomaterials and paper - just as the majority of biological and engineering materials - are microscopically heterogeneous even if they appear homogeneous at some natural scale of observation. Heterogeneous materials consist of clearly distinguishable constituents ("phases") that differ in mechanical and physical properties; and may themselves be inhomogeneous at smaller length scales. To describe such a material behavior, many researchers have embarked on continuum micromechanics-based approaches, see examples for concrete [Bernard et al., 2003, Constantinides and Ulm, 2004, Hellmich et al., 1999]; bone [Fritsch and Hellmich, 2007, Hamed et al., 2010, Hellmich and Ulm, 2002a, Hellmich et al., 2004a,b]; and wood [Hofstetter et al., 2005].

The central aim of continuum micromechanics is providing proper and reliable determination of macroscopic (or "large" scale) behavior of a medium which exhibits microscopic (or "small" scale) heterogeneity on the basis of appropriate and available microstructural information [Markov, 2000]. The basic idea is that of *homogenization*, which consists in replacement of a piece of microheterogeneous solid by a fictitious homogeneous one, which behaves globally in the same way [Zaoui, 2002]. As the first step of the homogenization procedure, we define a Representative Volume Element (RVE): a volume, which is sufficient in size to contain all information necessary to describe the behavior of the material at the macroscopic scale. On one hand, it is small enough from a macroscopic point of view and could be thus treated as a typical "point" of the investigated heterogeneous medium. On the other hand, it should be large enough in the microscopic scale, in order to contain a large number of single inhomogeneities and therefore to be indeed typical "representative" for the microstructure of the solid [Markov, 2000]. The length scales typically covered in this concept range from the low micrometer scale to macroscopic samples with sizes of millimeters to meters.

Micromechanics models (as shown in more detail for bone in Chapter 2, Section 2.7.1) are based on the assumption that these "microscopic" and "macroscopic" scales are well separated. Therefore, the studied RVE has a certain intermediate dimension ℓ, which is two-to-threefold when compared to the dimension of inhomogeneities d within the RVE [Drugan and Willis, 1996], but is 5 to 50-times smaller than the macroscopic dimensions of the whole sample $\mathscr{L}$, or the fluctuation length λ of its prescribed mechanical loading [Kohlhauser and Hellmich, 2013]. This condition is generally referred to as the separation of scales principle, and mathematically reads as

$$d \ll \ell \ll \mathscr{L} \tag{1.1}$$

For a volume element V_{RVE} of an inhomogeneous material that satisfies the separation of scales principle, homogenization relations take the form of volume averages of some variable $f(\mathbf{x})$

$$\langle f \rangle = \frac{1}{V_{RVE}} \int_{V_{RVE}} f(\mathbf{x})\, dV \tag{1.2}$$

The homogenization relation for stress and strain tensors can be given as

$$\mathbf{\Sigma} = \langle \boldsymbol{\sigma} \rangle = \frac{1}{V_{RVE}} \int_{V_{RVE}} \boldsymbol{\sigma}(\mathbf{x})\, dV \tag{1.3}$$

$$\mathbf{E} = \langle \boldsymbol{\varepsilon} \rangle = \frac{1}{V_{RVE}} \int_{V_{RVE}} \boldsymbol{\varepsilon}(\mathbf{x})\, dV \tag{1.4}$$

Eqs. (1.3) and (1.4) are also known as average theorems, whereby $\mathbf{\Sigma}$ and $\mathbf{E}$ are fully determined by surface displacements and tractions; with the local stress fields $\boldsymbol{\sigma}(\mathbf{x})$ being self-equilibrated (in the absence of volume forces), and the local strain fields $\boldsymbol{\varepsilon}(\mathbf{x})$ are geometrically compatible. If the displacements show discontinuities due to interfaces between constituents (as e.g. investigated in Chapter 4), correction terms involving the displacement jumps across the interfaces are introduced (see Eq. (4.5)). Additionally, a field of equilibrated local stresses and an independent field of compatible strains obey the following relation

$$\mathbf{\Sigma} : \mathbf{E} = \frac{1}{V_{RVE}} \int_{V_{RVE}} \boldsymbol{\sigma}(\mathbf{x}) : \boldsymbol{\varepsilon}(\mathbf{x}) dV = \langle \boldsymbol{\sigma} \rangle : \langle \boldsymbol{\varepsilon} \rangle \tag{1.5}$$

also known as Hill's macrohomogeneity condition [Hill, 1967], which states that the strain energy density of the microfields equals the strain energy density of the macrofields, making the microscopic and macroscopic descriptions energetically equivalent.

At the microscopic scale the stresses and strains are linearly related by the elastic stiffness tensors $\mathbb{c}(\mathbf{x})$

$$\boldsymbol{\sigma}(\mathbf{x}) = \mathbb{c}(\mathbf{x}) : \boldsymbol{\varepsilon}(\mathbf{x}) \tag{1.6}$$

In the above form Eq. (1.6) applies to linear elastic behavior, i.e. no eigenstrains are present, but it can be extended into the nonlinear range to tackle elastoplastic material behavior as described in detail in Chapter 3.
The microscopic stresses and strains are linked to corresponding macroscopic responses by the concentration relations

$$\boldsymbol{\sigma}(\mathbf{x}) = \mathbb{B}(\mathbf{x}) : \boldsymbol{\Sigma} \tag{1.7}$$

$$\boldsymbol{\varepsilon}(\mathbf{x}) = \mathbb{A}(\mathbf{x}) : \mathbf{E} \tag{1.8}$$

whereby $\mathbb{B}(\mathbf{x})$ and $\mathbb{A}(\mathbf{x})$ are the so-called stress and strain concentration tensors, respectively. On the basis of the stress (or strain) concentration tensors, the homogenized ("macroscopic") stiffness (or compliance) tensor, $\mathbb{C}$ (or $\mathbb{D} = \mathbb{C}^{-1}$), can be derived by combination of Eqs. (1.3), (1.6) and (1.8)

$$\mathbb{C} = \langle \mathbb{c}(\mathbf{x}) : \mathbb{A}(\mathbf{x}) \rangle \tag{1.9}$$

As exact expressions for concentration tensors $\mathbb{A}(\mathbf{x})$ are generally unknown, certain approximations in terms of elasticity estimates are applied. Since the microstructure within the RVE is so complex that it can not be described in complete detail, homogeneous subdomains, called material phases are introduced with known quantitative- (such as volume fractions, elastic properties) and qualitative properties (e.g. phase shapes and interactions). The concentration problem in terms of *phases* with index r leads to the following form of the elastic law

$$\boldsymbol{\sigma}_r = \mathbb{c}_r : \boldsymbol{\varepsilon}_r \tag{1.10}$$

of the the average rules

$$\boldsymbol{\Sigma} = \sum_r f_r \boldsymbol{\sigma}_r \tag{1.11}$$

$$\mathbf{E} = \sum_r f_r \boldsymbol{\varepsilon}_r \tag{1.12}$$

of the concentration relations

$$\boldsymbol{\sigma}_r = \mathbb{B}_r^{est} : \boldsymbol{\Sigma} \tag{1.13}$$

$$\boldsymbol{\varepsilon}_r = \mathbb{A}_r^{est} : \mathbf{E} \tag{1.14}$$

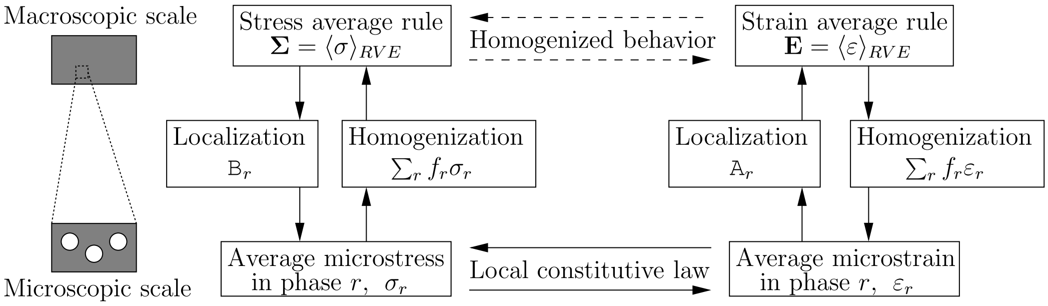
Macroscopic scale
Stress average rule
$\boldsymbol{\Sigma} = \langle \sigma \rangle_{RVE}$
Homogenized behavior
Strain average rule
$\mathbf{E} = \langle \varepsilon \rangle_{RVE}$
Localization
$\mathbb{B}_r$
Homogenization
$\sum_r f_r \sigma_r$
Localization
$\mathbb{A}_r$
Homogenization
$\sum_r f_r \varepsilon_r$
Average microstress
in phase r, σ_r
Local constitutive law
Average microstrain
in phase r, ε_r
Microscopic scale

Figure 1.6: Basic steps of continuum micromechanics

and of the estimates for stiffnesses

$$\mathbb{C}^{est} = \sum_r f_r \mathbb{c}_r : \mathbb{A}_r^{est} \tag{1.15}$$

with f_r as the volume fraction of phase r. The phase-specific stress and strain concentration tensors - which are key to solve both the macro-to-micro concentration (1.13)-(1.14) and the micro-to-macro homogenization problems (1.15) (see Figure 1.6) - can be derived from an Eshelby-type matrix-inclusion problem [Eshelby, 1957].

Eshelby solution Eshelby [1957] showed that if a single ellipsoidal inclusion (with uniform stiffness $\mathbb{c}_i$) in an infinite, linear matrix (with uniform stiffness $\mathbb{C}^0$) is subjected to homogeneous strains $\mathbf{E}^0$ at infinity, the strain states in the inclusion are uniform and related to macroscopic strains $\mathbf{E}^0$ by the expression [Eshelby, 1957]

$$\boldsymbol{\varepsilon}_i = \left[\mathbb{I} + \mathbb{P}_i^0 : \left(\mathbb{c}_i - \mathbb{C}^0\right)\right]^{-1} : \mathbf{E}^0 \tag{1.16}$$

where $\mathbb{I}$ stands for the fourth-order identity tensor with components $I_{ijkl} = \frac{1}{2}\left(\delta_{ik}\delta_{jl} + \delta_{il}\delta_{jk}\right)$, where δ_{ij} is the Kronecker delta with $\delta_{ij} = 1$ if $i = j$ and zero otherwise; $\mathbb{P}^0$ denotes the fourth-order Hill tensor depending on the shape of inclusion and on the elastic properties of the matrix.

For the estimation of the strain concentration tensor of phase r, the strains $\boldsymbol{\varepsilon}_r$ in each phase are considered equal to those of an ellipsoidal inhomogeneity with phase stiffness $\mathbb{c}_r$, submitted to macroscopic strain $\mathbf{E}^0$ at infinity

$$\boldsymbol{\varepsilon}_r = \left[\mathbb{I} + \mathbb{P}_r^0 : \left(\mathbb{c}_r - \mathbb{C}^0\right)\right]^{-1} : \mathbf{E}^0 \tag{1.17}$$

Combination of Eq. (1.12) with (1.17) results in

$$\mathbf{E} = \sum_r f_r \boldsymbol{\varepsilon}_r = \left\{ \sum_r f_r \left[\mathbb{I} + \mathbb{P}_r^0 : \left(\mathbb{c}_r - \mathbb{C}^0 \right) \right]^{-1} \right\} : \mathbf{E}^0 \tag{1.18}$$

Elimination of $\mathbf{E}^0$ yields the sought estimate of the strain concentration tensor as

$$\mathbb{A}_r^{est} = \left[\mathbb{I} + \mathbb{P}_r^0 : \left(\mathbb{c}_r - \mathbb{C}^0 \right) \right]^{-1} : \left\{ \sum_s f_s \left[\mathbb{I} + \mathbb{P}_s^0 : \left(\mathbb{c}_s - \mathbb{C}^0 \right) \right]^{-1} \right\}^{-1} \tag{1.19}$$

which in combination with (1.15) results in the homogenized macroscopic stiffness

$$\mathbb{C}^{est} = \sum_r f_r \mathbb{c}_r : \left[\mathbb{I} + \mathbb{P}_r^0 : \left(\mathbb{c}_r - \mathbb{C}^0 \right) \right]^{-1} : \left\{ \sum_s f_s \left[\mathbb{I} + \mathbb{P}_s^0 : \left(\mathbb{c}_s - \mathbb{C}^0 \right) \right]^{-1} \right\}^{-1} \tag{1.20}$$

Auxiliary matrix stiffness As regards the choice of the auxiliary matrix stiffness $\mathbb{C}^0$, it governs the interactions between the phases inside the RVE: $\mathbb{C}^0 = \mathbb{C}^{est}$ relates to a dispersed arrangement of phases where all phases "feel" the overall homogenized material, and the corresponding homogenization scheme is standardly called self-consistent [Hershey, 1954, Kröner, 1958], well-suited for polycrystalline materials. On the other hand, the matrix may be identified as a phase r itself, $\mathbb{C}^0 = \mathbb{C}_r$, which relates to matrix-inclusion-type composite, and the corresponding homogenization scheme is standardly referred to as Mori-Tanaka scheme [Benveniste, 1987, Mori and Tanaka, 1973].

Morphology As regards the choice of morphology taken into account in the Hill tensor $\mathbb{P}_r^0$, the real morphology of bone mineral crystals was for long an open question, therefore different hyptheses were tested. First, Fritsch and Hellmich [2007] envisioned hydroxyapatite biomaterials as porous polycrystals with non-porous matrix consisting of *spherical* crystals with weak interfaces. This idea was based on a precedent finding that up to 40% porosity, the self-consistent stiffness estimates based on uniformly oriented *cylindrical* inclusions are quasi-identical to those based on isotropic solid *spheres* [Fritsch et al., 2006]. As a second approach, Fritsch and Hellmich [2007] developed a micromechanical model for porous polycrystals by replacing the spherical solid inclusions by a set of infinitely many uniformly oriented *cylindrical* inclusions (needles); being identical in shape and in material behavior. That implied the evaluation of the Hill tensors employing the theory of rotational functions. Hence the Hill tensor is a function of the Euler angles φ and θ, and the corresponding part of Eq. (1.20) reads as follows

$$\left[\mathbb{I} + \mathbb{P}^0_r : \left(\mathbb{c}_r - \mathbb{C}^{est}\right)\right]^{-1} = \int_{\theta=0}^{\pi} \int_{\varphi=0}^{2\pi} \left[\mathbb{I} + \mathbb{P}^0_r(\theta, \varphi) : \left(\mathbb{c}_r - \mathbb{C}^{est}\right)\right]^{-1} \frac{\sin\theta}{4\pi} d\theta d\varphi \tag{1.21}$$

This results in an isotropic (overall) effective stiffness estimate. The experimental validation supported the latter model [Fritsch and Hellmich, 2007], which serves as the basis of the present developments for bone tissue modeling.

In case of paper material, we envision each material phase of the paper fiber network (i.e. the pore phase and the infinitely many solid fiber phases lying in the paper plane) as ellipsoidal inclusions embedded into a matrix with the properties of the RVE itself. As for the fiber phase, these inclusions are circular cylinders, i.e. ellipsoids with a slenderness ratio going to infinity and an aspect ratio of one. The pore phase is made up by circular oblate inclusions (ellipsoids with a slenderness ratio of 1, and an aspect ratio going to zero).

Elastic properties Once the homogenized elastic stiffness is determined, the components of the compliance tensor $\mathbb{D}^{est} = \mathbb{C}^{est,-1}$ give access to the engineering constants, such as the Young's moduli in transverse and in axial directions

$$E_1 = \frac{1}{D^{est}_{1111}} \qquad E_3 = \frac{1}{D^{est}_{3333}} \tag{1.22}$$

the transverse and longitudinal Poisson's ratios

$$\nu_{12} = -D^{est}_{1122} \times E_1 \qquad \nu_{13} = -D^{est}_{1133} \times E_3 \tag{1.23}$$

as well as the in-plane shear modulus of the bone material at the scale of interest

$$G_{12} = \frac{E_{12}}{2(1+\nu_{12})} \tag{1.24}$$

1.3 Beyond elasticity: Fundamentals of elastoplasticity

In line with the origin of the word “plastic”, derived from the Greek word *plastikós* meaning shapeable, mouldable; *plasticity* describes the deformation of a material undergoing non-reversible changes of shape in response to applied forces [Lubliner, 2008]. In order to detect such material behavior, one need to define (i) the elastic domain, i.e. the range of stresses within which the material behaves purely elastically (i.e. the deformations remain reversible); (ii) the yield stress (or critical stress value), beyond which the material undergoes plastic yielding (plastic flow), i.e. the evolution of plastic strains takes place; (iii) the flow rule, which provides a relation between the evolution of the plastic strains and the stresses.

In this sense, the basic components of a general elastoplastic model are

- decomposition of the total strain $\boldsymbol{\varepsilon}_r$ into elastic (revesible) and plastic (irreversible) parts
$$\boldsymbol{\varepsilon}_r = \boldsymbol{\varepsilon}_r^e + \boldsymbol{\varepsilon}_r^p \tag{1.25}$$
with $\boldsymbol{\varepsilon}_r^e$ as the elastic, $\boldsymbol{\varepsilon}_r^p$ as the plastic strain, respectively;
- elastic law relating the stresses and strains
$$\boldsymbol{\sigma}_r = \mathbb{C}_r : (\boldsymbol{\varepsilon}_r - \boldsymbol{\varepsilon}_r^p) \tag{1.26}$$
- yield function $\mathscr{F}(\boldsymbol{\sigma}_r)$ defining the elastic domain $\mathbb{E}_\sigma$ based on the yield stress $\boldsymbol{\sigma}_Y$
$$\mathbb{E}_\sigma = \{\boldsymbol{\sigma}_r \in \mathbb{R} \,|\, \mathscr{F}(\boldsymbol{\sigma}_r) := |\boldsymbol{\sigma}_r| - \boldsymbol{\sigma}_Y \le 0\} \tag{1.27}$$
- plastic flow rule defining the evolution of plastic strains
$$\begin{gathered} \dot{\boldsymbol{\varepsilon}}_r^p = \dot{\lambda} \frac{\partial \mathscr{G}}{\partial \boldsymbol{\sigma}_r}(\boldsymbol{\sigma}_r) \\ \dot{\lambda} \ge 0, \qquad \mathscr{F} \le 0, \qquad \dot{\lambda}\mathscr{F} = 0 \end{gathered} \tag{1.28}$$
with $\mathscr{G}(\boldsymbol{\sigma}_r)$ as the plastic potential, and $\dot{\lambda}$ as the plastic multiplier.

In contrast to the elastic case, the loading of the RVEs needs to be done in an incremental manner, so as to represent the load level-dependent plastic processes within the microstructure. Thus the loading path is decomposed into small increments labelled by n, such that the given increment in total strain $\Delta\boldsymbol{\varepsilon}_r^{n+1}$ drives the mechanical state to time $t^{n+1} = t^n + \Delta t^{n+1}$. To relate these increments to the evolution equations (1.28), we integrate the flow rule between time instant t^n and t^{n+1} employing a backward Euler integration scheme, yielding

$$\int_{t^n}^{t^{n+1}} \dot{\boldsymbol{\varepsilon}}_r^p dt = \Delta\boldsymbol{\varepsilon}_r^{p,n+1} = \Delta\lambda_r^{n+1}\frac{\partial\mathscr{G}}{\boldsymbol{\sigma}_r}\left(\boldsymbol{\sigma}_r^{n+1}\right) \tag{1.29}$$

with the corresponding Melan-Kuhn-Tucker conditions reading as

$$\begin{aligned} &\Delta\lambda_r^{n+1} \geq 0 \\ &\mathscr{F}(\boldsymbol{\sigma}_r^{n+1}) \leq 0 \\ &\Delta\lambda_r^{n+1} \times \mathscr{F}(\boldsymbol{\sigma}_r^{n+1}) = 0 \end{aligned} \tag{1.30}$$

The material phases being involved in plastic events need to be identified in each load step. Therefore, the concept of elastic trial states and return map algorithms is introduced into continuum micromechanics.

1.4 Return-mapping

Return mapping algorithms are probably the most popular means of numerically solving conventional plasticity equations [Brannon, 2002]. The solution of the constitutive problems by this procedure requires an iterative process: we assume that all mechanical variables are completely defined at time step t^n, and the general task is to derive the full set of variables at time step t^{n+1} based on the applied load increment $\Delta\boldsymbol{\varepsilon}_r^{n+1}$. The solution for each load increment is derived in two steps:

- First, we consider an auxiliary state, also known as trial stress state, which is achieved by freezing the plastic flow. In other words, first we assume the RVE to behave purely elastically and keep the plastic strain increment constant,

$$\begin{aligned} &\boldsymbol{\sigma}_r^{n+1,trial} = \mathbb{C}_r : \left(\boldsymbol{\varepsilon}_r^{n+1} - \boldsymbol{\varepsilon}_r^{n+1,p}\right) = \boldsymbol{\sigma}_r^n + \mathbb{C}_r : \Delta\boldsymbol{\varepsilon}_r^n \\ &\boldsymbol{\varepsilon}_r^{n+1,p} = \boldsymbol{\varepsilon}_r^{n,p} \end{aligned} \tag{1.31}$$

This trial state is used to evaluate the yield criterion: a negative yield criterion ensures that the response was effectively elastic, therefore the trial stress state is in fact the real mechanical state. However, a positive yield criterion highlights the violation of the constitutive law, so that $\boldsymbol{\varepsilon}_r^{n+1,p} \neq \boldsymbol{\varepsilon}_r^{n,p}$, thus the increments of the plastic strain have to be computed. In summary, the conclusion that an incremenental process for given incremental strain is elastic or plastic is drawn on the trial stress state according to the condition [Simo and Hughes, 1998]

$$\mathcal{F}\left(\boldsymbol{\sigma}_r^{n+1,trial}\right)\begin{cases} \leq 0 & \rightarrow \quad \text{elastic step} \quad \Delta\lambda_r^{n+1} = 0, \\ > 0 & \rightarrow \quad \text{plastic step} \quad \Delta\lambda_r^{n+1} > 0. \end{cases} \tag{1.32}$$

- Second, the return map step (also called corrector step) aims at determining the increments of the plastic strains according to the Melan-Kuhn-Tucker conditions to enforce the constitutive law. We express the final stress $\boldsymbol{\sigma}_r^{n+1}$ in terms of the trial stress and of the plastic multiplier as follows

$$\begin{aligned} \boldsymbol{\sigma}_r^{n+1} &= \mathbb{C}_r : \left(\boldsymbol{\varepsilon}_r^{n+1} - \boldsymbol{\varepsilon}_r^{p,n+1}\right) \\ &= \boldsymbol{\sigma}_r^{n+1,trial} - \mathbb{C}_r : \Delta\boldsymbol{\varepsilon}_r^{p,n+1} \\ &= \boldsymbol{\sigma}_r^{n+1,trial} - \mathbb{C}_r : \Delta\lambda_r^{n+1} : \frac{\partial \mathcal{G}}{\partial \boldsymbol{\sigma}_r}(\boldsymbol{\sigma}_r^{n+1}) \end{aligned} \tag{1.33}$$

The yield criterion evaluated at the final stress state can be written as

$$\begin{aligned} \mathcal{F}(\boldsymbol{\sigma}_r^{n+1}) &= 0 \\ &= \mathcal{F}\left(\boldsymbol{\sigma}_r^{n+1,trial}\right) \\ &- \frac{\partial \mathcal{F}}{\partial \boldsymbol{\sigma}_r}\left(\boldsymbol{\sigma}_r^{n+1,trial}\right) : \mathbb{C}_r : \Delta\lambda_r^{n+1} : \frac{\partial \mathcal{G}}{\partial \boldsymbol{\sigma}_r}(\boldsymbol{\sigma}_r^{n+1}) \end{aligned} \tag{1.34}$$

Solving Eq. (1.34) for the unknown plastic multipliers yields the desired result as

$$\Delta\lambda_r^{n+1} = \frac{\mathcal{F}\left(\boldsymbol{\sigma}_r^{n+1,trial}\right)}{\frac{\partial \mathcal{F}}{\partial \boldsymbol{\sigma}_r}(\boldsymbol{\sigma}_r^{n+1,trial}) : \mathbb{C}_r : \frac{\partial \mathcal{G}}{\partial \boldsymbol{\sigma}_r}(\boldsymbol{\sigma}_r^{n+1})} \tag{1.35}$$

Relevance to bone Damage and failure of bone materials is initiated at the scale of hydroxyapatite crystals and/or collagen molecules: it can be explained by mutual ductule sliding of hydroxyapatite mineral crystals along layered water films followed by the rupture of collagen crosslinks. Based on this vision, Fritsch et al. [2009c] predicted the uniaxial tensile and compressive strengths of various cortical bones, based on "universal" strength properties of molecular collagen and hydroxyapatite. The development of multiscale elastoplastic models capable of *multiaxial strength predictions* is the key issue of the present work, whereby we adapt the porous polycrystal representation of Fritsch et al. [2009c]: we introduce the extrafibrillar space of bone as the host of crystal needles oriented in all space directions, interacting with spherical, water-filled pores. We improve the approach of Fritsch et al. [2009c] by introducing a multi-surface plasticity criterion in a form

$$\begin{aligned}\mathscr{F}_1(\boldsymbol{\sigma}) &= (\sigma_1-\sigma_3)+(\sigma_1+\sigma_3)\sin\phi-2c\cos\phi\leq 0\\ \mathscr{F}_2(\boldsymbol{\sigma}) &= (\sigma_2-\sigma_3)+(\sigma_2+\sigma_3)\sin\phi-2c\cos\phi\leq 0\\ \mathscr{F}_3(\boldsymbol{\sigma}) &= (\sigma_1-\sigma_2)+(\sigma_1+\sigma_2)\sin\phi-2c\cos\phi\leq 0\end{aligned}\tag{1.36}$$

where $\sigma_1 \leq \sigma_2 \leq \sigma_3$ are the (ordered) principal stresses, ϕ is the angle of internal friction, and c is the cohesion. Since the crystal needles are sliding parallel to the maximum shear stress direction, we employ a non-associated elastoplastic constitutive law with the plastic flow rule reading as

$$\begin{aligned}\mathscr{G}_1(\boldsymbol{\sigma}) &= (\sigma_1-\sigma_3)-2c\\ \mathscr{G}_2(\boldsymbol{\sigma}) &= (\sigma_2-\sigma_3)-2c\\ \mathscr{G}_3(\boldsymbol{\sigma}) &= (\sigma_1-\sigma_2)-2c\end{aligned}\tag{1.37}$$

where the conventions for the principle stresses have been preserved. Thus, the needle-specific constitutive relations read as

$$\begin{aligned}&\boldsymbol{\sigma} = \mathbb{C} : (\boldsymbol{\varepsilon}-\boldsymbol{\varepsilon}^p)\\ &\dot{\boldsymbol{\varepsilon}}^p = \dot{\lambda}_1\frac{\partial\mathscr{G}_1}{\partial\boldsymbol{\sigma}}+\dot{\lambda}_2\frac{\partial\mathscr{G}_2}{\partial\boldsymbol{\sigma}}+\dot{\lambda}_3\frac{\partial\mathscr{G}_3}{\partial\boldsymbol{\sigma}}\\ &\dot{\lambda}_i\geq 0,\qquad \mathscr{F}_i\leq 0,\qquad \dot{\lambda}_i\mathscr{F}_i=0\qquad i=1...3\end{aligned}\tag{1.38}$$

This results in a non-associative, multi-phase, multi-surface elastoplastic problema, which we solve through a new variant of the aforementioned algorithmic strategy of return mapping, as described in Chapter 3.

The brittle failure of collagen crosslinks is considered through a Rankine-type criterion [Fritsch et al., 2009c], i.e. the crosslinks first fail in the direction of the largest absolute value of the principle stresses

$$\mathscr{F}_{col} = \max(\sigma_1,\sigma_3)-\sigma_{col}^{ult}\leq 0\tag{1.39}$$

with σ_{col}^{ult} being the ultimate stress of collagen, amounting to 20.6 GPa [Fritsch et al., 2009c]. The resulting nonlinear multiscale problem is solved in the general framework of continuum micromechanics. To our best knowledge, this is a true premiere in both multiscale elastoplasticity and bone mechanics, holding the promise for significantly improved computer-aided fracture risk assessment in orthopedics.

1.5 Outline of the thesis

The individual chapters of this thesis contain either already accepted or published scientific papers, or mature paper drafts planned to be submitted for publication. **Chapter 2** gives an overview on the universal rules regulating bone tissue composition, and shows how the elementary material constituents (hydroxyapatite mineral, collagen, water) govern the elastic properties of bone materials across the entire vertebrate kingdom, from the nano- to the centimetre scale. The mechanical behavior of the different micro- and nanostructures of bone are revealed through the theoretical tool of continuum micromechanics, and validated through a multitude of independent experimental data of bone across different observation scales, ages, species, and anatomical locations.

Motivated by our success in multiscale elasticity, the highly challenging task of upscaling strength of different bone materials is tackled in **Chapter 3**. Damage and failure of bone materials is initiated at the scale of hydroxyapatite crystals: ductile sliding along very-thin (liquid-crystalline) water layers forming interfaces between or within single crystal phases entails an ideal plastic behavior of the mineral crystals. Its occurence in the extrafibrillar space of bone ultrastructure, together with brittle rupture of collagen, well explains the strength of different bone samples. This explanation, however, required major micromechanical developments: the sliding-related elastic-perfectly plastic constitutive law [Fritsch et al., 2009c] is elaborated for a non-associative Mohr-Coulomb plasticity. Upscaling this elastoplastic behavior from the single crystal to the polycrystal scale is achieved through derivation of concentration and influence tensors for eigenstressed microheterogeneous materials [Pichler and Hellmich, 2010], which itself is a generalization of the well-known transformation field analysis [Dvorak and Benveniste, 1992]. The resulting multiscale-multisurface elastoplasticity problema is solved through a new variant of algorithmic strategy of return-mapping.

In **Chapter 4**, we consider fluids as a source of plastic sliding events of hydrated polycrystals in (bio-)materials, comprising heterogeneous microstructures and fluid-filled porosity at small length scales. In this context, fluid-filled interfaces are typically considered to act as a lubricant, once electrically charged solid interfaces start to glide along fluid sheets, while the fluid is typically in a liquid crystal state. The intimate bounding of fluid or water molecules to electrically charged solid surfaces stabilizes the interaction between mineral crystals: the hydrated crystals do not break or detach one from another once a critical stress threshold is reached, but when the intra- and intercrystalline loads accumulated up to the elastic limit, will be maintained through the crystals starting to glide upon each other, along the ice-like features, which prevent the sliding crystal surfaces from disintegration. This vision is consistent with an elastoplastic interface behavior between hydrated polycrystals. Bridging liquid crystals physics with continuum micromechanics of materials, we employ recently proposed micromechanical formulations for influence and concentration tensors valid for phases of arbitrary shapes and orientations [Pichler and Hellmich, 2010], specific choises of which lead to the well-known transformation field analysis [Dvorak and Benveniste, 1992, Pensée et al., 2002]. Then interfaces are regarded as zero-thickness limit case of spheroidal phase inclusions translating the inclusion plastic strains into displacement discontinuities (or jumps) across the interfaces, and the inclusion stresses into traction vectors acting on the interface planes [Shahidi et al., 2014]. Thereafter, we introduce an elastoplastic constitutive law for these interfaces, which links the traction vectors acting in the interfaces to corresponding plastic displacement discontinuities. The resulting homogenized macroscopic behavior is of the kinematic hardening type, which is explicitly confirmed by a dissipation analysis.

Chapter 5 and **Chapter 6** show application examples of how chemical information can be extracted from Computed Tomograpic (CT) data and converted via micromechanics laws, into object-specific, inhomogeneous and anisotropic material properties. The linear relationship between grey values and the X-ray attenuation coefficients, combined with the volume average rule for the latter allows for determination of voxel-specific composition, opening unprecedented avenues in bone disease therapies, including patient-specific bone fracture risk assessment relying on micromechanics based Finite Element analyses.

Chapter 7 investigates the mechanical properties of micro-heterogenous materials exhibiting planar fibrous microstructures. One example of such planar fibrous material is paper, which consists of a network of pulp fibers connected via fiber-fiber bonds. Hereby, paper fiber network is envisioned as a porous polycrystal: infinitely many, cylindrical fiber phases interact with one pore phase with vanishing stiffness. Specialization for a Dirac's Delta distribution for fiber orientation, shifted to the paper plane orientation, results in stress and strain average rules restricted to a planar (2D) Euclidean space. Definition of elastic properties, as well as of a strain concentration problem for the fiber and pore phases yields the concentration tensor-based elasticity fo the homogenized RVE. Validation of the proposed model relies on two independent sets of experiments.

Finally, the thesis is concluded and completed with a future outlook in **Chapter 8**.

Chapter 2

Review of "universal" rules governing bone composition, organization, and elasticity across organizational hierarchies

Authored by: Viktoria Vass, Claire Morin, Stefan Scheiner, and Christian Hellmich

Accepted as: Chapter in CISM Springer series Vol. 578, on Multiscale Mechanobiology of Bone Remodeling and Adaptation

Contribution: This chapter is part of the CISM book series intended to summarize the 20^{th} CISM-IUTAM International Summer School on "Multiscale Mechanobiology of Bone Remodeling and Adaptation". Viktoria Vass reviewed computational codes related to more than 15 years of research; developed a consistent new code out of them, in which she implemented a novel, substantially improved way for considering the molecular collagen stiffness. She optimized the multiscale elasticity model of bone, ran simulations, and carried out model validation based on an extensive literature survey. She documented the research results and wrote the first paper draft. Christian Hellmich supervised the model updating process, checked the key results, and, together with Stefan Scheiner, supported the documentation process.

Abstract

"Universal" organizational patterns in bone are reviewed and presented, in terms of mathematically expressed rules concerning the composition and elasticity of a large variety of tissues. Firstly, experimental data sets gained from dehydration-demineralization tests, dehydration-deorganification tests, and dehydration-ashing tests are thoroughly analyzed. On this basis, bilinear relations can be identified, between the mass density of the extracellular bone matrix on the one hand, and the apparent mass densities of its basic constituents (water, hydroxyapatite, and organic matter), on the other hand. Secondly, the question as to how hydroxyapatite is distributed in bone tissue is addressed. To that end, mass and volume measurements gained from wet, dehydrated, and demineralized tissue samples, as well as optical densities provided by transmission electron microscopy, are studied, confirming a rule on how the mineral is partitioned between fibrillar and extrafibrillar spaces in the ultrastructure of bone. Thirdly, a swelling rule for hydrating collagen is validated through processing of experimental data from X-ray diffraction, vacuum drying, and mass measurements, quantifying the change of the bone tissue composition upon hydration. And fourthly, application of the mass conservation law to extracellular bone matrix considered as closed thermodynamic system, allows for studying the change of bone tissue composition during mineralization. Finally, these compositional rules, which are shown to be "universally" valid throughout the vertebrate kingdom, enter a micromechanical homogenization scheme for upscaling the experimentally accessible elastic properties of the elementary mechanical building blocks of bone (hydroxyapatite minerals, type I collagen, and water with non-collageneous organics) to the macroscopic scale of cortical and trabecular bone.

2.1 Introduction

Many tasks in the diverse field of biomedical engineering involve ensuring the mechanical integrity of structures made up by biological tissues. The mechanical integrity of structures depends on the mechanical loading to which they are subjected, on the specific shapes of the structures (i.e. of the organs), and last, but not least on the mechanical properties of the materials (i.e. of the biological tissues) making up the structures. The aforementioned tissue properties, changing in time and space across the organs, depend on tissue composition and on the micro- and nanostructures within a piece of tissue. The present contribution reviews rigorously derived mathematical relations describing corresponding structure-property relations.

This topic is closely linked to the question on whether there are any non-changing, "universally" valid rules governing the composition and microstructure of biological tissues. Inspired by Rupert Riedl (1925-2005), the eminent Austro-American zoologist of the second half of the twentieth century, who stressed that *"the living world happens to be crowded by universal patterns of organizations, which, most obviously, find no direct explanation through environmental conditions or adaptive radiation"* [Riedl, 1977], we here report on the successful finding of mathematical rules reflecting the aforementioned patterns. Therefore, we apply an engineering science approach to the structural biology of bone tissue, also assessing how such rules or patterns affect the mechanical properties of bone tissue. For this purpose, we take into account the well-known fact that bone tissue features a distinctive hierarchical organization [Fritsch and Hellmich, 2007, Katz et al., 1984, Weiner and Wagner, 1998], as seen in Figure 2.1 and described in greater detail in Section 2.2. The involved organizational patterns (specific arrangements of water, hydroxyapatite-type mineral, and organic matter) can be found throughout different anatomical locations, different organs, and different species. However, the *dosages* of distinctive features within a specific material microstructure may well differ. These dosages follow the aforementioned "universal" composition rules, which arise from a vast amount of experimental data available in literature.

In particular, dehydration-demineralization tests, dehydration-deorganification tests, and dehydration-ashing tests were analyzed in order to quantify the relations between the mass density of extracellular bone matrix and the apparent mass densities of water, hydroxyapatite, and organic matter, see Section 2.3. Furthermore, mass and volume measurements on wet, dehydrated, and demineralized bone tissue samples, as well as optical densities obtained from transmission electron microscopy (TEM) of similar tissues are employed for assessing the distribution of hydroxyapatite within extracellular bone matrix, see Section 2.4. Thereafter, a swelling rule for hydrating collageneous tissues derived from processing and comparing data collected from X-ray diffraction, vacuum drying, and mass measurements, is presented in Section 2.5. Based on a mass conversation law formulated for closed systems representing both the bone ultrastructure, as well as the fibrillar and extrafibrillar spaces, the bone tissue evolution during mineralization can be predicted, see Section 2.6. Finally, we present how the hierarchical organization of bone tissue can be "translated" into a corresponding multiscale homogenization scheme, which allows for prediction of the macroscopic tissue stiffness. The corresponding microelastic model also incorporates the aforementioned four composition rules, so that they eventually govern "universal" structure-property relations in bone, as described in Section 2.7.

2.2 Morphological patterns of bone

Bone materials are characterized by an astonishing variability and diversity. Still, the fundamental hierarchical organization, or "once-chosen" basic "construction plans" of bone materials have remained largely unchanged during biological evolution; this has been coined, by Gould and Lewontin [1979], as an "architecturally constrained" situation. The aforementioned construction plans are reflected by typical morphological features (or patterns) which can be discerned across most bone organs and tissues occurring in the vertebrate kingdom. The corresponding hierarchical organization of bone can be described by means of the following five levels [Katz et al., 1984]:

- The macrostructure, with a characteristic length of several millimeters to centimeters, features cortical (or compact) bone and trabecular (or spongy) bone, see Figure 2.1(a).
- Zooming out pieces of cortical bone, see Figure 2.1(b), or trabecular bone, see Figure 2.1(c), reveals that actually both materials are porous in nature: The corresponding vascular porosity hosts various biological cells as well as blood vessels; in cortical bone this porosity is organized in a tree-type branching structure of canals (called Haversian canals if parallel to the main bone axis, and Volkmann canals at the branching junctions [Buckwalter et al., 1995, Cooper et al., 2003]); and in trabecular bone, these canals are penetrating each other, yielding eventually a microstructure made up by single plates or struts [Hahn et al., 1992]. The vascular pore channels are connected, via much smaller channels called canaliculi, to cave-like single pores called lacunae [Schneider et al., 2011], populated by individual osteocytes, and seen as small black dots in Figure 2.1(d).
- The entire domain outside the vascular, lacunar, and canalicular porosities is called extracellular space or matrix. It appears as a nanocomposite with a

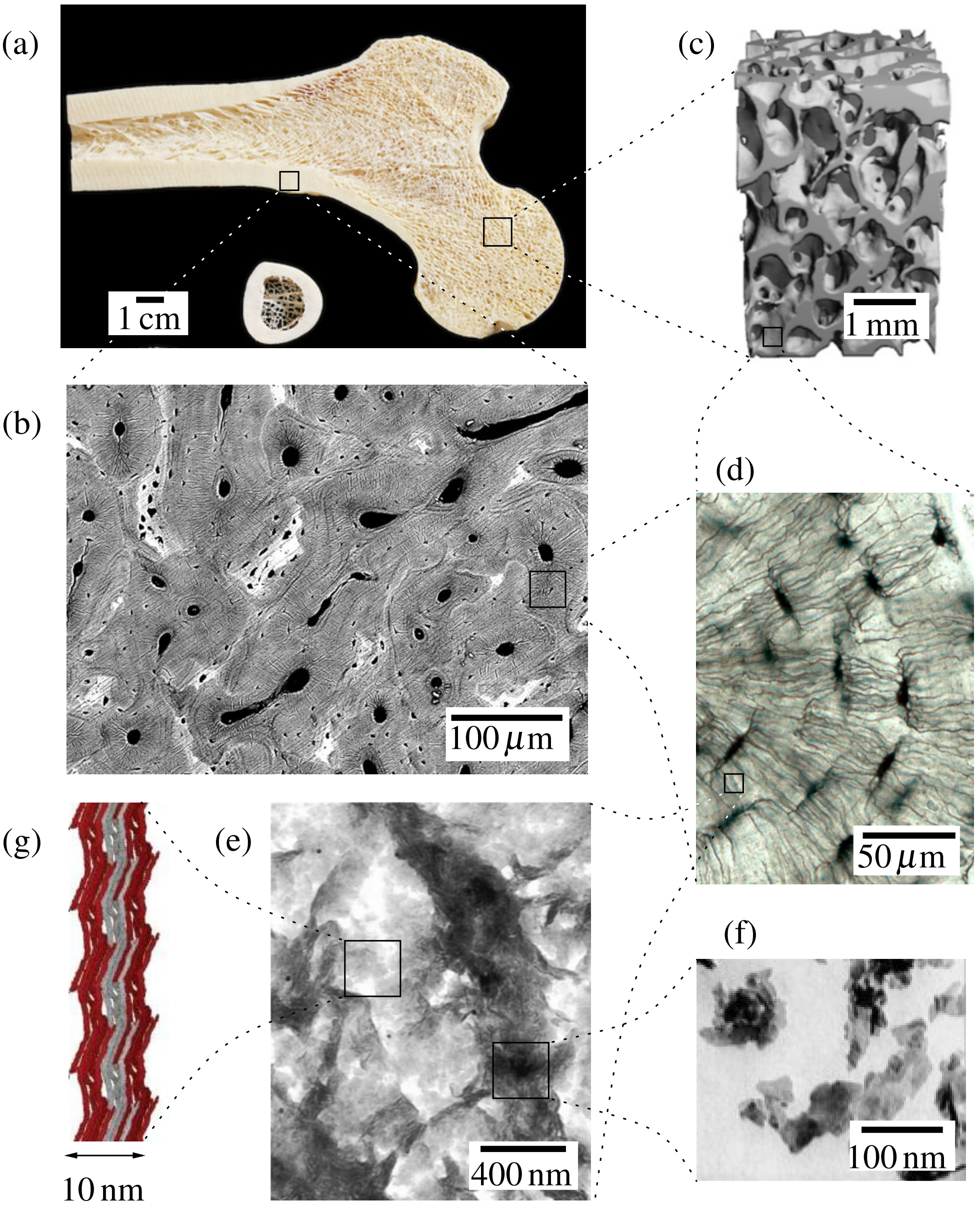

Figure 2.1: Hierarchical organization of bone: (a) photograph of a cross-section through and across a whole long bone (copyright Ralph Hutchings/Visuals Unlimited, Inc.), showing the macrostructure; microstructure featuring either (b) osteonal cortical bone, acquired by SEM [Hang and Barber, 2010], or (c) trabecular struts making up trabecular bone, visualized based on micro-computed tomography data [Metzger et al., 2015]; (d) osteocytic lacunae (brightfield light microscopy image taken by Tim Arnett); (e) ultrastructure, [Prostak and Lees, 1996]; (f) hydroxyapatite crystals, obtained by means of SEM [Weiner and Wagner, 1998]; (g) wet collagen, electron density map of [Orgel et al., 2006] [permission for reproduction requested from publisher: (b) The Royal Society; (c) ASME; (d) Annual Reviews; (e) Springer; (g) PNAS]

characteristic size of several micrometers, see Figure 2.1(e). Within this extracellular space, collagen-rich domains, see the light areas in Figure 2.1(e), and collagen-free domains, see the dark areas in Figure 2.1(e), can be distinguished, the characteristic length of both of which is several hundred nanometers. Commonly, these domains are referred to as fibrils and extrafibrillar space [Prostak and Lees, 1996].

- Finally, the so-called elementary components of mineralized tissues can be distinguished, with a characteristic lengths in the range of nanometers:
  - plate-shaped mineral crystals consisting of impure hydroxyapatite (HA, $Ca_{10}[PO_4]_6[OH]_2$) with typical 1-5 nm thickness, and 25-50 nm length [Weiner and Wagner, 1998], see Figure 2.1(f);
  - slender, helically round collagen molecules with a diameter of about 1.2 nm and a length of about 300 nm [Bozec and Horton, 2005, Orgel et al., 2006, Pradhan et al., 2011], which are self-assembled in staggered organizational schemes (fibrils) with characteristic diameters of 50-500 nm [Cusack and Miller, 1979, Lees et al., 1990, 1994a, Miller and Parker, 1984, Prostak and Lees, 1996, Rho et al., 1998, Weiner and Wagner, 1998, Weiner et al., 1997], see Figure 2.1(g) – several covalently bonded fibrils are sometimes referred to as fibers;
  - different non-collagenous organic molecules, predominantly lipids, proteglycans, and proteins [Hunter et al., 1996, Urist et al., 1983]; and
  - water.

Both the amount of these components, as well as their distribtution across the hierarchical levels described above, are the focus of the subsequent sections.

2.3 Mineral and collagen dosages in extracellular bone matrix

Data from bone drying, demineralization, and deorganification tests, collected over a time span of more than 80 years [Biltz and Pellegrino, 1969, Burns, 1929, Gong et al., 1964, Hammet, 1925, Lees, 2003, Lees and Page, 1992, Lees et al., 1979a, 1983, 1995], evidence a myriad of different chemical compositions of different bone materials. However, careful analysis of the data, as to extract the chemical concentrations of hydroxyapatite, water, and organic matter[1] in the extracellular bone matrix, reveals an astonishing fact [Vuong and Hellmich, 2011]: it appears that there exists a unique bilinear relationship between organic concentration and mineral concentration, across different species, different organs, and different age groups, from early childhood to old age.

Corresponding experimental endeavors typically started with the determination of the *"macroscopic"* mass density, i.e. that associated to millimeter-sized bone samples, by means of Archimedes' principle. Therefore, the mass of the (wet) bone sample is first measured in air, delivering the quantity M^{μ}_{air}. Thereafter, the weight of the bone sample when submerged in a liquid, is quantified as W^{μ}_{sub}. Both quantities then give access to the volume of the millimeter-sized sample, through

$$V^{\mu} = \frac{1}{\rho_{\text{liquid}}} \left(M^{\mu}_{\text{air}} - \frac{W^{\mu}_{\text{sub}}}{g} \right) , \tag{2.1}$$

with ρ_{liquid} as the mass density of the employed liquid, and g as the gravitational acceleration, $g = 9.81\,\text{m/s}^2$. Finally, the macroscopic mass density of the investigated samples follows from

$$\rho^{\mu} = \frac{M^{\mu}_{\text{air}}}{V^{\mu}} . \tag{2.2}$$

After having determined their samples' mass density, the experimenters typically turned towards determination of the samples' chemical composition; by one of three different experimental modalities, as described next.

2.3.1 Dehydration-demineralization tests

In a series of seminal experimental campaigns [Lees, 2003, Lees and Page, 1992, Lees et al., 1979a, 1995], see Tables 2.1 to 2.3, numerous millimeter-sized bone samples were first dried in a vacuum desiccator at room temperature, until a constant mass was observed, namely the mass of the dehydrated bone sample, M^{μ}_{dry}. The difference between the mass of wet sample in air and the mass of dehydrated sample obviously equals the mass of water which was originally contained in the sample, $M^{\mu}_{\text{H}_2\text{O}} = M^{\mu}_{\text{air}} - M^{\mu}_{\text{dry}}$. This water had filled all the bone pore spaces, from the vascular pore space seen in Figures 2.1(b) and 2.1(c), via the lacunar and

---

[1] 90% of which is collagen [Urist et al., 1983]

Table 2.1: Bone composition from dehydration-demineralization experiments of Lees et al. (1979)[a] and Lees et al. (1995)[b]

Tissue	ρ^{μ} (g/cm^3)	$\mathrm{WF}^{\mu}_{\mathrm{HA}}$ (-)	$\mathrm{WF}^{\mu}_{\mathrm{org}}$ (-)	$\mathrm{WF}^{\mu}_{\mathrm{H_2O}}$ (-)
Bovine tibia[a]	2.06	0.658	0.219	0.123
Bovine tibia[a]	2.05	0.656	0.219	0.126
Bovine tibia[a]	2.02	0.621	0.239	0.140
Bovine tibia[a]	2.02	0.627	0.232	0.140
Bovine tibia[a]	2.00	0.643	0.227	0.129
Bovine tibia[a]	2.05	0.643	0.230	0.127
Bovine tibia[a]	2.10	0.671	0.211	0.118
Bovine tibia[a]	2.08	0.664	0.216	0.120
Bovine tibia[a]	2.12	0.661	0.215	0.123
Bovine tibia[a]	2.08	0.663	0.221	0.116
Bovine tibia[a]	2.10	0.647	0.224	0.129
Bovine tibia[a]	1.98	0.654	0.217	0.128
Bovine tibia[a]	2.05	0.644	0.227	0.129
Bovine tibia[a]	2.11	0.649	0.229	0.122
Bovine tibia[a]	2.03	0.638	0.213	0.123
Bovine tibia[a]	2.06	0.699	0.184	0.117
Bovine tibia[a]	2.02	0.658	0.219	0.123
Bovine tibia[a]	1.99	0.656	0.219	0.126
Bovine tibia[a]	1.95	0.640	0.228	0.131
Bovine tibia[a]	2.01	0.659	0.218	0.123
Bovine tibia[a]	2.04	0.638	0.242	0.121
Bovine tibia[a]	2.05	0.674	0.210	0.116
Whale malleus[b]	2.49	0.860	0.100	0.040
Whale malleus[b]	2.45	0.800	0.130	0.070
Whale incus[b]	2.50	0.860	0.090	0.050
Whale stapes[b]	2.42	0.810	0.130	0.060
Whale stapes[b]	2.36	0.800	0.140	0.060
Whale periotic[b]	2.40	0.810	0.130	0.070
Whale periotic[b]	2.48	0.830	0.110	0.060
Whale periotic[b]	2.52	0.850	0.100	0.050
Whale periotic[b]	2.52	0.850	0.100	0.050
Whale periotic[b]	2.58	0.870	0.090	0.040
Whale t. bulla[b]	2.48	0.850	0.100	0.050

Table 2.2: Mineralized tendon composition from dehydration-demineralization experiments of Lees et al. (1992)

Tissue	ρ^μ (g/cm^3)	$\mathrm{WF}^\mu_{\mathrm{HA}}$ (-)	$\mathrm{WF}^\mu_{\mathrm{org}}$ (-)	$\mathrm{WF}^\mu_{\mathrm{H_2O}}$ (-)
Mineralized turkey leg tendon	1.33	0.286	0.250	0.465
Mineralized turkey leg tendon	1.50	0.445	0.239	0.316
Mineralized turkey leg tendon	1.50	0.410	0.217	0.374
Mineralized turkey leg tendon	1.51	0.437	0.217	0.346
Mineralized turkey leg tendon	1.52	0.454	0.239	0.308
Mineralized turkey leg tendon	1.52	0.437	0.219	0.343
Mineralized turkey leg tendon	1.52	0.396	0.244	0.360
Mineralized turkey leg tendon	1.53	0.443	0.222	0.335
Mineralized turkey leg tendon	1.54	0.459	0.244	0.297
Mineralized turkey leg tendon	1.58	0.473	0.228	0.299
Mineralized turkey leg tendon	1.58	0.462	0.217	0.321
Mineralized turkey leg tendon	1.59	0.476	0.228	0.297
Mineralized turkey leg tendon	1.60	0.487	0.230	0.283
Mineralized turkey leg tendon	1.61	0.459	0.230	0.310
Mineralized turkey leg tendon	1.61	0.495	0.244	0.261
Mineralized turkey leg tendon	1.62	0.500	0.228	0.272
Mineralized turkey leg tendon	1.64	0.506	0.228	0.266

canalicular pore spaces seen in Figure 2.1(d), down to the inter-crystalline and intermolecular pore spaces, as seen in Figures 2.1(e), (f), and (g). Next, the samples were rehydrated and then demineralized in a 0.5 M ethylenediaminetetraacetic acid (EDTA) solution at pH 7.5, until no calcium was detected anymore by an atomic absorption spectrometer. After drying such a demineralized sample in vacuum, one is left with the organic mass which had been contained in the originally mineralized and wet bone sample, M^μ_{org}. Finally, knowledge of the masses of organic matter and water gives access to the hydroxyapatite mass, $M^\mu_{\mathrm{HA}} = M^\mu_{\mathrm{air}} - M^\mu_{\mathrm{org}} - M^\mu_{\mathrm{H_2O}}$. Thereafter, the constituent masses can be readily converted into weight fractions, through

$$\mathrm{WF}^\mu_i = \frac{M^\mu_i}{M^\mu_{\mathrm{air}}}, \qquad i = \mathrm{org}, \mathrm{HA}, \mathrm{H_2O}\,, \tag{2.3}$$

see Tables 2.1 to 2.3. The weight fractions obviously fulfill

$$\mathrm{WF}^\mu_{\mathrm{H_2O}} + \mathrm{WF}^\mu_{\mathrm{HA}} + \mathrm{WF}^\mu_{\mathrm{org}} = 1\,. \tag{2.4}$$

Table 2.3: Bone composition from dehydration-demineralization experiments of Lees et al. (2003)

Tissue	$\mathrm{WF}^{\mu}_{\mathrm{HA}}$ (-)	$\mathrm{WF}^{\mu}_{\mathrm{org}}$ (-)	$\mathrm{WF}^{\mu}_{\mathrm{H_2O}}$ (-)	ρ^{μ} (g/cm^3)
Horse metacarpal	0.55	0.25	0.2	1.79
Horse metacarpal	0.57	0.26	0.17	1.84
Horse metacarpal	0.55	0.26	0.19	1.80
Horse metacarpal	0.54	0.28	0.18	1.79
Horse metacarpal	0.62	0.26	0.12	1.96
Horse metacarpal	0.62	0.27	0.11	1.97
Horse metacarpal	0.62	0.26	0.12	1.96
Horse metacarpal	0.61	0.26	0.13	1.94
Horse metacarpal	0.62	0.25	0.13	1.95
Horse metacarpal	0.54	0.23	0.23	1.75
Horse metacarpal	0.53	0.24	0.23	1.74
Horse metacarpal	0.54	0.27	0.19	1.79
Horse metacarpal	0.63	0.22	0.15	1.94
Horse metacarpal	0.62	0.25	0.13	1.95
Horse metacarpal	0.62	0.26	0.12	1.96
Horse metacarpal	0.64	0.23	0.13	1.98
Horse metacarpal	0.62	0.26	0.12	1.96
Horse metacarpal	0.66	0.23	0.12	1.99
Horse metacarpal	0.63	0.24	0.13	1.96

2.3.2 Dehydration-deorganification tests

Gong et al. [1964] weighed several (macroscopic) bone samples in the wet state, as well as after drying at 80°C for 72 hours - thereby getting access to their wet and dry masses, M^{μ}_{air} and M^{μ}_{dry}. As before, their difference is equal to the mass of water in the investigated bone sample, $M^{\mu}_{\mathrm{H_2O}} = M^{\mu}_{\mathrm{air}} - M^{\mu}_{\mathrm{dry}}$. Next, the samples were freed from fat and other organic material, using, in a soxhlet apparatus, a mixture of 80% ethyl ether and 20% ethanol, as well as an 80% aqueous solution of ethylene diamine. After drying such a deorganified sample at 80°C (until constant weight is attained), one is left with the hydroxyapatite mass contained in the investigated bone sample, M^{μ}_{HA}. Finally, when knowing the mass of hydroxyapatite and water contained in the originally wet bone sample, as well as its original mass, the mass of the organic matter can be readily determined through $M^{\mu}_{\mathrm{org}} = M^{\mu}_{\mathrm{air}} - M^{\mu}_{\mathrm{HA}} - M^{\mu}_{\mathrm{H_2O}}$, together with the corresponding weight fractions according to Eq. (2.3), see Table 2.4.

Table 2.4: Bone composition from dehydration-deorganification experiments of Gong et al. (1964)

Tissue	ρ^μ (g/cm^3)	$\mathrm{WF}^\mu_{\mathrm{HA}}$ (-)	$\mathrm{WF}^\mu_{\mathrm{org}}$ (-)	$\mathrm{WF}^\mu_{\mathrm{H_2O}}$ (-)
Steer tibial shaft	2.00	0.630	0.244	0.126
Dog femoral shaft	2.00	0.630	0.259	0.111
Humar femur and tibia	1.99	0.642	0.239	0.119
Monkey femur	2.04	0.643	0.239	0.117
Steer atlas bone	1.93	0.588	0.266	0.146
Dog lumbar vertebrae	1.91	0.582	0.265	0.153
Human thoracic and lumbar vertebrae	1.92	0.601	0.258	0.140
Monkey lumbar vertebrae	1.88	0.582	0.274	0.144

2.3.3 Dehydration-ashing tests

In an interesting experimental campaign of Biltz and Pellegrino [1969], cortical bone samples were dried until a constant mass, i.e. the dry bone mass, M^μ_{dry}, was attained, which, together with the original mass of the sample in air, M^μ_{air}, gives access to the mass of water in the investigated bone sample, $M^\mu_{\mathrm{H_2O}}$. Next, the dried bones were gently incinerated until all organic matter was burned off. Subsequent weighing evidenced the ash mass, M^μ_{ash}. As also some inorganic matter, namely 6.6% of the ash weight, is burned at an ashing temperature of 600°C [Gong et al., 1964], the ash mass provides access to the mineral mass, according to $\mathrm{M}^\mu_{\mathrm{HA}} = 1.066 \times \mathrm{M}^\mu_{\mathrm{ash}}$. The mass of organic matter follows from $M^\mu_{\mathrm{org}} = M^\mu_{\mathrm{air}} - M^\mu_{\mathrm{HA}} - M^\mu_{\mathrm{H_2O}}$. The corresponding weight fractions can be determined through Eqs. (2.3) and (2.4), which, in turn, provide access to ρ^μ, through

$$\rho^\mu = \left(\frac{\mathrm{WF}^\mu_{\mathrm{org}}}{\rho_{\mathrm{org}}} + \frac{\mathrm{WF}^\mu_{\mathrm{HA}}}{\rho_{\mathrm{HA}}} + \frac{\mathrm{WF}^\mu_{\mathrm{H_2O}}}{\rho_{\mathrm{H_2O}}} \right)^{-1}, \tag{2.5}$$

where $\rho_{\mathrm{org}} = 1.42\,\mathrm{g/cm^3}$, $\rho_{\mathrm{HA}} = 3\,\mathrm{g/cm^3}$, and $\rho_{\mathrm{H_2O}} = 1\,\mathrm{g/cm^3}$ are the constituents' *real* mass densities [Gong et al., 1964, Hellmich and Ulm, 2005a, Lees, 1987]. For a compilation of data derived from Biltz and Pellegrino [1969], see Table 2.5. For the sake of completeness, it should be noted that Biltz and Pellegrino [1969] actually reported the volume fraction of water

$$f^\mu_{\mathrm{H_2O}} = \frac{M^\mu_{\mathrm{air}} - M^\mu_{\mathrm{dry}}}{V^\mu}, \tag{2.6}$$

Table 2.5: Bone composition from dehydration-ashing experiments of Biltz and Pellegrino (1969)

Femoral and tibial samples of	ρ^μ (g/cm^3)	$\mathrm{WF}^\mu_{\mathrm{HA}}$ (-)	$\mathrm{WF}^\mu_{\mathrm{org}}$ (-)	$\mathrm{WF}^\mu_{\mathrm{H_2O}}$ (-)
Fish	1.80	0.507	0.273	0.220
Turtle	1.81	0.529	0.266	0.204
Frog	1.93	0.572	0.246	0.182
Polar bear	1.92	0.583	0.245	0.172
Man	1.94	0.657	0.263	0.080
Elephant	2.00	0.658	0.242	0.100
Monkey	2.09	0.653	0.237	0.110
Cat	2.05	0.652	0.233	0.115
Horse	2.02	0.648	0.228	0.124
Chicken	2.04	0.653	0.227	0.120
Dog	1.94	0.637	0.219	0.144
Goose	2.04	0.669	0.218	0.113
Cow	2.05	0.660	0.212	0.128
Guinea Pig	2.10	0.669	0.212	0.119
Rabbit	2.12	0.685	0.199	0.116
Rat	2.24	0.713	0.197	0.090

and the weight fraction of ash per mass of dried bone

$$\mathrm{WF}^{\mathrm{dry}}_{\mathrm{ash}} = \frac{M^\mu_{\mathrm{ash}}}{M^\mu_{\mathrm{air}} - M^\mu_{\mathrm{H_2O}}} \,. \tag{2.7}$$

Similar test campaigns were performed by Burns [1929] and Hammet [1925], see Table 2.6 for a compilation of test results.

2.3.4 Determination of tissue-specific volume fractions

Determination of the extracellular volume fractions of mineral and collagen, $f^{\mathrm{excel}}_{\mathrm{HA}}$ and $f^{\mathrm{excel}}_{\mathrm{col}}$, rests on the aforementioned volume and weighing measurements on wet, dehydrated, and demineralized bone specimens, and on techniques revealing the bone microstructure, such as light microscopy, confocal microscopy, or micro-computed tomography. These imaging techniques give access to the so-called microporosity $f_{\mu\mathrm{por}}$, the sum of the vascular, lacunar, and canalicular porosities,

$$f_{\mu\mathrm{por}} = f_{\mathrm{vas}} + f_{\mathrm{lac}} + f_{\mathrm{can}} \,. \tag{2.8}$$

Vascular porosity in cortical bone, also called Haversian porosity in that context, ranges from 2 % to typically 8 % [Bousson et al., 2000, 2001, Cooper et al.,

Table 2.6: Bone composition from dehydration-ashing experiments of Burns (1929)[a] and Hammett (1925)[b]

Tissue	$\mathrm{WF}^{\mu}_{\mathrm{HA}}$ (-)	$\mathrm{WF}^{\mu}_{\mathrm{org}}$ (-)	$\mathrm{WF}^{\mu}_{\mathrm{H_2O}}$ (-)	ρ^{μ} (g/cm^3)
Rabbit limb bones[a]	0.267	0.202	0.392	1.38
Rabbit limb bones[a]	0.210	0.194	0.581	1.25
Rat leg bones[a]	0.389	0.231	0.313	1.54
Rat leg bones[a]	0.345	0.224	0.375	1.46
Rat leg bones[a]	0.398	0.232	0.318	1.54
Rat leg bones[a]	0.378	0.218	0.334	1.52
Rat leg bones[a]	0.376	0.230	0.344	1.51
Humerus of rat[b]	0.171	0.180	0.650	1.20
Humerus of rat[b]	0.176	0.191	0.633	1.21
Humerus of rat[b]	0.235	0.199	0.567	1.27
Humerus of rat[b]	0.315	0.210	0.475	1.37
Humerus of rat[b]	0.337	0.208	0.456	1.40
Humerus of rat[b]	0.378	0.215	0.407	1.46
Humerus of rat[b]	0.434	0.222	0.344	1.55
Humerus of rat[b]	0.175	0.194	0.631	1.21
Humerus of rat[b]	0.180	0.193	0.627	1.21
Humerus of rat[b]	0.264	0.205	0.532	1.31
Humerus of rat[b]	0.315	0.209	0.476	1.37
Humerus of rat[b]	0.362	0.209	0.429	1.44
Humerus of rat[b]	0.420	0.219	0.361	1.53
Humerus of rat[b]	0.451	0.229	0.320	1.58
Femur of rat[b]	0.133	0.182	0.685	1.17
Femur of rat[b]	0.144	0.191	0.665	1.18
Femur of rat[b]	0.201	0.204	0.595	1.24
Femur of rat[b]	0.283	0.217	0.500	1.34
Femur of rat[b]	0.315	0.210	0.475	1.37
Femur of rat[b]	0.356	0.217	0.427	1.43
Femur of rat[b]	0.413	0.230	0.357	1.52
Femur of rat[b]	0.143	0.197	0.660	1.18
Femur of rat[b]	0.150	0.195	0.655	1.19
Femur of rat[b]	0.235	0.208	0.557	1.28
Femur of rat[b]	0.288	0.213	0.499	1.34
Femur of rat[b]	0.338	0.214	0.448	1.41
Femur of rat[b]	0.401	0.222	0.377	1.50
Femur of rat[b]	0.430	0.235	0.336	1.55

2007, Dong et al., 2014, Sietsema, 1995]. Under severe conditions such as bone disease like osteoporosis, overtraining, or drug treatment, it may increase up to 20 % [Sietsema, 1995]. In trabecular bone, the vascular porosity ranges from 30 to 90 % [Carter and Hayes, 1977]. On the other hand, the much smaller lacunar and canalicular porosities lie within a much narrower range of values; in recent years, they were quantitifed by micro-computed tomography. In this context, Schneider et al. [2007, 2011] reported 1.3% and 0.7% lacunar and canalicular porosity values, respectively. These values are close to those reported by Palacio-Mancheno et al. [2012], Tommasini et al. [2012], and Hesse et al. [2015]. Considering 3 % vascular porosity as relevant for mammalian bone of medium-to-large-sized animals (see e.g. evaluation of microscopic images of Lees et al. [1979a] as reported in Fritsch and Hellmich [2007]), we account for 5 % microporosity $f_{\mu\text{por}}$ when assessing the extracellular (ultrastructural) characteristics of the bones tested by Biltz and Pellegrino [1969], Burns [1929], Gong et al. [1964], Hammet [1925], Lees [2003], Lees et al. [1979a]. Accordingly, the extracellular mass density reads as

$$\rho^{\text{excel}} = \frac{\rho^{\mu} - \rho_{\text{H}_2\text{O}} \times f_{\mu\text{por}}}{1 - f_{\mu\text{por}}}\,, \tag{2.9}$$

and the weight fraction of water-filled micropores (i.e vascular, lacunar, and canalicular pores) in (wet) bone specimens reads as

$$\text{WF}^{\mu}_{\mu\text{por}} = \frac{\rho_{\text{H}_2\text{O}} \times f_{\mu\text{por}}}{\rho^{\mu}}. \tag{2.10}$$

$\text{WF}^{\mu}_{\mu\text{por}}$ allows for scale transition from the macroscopic (microstructural) to the extracellular (ultrastructural) scale,

$$\text{WF}^{\text{excel}}_{\text{HA}} = \frac{\text{WF}^{\mu}_{\text{HA}}}{1 - \text{WF}^{\mu}_{\mu\text{por}}}, \tag{2.11}$$

$$\text{WF}^{\text{excel}}_{\text{org}} = \frac{\text{WF}^{\mu}_{\text{org}}}{1 - \text{WF}^{\mu}_{\mu\text{por}}}, \tag{2.12}$$

$$\text{WF}^{\text{excel}}_{\text{H}_2\text{O}} = 1 - \text{WF}^{\text{excel}}_{\text{HA}} - \text{WF}^{\text{excel}}_{\text{org}}. \tag{2.13}$$

From Eqs. (2.5), (2.11)-(2.13), one can determine the apparent mass densities of organics, water, and hydroxyapatite through

$$\rho^{\text{excel}}_{\text{i}} = \text{WF}^{\text{excel}}_{\text{i}} \rho^{\text{excel}}, \qquad i = \text{org}, \text{HA}, \text{H}_2\text{O}\,. \tag{2.14}$$

The microporosity is negligible in size as regards the mineralized turkey leg tendon [Currey, 1988] and otic bones [Zylberberg et al., 1998]. Thus, weight fractions and mass densities are not to be differentiated between the microstructural and the ultrastructural scale, as concerns the tissue samples of Lees and Page [1992] and Lees et al. [1995].

2.3.5 "Universal" rules in bone fibrillogenesis and mineralization

Applying the presented evaluation procedures to the collected experimental data, see Tables 2.1-2.6, results in a remarkable finding concerning the apparent mass densities of hydroxyapatite mineral, organic, and water; i.e. the masses of these constituents found in a millimeter-sized sample divided by the volume of the extracellular portion within this millimeter-sized sample; across a great variety of species, organs, and ages. The aforementioned apparent mass densities (or concentrations) strongly correlate with each other, see Figure 2.2, as well as with the bone tissue mass density, see Figure 2.3. Interestingly, all these correlations can be represented by bilinear functions, whereby the increasing branch depicted in Figure 2.2(a) relates to tissues taken from growing organisms (being in the states of childhood and adolescence), while the descending branch relates to tissues taken from adult organisms. The apparent mass densities can be translated into volume fractions through

$$f_{\mathrm{i}}^{\mathrm{excel}} = \frac{\rho_{\mathrm{i}}^{\mathrm{excel}}}{\rho_{\mathrm{i}}}, \qquad i = \mathrm{org}, \mathrm{HA}, \mathrm{H_2O}\,. \tag{2.15}$$

so that the constituents' volume fractions can be expressed by the following regression functions depending on the extracellular mass density,

$$\text{if} \quad \rho^{\mathrm{excel}} \leq 1.978\,\mathrm{g/cm^3} \qquad \begin{cases} f_{\mathrm{HA}}^{\mathrm{excel}} = \frac{1}{\rho_{\mathrm{HA}}}\left(1.3275\rho^{\mathrm{excel}} - 1.3938\right), \\ f_{\mathrm{org}}^{\mathrm{excel}} = \frac{1}{\rho_{\mathrm{org}}}\left(0.3888\rho^{\mathrm{excel}} - 0.2393\right), \\ f_{\mathrm{H_2O}}^{\mathrm{excel}} = 1 - f_{\mathrm{HA}}^{\mathrm{excel}} - f_{\mathrm{org}}^{\mathrm{excel}}, \end{cases} \tag{2.16}$$

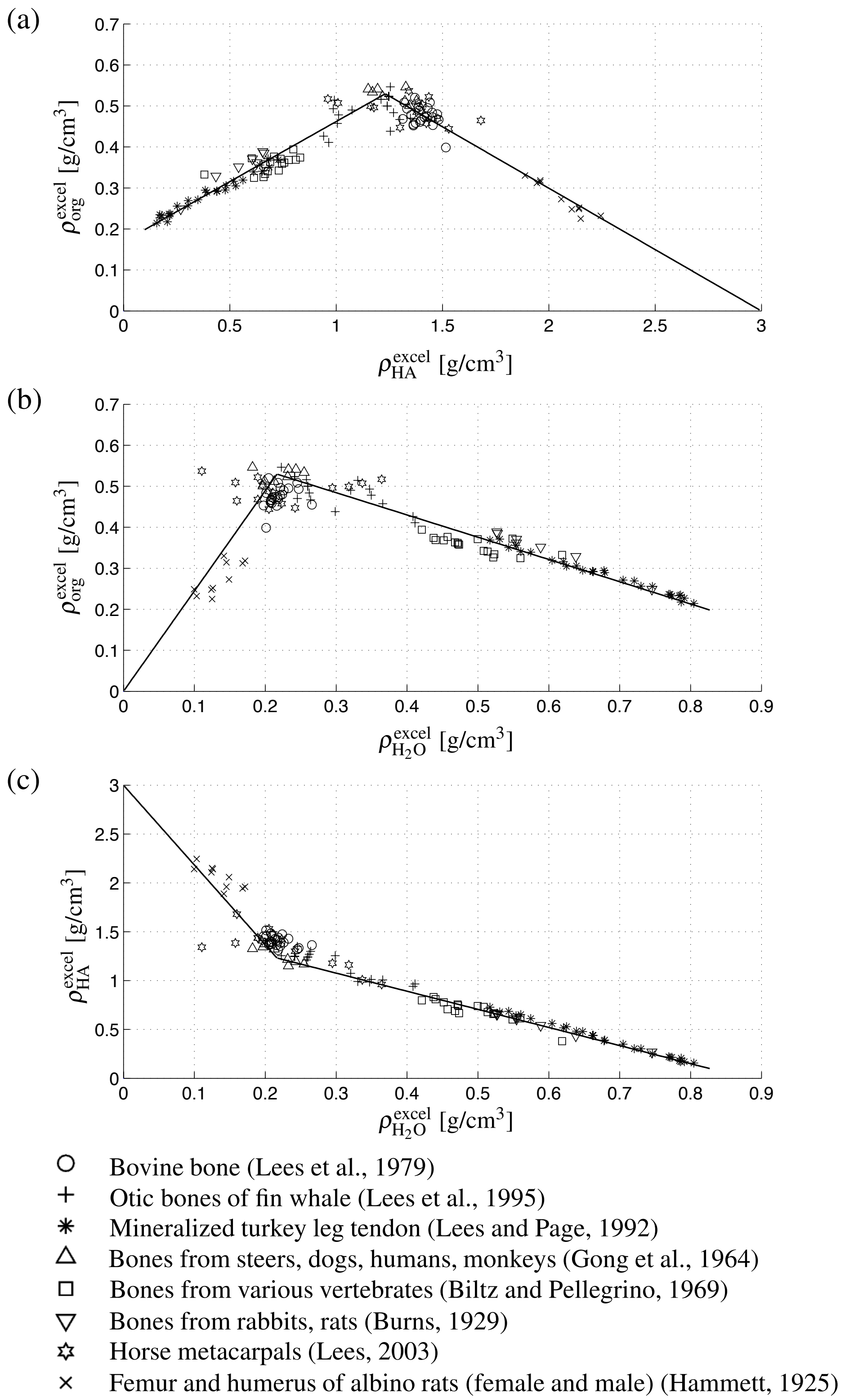

Figure 2.2: Relations between apparent mass densities in extracellular bone matrix in the line of Vuong and Hellmich [2011]: (a) hydroxyapatite versus organic matter, (b) water versus organic matter, and (c) water versus hydroxyapatite; across different species, organs, and ages

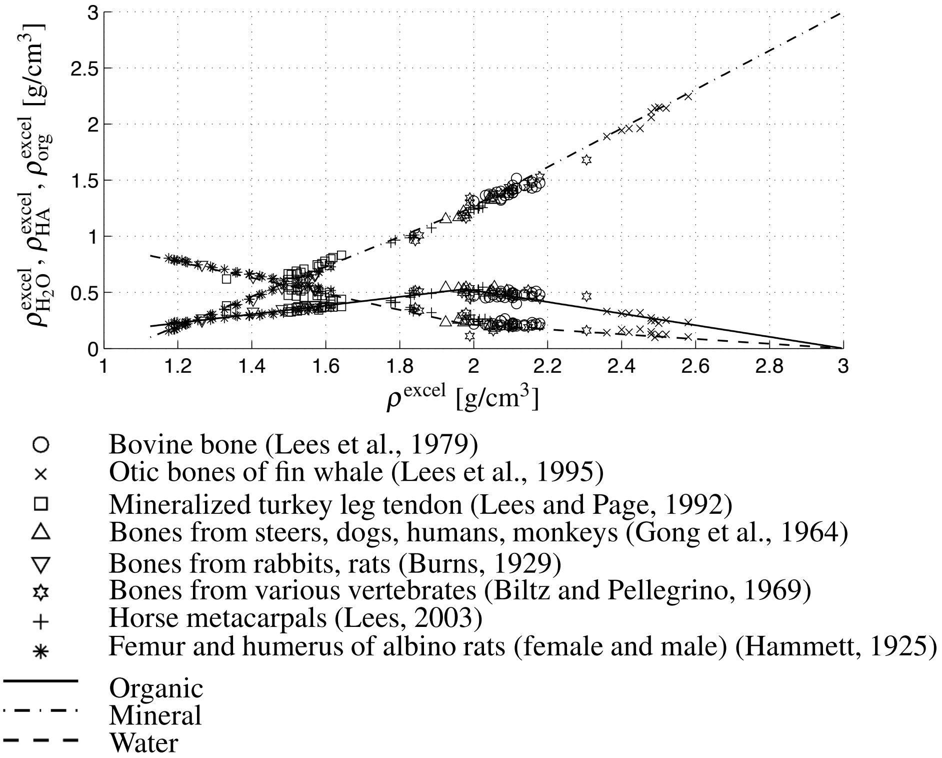

Figure 2.3: Apparent mass densities of water, hydroxyapatite, and organic matter, versus overall mass density of extracellular bone matrix, ρ^{excel}, across different species, organs, and ages

relating to growing organisms, and

$$\text{if} \quad \rho^{excel} \geq 1.978\,\text{g/cm}^3 \qquad \begin{cases} f_{HA}^{excel} = \frac{1}{\rho_{HA}}\left(1.7298\rho^{excel} - 2.1895\right), \\ f_{org}^{excel} = \frac{1}{\rho_{org}}\left(-0.5180\rho^{excel} + 1.5541\right), \\ f_{H_2O}^{excel} = 1 - f_{HA}^{excel} - f_{org}^{excel}, \end{cases} \tag{2.17}$$

relating to aging organisms. As 90% of the organic matter in bone is collagen [Urist et al., 1983], the extracellular volume fraction of collagen follows as

$$f_{col}^{excel} = 0.9 \times f_{org}^{excel}. \tag{2.18}$$

2.3.6 Cell biology aspects

It is interesting to discuss the mineral-versus-organics concentration relation of Figure 2.2(a) from the viewpoint of cell biology: during growth, the mineral-to-organic mass apposition ratio in extracellular bone tissue is a constant, $d\rho_{\mathrm{HA}}^{\mathrm{excel}}/d\rho_{\mathrm{org}}^{\mathrm{excel}} = 3.4$, "universally" valid throughout different tissues of different growing species at different ages. This constant reflects the working mode of osteoblasts (cuboidal or polygonal bone cells with several tens of micrometers characteristic length [Aaron, 1971, Bonewald and Johnson, 2008, Jilka et al., 1998, Noble, 2008, Parfitt, 1983, Roholl et al., 1994, Zhu et al., 2001]. Pre-osteoblasts [Engler et al., 2006, Lemaire et al., 2004, Parfitt, 1983] deposit new osteoid, in the form of seams of some 8 to 10 μm thickness, made of proteoglycan gel reinforced by fairly randomly oriented collagen fibrils [Buxboim et al., 2010, Engler et al., 2006, Zajac and Discher, 2008], see Figure 2.4(a). Thereafter, osteoblasts order the collagen fibrils through stretching [Engler et al., 2006], and mediate, through budding of matrix vesicles from cell processes [Anderson, 2005], the precipitation of hydroxyapatite, see Figure 2.4(b). This results in the so-called primary mineralization [Parfitt, 1983], with a characteristic time of hours to days [Wergedal and Baylink, 1974]. From a chemical viewpoint, specially synthesized matrix molecules, such as bone sialoprotein, osteopontin, or osteocalcin [Wiesmann et al., 2005], induce mineral formation, and such non-collagenous organic molecules typically make up 10% of the overall organic volume fraction [Buckwalter et al., 1995, Lees, 1987, Urist et al., 1983], regardless of the magnitude of the latter. Accordingly, one would expect the more mineral precipitation, the more non-collagenous organics to be present, the amount of the latter being proportional to that of the overall organic matter. This is perfectly consistent with the aforementioned tissue- and species-independent, "universal" mineral-per-organics apposition ratio of 3.4, suggesting primary mineralization as the dominant mineralization mechanism in growing organisms.

In such organisms, the mineral is hindered from further precipitation in the highly ionic fluids, through the action of the most abundant biological bone cells, namely the osteocytes [Aaron, 1971, Baylink and Wergedal, 1971, Bell et al., 2008, Bonucci, 2009, Noble, 2008, Parfitt, 1983, Teitelbaum, 2000], residing in the lacunar porosity of extravascular bone matrix. Originating from osteoblasts which were buried in the course of ongoing osteoid formation and mineralization, osteocytes maintain a widely spread network, through channels called canaliculi, among themselves and with the osteoblasts located at the bone tissue surface. This network is thought to effectively transfer mechanical stimuli related to tissue deformation, to the osteoblasts [Bonewald and Johnson, 2008, Cowin, 2007], so as to trigger their bone formation activity, as described before. In addition to mechanosensing, osteocytes may inhibit mineralization around their lacunae [Bonucci, 2009], and therefore set an upper limit to the asymptotic mineral concentration which may be attained during the process called secondary mineralization. This process exhibits a characteristic time of weeks to months [Bala et al., 2010], see Figure 2.4(c), and before reaching its asymptote, secondary mineralization is not controlled by the local biological cells, but by the diffusion and composition properties of the fluids saturating the extracellular bone tissue [Parfitt, 1983]. However, at higher ages, the aforementioned inhibitive activity of osteocytes steadily decreases, so that, in the end, even the lacunae themselves may be filled with mineral, as evidenced in Bell et al. [2008], Frost [1960], Jowsey [1960]. As a consequence, the organic-to-mineral concentration ratio decreases and the mineral-to-organic mass apposition ratio is not equal to 3.4 anymore. At the same time, osteoblastic activity also decreases at more advanced ages [Aaron, 1971], leading to a reduction of the (absolute) organic concentration in extraxcellular bone matrix. This combined effect of both

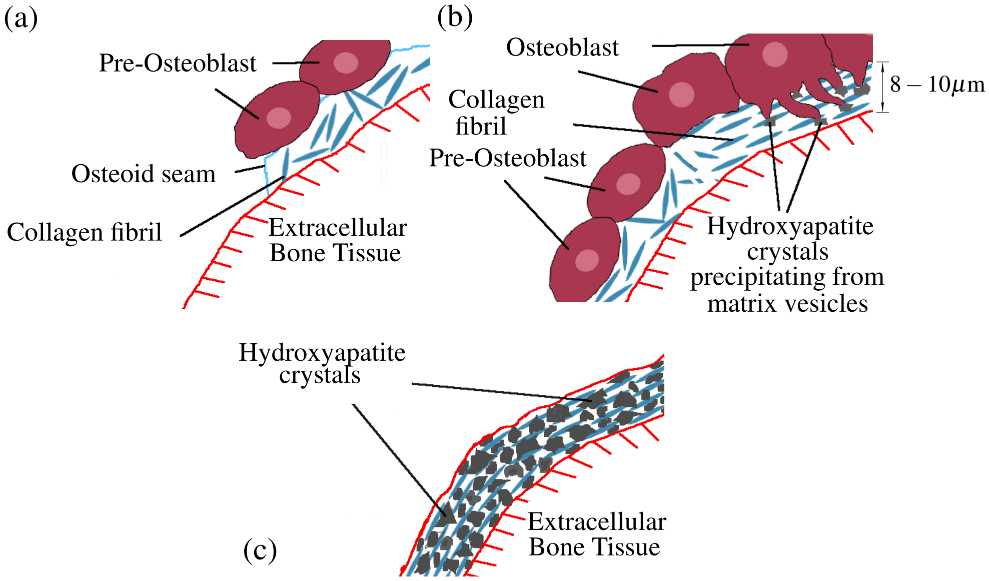
(a)
Pre-Osteoblast
Osteoid seam
Collagen fibril
Extracellular Bone Tissue
(b)
Osteoblast
Collagen fibril
Pre-Osteoblast
8 − 10μm
Hydroxyapatite crystals precipitating from matrix vesicles
Hydroxyapatite crystals
Extracellular Bone Tissue
(c)

Figure 2.4: Working mode of pre-osteoblasts and osteoblasts: primary and secondary mineralization of an unmineralized osteoid; (a) pre-osteoblasts lay down an osteoid seam, reinforced by randomly oriented collagen fibrils; (b) primary mineralization: osteoblasts order the collagen fibrils through cell-driven stretch, and mediate, through budding of matrix vesicles from cell processes, the precipitation of hydroxyapatite; (c) secondary mineralization: crystals grow without control of local biological cells

osteoblastic and osteocytic activity reduction is expressed by a (negative) mineral-growth-to-organic-removal ratio, see Figure 2.2(a), which reveals secondary mineralization as the dominant mineralization mechanism in adult, aging organisms. We also remark that the results presented here refer to physiologically normal conditions, while drug treatments may lead to considerable deviations from these rules for fibrillogenesis and mineralization, see [Vuong and Hellmich, 2011] for further details.

2.4 Mineral distribution in extracellular bone matrix

At the ultrastructural observation scale (1 to 10 μm) of fully mineralized tissues, transmission electron micrographs (TEM) reveal that hydroxyapatite is situated both within and outside of the collagen fibrils, and that the majority of hydroxyapatite lies outside the fibrils [Alexander et al., 2012, Lees and Prostak, 1988, McNally et al., 2012, Prostak and Lees, 1996, Schwarcz et al., 2014, Zylberberg et al., 1998]. The question arises whether the distribution of mineral between the fibrillar and extrafibrillar spaces follows a general rule. And indeed, Hellmich and Ulm [2003] found out that the average mineral concentration in the extrafibrillar space equals that in the extracollageneous space. The underlined arguments are as follows: The ultrastructural volume element with a characteristic size of some micrometers, consists of fibrillar and extrafibrillar space; see Figure 2.5(a), with corresponding volumes $V_{\text{fib}}^{\text{excel}}$ and $V_{\text{exfib}}^{\text{excel}}$. The fibrils are made up by collagen molecules exhibiting a triple helix structure arranged more or less cylindrically, with diameters ranging from 50 to 500 nm [Cusack and Miller, 1979, Lees et al., 1990, 1994a, Miller and Parker, 1984, Prostak and Lees, 1996, Rho et al., 1998, Weiner and Wagner, 1998, Weiner et al., 1997]. The fibrillar volume $V_{\text{fib}}^{\text{excel}}$ comprises all fibrils within the ultrastructural (or extracellular) volume V^{excel}. $V_{\text{col}}^{\text{fib}}$, the volume of collagen within the fibrils, is a subspace of $V_{\text{fib}}^{\text{excel}}$, as is $(V_{\text{fib}}^{\text{excel}} - V_{\text{col}}^{\text{fib}})$, see Figure 2.5c. The latter is the volume within the fibrils which is not occupied by collagen molecules, subsequently referred to as extracollagenous fibrillar volume, $V_{\text{excol}}^{\text{fib}}$. The space within the ultrastructure (or extracellular bone matrix) that is not occupied by fibrils is called extrafibrillar space, $V_{\text{exfib}}^{\text{excel}} = V^{\text{excel}} - V_{\text{fib}}^{\text{excel}}$. The union of the spaces $V_{\text{exfib}}^{\text{excel}}$ and $V_{\text{excol}}^{\text{fib}}$, $V_{\text{exfib}}^{\text{excel}} + V_{\text{excol}}^{\text{fib}} = V^{\text{excel}} - V_{\text{col}}^{\text{excel}} = V_{\text{excol}}^{\text{excel}}$, is the total extracollagenous space within the extracellular bone, see Figure 2.5b.

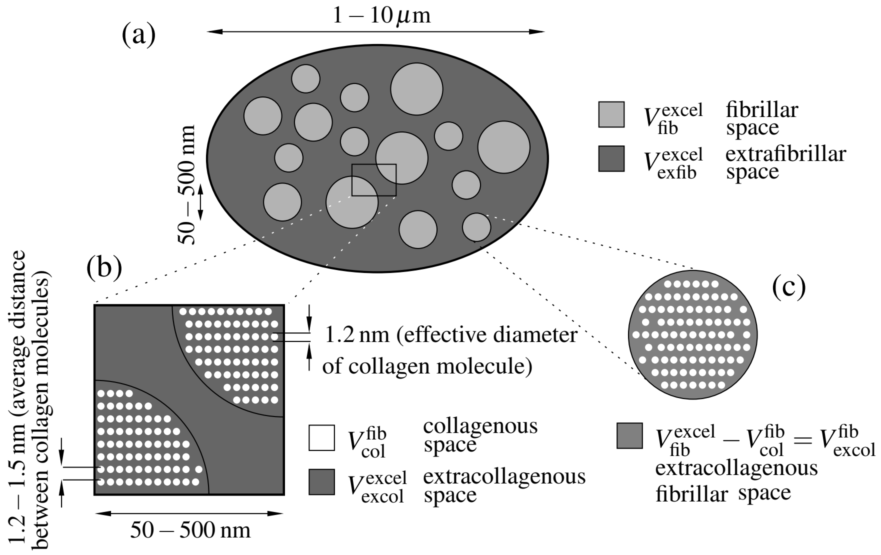
(a)
$1-10\,\mu\mathrm{m}$
$50-500$ nm
$V_{\mathrm{fib}}^{\mathrm{excel}}$ fibrillar space
$V_{\mathrm{exfib}}^{\mathrm{excel}}$ extrafibrillar space
(b)
(c)
1.2 nm (effective diameter of collagen molecule)
$1.2-1.5$ nm (average distance between collagen molecules)
$50-500$ nm
$V_{\mathrm{col}}^{\mathrm{fib}}$ collagenous space
$V_{\mathrm{excol}}^{\mathrm{excel}}$ extracollagenous space
$V_{\mathrm{fib}}^{\mathrm{excel}}-V_{\mathrm{col}}^{\mathrm{fib}}=V_{\mathrm{excol}}^{\mathrm{fib}}$ extracollagenous fibrillar space

Figure 2.5: Schematical sketch of spaces in the extracellular bone matrix or ultrastructure, (a) section through the ultrastructural representative volume element perpendicular to the direction of the fibrils, (b) and (c) close-ups

Based on these notions, the aforementioned rule would imply that the ratio of the mass of the extrafibrillarly located mineral $\left(M_{\mathrm{HA}}^{\mathrm{exfib}}\right)$, over the volume of the extrafibrillar space needs to be equal to the ratio of the entire mineral mass (M_{HA}), over the extracollageneous volume

$$\rho_{\mathrm{HA}}^{\mathrm{exfib}}=\frac{M_{\mathrm{HA}}^{\mathrm{exfib}}}{V_{\mathrm{exfib}}^{\mathrm{excel}}}\equiv\frac{M_{\mathrm{HA}}}{V_{\mathrm{excol}}^{\mathrm{excel}}}=\rho_{\mathrm{HA}}^{\mathrm{excol}}\,, \tag{2.19}$$

with $\rho_{\mathrm{HA}}^{\mathrm{exfib}}$ and $\rho_{\mathrm{HA}}^{\mathrm{excol}}$ being the apparent mineral densities relating to the extrafibrillar and the extracollagenous volumes, respectively. Eq. (2.19) can be rearranged as follows

$$\phi_{\mathrm{HA}}^{\mathrm{exfib}}=\frac{M_{\mathrm{HA}}^{\mathrm{exfib}}}{M_{\mathrm{HA}}}\equiv\frac{V_{\mathrm{exfib}}^{\mathrm{excel}}}{V_{\mathrm{excol}}^{\mathrm{excel}}}=\frac{f_{\mathrm{exfib}}^{\mathrm{excel}}}{1-f_{\mathrm{col}}^{\mathrm{excel}}}\,, \tag{2.20}$$

where $f_{\mathrm{exfib}}^{\mathrm{excel}}=V_{\mathrm{exfib}}^{\mathrm{excel}}/V^{\mathrm{excel}}$ is the extrafibrillar volume fraction, $f_{\mathrm{col}}^{\mathrm{excel}}=V_{\mathrm{col}}^{\mathrm{excel}}/V^{\mathrm{excel}}$ is the collagen volume fraction, both quantified within the volume of extracellular bone, and $\phi_{\mathrm{HA}}^{\mathrm{exfib}}$ is the relative amount of extrafibrillar mineral.

Two independent sets of experimental observations covering a large range of tissue mass densities were considered for checking the relevance of Eq. (2.20), as discussed next.

Experimental set I: Mass and volume measurements

First, $f_{\text{exfib}}^{\text{excel}}/(1-f_{\text{col}}^{\text{excel}})$ is determined from weighing experiments and diffraction spacing measurements. In order to determine the apparent mass density of collagen, we adopt a value of $\rho_{\text{org}} = 1.42\,\text{g/cm}^3$ [Katz and Li, 1973, Lees, 1987], and consider the fact that collagen constitutes approximately 90% by weight of the organic matter in mineralized tissues [Biltz and Pellegrino, 1969, Lees, 1987, Urist et al., 1983, Weiner and Wagner, 1998]. The mass of organic matter can be determined from weighing experiments on demineralized and dehydrated specimens [Biltz and Pellegrino, 1969, Lees, 1987, Lees and Page, 1992, Lees et al., 1979a], harvested from different anatomical locations of different vertebrates at different ages, see Section 2, in particular Tables 2.1-2.3 and 2.5. On the other hand, the determination of the extrafibrillar volume fraction $f_{\text{exfib}}^{\text{excel}} = 1 - f_{\text{fib}}^{\text{excel}}$ requires quantification of the fibrillar space within the mineralized tissue. This can be achieved by application of a model for the organization of collagen: we use Lees' generalized packing model [Bonar et al., 1985, Lees, 1987], as the simplest model to quantify the average crosslink length between collagen molecules, see also [Hellmich and Ulm, 2003].

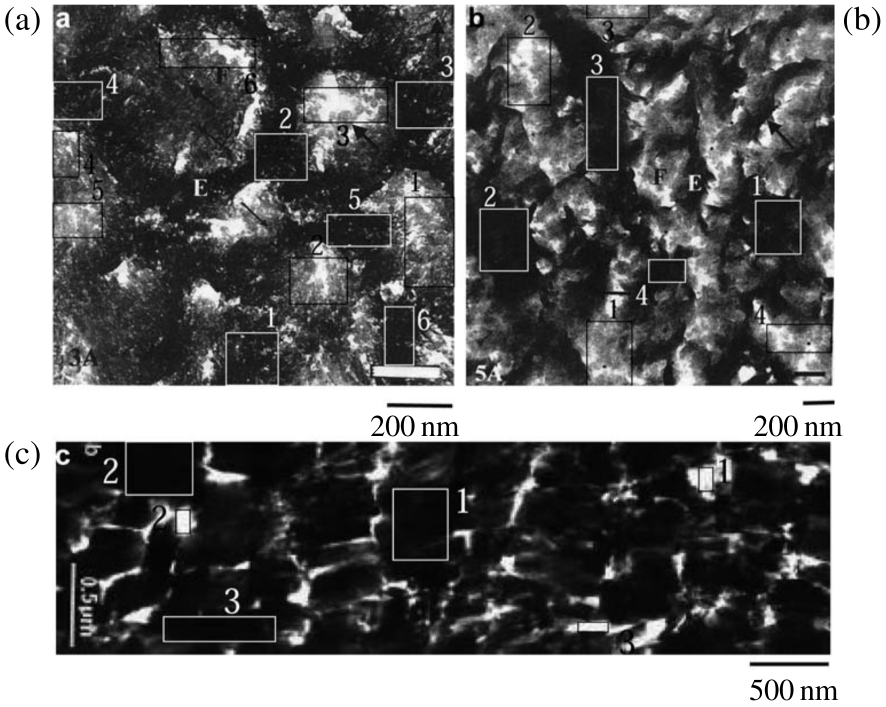

Figure 2.6: Transmission electron micrographs of cross sections through: (a) mineralized turkey leg tendon [Prostak and Lees, 1996]; (b) human tibia [Prostak and Lees, 1996] and (c) whale rostrum [Zylberberg et al., 1998]

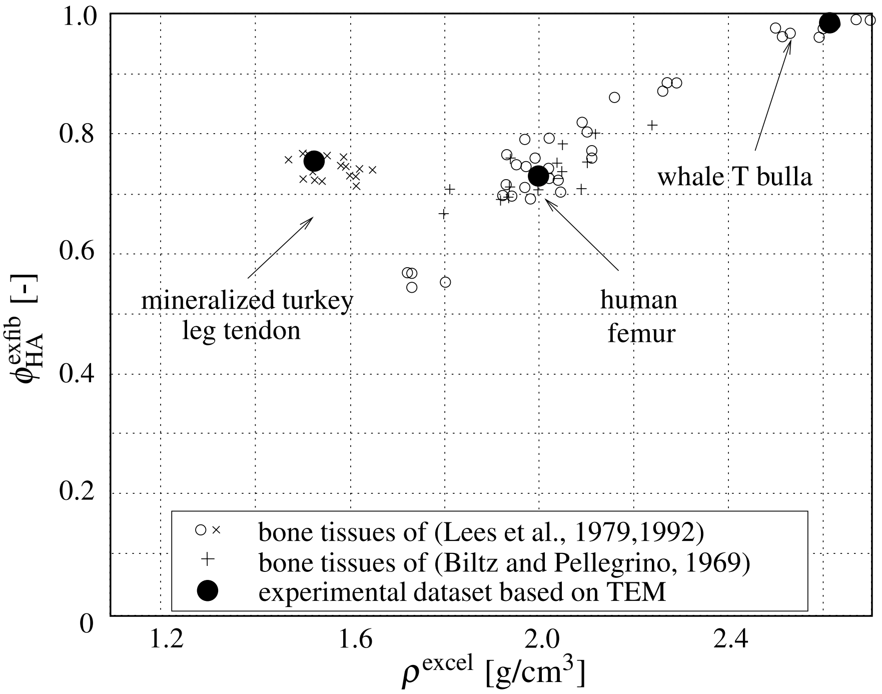

Figure 2.7: Relative amount of extrafibrillar mineral, ϕ_{HA}^{exfib}, as a function of extracellular mass density ρ^{excel}, according to Hellmich and Ulm [2003]

2.4.1 Experimental set II: Transmission electron microscopy

As a second, independent set of observations, we consider optical density measurements from TEMs, in order to determine ϕ_{HA}^{exfib}. Figure 2.6 displays three TEMs of cross sections of mineralized tissues, covering a wide range of extracellular mass densities; from $\rho^{excel} = 1.5\,\text{g/cm}^3$ for mineralized turkey leg tendon, see Figure 2.6(a), to $\rho^{excel} = 2.6\,\text{g/cm}^3$ for the rostrum of whale, see Figure 2.6(c). These micrographs reflect the electron density of material phases. The higher the electron density, the darker the respective area of the TEM images. Since hydroxyapatite exhibits by far the largest electron density of all elementary components, the TEM images displayed in Figure 2.6 highlight that hydroxyapatite is mainly located outside the fibrils. First, the relative optical density is determined using the protocol of Lees et al. [1994a]: the TEM images are scanned and then captured by a frame grabber [Bradley, 1994]. The optical density is considered to be linearly proportional to the number of electrons transmitted through the particular area [Lees et al., 1994a], the number of electrons to be linearly proportional to the local hydroxyapatite mass density in the fibrillar or extrafibrillar space. The average densities are then related to the apparent mineral densities, allowing for the determination of the extrafibrillar volume fraction of tissues, $f_{\mathrm{exfib}}^{\mathrm{excel}}$, shown in TEM images. $f_{\mathrm{exfib}}^{\mathrm{excel}}$ turns out to be 60% for the mineralized turkey leg tendon micrograph of Figure 2.6(a) ($\rho^{\mathrm{excel}} = 1.5\,\mathrm{g/cm^3}$), 53% for the human tibia ($\rho^{\mathrm{excel}} = 2.0\,\mathrm{g/cm^3}$), see Figure 2.6(b), and 85% for the whale rostrum ($\rho^{\mathrm{excel}} = 2.6\,\mathrm{g/cm^3}$), see Figure 2.6(c).

2.4.2 Comparison of independently derived values of the relative amount of extrafibrillar mineral

Next, the sample-specific relative amount of extrafibrillar mineral, $\phi_{\mathrm{HA}}^{\mathrm{exfib}}$, of very different bone tissues, derived from the independent methods related to the experiment sets I and II, respectively, are compared, as shown in Figure 2.7. It can be seen that the values derived from both experimental data sets are in perfect agreement when comparing similar tissues. This surprisingly good agreement of values obtained from two independent assessment methods provides the sought after evidence that the average mineral concentration in the extrafibrillar and the extracollageneous spaces are indeed equal; see Hellmich and Ulm [2003] for further details.

2.5 Hydration-dependent evolution of unmineralized collagenous tissues

Hydration of collagenous tissues, consisting of fibrillar and extrafibrillar constituents, causes swelling, as well as mechanical softening (i.e. reduction of stiffness). The underlying mechanism can be quantified in terms of the following mathematical rule [Morin et al., 2013]: After drying the tissue in air, water remains only in the gap zones between the triple-helical collagen molecules making up 12 % of the total volume [Lees and Heeley, 1981]. Upon rehydration, the extrafibrillar space is established at volumes directly proportional to the hydration-induced swelling of the (micro) fibrils, until the maximum equatorial distance between the long collagen molecules is reached. Thereafter, the volume of the fibrils stays constant, and only the extrafibrillar volume continues to grow. Mathematically, the proportionality between the extrafibrillar space growth and the swelling of fibrils (in case the fibrils still swell, which occurs if they are not fully hydrated) can be expressed as follows

$$V^{\text{excel}}_{\text{exfib}} = \beta(V^{\text{excel}}_{\text{fib}} - V^{\text{col}}_{\text{dry}}), \quad V^{\text{col}}_{\text{dry}} \le V^{\text{excel}}_{\text{fib}} \le V^{\text{excel}}_{\text{fib,max}}, \tag{2.21}$$

with β as proportionality constant, with $V^{\text{excel}}_{\text{exfib}}$ as the volume of extrafibrillar space within the collageneous tissue, $V^{\text{excel}}_{\text{fib}}$ as fibrillar volume within the collageneous tissue, which is smaller than or equal to the maximum attainable value $V^{\text{excel}}_{\text{fib,max}}$, and larger than a minimum value $V^{\text{col}}_{\text{dry}}$ corresponding to the dry volume of the collageneous tissue, V^{excel}. The fibrillar and extrafibrillar volumes, $V^{\text{excel}}_{\text{fib}}$ and $V^{\text{excel}}_{\text{exfib}}$, fill the entire tissue volume V^{excel}, $V^{\text{excel}}_{\text{fib}} + V^{\text{excel}}_{\text{exfib}} = V^{\text{excel}}$, yielding, together with (2.21), a tissue swelling rule in the following form

$$\frac{V^{\text{excel}}}{V^{\text{col}}_{\text{dry}}} = \beta\left(\frac{V^{\text{excel}}_{\text{fib}}}{V^{\text{col}}_{\text{dry}}} - 1\right) + \frac{V^{\text{excel}}_{\text{fib}}}{V^{\text{col}}_{\text{dry}}}, \quad V^{\text{col}}_{\text{dry}} \le V^{\text{excel}}_{\text{fib}} \le V^{\text{excel}}_{\text{fib,max}}\,. \tag{2.22}$$

We regard the fibrils as continua with one to several hundreds of nanometers characteristic size, these continua being built up by representative volume elements of several to several tens of nanometers characteristic size, see Figure 2.8. Microscopic images [Chung et al., 2010] show that hydration affects volume changes in a fibril in a homogeneous fashion. Therefore, following the deformation laws of continuum mechanics [Salençon, 2001], the current fibrillar volume $V^{\text{excel}}_{\text{fib}}$ is related to the initial volume $V^{\text{col}}_{\text{dry}}$ by the Jacobian J, which is standardly expressed by the product of the principal stretches λ_1, λ_2, and λ_3 of the volume elements, thus

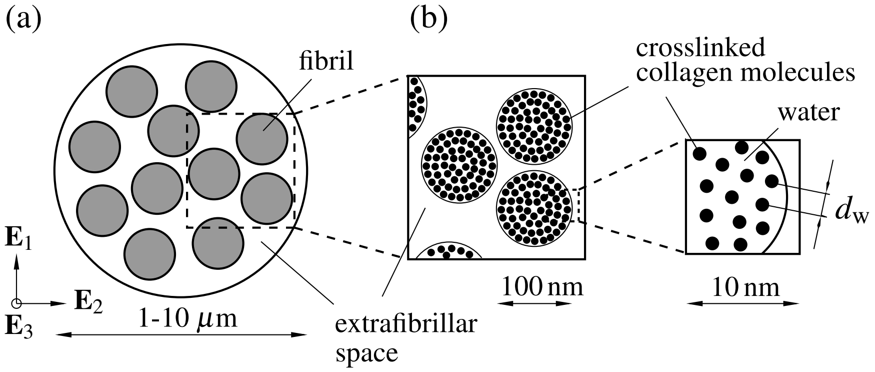

Figure 2.8: Scheme concerning hierarchical structure of collagen: (a) collagenous tissue, (b) wet collagen

$$\frac{V^{\text{excel}}_{\text{fib}}}{V^{\text{col}}_{\text{dry}}} = J = \lambda_1 \times \lambda_2 \times \lambda_3\,. \tag{2.23}$$

The principal stretches are defined as the ratio of the current length to the initial length of the line elements $\mathrm{d}\mathbf{x}_1$, $\mathrm{d}\mathbf{x}_2$, and $\mathrm{d}\mathbf{x}_3$ attached to the fibrils and oriented in the principle deformation directions $\mathbf{e}_1$, $\mathbf{e}_2$, and $\mathbf{e}_3$ (see Figure 2.8). These principle stretches are related to the ratios of diffraction spacings in the current and initial elementary volumes, in the line of standard stretch measurements in lattice-like microstructures [Warren, 1941, Warren and Averbach, 1950]. As regards λ_1 and λ_2, the aforementioned diffraction spacings are related to the (on-average) lateral (transversal, equatorial) distances between collagen molecules,

$$\lambda_1 = \lambda_2 = \lambda_{\mathrm{tr}} = \frac{d_{\mathrm{w}}}{d_{\mathrm{dry}}}\,, \tag{2.24}$$

with d_{w} as the lateral diffraction spacing related to some more or less hydrated state of the fibril, and $d_{\mathrm{dry}} = 1.09\,\mathrm{nm}$ as the lateral diffraction spacing in dry tissues [Lees et al., 1984]. As regards λ_3, diffraction peaks relate to the axial macroperiod D_{w} of collagen, comprising repeating units of one gap zone and one overlap zone each, as discovered by Hodge and Petruska [1963]; this axial macroperiod increases, albeit only slightly, upon hydration (up to a value of 67 nm). Since this increase is clearly less than 5 % when compared to the axial macroperiod measured by dry tissues, $D_{\mathrm{dry}} = 64\,\mathrm{nm}$, we consider D_{w} as a constant, and hence

$$\lambda_3 = \lambda_{\mathrm{ax}} = \frac{D_{\mathrm{w}}}{D_{\mathrm{dry}}} = 1. \tag{2.25}$$

Finally, the variation of the current fibrillar volume with respect to the initial one reads as

$$\frac{V_{\mathrm{fib}}^{\mathrm{excel}}}{V_{\mathrm{dry}}^{\mathrm{col}}} = \lambda_1 \cdot \lambda_2 \cdot \lambda_3 = \left(\frac{d_{\mathrm{w}}}{d_{\mathrm{dry}}}\right)^2 . \tag{2.26}$$

However, the diffraction spacings are limited, and cannot exceed a maximum value of 1.38 nm in the equatorial direction [Meek et al., 1991]. Therefore, the amount of water which can be accommodated in the fibrils is also limited. Upon further hydration, namely beyond the so-called fibrillar saturation limit, only the extrafibrillar volume continues to grow. The mathematically expressed swelling rule (2.21), together with volume relations (2.22) to (2.26), was experimentally validated by means of the measurement results of Meek et al. [1991], Robinson [1960], Rougvie and Bear [1953]. Therefore, the water-to-organic ratios $\mathscr{R}$ given

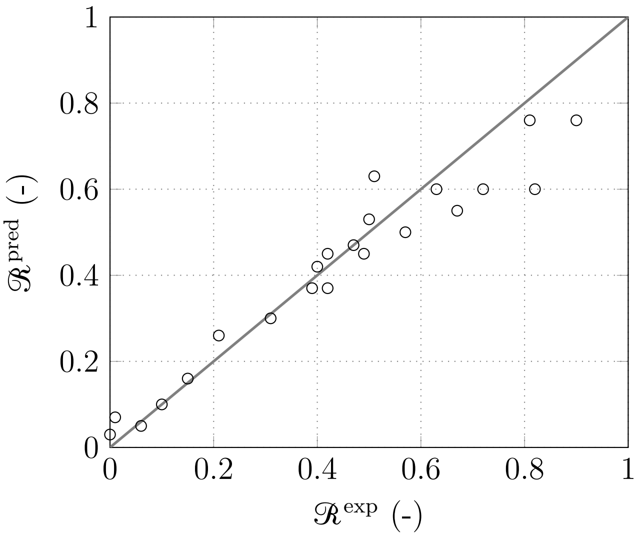

Figure 2.9: Water-to-organic mass ratio: diffraction- and swelling rule-based predictions $\mathscr{R}^{\text{pred}}$ versus direct experiments $\mathscr{R}^{\text{exp}}$

in these papers, were converted into volumes according to

$$\frac{V^{\text{excel}}}{V^{\text{col}}_{\text{dry}}} = 0.88 \frac{\mathscr{R}\rho_{\text{col}} + \rho_{\text{H}_2\text{O}}}{\rho_{\text{H}_2\text{O}}}, \tag{2.27}$$

where $\rho_{\text{col}} = 1.42\,\text{g/cm}^3$ [Lees and Heeley, 1981] and $\rho_{\text{H}_2\text{O}} = 1\,\text{g/cm}^3$ are the mass densities of molecular collagen and water, respectively; obviously, this equation accounts for the existence of 12 % gap zones in the collagenous dry matrix [Hodge and Petruska, 1963, Lees and Heeley, 1981], relating to an intermolecular pore saturation limit amounting to $\mathscr{R}^{\text{imsat}} = 0.096$. Based on relations (2.22) and (2.27), combined with the observations of Meek et al. [1991], that the fibrillar swelling stops at a water-to-organic mass ratio of $\mathscr{R}^{\text{fibsat}} = 0.82$, one can translate the swelling rule (2.22) into a mathematical relation between water-to-organic mass ratios and corresponding diffraction spacings,

$$\mathscr{R}^{\text{pred}} = \frac{1}{\rho_{\text{col}}} \left(\frac{\rho_{\text{H}_2\text{O}}}{0.88} \left[(\beta + 1) \left(\frac{d_{\text{w}}}{d_{\text{dry}}} \right)^2 - \beta \right] - \rho_{\text{H}_2\text{O}} \right). \tag{2.28}$$

It is directly tested against respective experimental values provided by Katz and Li [1973], Meek et al. [1991], Rougvie and Bear [1953], see Figure 2.9, with a relative error as low as 0.98 %±12.56 % (mean value plus standard deviation), see [Morin et al., 2013] for further details. Given the excellent confirmation of the swelling rule, it allows for quantifying the evolution of subvolumes and volume fractions in hydrating tissues: during hydration, the fibrillar volume fraction decreases by more than 50 %, see Figure 2.10(b). At the same time, the tissue is swelling to its triple size, as seen in Figure 2.10(a). Also during hydration, the volume fraction of molecular collagen within a fibril decreases from 88% to 54.7 %, while that of water increases from 0 % to 45.3 %, see Figure 2.11(b). At the same time, the fibrils grow by about 60 % in volume, see Figure 2.11(a).

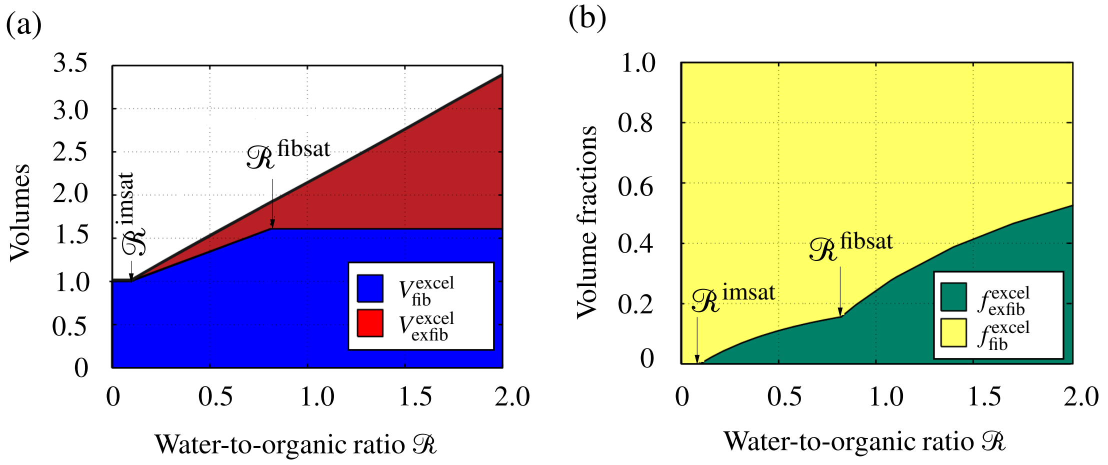

Figure 2.10: Tissue swelling (a) and evolution of tissue composition (b) during hydration: (a) water-to-organic mass ratio $\mathscr{R}$ over the fibrillar and extrafibrillar volumes making up the tissue; (b) water-to-organic mass ratio $\mathscr{R}$ over the fibrillar and extrafibrillar volume fractions at the tissue scale

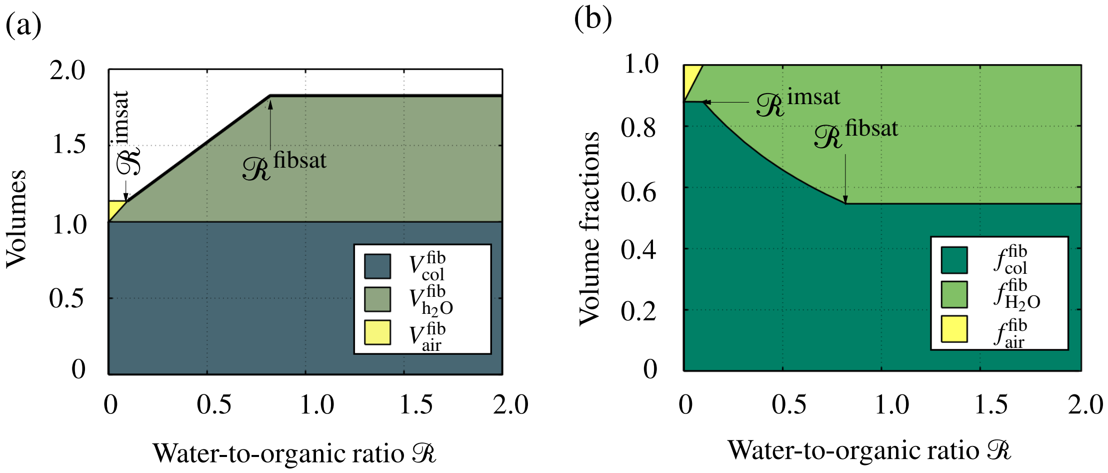

Figure 2.11: Fibrillar swelling (a) and evolution of fibrillar composition (b) during hydration: (a) water-to-organic mass ratio $\mathscr{R}$ over the volumes of molecular collagen, water, and air making up the fibrils; (b) water-to-organic mass ratio $\mathscr{R}$ over the volume fractions of collagen, water, and air at the tissue scale

2.6 Bone tissue evolution during mineralization

Inspired by an interesting idea of Lees [2003], Morin and Hellmich [2013] showed that the volume and structure changes in mineralizing bone tissues can be mathematically predicted when considering the extracellular bone tissue and its subvolumes (both the fibrils and the extrafibrillar space) as closed thermodynamic systems: i.e. if no fluid mass leaves or enters these volumes during the mineralization process, then the precipitation of hydroxyapatite crystals entails that the mass of lost ionic fluid equals the mass of formed solid hydroxyapatite crystal in the fibrillar and extrafibrillar subvolumes, as well as in the entire tissue volume, while the collagen mass remains unaltered. The precipitation of dissolved ions into solid mineral crystals is accompanied by an increase in mass density, which, upon overall conservation under closed conditions, leads to a volume decrease (or shrinkage) of the tissues during the biomineralization process. This shrinkage affects both the fibrillar and the extrafibrillar tissue compartments. Thereby, the fibrillar shrinkage can be experimentally accessed through equatorial neutron diffraction spacings $d_{\mathrm{w},\infty}$, measured on fully mineralized tissues [Miles and Ghelashvili, 1999, Morin et al., 2013]

$$\left(\frac{d_{\mathrm{w},\infty}}{d_{\mathrm{w},0}}\right)^2 = \frac{V^{\mathrm{excel}}_{\mathrm{fib},\infty}}{V^{\mathrm{excel}}_{\mathrm{fib},0}}\,, \tag{2.29}$$

with $d_{\mathrm{w},0}$ as the neutron diffraction spacing at the time of osteoid deposition (i.e. the beginning of the mineralization process), and $V^{\mathrm{excel}}_{\mathrm{fib},0}$ and $V^{\mathrm{excel}}_{\mathrm{fib},\infty}$ as the fibrillar volume in unmineralized and fully mineralized tissues, respectively.

The mass density-diffraction relation ($\rho^{\mathrm{excel}}_{\infty}$-$d_{\mathrm{w},\infty}$-relation) is derived in three consecutive steps: First, the mineralization-induced tissue shrinkage is evaluated at the tissue level, based on the "universal" composition rules described in Section 3, yielding [Morin and Hellmich, 2013]

$$\frac{V^{\mathrm{excel}}_{\infty}}{V^{\mathrm{excel}}_{0}} = \frac{1}{1 + (\rho_{\mathrm{HA}}/\rho_{\mathrm{fl}} - 1) \times f^{\mathrm{excel}}_{\mathrm{HA},\infty}(\rho^{\mathrm{excel}}_{\infty})}\,, \tag{2.30}$$

with V^{excel}_{0} and $V^{\mathrm{excel}}_{\infty}$ as the extracellular tissue volumes at the beginning and the end of the mineralization process, ρ_{HA} and ρ_{fl} as the mass densities of hydroxyapatite and ionic fluid, $f^{\mathrm{excel}}_{\mathrm{HA},\infty}$ as the mineral volume fraction in the fully mineralized tissue, which depends on the tissue mass density, $\rho^{\mathrm{excel}}_{\infty}$.

Secondly, this relation is downscaled to the extrafibrillar space, by considering the equality of mineral concentrations in the extracollagenous and the extrafibrillar spaces [Hellmich and Ulm, 2003], see Section 2.4, and the hydration swelling rule for unmineralized tissues [Morin et al., 2013], as described in Section 2.5. The corresponding volume change reads as [Morin and Hellmich, 2013]

$$\frac{V^{\text{excel}}_{\text{exfib},\infty}}{V^{\text{excel}}_{\text{exfib},0}} = 1 + \frac{(1-\rho_{\text{HA}}/\rho_{\text{fl}})}{1-f^{\text{excel}}_{\text{col},0}}\frac{V^{\text{excel}}_{\infty}}{V^{\text{excel}}_{0}} \times f^{\text{excel}}_{\text{HA},\infty}(\rho^{\text{excel}}_{\infty})\,, \tag{2.31}$$

where $V^{\text{excel}}_{\infty}/V^{\text{excel}}_{0}$ obeys Eq. (2.30), $f^{\text{excel}}_{\text{HA},\infty}(\rho^{\text{excel}}_{\infty})$ follows from the universal composition rules (see Section 2.3), and $f^{\text{excel}}_{\text{col},0}$ is the collagen volume fraction in unmineralized tissue, which can be quantified from the hydration-dependent swelling rules described in Section 2.5, see [Morin et al., 2013] for details.
Thirdly, the fibrillar shrinkage is analogously derived,

$$\frac{V^{\text{excel}}_{\text{fib},\infty}}{V^{\text{excel}}_{\text{fib},0}} = \frac{f^{\text{excel}}_{\text{fib},\infty}}{f^{\text{excel}}_{\text{fib},0}}\frac{V^{\text{excel}}_{\infty}}{V^{\text{excel}}_{0}}\,, \tag{2.32}$$

and this ratio is related to the change in diffraction spacing, as given in Eq. (2.29), with $d_{\text{w},0} = d_{\max} = 1.52\,\text{nm}$ as the diffraction spacing of fully saturated unmineralized collageneous tissues [Brodsky et al., 1982, Eanes and Lundy, 1970, Katz and Li, 1973, Lees et al., 1984]. Finally, these relations are translated into the sought mass density-diffraction spacing relations, according to continuum geometry and considering negligible length changes in the meridional direction of the tissue [Morin et al., 2013]. In case of fully-hydrated tissues, this relation reads as

$$d_{\text{w},\infty} = d_{\max}\sqrt{\frac{1-f^{\text{excel}}_{\text{exfib},0}\times\left[1-(\rho_{\text{HA}}/\rho_{\text{fl}}-1)\times f^{\text{excel}}_{\text{HA},\infty}\times\frac{f^{\text{excel}}_{\text{col},\infty}}{\rho_{\text{HA}}f^{\text{excel}}_{\text{HA},\infty}/\rho_{\text{fl}}+f^{\text{excel}}_{\text{fl},\infty}}\right]}{(1-f^{\text{excel}}_{\text{exfib},0})\times\left[1+(\rho_{\text{HA}}/\rho_{\text{fl}}-1)\times f^{\text{excel}}_{\text{HA},\infty}\right]}}\,, \tag{2.33}$$

with

$$f^{\text{excel}}_{\text{exfib},0} = 1 - \frac{1}{0.88}\left(\frac{d_{\max}}{d_{\text{dry}}}\right)^2 \frac{f^{\text{excel}}_{\text{col},\infty}}{\rho_{\text{HA}}f^{\text{excel}}_{\text{HA},\infty}/\rho_{\text{fl}}+f^{\text{excel}}_{\text{fl},\infty}+f^{\text{excel}}_{\text{col},\infty}}\,, \tag{2.34}$$

where $d_{\max} = 1.52\,\text{nm}$ and $d_{\text{dry}} = 1.09\,\text{nm}$, and with dependencies $f^{\text{excel}}_{\text{HA},\infty}$, $f^{\text{excel}}_{\text{col},\infty}$, and $f^{\text{excel}}_{\text{fl},\infty}$ on tissue mass density as given in Section 2.3 (see Eqs. (2.16) and (2.17)).
In case of partially dehydrated tissues, some fluid mass (and corresponding volume)

will be lost during dehydration,

$$\Delta f^{\mu,\mathrm{dh}}_{\mathrm{fl},\infty} = f^{\mu}_{\mathrm{fl},\infty} - f^{\mu,\mathrm{dh}}_{\mathrm{fl},\infty} = f^{\mu}_{\mathrm{fl},\infty} - \mathscr{R}^{\infty,dh} f^{\mu}_{\mathrm{col},\infty} \rho_{\mathrm{col}}/\rho_{\mathrm{fl}}\,, \tag{2.35}$$

with $\mathscr{R}^{\infty,dh}$ as the experimentally measured water-to-organic mass ratio of partially dehydrated tissues at the macroscopic scale, as e.g. given by Lees and Mook [1986]. The volume fraction of the remaining fluid after dehydration per extracellular bone matrix reads as

$$f^{\mathrm{excel,dh}}_{\mathrm{fl},\infty} = \frac{f^{\mu}_{\mathrm{fl},\infty} - \min(\Delta f^{\mu,\mathrm{dh}}_{\mathrm{fl},\infty}, f_{\mu\mathrm{por}})}{1 - f_{\mu\mathrm{por}}}\,. \tag{2.36}$$

The lost fluid volume fraction in the extracellular scale amounts to

$$\Delta f^{\mathrm{excel,dh}}_{\mathrm{fl},\infty} = f^{\mathrm{excel}}_{\mathrm{fl},\infty} - f^{\mathrm{excel,dh}}_{\mathrm{fl},\infty}\,. \tag{2.37}$$

The mass density-diffraction spacing relation for partially dehydrated tissues reads as

$$d^{dh}_{\mathrm{w},\infty} = d_{\mathrm{w},\infty} \sqrt{1 - \frac{\Delta f^{\mathrm{excel,dh}}_{\mathrm{fl},\infty} - f^{\mathrm{excel}}_{\mathrm{exfib},0} \Delta f^{\mathrm{excel,dh}}_{\mathrm{fl},\infty} / (1 - f^{\mathrm{excel}}_{\mathrm{col},0})}{f^{\mathrm{excel}}_{\mathrm{fib},\infty}}}\,, \tag{2.38}$$

with

$$f^{\mathrm{excel}}_{\mathrm{fib},\infty} = 1 - \left\{ \frac{f^{\mathrm{excel}}_{\mathrm{exfib},0}}{\frac{1}{1+(\rho_{\mathrm{HA}}/\rho_{\mathrm{fl}}-1)\times f^{\mathrm{excel}}_{\mathrm{HA},\infty}}} + \frac{f^{\mathrm{excel}}_{\mathrm{exfib},0}}{1 - f^{\mathrm{excel}}_{\mathrm{col},0}} \times (1 - \rho_{\mathrm{HA}}/\rho_{\mathrm{fl}}) \times f^{\mathrm{excel}}_{\mathrm{HA},\infty} \right\}\,, \tag{2.39}$$

and

$$f^{\mathrm{excel}}_{\mathrm{col},0} = \frac{f^{\mathrm{excel}}_{\mathrm{col},\infty}}{\rho_{\mathrm{HA}} f^{\mathrm{excel}}_{\mathrm{HA},\infty}/\rho_{\mathrm{fl}} + f^{\mathrm{excel}}_{\mathrm{fl},\infty} + f^{\mathrm{excel}}_{\mathrm{col},\infty}}\,. \tag{2.40}$$

Identification of $\Delta f^{\mathrm{excel,dh}}_{\mathrm{fl},\infty} = f^{\mathrm{excel}}_{\mathrm{fl},\infty}$ delivers model predictions for the diffraction spacings in fully dried tissues. These mass density-diffraction spacing relations are fed with experimental data for tissue mass density and the corresponding predictions for diffraction spacing are validated through comparison with experimental results [Lees, 2003, Lees and Mook, 1986, Lees et al., 1984]. Very low prediction errors of 1.8 ± 3.1 % underline the relevance of the model-predicted evolutions of the tissue compartment volumes, and of the model-predicted volume fractions during the mineralization process in different bone tissues (see Figure 2.12); and hence, the idea of hydroxyapatite precipitating under closed thermodynamic conditions

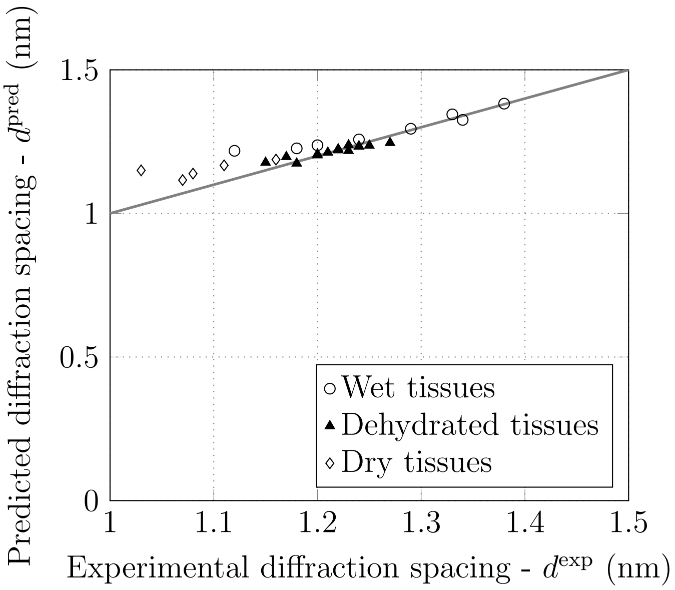

Figure 2.12: Predicted vs. experimental diffraction spacing for wet, dry, and partially dehydrated, mineralized tissues

from an ionic solution in the fibrillar and extrafibrillar spaces of bone tissue. Accordingly, the structural (volumetric) evolution of mineralizing bone tissue can be quantified as follows: during mineralization, the volume of the overall collagenous tissue is shrinking because the mass density of hydroxyapatite is around three times larger than that of liquid ionic solution. In general, the more mineral is present in the tissue, the higher the shrinkage of the volumes of the different compartments (see Figure 2.13). More specifically, this volume loss is minimal for low-mineralized tissues at the beginning of the mineralization process (see the left lower corner of Figure 2.13), whereas highly mineralized bone tissue has lost up to 60 % of its initial (osteoid) volume (see the right upper corner of Figure 2.13). The compositional evolution can be also quantified in terms of volume fractions: the mineralization process leads to a slight increase of the fibrillar volume fractions, since the fibrils, thanks to the presence of chemically inert collagen, are less affected by the fluid-to-crystal transformation-induced volume loss, as compared to the extrafibrillar space. Within the fibrils, the fluid volume fraction, starting from around 50% in the unmineralized osteoid, is reduced by one third in the case of low-mineralized tissues (see Figure 2.14(a)), while it is almost completely consumed in the case of very highly mineralized tissues (see Figure 2.14(d)). Thereby, “lost” fluid volume fractions are replaced by collagen and mineral volume fractions, at about the same shares (see Figure 2.14(a)-(d)). In the extrafibrillar space, mineral volume fractions increase overlinearly with the mineralization degree, the more so

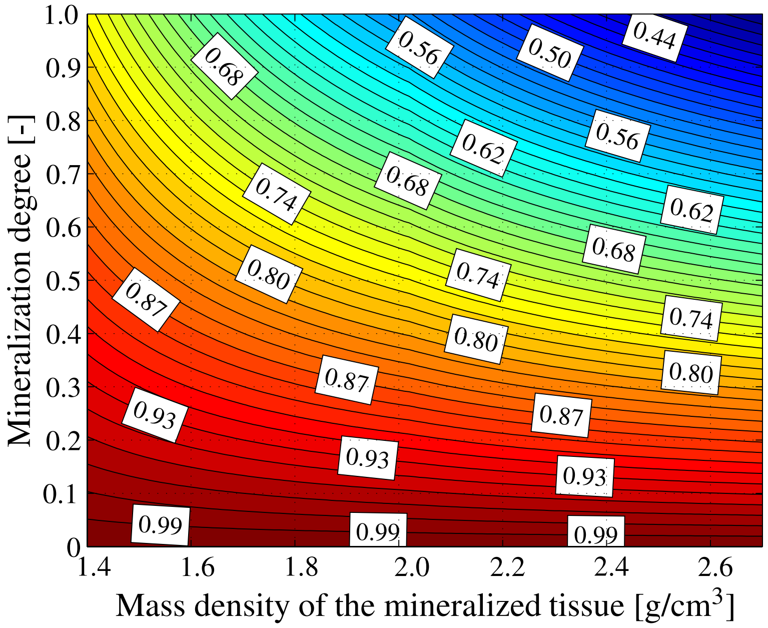

Figure 2.13: Normalized tissue volume as function of the mineralization degree for different final tissue mass densities

the more highly the tissue is mineralized.

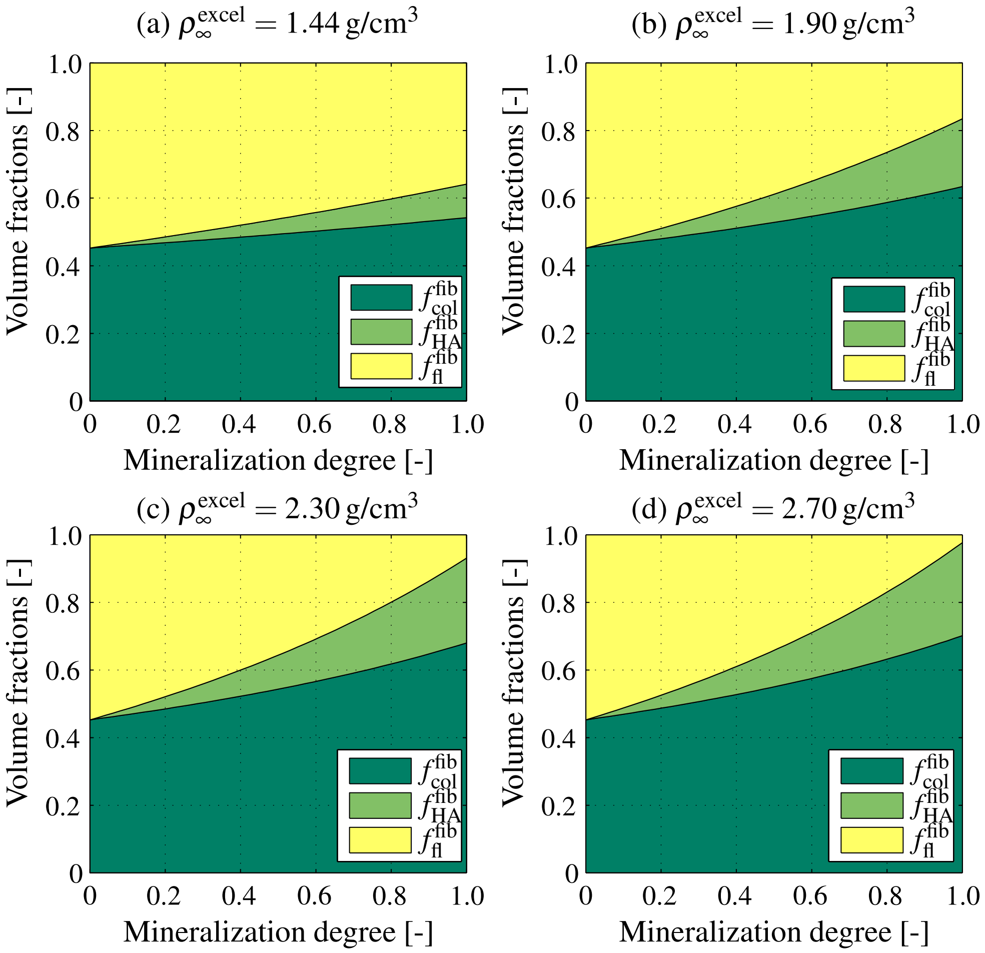

Figure 2.14: Normalized tissue volume as function of the mineralization degree, for different final tissue mass densities

2.7 Nano- and microstructural patterns governing anisotropic tissue elasticity

Throughout the last two decades, hierarchical material models for bone [Aoubiza et al., 1996, Crolet et al., 1993, Grimal et al., 2011, Hamed et al., 2010, 2015, Hellmich and Ulm, 2002a, 2005a,b, Hellmich et al., 2004a,b, Martínez-Reina et al., 2011, Morin and Hellmich, 2014, Nikolov and Raabe, 2008, Parnell and Grimal, 2009, Pidaparti and Burr, 1992, Pidaparti et al., 1996, Reisinger et al., 2010, Sansalone et al., 2010, Yoon and Cowin, 2008], developed within the frameworks of homogenization theory and continuum micromechanics [Auriault et al., 2009, Dormieux et al., 2006a, Zaoui, 2002] and validated through a multitude of biochemical, biophysical, and biomechanical experiments [Biltz and Pellegrino, 1969, Bonar et al., 1985, Burns, 1929, Gong et al., 1964, Hammet, 1925, Keaveny et al., 1994, Lees, 1987, 2003, Lees and Page, 1992, Lees et al., 1979a, 1983, 1994b, 1995, McCarthy et al., 1990, Rho et al., 1995, Turner et al., 1990], have opened the way to translate the chemical composition of extracellular bone material (i.e. the volume fractions of organics, water, and hydroxyapatite) into the tissue's anisotropic elasticity. This section is devoted to briefly introducing the fundamentals of continuum micromechanics, and to presenting how this theoretical framework has elucidated the "construction plans" providing the most fascinating mechanical properties of bone.

2.7.1 Micromechanical representation of bone tissue by means of representative volume elements (RVEs)

In continuum micromechanics [Dormieux et al., 2006a, Hill, 1963, Zaoui, 1997, 2002], a material is understood as a macro-homogeneous, but micro-heterogeneous body filling a representative volume element (RVE) with characteristic length ℓ, which must be both considerably larger than the dimensions of heterogeneities within the RVE, d, and significantly smaller than the characteristic lengths of geometry or loading of a structure built up by the material defined on the RVE, $\mathscr{L}$. The characteristic length of structural loading typically coincides with wave lengths of signals traveling through the structure, or relates to macroscopic stress gradients according to $\mathscr{L} \approx ||\boldsymbol{\Sigma}||/||\mathrm{GRAD}\boldsymbol{\Sigma}||$ [Auriault et al., 2009], with the "macroscopic" stress tensor $\boldsymbol{\Sigma}$. In mathematical terms, the aforementioned separation of scales requirement reads as

$$d \ll \ell \ll \mathscr{L} \, . \tag{2.41}$$

Hereby, the first inequality sign typically relates to a factor of 2 to 3 [Drugan and Willis, 1996]; while the second one typically relates to a factor of 5 to 50 [Kohlhauser and Hellmich, 2013].

In general, the microstructure within one RVE is so complex that it cannot be described in complete detail. Therefore, quasi-homogeneous subdomains, called material phases, with known physical quantities are reasonably chosen. Quantitative phase properties are volume fractions f_r of phases $r = 1, \ldots, N_r$, (average) elastic properties, as well as the morphological description, as, e.g. the isotropy or the symmetries of anisotropy of the spatial distribution of the phases, the existence of one connected "matrix phase" in which one or several "inclusion phases" with different shapes are embedded (as in reinforced composite material), or the disordered arrangement of all phases (as in a polycrystal).

The central goal of continuum micromechanics is to estimate the mechanical properties (such as elasticity or strength) of the material defined on the RVE from the aforementioned phase properties. This procedure is referred to as homogenization or one homogenization step. If a single phase exhibits a heterogeneous microstructure itself, its mechanical behavior can be estimated by introduction of an RVE within this phase [Fritsch and Hellmich, 2007], with dimensions $\ell_2 \leq d$, comprising again smaller phases with characteristic length $d_2 \ll \ell_2$, and so on, leading to a multistep homogenization scheme, as in case of bone (see Figure 2.15). In this context, the following "universal" microstructural patterns are considered across the hierarchical organization of bone materials:

- an RVE of wet collagen, with a characteristic length of several nanometers [see Figure 2.15(a)], represents the staggered organization of cylindrical collagen molecules [see Figure 2.1(h)], which are attached to each other by ∼ 1.5 nm long crosslinks [Bailey et al., 1998, Lees et al., 1984, Orgel et al., 2006]. These crosslinks imply the existence of a contiguous matrix built up by molecular collagen, hosting fluid-filled intermolecular spaces, which are represented by cylindrical inclusions;
- an RVE of mineralized collagen fibril, with a characteristic length of several hundred nanometers [see Figure 2.15(b)], hosts hydroxyapatite crystal clusters filling the gap zones in and spreading through the cylindrical microfibrils of wet collagen;
- an RVE of extrafibrillar space (hydroxyapatite foam), with a characteristic length of several hundred nanometers [see Figure 2.15(c)], hosts crystal needles (represented through infinitely many uniformly oriented cylindrical hydroxyapatite inclusions) oriented in all space directions; in mutual interaction with spherical, water-filled pores in-between;
- an RVE of extracellular bone matrix or ultrastructure, with a characteristic length of several micrometers [see Figure 2.15(d)], hosts cylindrical, mineralized fibrils being embedded into a contiguous matrix built up by hydroxyapatite foam material;

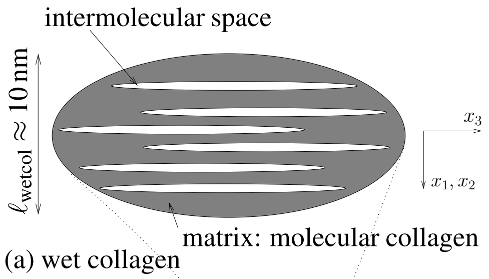
intermolecular space
$\ell_{\text{wetcol}} \approx 10\,\text{nm}$
x_3
x_1, x_2
matrix: molecular collagen

(a) wet collagen

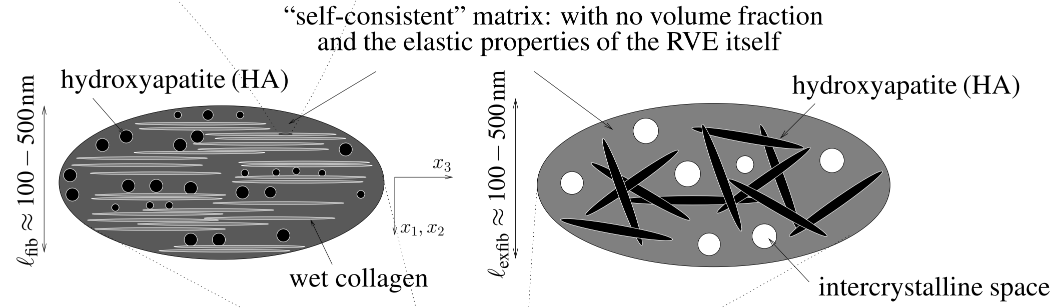
"self-consistent" matrix: with no volume fraction and the elastic properties of the RVE itself
hydroxyapatite (HA)
$\ell_{\text{fib}} \approx 100 - 500\,\text{nm}$
x_3
x_1, x_2
wet collagen
$\ell_{\text{exfib}} \approx 100 - 500\,\text{nm}$
hydroxyapatite (HA)
intercrystalline space

(b) collagen - hydroxyapatite network (fibril) (c) hydroxyapatite foam (extrafibrillar space)

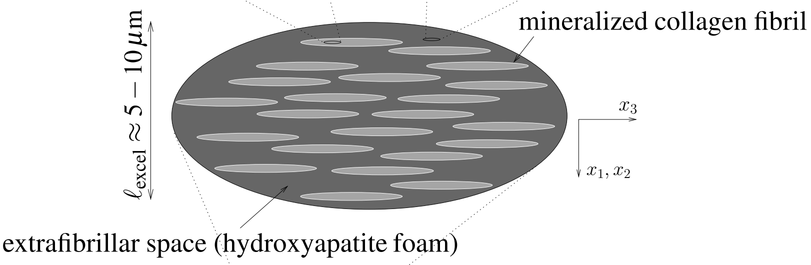
$\ell_{\text{excel}} \approx 5 - 10\,\mu\text{m}$
mineralized collagen fibril
x_3
x_1, x_2
extrafibrillar space (hydroxyapatite foam)

(d) extracellular bone matrix or ultrastructure

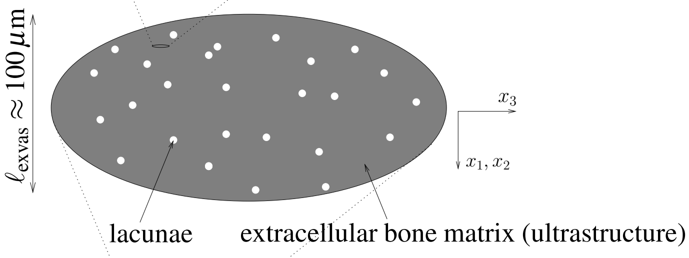
$\ell_{\text{exvas}} \approx 100\,\mu\text{m}$
x_3
x_1, x_2
lacunae
extracellular bone matrix (ultrastructure)

(e) extravascular bone material

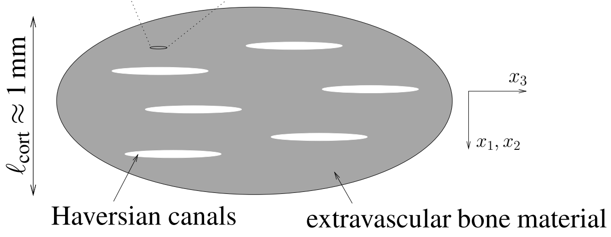
$\ell_{\text{cort}} \approx 1\,\text{mm}$
x_3
x_1, x_2
Haversian canals
extravascular bone material

(f) bone microstructure (cortical bone)

Figure 2.15: Micromechanical representation of bone material by means of a six-step homogenization scheme, according to Fritsch et al. [2009c]

- an RVE of extravascular bone material, with a characteristic length of several hundred micrometers [see Figure 2.15(e)], hosts spherical, osteocyte-filled cavities called lacunae being embedded into a contiguous matrix built up by the extracellular bone material; and
- an RVE of cortical bone material, with a characteristic length of several millimeters [see Figure 2.15(f)], hosts cylindrical vascular pores being embedded into a matrix of extravascular bone material.

2.7.2 Elasticity homogenization

As concerns the homogenization (or upscaling) of the elastic properties of bone, starting from the level of its basic building blocks, up to the level of the bone microstructure, see Figure 2.15, we start with focusing on a single RVE built up by phases enumerated by r. The second-order strain tensor, $\boldsymbol{\varepsilon}_r$, is related to the (average "microscopic") second-order stress tensor in phase r, $\boldsymbol{\sigma}_r$, by the phase elasticity tensor $\mathbb{c}_r$

$$\boldsymbol{\sigma}_r = \mathbb{c}_r : \boldsymbol{\varepsilon}_r \, . \tag{2.42}$$

The RVE is subjected to homogeneous (macroscopic) strains $\boldsymbol{E}$ at its boundary [Hashin, 1983], prescribed in terms of displacements

$$\forall \mathbf{x} \in \partial V_{RVE} : \qquad \boldsymbol{\xi}(\mathbf{x}) = \mathbf{E} \cdot \mathbf{x} \, , \tag{2.43}$$

whereby $\mathbf{x}$ is the position vector for locations within or at the boundary of the RVE. As a consequence, the resulting kinematically compatible microstrains $\boldsymbol{\varepsilon}(\mathbf{x})$ throughout the RVE fulfill the average condition,

$$\mathbf{E} = \frac{1}{V_{RVE}} \int_{V_{RVE}} \boldsymbol{\varepsilon} dV = \langle \boldsymbol{\varepsilon} \rangle = \sum_r f_r \boldsymbol{\varepsilon}_r \, , \tag{2.44}$$

providing a link between the (average) microscopic and macroscopic strains. Furthermore, the aforementioned deformations provoke traction forces $\mathbf{T}(\mathbf{x})$ on the boundary of the RVE, and microstresses $\boldsymbol{\sigma}(\mathbf{x})$ throughout the RVE, fulfilling the equilibrium conditions

$$\begin{aligned} &\forall \mathbf{x} \in V_{RVE} \quad \operatorname{div} \boldsymbol{\sigma}(\mathbf{x}) = 0 \, , \\ &\forall \mathbf{x} \in \partial V_{RVE} \quad \mathbf{T}\left(\mathbf{x}\right) = \boldsymbol{\sigma}\left(\mathbf{x}\right) \cdot \mathbf{n}\left(\mathbf{x}\right) \, , \end{aligned} \tag{2.45}$$

with $\mathbf{n}\left(\mathbf{x}\right)$ as the normal to the boundary at position $\mathbf{x}$. The external work done by these traction forces reads as

$$\begin{aligned}\mathscr{W}^{ext} &= \int_{\partial V_{RVE}} \mathbf{T}\left(\mathbf{x}\right)\cdot\boldsymbol{\xi}\left(\mathbf{x}\right)dS = \int_{\partial V_{RVE}} \left(\mathbf{E}\cdot\mathbf{x}\right)\cdot\left[\boldsymbol{\sigma}\left(\mathbf{x}\right)\cdot\mathbf{n}\left(\mathbf{x}\right)\right]dS \\ &= \mathbf{E} : \int_{V_{RVE}} \boldsymbol{\sigma}\left(\mathbf{x}\right)dV\,,\end{aligned} \tag{2.46}$$

whereby we made use of boundary condition (2.43) and of the divergence theorem. Hence, the force quantity doing work on the macroscopic strains $\mathbf{E}$ is the volume integral over the microscopic stress, which is independent of microscopic position and of dimension “stress times volume”. This induces the existence of the macroscopic stress $\boldsymbol{\Sigma}$ in the form

$$\boldsymbol{\Sigma}\,V_{RVE} = \int_{V_{RVE}} \boldsymbol{\sigma}\left(\mathbf{x}\right)dV \;\;\Leftrightarrow\;\; \boldsymbol{\Sigma} = \frac{1}{V_{RVE}}\int_{V_{RVE}} \boldsymbol{\sigma}\left(\mathbf{x}\right)dV = \langle\boldsymbol{\sigma}\rangle = \sum_r f_r\boldsymbol{\sigma}_r, \tag{2.47}$$

i.e. the well-known stress average rule. Insertion of (2.47) into the principle of virtual power [Germain, 1973, Maugin, 2013, Salençon, 2001], which in the case of linearized strains, can be expressed in terms of an expression with the dimension “work”,

$$\mathscr{W}^{ext} = -\mathscr{W}^{int} = \int_{V_{RVE}} \boldsymbol{\sigma}\left(\mathbf{x}\right) : \boldsymbol{\varepsilon}\left(\mathbf{x}\right)dV\,, \tag{2.48}$$

yields the so-called Hill’s lemma

$$\boldsymbol{\Sigma} : \mathbf{E} = \frac{1}{V_{RVE}}\int_{V_{RVE}} \boldsymbol{\sigma}\left(\mathbf{x}\right) : \boldsymbol{\varepsilon}\left(\mathbf{x}\right)dV = \langle\boldsymbol{\sigma} : \boldsymbol{\varepsilon}\rangle\,. \tag{2.49}$$

Linearity of elastic law (2.42) and of partial differential equation $(2.45)_1$ imply a multi-linear relation between the homogenized (macroscopic) strain $\mathbf{E}$ and the average (microscopic) strain $\boldsymbol{\varepsilon}_r$, expressed by the fourth-order concentration tensors $\mathbb{A}_r$ of each of the phases r,

$$\boldsymbol{\varepsilon}_r = \mathbb{A}_r : \mathbf{E}\,. \tag{2.50}$$

Insertion of Eq. (2.50) into Eq. (2.42) and averaging over all phases according to Eq. (2.47) leads to

$$\boldsymbol{\Sigma} = \sum_r f_r\mathbb{C}_r : \mathbb{A}_r : \mathbf{E}\,. \tag{2.51}$$

Eq. (2.51) implies the existence of a macroscopic "homogenized" stiffness tensor linking macroscopic stresses to macroscopic strains in the format

$$\boldsymbol{\Sigma} = \mathbb{C}^{\text{hom}} : \mathbf{E}\,, \tag{2.52}$$

yielding $\mathbb{C}^{\text{hom}}$ as

$$\mathbb{C}^{\text{hom}} = \sum_r f_r \mathbb{c}_r : \mathbb{A}_r\,. \tag{2.53}$$

The concentration tensors $\mathbb{A}_r$ are estimated from matrix-inclusion problems, pioneered by Eshelby [1957]. On a mathematical level, this is achieved by setting the phase strains equal to those in ellipsoidal inclusions in infinitely extending matrices of stiffness $\mathbb{C}^0$ subjected to remote strains, and by combining respective semi-analytical relationships [Eshelby, 1957, Laws, 1977b] with stress and strain average rules [Hashin, 1983, Zaoui, 2002], yielding

$$\mathbb{A}_r = \left[\mathbb{I} + \mathbb{P}^0_r : \left(\mathbb{c}_r - \mathbb{C}^0\right)\right]^{-1} : \left\{\sum_s f_s \left[\mathbb{I} + \mathbb{P}^0_s : \left(\mathbb{c}_s - \mathbb{C}^0\right)\right]^{-1}\right\}^{-1}. \tag{2.54}$$

Insertion of Eq. (2.54) into (2.51) yields an expression for the macroscopic homogenized stiffness tensor as function of their volume fractions, shapes and interactions

$$\mathbb{C}^{\text{hom}} = \sum_r f_r \mathbb{c}_r : \left[\mathbb{I} + \mathbb{P}^0_r : (\mathbb{c}_r - \mathbb{C}^0)\right]^{-1} : \left\{\sum_s f_s \left[\mathbb{I} + \mathbb{P}^0_s : (\mathbb{c}_s - \mathbb{C}^0)\right]^{-1}\right\}^{-1}, \tag{2.55}$$

where f_r and $\mathbb{c}_r$ are the volume fraction and the elastic stiffness of phase r, $\mathbb{I}$ is the fourth-order unity tensor, $\mathbb{P}^0_r$ the fourth-order Hill tensor accounting for the characteristic shape of phase r, which, in case of ellipsoidal inclusions in anisotropic media [Laws, 1977b, 1985], reads as

$$P^0_{r,ijkl} = \frac{1}{16\pi\alpha^{1/2}} \int_\Omega \frac{1}{t^3} \left\{\hat{g}_{il} w_j w_k + \hat{g}_{ik} w_j w_l + \hat{g}_{jl} w_i w_k + \hat{g}_{jk} w_i w_l\right\} dS(\mathbf{w})\,. \tag{2.56}$$

In Eq. (2.56), the shape of the ellipsoid is considered by $\alpha = \det \alpha_{ij}$, being related to the equation of the ellipsoid, $\alpha_{ij} x_i x_j = 1$, $dS(\mathbf{w})$ is a surface element of the unit sphere (with surface Ω); w_1, w_2 and w_3 are the components of the unit length vector $\mathbf{w}$ pointing from the origin of the sphere to the surface element $dS(\mathbf{w})$, and $t^2 = \alpha^{-1}_{ij} w_i w_j$. Finally, $\hat{g}_{ik}$ are the components of the inverse of the second-order tensor $C^0_{ijkl} w_j w_l$, with C^0_{ijkl} denoting the stiffness of anisotropic matrix.

As regards the matrix stiffness, $\mathbb{C}^0$, its choice governs the interactions between the phases inside the RVE: $\mathbb{C}^0 = \mathbb{C}^{\text{hom}}$ relates to a dispersed arrangement of phases where all phases “feel” the overall homogenized material, and the corresponding homogenization scheme is standardly called self-consistent [Hershey, 1954, Kröner, 1958], well-suited for polycrystalline materials [applied for RVEs depicted in Figure 2.15(b) and (c)]. On the other hand, the matrix may be identified as a phase m itself, $\mathbb{C}^0 = \mathbb{c}_m$, which relates to matrix-inclusion-type composite, and the corresponding homogenization scheme is standardly referred to as Mori-Tanaka scheme [Benveniste, 1987, Mori and Tanaka, 1973] [applied for RVEs depicted in Figure 2.15(a), (d), (e), and (f)].

Strictly speaking, the RVE of extrafibrillar space [see Figure 2.15(c)] requires a slight (but important) modification of the aforementioned developments: it consists of one pore space and infinitely many cylindrical solid phases which are oriented in all space directions. This requires modification of Eqs. (2.44), (2.47), (2.53), and (2.55) in terms of integrals over the unit sphere [Fritsch et al., 2006]. Accordingly, the homogenized stiffness of the extrafibrillar RVE of Figure 2.15(c) reads as

$$
\begin{aligned}
\mathbb{C}^{\text{hom}}_{\text{exfib}} = \Bigg\{ & f^{\text{exfib}}_{\text{HA}} \mathbb{c}_{\text{HA}} : \int_{\varphi=0}^{2\pi} \int_{\theta=0}^{\pi} \left[\mathbb{I} + \mathbb{P}^{\text{exfib}}_{\text{cyl}}(\theta,\varphi) : (\mathbb{c}_{\text{HA}} - \mathbb{C}^{\text{hom}}_{\text{exfib}})\right]^{-1} \frac{\sin\theta d\theta d\varphi}{4\pi} + \\
& \left(1 - f^{\text{exfib}}_{\text{HA}}\right) \mathbb{c}_{\text{H}_2\text{O}} : \left[\mathbb{I} + \mathbb{P}^{\text{exfib}}_{\text{sph}} : (\mathbb{c}_{\text{H}_2\text{O}} - \mathbb{C}^{\text{hom}}_{\text{exfib}})\right]^{-1} \Bigg\} : \\
& \Bigg\{ f^{\text{exfib}}_{\text{HA}} \int_{\varphi=0}^{2\pi} \int_{\theta=0}^{\pi} \left[\mathbb{I} + \mathbb{P}^{\text{exfib}}_{\text{cyl}}(\theta,\varphi) : (\mathbb{c}_{\text{HA}} - \mathbb{C}^{\text{hom}}_{\text{exfib}})\right]^{-1} \frac{\sin\theta d\theta d\varphi}{4\pi} + \\
& \left(1 - f^{\text{exfib}}_{\text{HA}}\right) \left[\mathbb{I} + \mathbb{P}^{\text{exfib}}_{\text{sph}} : (\mathbb{c}_{\text{H}_2\text{O}} - \mathbb{C}^{\text{hom}}_{\text{exfib}})\right]^{-1} \Bigg\}^{-1},
\end{aligned}
\tag{2.57}
$$

with $\mathbb{P}^{\text{exfib}}_{\text{cyl}}$ and $\mathbb{P}^{\text{exfib}}_{\text{sph}}$ standing for the Hill tensor of a cylindrical or a spherical inclusion embedded in a matrix with a stiffness of $\mathbb{C}^{\text{hom}}_{\text{exfib}}$, respectively.

2.7.3 Elasticity of elementary components

The micromechanical representation of Figure 2.15 is validated at different observation scales, namely at the extracellular, the extravascular, and the cortical/trabecular scales. All corresponding computations are based on the *same* elasticity properties assigned to bone's elementary constituents: hydroxyapatite, (molecular) collagen, and water (with some non-collagenous organics). The elastic properties of hydroxyapatite are obtained from tests with an ultrasonic interferometer coupled with a solid media pressure apparatus [Katz and Ukraincik, 1971], which reveal the isotropic elastic properties of hydroxyapatite powder,

$$\mathbb{c}_{\mathrm{HA}} = 3k_{\mathrm{HA}}\mathbb{I}_{\mathrm{vol}} + 2\mu_{\mathrm{HA}}\mathbb{I}_{\mathrm{dev}}\,, \tag{2.58}$$

with $\mathbb{I}_{\mathrm{vol}}$ and $\mathbb{I}_{\mathrm{dev}}$ as the volumetric and deviatoric part of the fourth-order identity tensor $\mathbb{I}$, and with $k_{\mathrm{HA}} = 82.6\,\mathrm{GPa}$ and $\mu_{\mathrm{HA}} = 44.9\,\mathrm{GPa}$, as the bulk and shear moduli of hydroxyapatite. In view of the largely disordered arrangement of poorly crystalline minerals [Epple, 2001, Fratzl et al., 1996, Hellmich and Ulm, 2002b, 2003, Hellmich et al., 2004a, Lees et al., 1994a, Peters et al., 2000], this isotropic characterization is sufficient for successful bone elasticity upscaling [Crolet et al., 1993, Fritsch et al., 2006, Hellmich and Ulm, 2002a, Hellmich et al., 2004b, Yoon and Cowin, 2008], as is also confirmed by the validation diagrams of Figures 2.16 to 2.21. Sasaki and Odajima [1996] determined the Young's modulus of molecular collagen by a hybrid mechanical–X-ray technique, considering Lees' 1987 packing model [Lees, 1987] for the cross-sectional arrangement of collagen molecules. This resulted in an elastic Young's modulus of 2.9 GPa. As they did not account for the additional 12 % microporosity which is still present in "fully dehydrated" collagen [Lees and Heeley, 1981], the aforementioned values relate to the RVE of Figure 2.15(a) with 12 % intermolecular space. Adopting a Poisson's ratio of 0.34 for such an RVE [Cusack and Miller, 1979], the corresponding homogenization relation allows for back-analysis of an isotropic estimate of the stiffness tensor of molecular collagen, which reads in Kelvin-Mandel notation (see e.g. Eq. (44) of Helnwein [2001] or Eq. (2a) of Cowin [2003]) as

$$\mathbb{c}_{\mathrm{col}} = \left\{\begin{array}{cccccc} 4.86 & 2.39 & 2.39 & 0 & 0 & 0 \\ 2.39 & 4.86 & 2.39 & 0 & 0 & 0 \\ 2.39 & 2.39 & 4.86 & 0 & 0 & 0 \\ 0 & 0 & 0 & 1.23 & 0 & 0 \\ 0 & 0 & 0 & 0 & 1.23 & 0 \\ 0 & 0 & 0 & 0 & 0 & 1.23 \end{array}\right\} \mathrm{GPa}\,, \tag{2.59}$$

with a Young's modulus of 3.28 GPa and a Poisson's ratio of 0.33. We assign the standard bulk modulus of water, $k_{\mathrm{H_2O}} = 2.3\,\mathrm{GPa}$, to phases comprising water with mechanically insignificant amounts of non-collagenous organic matter.

Model validation at the extracellular scale

At the extracellular level, we compare the micromechanical elasticity predictions to ultrasonic tests with 10 MHz frequency, performed on cortical bone samples of bovine, human, elephant, deer, cod, and dugong tissues [Lees et al., 1979a, 1983]. Given the measured wave velocities ranging from 2.38 to 4.18 km/s, the wave exhibited wave lengths between 238 and 418 μm, being by a factor of 23.8 to 41.8 larger than the RVE of Figure 2.15(d), hence they characterize the latter according to Eq. (2.41). As tissue-specific input values for the micromechanical model, the volume fractions entering the RVE descriptions of wet collagen [Figure 2.15(a)], of the fibrillar and extrafibrillar spaces [Figure 2.15(b) and (c)], and of the extracellular matrix [Figure 2.15(d)] are needed.

As regards the cortical bone samples from bovine tibia [Lees et al., 1979a], the macroscopic mass densities and weight fractions are given, see Table 2.1. Based on a typical microporosity of $f_{\mu\text{por}} = 5\,\%$, see our discussion around Eq. (2.9), the aforementioned quantities are transformed into ultrastructural (extracellular) weight fractions and apparent mass densities according to Eqs. (2.10)-(2.13), and into extracellular (ultrastructural) volume fractions according to Eqs. (2.16) and (2.17). Then, the mineral distribution rules of Section 2.4, and the swelling and shrinkage rules of Section 2.5 and 2.6 allow for quantification of the extrafibrillar and fibrillar volume fractions per volume of extracellular matrix as

$$\begin{aligned} f_{\text{exfib}}^{\text{excel}} &= \frac{f_{\text{exfib},0}^{\text{excel}}}{\frac{1}{1+(\rho_{\text{HA}}/\rho_{\text{fl}}-1)\times f_{\text{HA}}^{\text{excel}}}} + \frac{f_{\text{exfib},0}^{\text{excel}}}{1-f_{\text{col},0}^{\text{excel}}} \times (1-\rho_{\text{HA}}/\rho_{\text{fl}}) \times f_{\text{HA}}^{\text{excel}}\,, \\ f_{\text{fib}}^{\text{excel}} &= 1 - f_{\text{exfib}}^{\text{excel}}\,, \end{aligned} \tag{2.60}$$

whereby $f_{\text{exfib},0}^{\text{excel}}$ and $f_{\text{col},0}^{\text{excel}}$ are determined from Eqs. (2.34) and (2.40), with $f_{\text{col},\infty}^{\text{excel}} = f_{\text{col}}^{\text{excel}}$ according to Eq. (2.18), with $f_{\text{HA},\infty}^{\text{excel}} = f_{\text{HA}}^{\text{excel}}$ according to Eqs. $(2.16)_2$ and $(2.17)_2$. They are the basis for the determination of the phase volume fractions within the lower scale RVEs: In this context, the fact that the average hydroxyapatite concentration in the extracollagenous space is the same inside and outside the fibrils [Hellmich and Ulm, 2003], see also Section 2.4, allows for quantification of the mineral and collagen volume fractions within the fibrillar and extrafibrillar compartments. Accordingly, in the extrafibrillar space, the volume

Table 2.7: Experimental characterization of various cortical bone samples by Lees et al. [1979a][a], Lees et al. [1983][b], and Lees et al. [1995][c]; Macroscopic and extracellular bone mass densities, ρ^{μ} and ρ^{excel}, longitudinal ultrasonic velocities in radial material directions, v_1, experimental and model-predicted normal stiffness values in radial direction, C^{exp}_{1111} and C^{pred}_{1111}, respectively

Tissue	ρ^{μ} (g/cm^3)	ρ^{excel} (g/cm^3)	v_1 (km/s)	C^{exp}_{1111} (GPa)	C^{pred}_{1111} (GPa)
Bovine tibia[a]	2.02	2.07	3.18	21.0	24.1
Bovine tibia[a]	1.99	2.04	3.18	20.7	22.1
Bovine tibia[a]	1.95	2.00	3.18	20.2	19.7
Bovine tibia[a]	2.01	2.06	3.16	20.6	22.3
Bovine tibia[a]	2.04	2.09	3.27	22.4	21.7
Bovine tibia[a]	2.05	2.11	3.26	22.4	24.4
Bovine tibia[b]	2.07	2.13	3.32	23.4	25.7
Dugong rib[b]	2.02	2.07	3.00	18.7	22.5
Elephant radius[b]	1.94	1.99	3.05	18.5	18.1
Human femur[b]	1.93	1.98	3.13	19.4	17.6
Deer antler[b]	1.78	1.82	2.38	10.3	12.5
Deer antler[b]	1.74	1.78	2.40	10.2	11.5
Whale malleus[c]	2.49	2.49	4.85	58.6	57.2
Whale malleus[c]	2.53	2.53	4.89	60.5	61.8
Whale malleus[c]	2.51	2.51	4.55	52.0	59.4
Whale malleus[c]	2.45	2.45	4.61	52.1	52.8
Whale incus[c]	2.50	2.50	4.79	57.4	58.3
Whale incus[c]	2.46	2.46	4.70	54.3	53.9
Whale periotic[c]	2.40	2.40	4.15	41.3	47.7
Whale periotic[c]	2.48	2.48	4.60	52.5	56.0
Whale periotic[c]	2.50	2.50	4.53	51.3	58.3
Whale periotic[c]	2.52	2.52	4.65	54.5	60.6
Whale periotic[c]	2.58	2.58	4.84	60.4	67.9
Whale typamic bulla[c]	2.54	2.54	4.60	53.7	63.0
Whale typamic bulla[c]	2.50	2.50	4.53	51.3	58.3
Whale typamic bulla[c]	2.53	2.53	4.53	51.9	61.8
Whale typamic bulla[c]	2.54	2.54	4.54	52.4	63.0
Whale typamic bulla[c]	2.49	2.49	4.48	50.0	57.2

fractions of mineral, $f^{\text{exfib}}_{\text{HA}}$, and of the intercrystalline fluid, $f^{\text{exfib}}_{\text{ic}}$, read as [Morin and Hellmich, 2014]

$$\begin{aligned} f^{\text{exfib}}_{\text{HA}} &= \frac{f^{\text{excel}}_{\text{HA}}\,\phi^{\text{exfib}}_{\text{HA}}}{f^{\text{excel}}_{\text{exfib}}} \quad \text{with} \quad \phi^{\text{exfib}}_{\text{HA}} = \frac{1-f^{\text{excel}}_{\text{fib}}}{1-f^{\text{excel}}_{\text{col}}}\,, \\ f^{\text{exfib}}_{\text{ic}} &= 1-f^{\text{exfib}}_{\text{HA}}\,. \end{aligned} \tag{2.61}$$

Table 2.8: Experimental characterization of various cortical bone samples by Lees et al. [1979a][a] and Lees et al. [1983][b]; Macroscopic and extracellular bone mass densities, ρ^{μ} and ρ^{excel}, longitudinal ultrasonic velocities in axial material directions, v_3, experimental and model-predicted normal stiffness values in axial direction, C_{3333}^{exp} and C_{3333}^{pred}, respectively

Tissue	ρ^{μ} (g/cm^3)	ρ^{excel} (g/cm^3)	v_3 (km/s)	C_{3333}^{exp} (GPa)	C_{3333}^{pred} (GPa)
Bovine tibia[a]	2.06	2.12	3.92	32.5	32.3
Bovine tibia[a]	2.05	2.11	3.92	32.4	31.6
Bovine tibia[a]	2.02	2.07	3.81	30.1	27.3
Bovine tibia[a]	2.02	2.07	3.86	30.9	27.6
Bovine tibia[a]	2.00	2.05	3.90	31.2	28.3
Bovine tibia[a]	2.05	2.11	3.88	31.7	30.7
Bovine tibia[a]	2.10	2.16	3.88	32.5	35.4
Bovine tibia[a]	2.08	2.14	3.92	32.8	33.8
Bovine tibia[b]	2.06	2.12	4.18	37.0	34.3
Elephant radius[b]	1.93	1.98	3.89	29.9	23.5
Human femur[b]	1.96	2.01	3.76	28.4	25.8
Deer antler[b]	1.74	1.78	3.08	16.9	13.1
Deer antler[b]	1.73	1.77	3.15	17.5	12.8

Within the fibrillar space, the volume fractions of mineral, $f_{\text{HA}}^{\text{fib}}$, and of wet collagen, $f_{\text{wetcol}}^{\text{fib}}$ read as [Morin and Hellmich, 2014]

$$\begin{aligned} f_{\text{HA}}^{\text{fib}} &= \frac{f_{\text{HA}}^{\text{excel}}\left(1-\phi_{\text{HA}}^{\text{exfib}}\right)}{f_{\text{fib}}^{\text{excel}}}\,, \\ f_{\text{wetcol}}^{\text{fib}} &= 1 - f_{\text{HA}}^{\text{fib}}\,. \end{aligned} \tag{2.62}$$

Finally, the volume fractions of molecular collagen and the intermolecular space at the wet collagen level, $f_{\text{col}}^{\text{wetcol}}$ and $f_{\text{im}}^{\text{wetcol}}$, can be calculated from the extracellular volume fractions of collagen as [Morin and Hellmich, 2014]

$$\begin{aligned} f_{\text{col}}^{\text{wetcol}} &= \frac{f_{\text{col}}^{\text{excel}}}{f_{\text{fib}}^{\text{excel}}\, f_{\text{wetcol}}^{\text{fib}}}\,, \\ f_{\text{im}}^{\text{wetcol}} &= 1 - f_{\text{col}}^{\text{wetcol}}\,. \end{aligned} \tag{2.63}$$

The corresponding micromechanical elasticity predictions of the bovine tibial bone samples of Lees et al. [1979a] agree well with the actual experimental data. This is underlined by relative errors of 5.47±7.01 % for the radial normal stiffness, and of -2.84±6.70 % for the axial normal stiffness components, see also Figures 2.16 and 2.17.

As regards the wet cortical bone samples from deer antler, human femur, elephant radius, and dugong rib of Lees et al. [1983], and the various whale bones of Lees

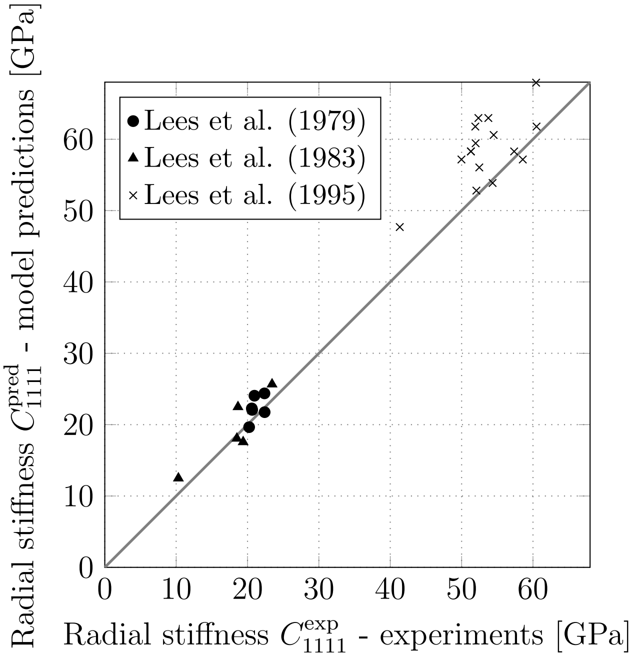

Figure 2.16: Comparison between model predictions and experiments of radial normal stiffness values at the extracellular scale (10 MHz experiments: Lees et al. [1979a, 1983, 1995], see also Table 2.7)

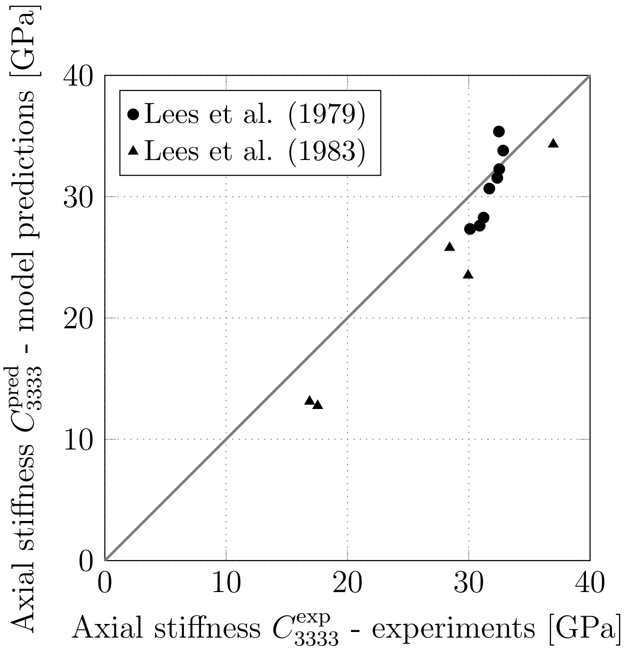

Figure 2.17: Comparison between model predictions and experiments of axial normal stiffness values at the extracellular scale (10 MHz experiments: Lees et al. [1979a, 1983], see also Table 2.8)

et al. [1995], the macroscopic mass densities are given, see Table 2.7. Based on a typical microstructural porosity of $f_{\mu\text{por}} = 5\,\%$, these macroscopic mass densities are transformed into ultrastructural (extracellular) mass densities, by means of Eq. (2.9). The latter mass densities then enter the bilinear relation of Figure 2.2(a), so as to deliver the extracellular volume fractions of mineral, organic and water according to Eqs. (2.16) and (2.17). These volume fractions are then used to quantify the composition of the lower scale RVEs of Figure 2.1(d) and (e). The corresponding micromechanical elasticity predictions of the bone samples of Lees et al. [1983] and of Lees et al. [1995] agree well with the actual experimental data. This is underlined by relative errors of 7.18±12.13 % for the radial normal stiffness, and of -15.61±6.17 % for the axial normal stiffness components for the different bone tissues reported by Lees et al. [1983], and by a relative error of 9.71±7.21 % for the radial normal stiffness of whale bones reported by Lees et al. [1995], see Figures 2.16 and 2.17.

2.7.4 Model validation at the extravascular scale

At the extravascular level, we compare the micromechanical elasticity predictions to ultrasonic tests carried out by McCarthy et al. [1990] on equine bones; at a frequency of 2.25 MHz. The measured velocities range from 3.13 to 4.4 km/s, resulting in a wave length ranging from 1.4 to 2.0 mm. The characteristic length of experimentally characterized RVE of Figure 2.15(e) is by a factor of 14 to 20 smaller, hence they characterize the latter according to Eq. (2.41). As tissue-specific input values for the micromechanical model, the volume fractions entering the RVE descriptions of wet collagen [Figure 2.15(a)], of the fibrillar and extrafibrillar spaces [Figure 2.15(b) and (c)], of the extracellular matrix [Figure 2.15(d)], and of the extravascular matrix [Figure 2.15(e)] are needed.

McCarthy et al. [1990] reported the macroscopic mass densities, ρ^{μ}, and the vascular porosities f_{vas}, which give access, based on the typical lacunar and canalicular porosities of 1.3 % and 0.7 %, respectively, to the extravascular and extracellular mass densities, ρ^{exvas} and ρ^{excel}. The latter enters the bilinear relations given by Eqs. (2.16) and (2.17), delivering the extracellular volume fractions of hydroxyapatite, collagen and water. The volume fractions of the lower scale RVEs of Figure 2.15 follow from Eqs. (2.60)-(2.63). The corresponding micromechanical elasticity prediction of the equine metacarpal bone samples of McCarthy et al. [1990] agree well with the actual experimental data. This is underlined by relative errors of

Table 2.9: Experimental characterization of equine cortical bone samples by McCarthy et al. [1990]; Macroscopic and extravascular bone mass densities, ρ^{μ} and ρ^{exvas}, longitudinal ultrasonic velocities in radial and axial material directions, v_1 and v_3, experimental and model-predicted normal stiffness values in radial and axial direction, C_{1111}^{exp}, C_{3333}^{exp}, C_{1111}^{pred}, C_{3333}^{pred}, respectively

ρ^{μ} (g/cm^3)	ρ^{exvas} (g/cm^3)	v_1 (km/s)	v_3 (km/s)	C_{1111}^{exp} (GPa)	C_{3333}^{exp} (GPa)	C_{1111}^{pred} (GPa)	C_{3333}^{pred} (GPa)
2.03	2.14	3.60	4.30	27.8	39.7	27.4	37.5
2.02	2.11	3.55	4.20	26.6	37.2	25.1	34.3
2.01	2.13	3.45	4.10	25.4	35.9	26.8	36.6
2.01	2.09	3.65	4.40	27.8	40.4	23.7	32.4
2.00	2.10	3.55	4.20	26.5	37.0	24.5	33.5
2.00	2.08	3.40	4.20	24.0	36.6	23.1	31.5
2.00	2.06	3.58	4.30	26.5	38.2	22.4	30.5
1.98	2.11	3.42	4.10	24.7	35.5	25.4	34.8
1.98	2.11	3.35	4.15	23.7	36.4	25.4	34.8
1.98	2.09	3.50	4.15	25.6	36.0	23.9	32.6
1.98	2.09	3.60	4.30	27.1	38.6	23.9	32.6
1.97	2.08	3.50	4.03	25.5	33.7	23.2	31.7
1.97	2.10	3.35	4.20	23.6	37.1	24.7	33.8
1.96	2.08	3.50	4.03	25.5	33.8	23.3	31.8
1.96	2.07	3.60	4.20	26.8	36.5	22.6	30.8
1.95	2.10	3.52	3.95	26.1	32.8	24.9	34.0
1.95	2.04	3.40	4.03	23.6	33.2	21.3	28.9
1.95	2.08	3.35	4.10	23.3	35.0	23.3	31.8
1.95	2.16	3.42	4.10	25.2	36.3	28.4	38.8
1.95	2.07	3.45	4.15	24.6	35.6	22.6	30.8
1.95	2.10	3.55	4.15	26.5	36.2	24.9	34.0
1.93	2.06	3.35	4.03	23.1	33.4	22.0	30.0
1.93	2.02	3.30	4.10	22.0	34.0	20.1	27.2
1.93	2.07	3.48	4.25	25.1	37.4	22.7	31.0
1.92	2.05	3.35	4.00	23.0	32.7	21.4	29.1
1.92	2.02	3.40	4.03	23.4	32.8	20.1	27.2
1.92	2.05	3.35	4.20	23.0	36.1	21.4	29.1
1.92	2.03	3.40	4.20	23.5	35.9	20.7	28.1
1.91	2.03	3.35	4.13	22.8	34.7	20.7	28.2
1.91	2.17	3.48	4.17	26.2	37.7	29.0	39.5
1.91	2.11	3.45	4.35	25.1	39.9	25.2	34.4
1.90	2.20	3.13	3.95	21.6	34.3	31.3	42.7
1.90	2.02	3.40	4.00	23.4	32.4	20.1	27.3
1.82	1.90	3.30	4.00	20.7	30.4	14.9	18.9
1.76	2.09	3.20	3.85	21.4	30.9	23.7	32.4

-4.23±11.33 % for the radial normal stiffness, and of -9.78±10.52 % for the axial normal stiffness components, see Figure 2.18.

In order to check the predictive capabilities of the micromechanical model concerning the off-diagonal and shear stiffness components of the elasticity tensor, we consider the stiffness tensor given by Ashman et al. [1984] on the basis of 2.25 MHz ultrasonic tests on human femoral samples, reading in Kelvin-Mandel notation (see e.g. Eq. (44) of Helnwein [2001] or Eq. (20) of Cowin [2003]) as

$$\mathbb{C}^{\text{exp}} = \begin{Bmatrix} 18.0 & 9.98 & 10.1 & 0 & 0 & 0 \\ 9.98 & 20.2 & 10.7 & 0 & 0 & 0 \\ 10.1 & 10.7 & 27.6 & 0 & 0 & 0 \\ 0 & 0 & 0 & 12.46 & 0 & 0 \\ 0 & 0 & 0 & 0 & 11.22 & 0 \\ 0 & 0 & 0 & 0 & 0 & 9.04 \end{Bmatrix} \text{ GPa.} \tag{2.64}$$

It should be noted that Ashman et al. [1984] use macroscopic mass density values for the evaluation of the ultrasonic velocity measurements, while 2.25 MHz, as stated previously, actually refer to the extravascular RVE of Figure 2.1(d). Accordingly, the values given in (2.64) need to be corrected by a factor of

$$\frac{\rho^{\text{exvas}}}{\rho^{\mu}} = \frac{\rho^{\mu} - \rho_{\text{H}_2\text{O}} f_{\text{vas}}}{(1 - f_{\text{vas}})\rho^{\mu}} = 1.04 \tag{2.65}$$

taking $\rho^{\mu} = 1.90\,\text{g/cm}^3$ from the tests of Ashman et al. [1984]. Considering a typical vascular porosity of 8 % in human femoral bone [Bousson et al., 2000, 2001, Cooper et al., 2007, Dong et al., 2014, Sietsema, 1995], yields

$$\mathbb{C}^{\text{exp}}_{\text{exvas}} = \begin{Bmatrix} 18.74 & 10.39 & 10.52 & 0 & 0 & 0 \\ 10.39 & 21.03 & 11.14 & 0 & 0 & 0 \\ 10.52 & 11.14 & 28.74 & 0 & 0 & 0 \\ 0 & 0 & 0 & 12.97 & 0 & 0 \\ 0 & 0 & 0 & 0 & 11.68 & 0 \\ 0 & 0 & 0 & 0 & 0 & 9.41 \end{Bmatrix} \text{ GPa.} \tag{2.66}$$

Applying the mass-density based volume fraction evaluation procedure to the same human femur sample provided by Ashman et al. [1984] delivers the volume fractions entering the RVEs at all scales of Figure 2.15. Based on a microporosity of $f_{\mu\text{por}} = 10\,\%$ in consistency with the vascular porosity value given further above

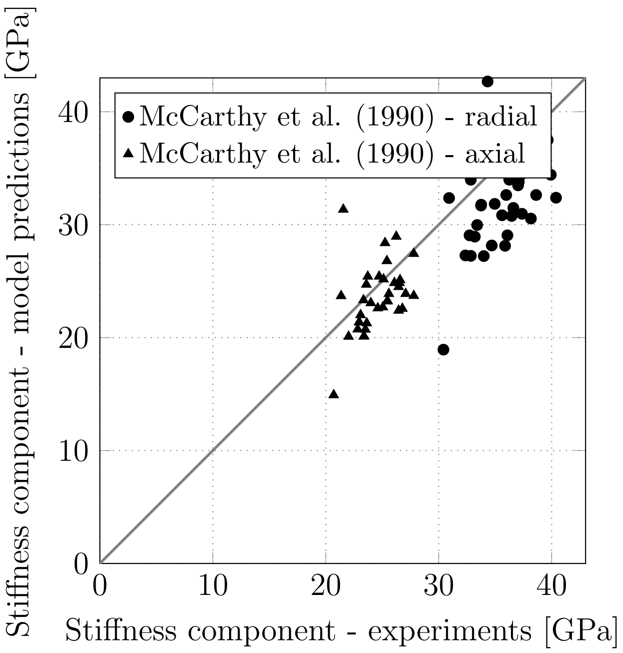

Figure 2.18: Comparison between model predictions and experiments of radial and axial normal stiffness values at the extravascular scale (2.25 MHz experiments: McCarthy et al. [1990], see also Table 2.9)

and the lacunar and canalicular porosities given below Eq. (2.8), the macroscopic mass density $\rho^{\mu} = 1.90\,\mathrm{g/cm^3}$ is translated into an extracellular mass density entering Eq. (2.16). The volume fractions of the lower scale RVEs then follow from Eqs. (2.61) - (2.63). The corresponding micromechanical model prediction reads as

$$\mathbb{C}^{\text{pred}}_{\text{exvas}} = \left\{\begin{matrix} 17.71 & 6.88 & 6.76 & 0 & 0 & 0 \\ 6.88 & 17.71 & 6.76 & 0 & 0 & 0 \\ 6.76 & 6.76 & 23.92 & 0 & 0 & 0 \\ 0 & 0 & 0 & 11.09 & 0 & 0 \\ 0 & 0 & 0 & 0 & 11.09 & 0 \\ 0 & 0 & 0 & 0 & 0 & 9.68 \end{matrix}\right\} \text{GPa}. \tag{2.67}$$

The satisfactory agreement between model prediction and experimental data is underlined by an absolute error of -9.13±7.8 % for the diagonal stiffness components. The off-diagonal stiffness components are less well predicted; however, these components are particularly prone to experimental errors, see e.g. [Every and Sachse, 1992, Kohlhauser and Hellmich, 2012, Kriz and Stinchcomb, 1979, Papadakis et al., 1991].

Model validation at the macroscopic scale

At the trabecular level, we compare the micromechanical elasticity predictions to ultrasonic tests [Rho et al., 1995, Turner et al., 1990] on bovine femoral and human tibial tissues; at a frequency of 50 kHz, as well as to mechanical tests of Keaveny et al. [1994] on bovine tibial tissue samples. Given a typical wave propagation velocity of 3 km/s in the tested bone specimens, the characteristic wave length was of the order of 6 cm, being by a factor of 60 larger than the RVE of Figure 2.15(f), hence they characterize the latter according to Eq. (2.41). As tissue-specific input values for the micromechanical model, the volume fractions entering the RVE descriptions of wet collagen [Figure 2.15(a)], of the fibrillar and extrafibrillar spaces [Figure 2.15(b) and (c)], of the extracellular matrix [Figure 2.15(d)], of the extravascular matrix [Figure 2.15(e)], and of the bone microstructure [Figure 2.15(f)] are needed.

For marrow-cleared trabecular bone, as tested by Keaveny et al. [1994], Rho et al. [1995], Turner et al. [1990], the corresponding volume fractions can be derived from the measured macroscopic mass density, ρ^{μ}, see Figure 2.19. For the extravascular mass density of bone, we take $\rho^{exvas} = 1.74\,\mathrm{g/cm}^3$ for bovine, and $\rho^{exvas} = 1.76\,\mathrm{g/cm}^3$ for human bone specimens [Ashman and Rho, 1988]. Assuming that the lacunar-canalicular volume fraction per extravascular bone, $f^{\mathrm{exvas}}_{lac+can} = 0.021$, is the same in cortical and trabecular bone, the extracellular mass density follows from

$$\rho^{\mathrm{excel}} = \frac{\rho^{\mathrm{exvas}} - \rho_{\mathrm{H_2O}} \times f^{\mathrm{exvas}}_{lac+can}}{1 - f^{\mathrm{exvas}}_{lac+can}}\,. \tag{2.68}$$

The sought volume fractions can be computed from Eqs. (2.16)-(2.17) and (2.60)-(2.63). The relative errors of the corresponding micromechanical elasticity predictions amount to 23.62±16.75 % in radial, and 23.39±30.83 % in axial direction for the bovine samples of Turner et al. [1990]; 24.67±20.72 % in radial, and 31.45±25.45 % in axial direction for the human samples of Turner et al. [1990]; 12.72±21.40 % in radial direction for the bovine samples of Keaveny et al. [1994]; and 0.09±28.44 % in radial, and 28.26±17.03 % in axial direction for the human samples of Rho et al. [1995], see Figures 2.20 and 2.21.

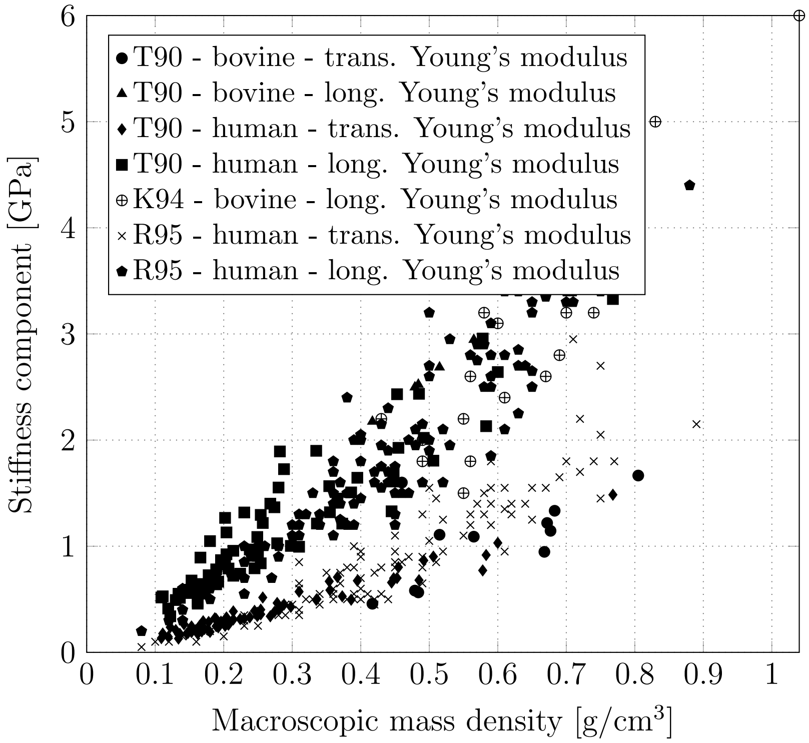

Figure 2.19: Experimental data used for model validation: Macroscopic elastic stiffness constants of trabecular bone as a function of macroscopic mass density ρ^{μ}; T90...[Turner et al., 1990], K94... [Keaveny et al., 1994], R95... [Rho et al., 1995]

2.7.5 Concluding remarks

Multiscale homogenization schemes similar to the one of Figure 2.15 can also be employed for successful upscaling of mechanical properties of bone beyond the realm of elasticity. This was reported for poroelasticity [Hellmich and Ulm, 2005a,b, Hellmich et al., 2009, Morin and Hellmich, 2014], for strength [Fritsch et al., 2009c], and for viscoelasticity [Eberhardsteiner et al., 2014]. While we refer to the aforementioned references concerning experimental data bases used for micromechanics model validation, we note in passing that a satisfactory performance of the strength and viscoelastic upscaling schemes stems from the consideration of sliding processes between the nanoscaled mineral crystals. This is in line with ongoing discussions in the bone materials science at large, be it in the context of Mohr-Coulomb-type, nano-granular behavior eluciated by nanoindentation and atomic force microscopy [Tai et al., 2006]; or in the context of interface nanomechanics cast in the framework of molecular dynamics simulations [Qu et al., 2015b]. The aforementioned poromechanics approaches are particularly valuable for quantifying the mechanical state in the vascular and lacunar pore spaces when the

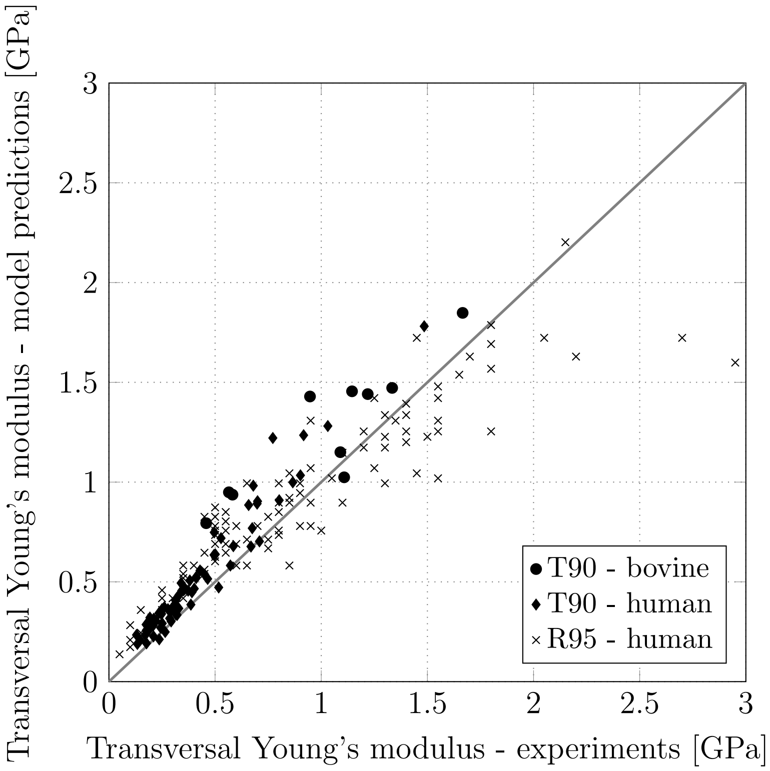

Figure 2.20: Comparison between model predicted and experimental macroscopic elastic stiffness constants of trabecular bone in transversal direction (50 kHz ultrasonic and mechanical experiments); T90...[Turner et al., 1990], K94... [Keaveny et al., 1994], R95... [Rho et al., 1995]

biological cells reside, i.e. the oscillating hydrostatic pressure to which they respond in a chemical fashion, see [Scheiner et al., 2016] and references therein. They also provide a natural link between micromechanics on the one hand, and system biology and cell population models on the other hand [Scheiner et al., 2013, 2014]. This results in a rather "rigorously" derived "mechano-biology of bone". Finally, multiscale micromechanics models can be readily combined with physics results, then allowing for the in-depth use and evaluation of clinical X-ray data from Computed Tomography yielding micromechanics-based Finite Element models at the organ scale. The latter elucidates the fascinating load carrying behavior of these organs, and also pave the way to patient-specific bone fracture risk assessment [Blanchard et al., 2013, 2016].

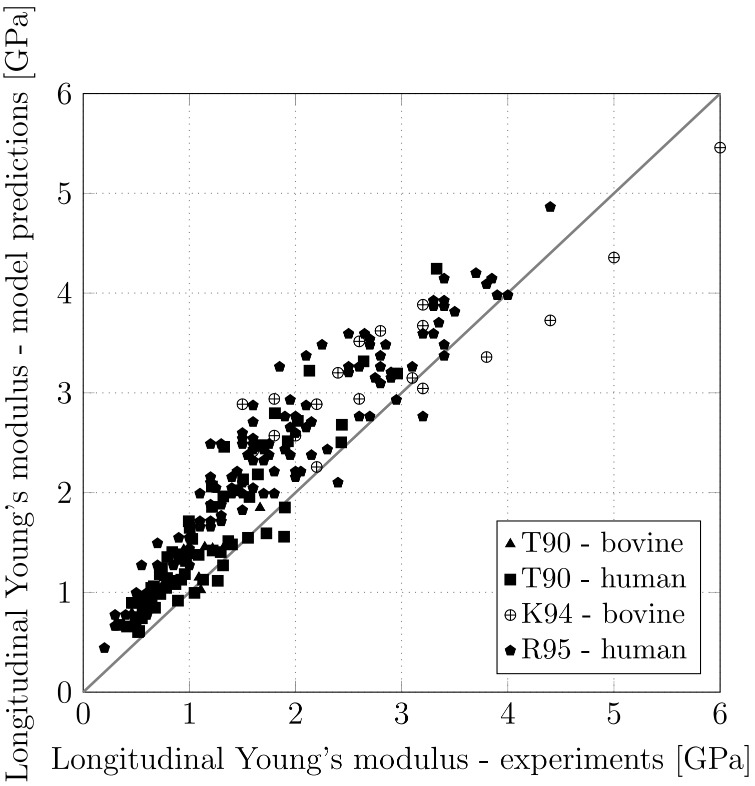

Figure 2.21: Comparison between model predicted and experimental macroscopic elastic stiffness constants of trabecular bone in longitudinal direction (50 kHz ultrasonic and mechanical experiments); T90...[Turner et al., 1990], K94... [Keaveny et al., 1994], R95... [Rho et al., 1995]

Nomenclature

$\mathbb{A}$	fourth-order strain concentration tensor
$\mathbb{c}$, $\mathbb{C}$	fourth-order elasticity tensor at the “microscopic ” and “macroscopic” scale, respectively
d	lateral/equatorial diffraction spacing
đ	characteristic length of the heterogeneities inside the RVE
div	divergence (mathematical operator)
$\mathbb{D}$	fourth-order compliance tensor
D_{ijkl}	component $ijkl$ of tensor $\mathbb{D}$
D	axial diffraction spacing / axial macroperiod
$d\mathbf{x}_i$	line element along the principal direction i
E	Young’s modulus
$\mathbf{E}$	macroscopic strain tensor
f	volume fraction
g	gravitational acceleration
GRAD	gradient operator at the structure scale
$\mathbb{I}$	fourth-order identity tensor
J	Jacobian, quantifying volume change during hydration process
k	elastic bulk modulus
ℓ	characteristic length of the RVE
$\mathscr{L}$	characteristic length of the structure built up by RVEs, or of its loading
M	mass concerning a millimeter-sized bone sample
min	minimum value (mathematical operator)
N_r	number of phases
$\mathbf{n}$	outwardly pointing vector normal to a surface element of an RVE
$\mathbb{P}_r^s$	fourth-order Hill tensor of inclusion with shape r (or phase r) embedded in matrix with stiffness $\mathbb{C}_r$ (or $\mathbb{C}^0$ if $s = 0$), or with symmetry property s otherwise
$\mathscr{R}$	water-to-organic mass ratio
RVE	Representative Volume Element
$\mathbf{T}$	traction vector
v	velocity
V	volume quantity concerning a millimeter-sized bone sample
W	weight quantity concerning a millimeter-sized bone sample
$\mathscr{W}$	work
WF	weight fraction
$\mathbf{x}$	location vector

β	proportionality constant between extrafibrillar space and fibrillar space increase during hydration
∂V	boundary of volume V
$\boldsymbol{\varepsilon}$	microscopic strain field
$\boldsymbol{\varepsilon}_r$	average (micro-)strain in phase r
λ_i	principal stretch in direction i
μ	elastic shear modulus
ϕ	relative mineral portion in extrafibrillar space
ρ	mass density
$\boldsymbol{\sigma}$	microscopic stress field
$\boldsymbol{\sigma}_r$	average (micro-)stress in phase r
$\boldsymbol{\Sigma}$	macroscopic stress tensor
$\boldsymbol{\xi}$	displacement field

Operators

$\langle(.)\rangle$	average of quantity (.) over the volume of the RVE
:	double contraction
.	simple contraction (dot product)

Subscripts

air	measured in air
ash	...of ash
ax	...in axial direction
can	...of canalicular porosity
col	...of collagen
dev	deviatoric part
dry	in dry state
excol	...of extracollageneous space
exfib	...of extrafibrillar space
fib	...of fibril
fl	...of ionic fluid
HA	...of hydroxyapatite
H_2O	...of water
i	...of constituent i
lac	...of lacunar porosity
liquid	...of liquid used for the Archimedes' tests
m	...of the matrix phase
max	maximum value (typically related to full saturation)
org	...of organic matter
r	...of phase r

RVE	...of the Representative Volume Element
sub	measured when submerged in water
tr	...in transverse direction
vas	...of vascular porosity
vol	volumetric part
w	...in wet (hydrated) state
wetcol	...of wet collagen
0	at the time of osteoid deposition
1, 2	...in transverse direction
3	...in axial direction
∞	...in fully mineralized state
μpor	...of microporosity

Superscripts

col	...per volume of molecular collagen
cort	...per volume of cortical space
dry	...per volume of dry bone tissue
dh	...of partially dehydrated tissue
excel	...per volume of extracellular space
excol	...per volume of extracollageneous space
exfib	...per volume of extrafibrillar space
exp	experimental value
ext	...of external forces acting on the RVE
exvas	...per volume of extravascular space
fib	...per volume of fibrillar space
fibsat	at fibrillar saturation limit
hom	homogenized
int	...of internal forces acting within the RVE
imsat	at intermolecular pore saturation limit
pred	model-predicted value
μ	...of a millimeter-sized bone sample
0	related to the matrix phase in the auxiliary Eshelby problem

Chapter 3

Micromechanics of elastoplastic porous polycrystals: theory, algorithm, and application to osteonal bone

Authored by: Claire Morin, Viktoria Vass, and Christian Hellmich

Published in: *International Journal of Plasticity*, 91, p. 238-267.
http://dx.doi.org/10.1016/j.ijplas.2017.01.009, 2017

Contribution: This paper results from the extension of the elastoplastic model initially conceived by Claire Morin. Christian Hellmich set up the overall research strategy, and together with Claire Morin, supervised the research progress and the documentation of the key results. Viktoria Vass extended the MatLab code, improved and optimized the return-mapping algorithm, ran simulations, documented the results, performed extensive literature research, and carried out model validation based on experimental data she found in the literature.

Abstract

Since its advent in the 1960s, elastoplastic micromechanics has been confronted by continuous challenges, as the classical incremental elastoplastic tangents are known to deliver unrealistically stiff material responses. As a complement to the various "secant" approximations targeting this challenge, we here develop a theoretical framework based on an extension of Dvorak's transformation field analysis, comprising the derivation of concentration and influence tensors. We thereby overcome the problem of actually non-homogeneous stress distributions across finite (often spherical) material phases, through consideration of infinitely many (non-spherical) solid phases oriented in all space directions, arriving at a micro-elastoplasticity theory of porous polycrystals. The resulting governing equations are discretized in time and space, and then solved in the framework of a new return mapping algorithm, the realization of which we exemplify by means of Mohr-Coulomb plasticity at the solid phase level. The corresponding homogenized material law is finally shown to satisfactorily represent the behavior of the porous hydroxyapatite polycrystals making up the so-called cement lines in osteonal bone. This is experimentally validated through strength and ultrasonic tests on hydroxyapatite, as well as through mass density, light microscopy, chemical composition, and osteon pushout tests on bone.

3.1 Introduction

Homogenization theories for elastic properties, whose high maturity has been reviewed in many textbooks and review papers [Dormieux et al., 2006a, Nemat-Nasser and Hori, 1999, Zaoui, 2002], have fundamentally shaped the understanding and design of microheterogeneous materials, such as metals [Mori and Tanaka, 1973], ceramics [Constantinides and Ulm, 2004], or hard biological materials [Fritsch and Hellmich, 2007]. By comparison, the field of micro-elastic-*plasticity*, although emerging almost as early as the elasticity homogenization theories, namely in the 1960s, seems to remain remarkably less influential on materials research and design. It appears that elastoplastic homogenization is much more tricky than its purely elastic counterpart. This becomes already obvious from a very compact historical review: Already in 1965, Hill proposed an incremental method [Hill, 1965a] for elastoplastic upscaling: The microscopic elastoplastic behavior is represented by a (time-dependent) phase-specific elastoplastic tangent tensor which multilinearly relates microstresses to microstrains; and this formally "elastic" relation is then simply inserted into classical homogenization schemes for the realm of elasticity, such as the self-consistent method [Hershey, 1954, Kröner, 1958] or the Mori-Tanaka method [Benveniste, 1987, Mori and Tanaka, 1973]. However, the results obtained by this approach appeared as consistently too stiff when compared to full elastoplastic Finite Element simulations of the microstructure - and this has, up to the present day, motivated a series of interesting correction schemes, such as "isotropization" of the (originally anisotropic) elastoplastic tangent (or secant) operators, see e.g. [Berveiller and Zaoui, 1978, Cayzac et al., 2013, Chaboche et al., 2005, Doghri and Ouaar, 2003, Rousselier and Luo, 2014, Shen and Shao, 2016, Shen et al., 2012] and the various references cited there.

It took until the early 1990s that Dvorak and coworkers proposed a more fundamental approach to the topic. Considering that plastic microstrains are, as of their nature, kinematically incompatible, and therefore qualify as free strains or eigenstrains, Dvorak and co-workers developed a new type of homogenization theory, called "transformation field analysis - TFA" [Dvorak, 1992, Dvorak and Benveniste, 1992, Dvorak et al., 1994]. Corresponding homogenization schemes (which will be more deeply reviewed and described in Section 3.3) provide access to the so-called concentration tensors $\mathbb{A}_i$ and influence tensors $\mathbb{D}_{ij}$, which relate the microscopic strains in the i-th material phase, $\boldsymbol{\varepsilon}_i$, to the macroscopic strains $\mathbf{E}$ prescribed at the boundary of the Representative Volume Element (RVE) and to all the free (here plastic) strains $\boldsymbol{\varepsilon}_j^p$ occurring in all the other material phases,

$$\boldsymbol{\varepsilon}_i = \mathbb{A}_i : \mathbf{E} + \sum_j \mathbb{D}_{ij} : \boldsymbol{\varepsilon}_j^p \tag{3.1}$$

Derivation of (3.1) with respect to time readily delivers

$$\dot{\boldsymbol{\varepsilon}}_i = \mathbb{A}_i : \dot{\mathbf{E}} + \sum_j \mathbb{D}_{ij} : \dot{\boldsymbol{\varepsilon}}_j^p \tag{3.2}$$

It is instructive to note that relation (3.2) is fundamentally different from the standard concentration relation in elastic homogenization, which for the case of elastoplastic tangent upscaling according to Hill's incremental method would read as [Hill, 1965b, Zaoui, 2002]

$$\dot{\boldsymbol{\varepsilon}}_i = \mathbb{A}_i \left(\mathbb{C}_i = \mathbb{C}_i^{eps}\right) : \dot{\mathbf{E}} \tag{3.3}$$

Comparison of (3.3) and (3.2) highlights that the use of the elastic concentration (or localization) problem for upscaling elasto*plastic tangent* tensors $\mathbb{C}_i^{eps}$ (rather than elasticity tensors $\mathbb{C}_i$) obviously neglects several sources for microscopic deformations. This is consistent with the repeatedly made statement that the incremental homogenization method delivers results which are too stiff. Accordingly, very promising examples for the use of (3.1) and (3.2), with properties derived from unit cell methods, could be given for periodic microstructures by Cavalcante and Pindera [2016], Dvorak et al. [1994], Kruch and Chaboche [2011]. However, in case of more complex and more random micromorphologies, the proper choice and number of phases (with uniform plastic strains), which would actually allow for appropriately covering the complex plastic flow patterns across the microstructures, often appears as the real (and hard-to-master) challenge when applying the "classical" TFA. While the introduction of "plastic modes" across material phases [in the course of non-uniform TFA - NTFA [Fritzen and Böhlke, 2011, Michel and Suquet, 2003, 2004, Roussette et al., 2009]] showed interesting ways to overcome the aforementioned problem for various applications, we here follow yet another approach, which proved recently very successful in the context of elastic, of poroelastic, and of brittle strength upscaling; across various material classes such as hydroxyapatite, bioactive glass ceramics, gypsum, cementitious materials, and piezoelectric ceramics [Fritsch et al., 2006, 2009b,c, 2013b, Pichler and Hellmich, 2011, Pichler et al., 2009, 2013]. In this approach, the representative volume element is divided into infinitely many non-spherical solid phases oriented in all space directions, and spherical pores in-between. It is for this micromechanical representation, that we here develop an elastoplastic homogenization theory based on a recent extension and generalization of the transformation field analysis [Dvorak et al., 1994]. This is described in the remainder of the present paper: In Section 3.2, the concept of the representative volume element is reviewed in the framework of the principle of virtual power [Germain, 1973, Salençon, 2001], and then specified for a porous polycrystalline material system built up by elastoplastic needle-shaped solid elements and pores in-between. Thereafter, upscaling of elastoplastic behavior from the level of the solid needles to that of the overall polycrystalline material is covered in Section 3.3, by introducing phase-specific concentration, influence, as well as homogenized stiffness tensors. Semi-analytical expressions for the latter are derived in Section 3.4, based on eigenstressed matrix-inclusion problems of the Eshelby-Laws type. The resulting governing equations are then discretized in time and space, and solved in the framework of a return mapping algorithm described in Section 3.5; the realization of which we exemplify by means of Mohr-Coulomb plasticity at the solid phase level in Section 3.6. Finally, the new theory and computational model is applied to osteoneal bone, in Section 3.7; followed by Conclusions in Section 3.8.

3.2 Representative volume element (RVE) - momentum balance and kinematic compatibility - microstructural characteristics of porous polycrystals

The investigated material is considered as a macro-homogeneous but micro-heterogeneous matter filling a Representative Volume Element (RVE) [Hill, 1963, Zaoui, 2002]. Such RVEs fulfill the separation of scales requirement:

$$d \ll l \ll \mathscr{L} \tag{3.4}$$

with d as the characteristic length of the inhomogeneities within the RVE, l as the characteristic length of the RVE, and $\mathscr{L}$ as the characteristic size of the body or structure made up by the material, or of loads acting on this body, such as wavelengths in case of dynamic loading. We consider an RVE subjected to homogeneous linearized macroscopic strains prescribed in terms of displacements

$$\text{on } \partial V_{RVE} \qquad \boldsymbol{\xi}\left(\mathbf{x}\right) = \mathbf{E} \cdot \mathbf{x} \tag{3.5}$$

with $\mathbf{x}$ as the location vector labeling points within the RVE and at its boundary. Homogeneous boundary conditions (3.5) and compatibility of microstrains within the RVE

$$\forall \mathbf{x} \in V_{RVE} \qquad \boldsymbol{\varepsilon}\left(\mathbf{x}\right) = \nabla^S \boldsymbol{\xi}\left(\mathbf{x}\right) \tag{3.6}$$

directly imply the so-called strain average rule [Hashin, 1983]

$$\frac{1}{V_{RVE}} \int_{V_{RVE}} \boldsymbol{\varepsilon}\left(\mathbf{x}\right) dV = \langle \boldsymbol{\varepsilon} \rangle = \mathbf{E}, \tag{3.7}$$

Furthermore, the aforementioned deformations provoke traction forces $\mathbf{T}(\mathbf{x})$ on the boundary of the RVE, and microstresses $\boldsymbol{\sigma}(\mathbf{x})$ throughout the RVE, fulfilling the equilibrium conditions

$$\begin{aligned} &\forall \mathbf{x} \in V_{RVE} \quad \operatorname{div}\boldsymbol{\sigma}(\mathbf{x}) = 0 \\ &\forall \mathbf{x} \in \partial V_{RVE} \quad \mathbf{T}(\mathbf{x}) = \boldsymbol{\sigma}(\mathbf{x}) \cdot \mathbf{n}(\mathbf{x}) \end{aligned} \tag{3.8}$$

with $\mathbf{n}(\mathbf{x})$ as the normal to the boundary at position $\mathbf{x}$. The external work done by these traction forces reads as

$$\begin{aligned} W^{ext} &= \int_{\partial V_{RVE}} \mathbf{T}(\mathbf{x}) \cdot \boldsymbol{\xi}(\mathbf{x})\, dS = \int_{\partial V_{RVE}} (\mathbf{E} \cdot \mathbf{x}) \cdot [\boldsymbol{\sigma}(\mathbf{x}) \cdot \mathbf{n}(\mathbf{x})]\, dS \\ &= \mathbf{E} : \int_{V_{RVE}} \boldsymbol{\sigma}(\mathbf{x})\, dV \end{aligned} \tag{3.9}$$

Hence, the force quantity doing work on the macroscopic strains $\mathbf{E}$ is the volume integral over the microscopic stress, which is independent of microscopic position and dimension "stress times volume". This induces the existence of the macroscopic stress $\boldsymbol{\Sigma}$ in the form

$$\boldsymbol{\Sigma}\, V_{RVE} = \int_{V_{RVE}} \boldsymbol{\sigma}(\mathbf{x})\, dV \quad \Leftrightarrow \quad \boldsymbol{\Sigma} = \frac{1}{V_{RVE}} \int_{V_{RVE}} \boldsymbol{\sigma}(\mathbf{x})\, dV = \langle \boldsymbol{\sigma} \rangle, \tag{3.10}$$

i.e. the well-known stress average rule. Insertion of (3.10) into the principle of virtual power [Germain, 1973, Salençon, 2001], which in the case of linearized strains, can be expressed in terms of an expression with the dimension "work",

$$W^{ext} = -W^{int} = \frac{1}{V_{RVE}} \int_{V_{RVE}} \boldsymbol{\sigma}(\mathbf{x}) : \boldsymbol{\varepsilon}(\mathbf{x})\, dV = \langle \boldsymbol{\sigma} : \boldsymbol{\varepsilon} \rangle \tag{3.11}$$

yields the so-called Hill's lemma

$$\boldsymbol{\Sigma} : \mathbf{E} = \frac{1}{V_{RVE}} \int_{V_{RVE}} \boldsymbol{\sigma}(\mathbf{x}) : \boldsymbol{\varepsilon}(\mathbf{x})\, dV. \tag{3.12}$$

As the microstructure cannot be described in complete detail, the morphological description is restricted to mechanically relevant features, through introduction of subdomains within the RVE, called phases. The latter exhibit homogeneous mechanical properties as described in further detail in Section 3.3. The mechanical state of these phases is characterized by stress and strain averages. For the present case of a porous polycrystal as depicted in Figure 3.1, a "pore phase" fills subvolume V_{pore} within the RVE, with respective stress and strain averages following

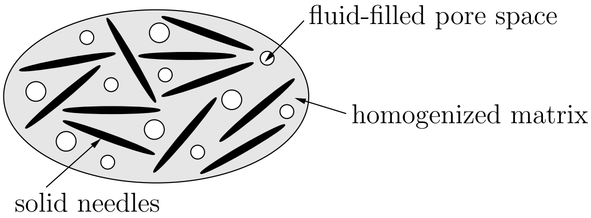

Figure 3.1: Representative Volume Element of the porous polycrystal

from

$$\begin{aligned}\boldsymbol{\sigma}_{pore} &= \frac{1}{V_{pore}} \int_{V_{pore}} \boldsymbol{\sigma}\left(\mathbf{x}\right) d\mathbf{x} \\ \boldsymbol{\varepsilon}_{pore} &= \frac{1}{V_{pore}} \int_{V_{pore}} \boldsymbol{\varepsilon}\left(\mathbf{x}\right) d\mathbf{x}\end{aligned} \tag{3.13}$$

The rest of the RVE is filled by elongated solid crystal phases which are fully characterized by the orientation in space, through orientation vector $\mathbf{e}_r$ (see Figure 3.2): The latter can be given as a function of an orthonormal base frame $\mathbf{e}_1$, $\mathbf{e}_2$, and $\mathbf{e}_3$, and of longitudinal and co-latitudinal angles ϕ and θ,

$$\boldsymbol{e}_r = \sin\theta\left(\cos\phi\,\boldsymbol{e}_1 + \sin\phi\,\boldsymbol{e}_2\right) + \cos\theta\,\boldsymbol{e}_3 \tag{3.14}$$

The corresponding stress and strain averages depend on the aforementioned angles, and read as

$$\begin{aligned}\boldsymbol{\sigma}_{\theta\phi} &= \frac{1}{l_{\theta\phi}} \int_{l_{\theta\phi}} \boldsymbol{\sigma}\left(s\right) ds \\ \boldsymbol{\varepsilon}_{\theta\phi} &= \frac{1}{l_{\theta\phi}} \int_{l_{\theta\phi}} \boldsymbol{\varepsilon}\left(s\right) ds\end{aligned} \tag{3.15}$$

with $l_{\theta\phi}$ as the length of all needle-shaped crystals oriented in (θ, ϕ)-direction. As a result, the strain average rules can be given in the following form, respectively

$$\boldsymbol{\Sigma} = f_{pore}\boldsymbol{\sigma}_{pore} + \left(1 - f_{pore}\right) \int_{\theta=0}^{\pi} \int_{\phi=0}^{2\pi} \boldsymbol{\sigma}_{\theta\phi} \frac{\sin\theta}{4\pi} d\theta d\phi \tag{3.16}$$

$$\boldsymbol{E} = f_{pore}\boldsymbol{\varepsilon}_{pore} + \left(1 - f_{pore}\right) \int_{\theta=0}^{\pi} \int_{\phi=0}^{2\pi} \boldsymbol{\varepsilon}_{\theta\phi} \frac{\sin\theta}{4\pi} d\theta d\phi \tag{3.17}$$

whereby $f_{pore} = V_{pore}/V_{RVE}$ is the volume fraction of the pore space (i.e. the porosity).

3.3 Elastoplasticity of solid phases - upscaling to porous polycrystal scale

The following constitutive laws are assigned to the material phases depicted in Figure 3.1: In order to keep the mathematical descriptions of our developments as concise as possible, the spherical pore phase is simply characterized by a linear elastic material behavior

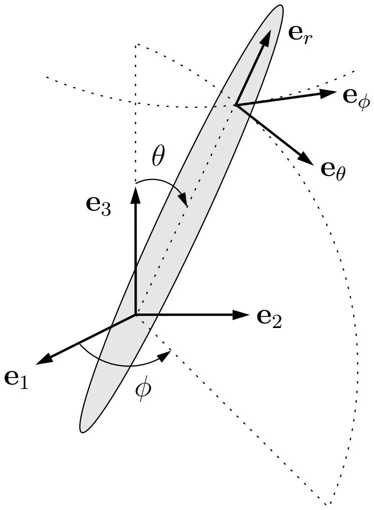

Figure 3.2: Orientation of solid needle by means of spherical coordinates θ and ϕ, and definition of corresponding spherical base frame

$$\boldsymbol{\sigma}_{pore} = \mathbb{C}_{pore} : \boldsymbol{\varepsilon}_{pore} \tag{3.18}$$

with $\mathbb{C}_{pore}$ as the fourth-order isotropic stiffness tensor of the pore space. In case of drained conditions, $\mathbb{C}_{pore}$ may be typically set to zero; and the extension to a full poromechanical formulation [Dormieux et al., 2006a] may be realized through the introduction of additional eigenstresses representing pore pressures [Fritsch et al., 2013b, Pichler and Hellmich, 2010]. The needle-shaped solid phases exhibit an elastic-perfectly plastic behavior

$$\boldsymbol{\sigma}_{\theta\phi} = \mathbb{C}_{solid} : \left[\boldsymbol{\varepsilon}_{\theta\phi} - \boldsymbol{\varepsilon}^p_{\theta\phi}\right] \tag{3.19}$$

with $\mathbb{C}_{solid}$ as their (isotropic) fourth-order stiffness tensor and $\boldsymbol{\varepsilon}^p_{\theta\phi}$ as the average plastic strain in the solid needle phase oriented in (θ, ϕ)-direction. These plastic strains follow the multisurface plasticity flow rule according to Koiter [1953]

$$\dot{\boldsymbol{\varepsilon}}^p_{\theta\phi} = \sum_{\alpha=1}^{N_{Fact,max}} \dot{\lambda}^{(\alpha)}_{\theta\phi} \frac{\partial \mathfrak{G}^{(\alpha)}\left(\boldsymbol{\sigma}_{\theta\phi}\right)}{\partial \boldsymbol{\sigma}_{\theta\phi}} \tag{3.20}$$

and occurrence of these strains is governed by the Melan-Kuhn-Tucker conditions

$$\forall \alpha \in \{1, \ldots, N_{Fact,max}\} \qquad \begin{aligned} &\dot{\lambda}^{(\alpha)}_{\theta\phi} \geq 0 \\ &\mathscr{F}^{(\alpha)}\left(\boldsymbol{\sigma}_{\theta\phi}\right) \leq 0 \\ &\dot{\lambda}^{(\alpha)}_{\theta\phi} \times \mathscr{F}^{(\alpha)}\left(\boldsymbol{\sigma}_{\theta\phi}\right) = 0 \end{aligned} \tag{3.21}$$

with $N_{Fact,max}$ as the total number of yield surfaces $\mathscr{F}^{(\alpha)}$ and of plastic potentials $\mathscr{G}^{(\alpha)}$ defining the multisurface yield criteria and flow rules; with associated plastic multipliers $\lambda^{(\alpha)}_{\theta\phi}$, governing the magnitude of the plastic strain rate.

For a linear elastic medium with eigenstrains, the latter (in our case, the plastic strains $\boldsymbol{\varepsilon}^{p}_{\theta\phi}$) are related to the macroscopic strains through the so-called concentration-influence relations [Dvorak and Benveniste, 1992, Pichler and Hellmich, 2010]; reading in the present case for the solid needle phases as

$$\boldsymbol{\varepsilon}_{\theta\phi} = \mathbb{A}_{\theta\phi} : \boldsymbol{E} + \int_{\Theta=0}^{\pi} \int_{\Phi=0}^{2\pi} \mathbb{D}_{\theta\phi;\Theta\Phi} : \boldsymbol{\varepsilon}^{p}_{\Theta\Phi} \frac{\sin\Theta}{4\pi} d\Theta d\Phi \tag{3.22}$$

and for the pores

$$\boldsymbol{\varepsilon}_{pore} = \mathbb{A}_{pore} : \boldsymbol{E} + \int_{\Theta=0}^{\pi} \int_{\Phi=0}^{2\pi} \mathbb{D}_{pore;\Theta\Phi} : \boldsymbol{\varepsilon}^{p}_{\Theta\Phi} \frac{\sin\Theta}{4\pi} d\Theta d\Phi \tag{3.23}$$

In these relations, $\mathbb{A}_{\theta\phi}$ and $\mathbb{A}_{pore}$ are the strain concentration tensors in the needle-shaped particles with orientation (θ, ϕ) and in the spherical pore phase respectively; $\mathbb{D}_{\theta\phi;\Theta\Phi}$ is the influence tensor expressing the effect of the plastic strain in the solid needles with orientation (Θ, Φ) on the overall strain in the solid needles with orientation (θ, ϕ); $\mathbb{D}_{pore;\Theta\Phi}$ is the influence tensor expressing the effect of the plastic strain in the solid needles with orientation (Θ, Φ) on the overall strain in the pore phase. The stress and strain average rules allow for upscaling the microscopic constitutive law to the macroscopic scale. In the presence of eigenstrains inside the RVE, the homogenized constitutive law is accessed through Levin's theorem [Laws, 1973, Levin, 1967]

$$\boldsymbol{\Sigma} = \mathbb{C}_{hom} : (\boldsymbol{E} - \boldsymbol{E}^{p}) \tag{3.24}$$

with $\mathbb{C}_{hom}$ as the homogenized stiffness tensor [Zaoui, 2002], defined by

$$\begin{aligned} \mathbb{C}_{hom} = \langle \mathbb{C} : \mathbb{A} \rangle_{V_{RVE}} &= f_{pore} \mathbb{C}_{pore} : \mathbb{A}_{pore} \\ &+ \left(1 - f_{pore}\right) \mathbb{C}_{solid} : \int_{\theta=0}^{\pi} \int_{\phi=0}^{2\pi} \mathbb{A}_{\theta\phi} \frac{\sin\theta}{4\pi} d\theta d\phi \end{aligned} \tag{3.25}$$

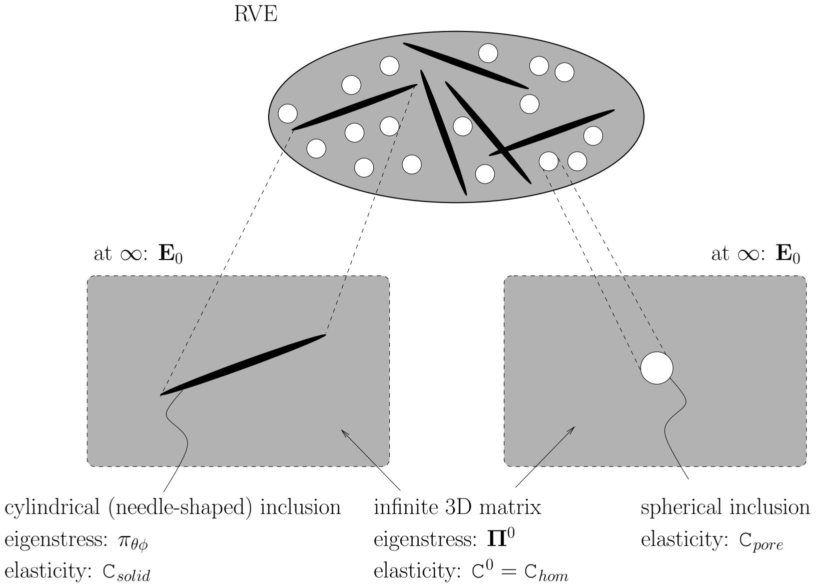
RVE
at ∞: $\mathbf{E}_0$
at ∞: $\mathbf{E}_0$
cylindrical (needle-shaped) inclusion
eigenstress: $\pi_{\theta\phi}$
elasticity: $\mathbb{C}_{solid}$
infinite 3D matrix
eigenstress: $\mathbf{\Pi}^0$
elasticity: $\mathbb{C}^0 = \mathbb{C}_{hom}$
spherical inclusion
elasticity: $\mathbb{C}_{pore}$

Figure 3.3: Quantifying RVE behavior through generalized Eshelby matrix-inclusion problems with eigenstresses

and with $\boldsymbol{E}^p$ as the macroscopic "plastic" strain, reading as [Laws, 1973, Levin, 1967, Zaoui, 2002]

$$\begin{aligned} \boldsymbol{E}^p &= \langle \boldsymbol{\varepsilon}^p : \mathbb{C} : \mathbb{A} : \mathbb{C}_{hom}^{-1} \rangle \\ &= (1 - f_{pore})\, \mathbb{C}_{hom}^{-1} : \int_{\theta=0}^{\pi} \int_{\phi=0}^{2\pi} \mathbb{A}_{\theta\phi}^{T} : \mathbb{C}_{solid} : \boldsymbol{\varepsilon}_{\theta\phi}^{p} \frac{\sin\theta}{4\pi} d\theta d\phi \end{aligned} \tag{3.26}$$

3.4 Self-consistent estimation of concentration and influence tensors from eigenstressed Eshelby problems

Self-consistent estimates for the strain concentration and influence tensors appearing in (3.22) and (3.23) are obtained by means of generalized Eshelby matrix-inclusion-type problems [Pichler and Hellmich, 2010, Zaoui, 2002]. The pore phase is represented as a spherical inclusion embedded in a matrix with stiffness $\mathbb{C}_{hom}$ and eigenstress $\mathbf{\Pi}^0$, subjected to homogeneous strains $\boldsymbol{E}_0$ acting at the infinite boundary of the aforementioned matrix, see Figure 3.3. The needle-shaped solid phases are represented each as a cylindrical inclusion with stiffness $\mathbb{C}_{solid}$ and eigenstresses $\boldsymbol{\pi}_{\theta\phi} = -\mathbb{C}_{solid} : \boldsymbol{\varepsilon}_{\theta\phi}^p$, embedded into the very same matrix, and subjected to the very same strains $\boldsymbol{E}_0$, see Figure 3.3. This results to inclusion/phase strains reading as [Zaoui, 2002]

$$\boldsymbol{\varepsilon}_{\theta\phi} = \mathbb{A}^{\infty}_{\theta\phi} : \left[\boldsymbol{E}_0 - \mathbb{P}_{cyl}(\theta,\phi) : \left(\boldsymbol{\pi}_{\theta\phi} - \boldsymbol{\Pi}^0\right)\right] \tag{3.27}$$

$$\boldsymbol{\varepsilon}_{pore} = \mathbb{A}^{\infty}_{pore} : \left[\boldsymbol{E}_0 - \mathbb{P}_{sph} : \left(-\boldsymbol{\Pi}^0\right)\right] \tag{3.28}$$

with the abbreviations $\mathbb{A}^{\infty}_{\theta\phi}$ and $\mathbb{A}^{\infty}_{pore}$ standing for

$$\mathbb{A}^{\infty}_{\theta\phi} = \left[\mathbb{I} + \mathbb{P}_{cyl}(\theta,\phi) : (\mathbb{C}_{solid} - \mathbb{C}_{hom})\right]^{-1} \tag{3.29}$$

and

$$\mathbb{A}^{\infty}_{pore} = \left[\mathbb{I} + \mathbb{P}_{sph} : (\mathbb{C}_{pore} - \mathbb{C}_{hom})\right]^{-1} \tag{3.30}$$

whereby $\mathbb{I}$ is the fourth-order identity tensor, with components $I_{ijkl} = \frac{1}{2}(\delta_{ik}\delta_{jl} + \delta_{il}\delta_{jk})$, δ_{ij} is the Kronecker delta: $\delta_{ij} = 1$ if $i = j$ and zero otherwise; $\mathbb{P}_{cyl}$ and $\mathbb{P}_{sph}$, respectively, are the Hill tensors of cylindrical and spherical inclusions embedded into a matrix with stiffness $\mathbb{C}_{hom}$. Insertion of (3.27) and (3.28) into the strain average rule (3.17) delivers

$$\begin{aligned}\boldsymbol{E} = \Bigg\{ & f_{pore}\mathbb{A}^{\infty}_{pore} : \left[\boldsymbol{E}_0 - \mathbb{P}_{sph} : \left(-\boldsymbol{\Pi}^0\right)\right] \\ & + (1 - f_{pore}) \int_{\theta=0}^{\pi}\int_{\phi=0}^{2\pi} \mathbb{A}^{\infty}_{\theta\phi} : \left[\boldsymbol{E}_0 - \mathbb{P}_{cyl}(\theta,\phi) : \left(\boldsymbol{\pi}_{\theta\phi} - \boldsymbol{\Pi}^0\right)\right] \frac{\sin\theta}{4\pi} d\theta d\phi \Bigg\}\end{aligned} \tag{3.31}$$

Solving (3.31) for $\boldsymbol{E}_0$ yields

$$\begin{aligned}\boldsymbol{E}_0 = \Bigg\{ & f_{pore}\mathbb{A}^{\infty}_{pore} \\ & + (1 - f_{pore}) \int_{\theta=0}^{\pi}\int_{\phi=0}^{2\pi} \mathbb{A}^{\infty}_{\theta\phi} \frac{\sin\theta}{4\pi} d\theta d\phi \Bigg\}^{-1} : \left\{\boldsymbol{E} + \boldsymbol{E}^{\pi}_0\right\}\end{aligned} \tag{3.32}$$

with

$$\begin{aligned}\boldsymbol{E}^{\pi}_0 = & f_{pore}\mathbb{A}^{\infty}_{pore} : \mathbb{P}_{sph} : \left(-\boldsymbol{\Pi}^0\right) \\ & + (1 - f_{pore}) \int_{\theta=0}^{\pi}\int_{\phi=0}^{2\pi} \mathbb{A}^{\infty}_{\theta\phi} : \mathbb{P}_{cyl}(\theta,\phi) : \left(\boldsymbol{\pi}_{\theta\phi} - \boldsymbol{\Pi}^0\right) \frac{\sin\theta}{4\pi} d\theta d\phi\end{aligned} \tag{3.33}$$

Insertion of (3.32) into (3.27) and (3.28) yields

$$\boldsymbol{\varepsilon}_{\theta\phi} = \mathbb{A}_{\theta\phi} : \left\{\boldsymbol{E} + \boldsymbol{E}^{\pi}_0\right\} - \mathbb{A}^{\infty}_{\theta\phi} : \mathbb{P}_{cyl}(\theta,\phi) : \left(\boldsymbol{\pi}_{\theta\phi} - \boldsymbol{\Pi}^0\right) \tag{3.34}$$

$$\boldsymbol{\varepsilon}_{pore} = \mathbb{A}_{pore} : \left\{\boldsymbol{E} + \boldsymbol{E}^{\pi}_0\right\} - \mathbb{A}^{\infty}_{pore} : \mathbb{P}_{sph} : \left(-\boldsymbol{\Pi}^0\right) \tag{3.35}$$

with

$$\mathbb{A}_{\theta\phi} = \mathbb{A}^{\infty}_{\theta\phi} : \left\{ f_{pore}\mathbb{A}^{\infty}_{pore} + (1 - f_{pore}) \int_{\Theta=0}^{\pi} \int_{\Phi=0}^{2\pi} \mathbb{A}^{\infty}_{\Theta\Phi} \frac{\sin\Theta}{4\pi} d\Theta d\Phi \right\}^{-1} \tag{3.36}$$

$$\mathbb{A}_{pore} = \mathbb{A}^{\infty}_{pore} : \left\{ f_{pore}\mathbb{A}^{\infty}_{pore} + (1 - f_{pore}) \int_{\theta=0}^{\pi} \int_{\phi=0}^{2\pi} \mathbb{A}^{\infty}_{\theta\phi} \frac{\sin\theta}{4\pi} d\theta d\phi \right\}^{-1} \tag{3.37}$$

Comparison of (3.34) and (3.35) with (3.22) and (3.23) makes readily evident that $\mathbb{A}_{\theta\phi}$ and $\mathbb{A}_{pore}$ are the sought expressions for the concentration tensors appearing in (3.22) and (3.23). As a second step, the stress average rule, combined with the Levin's theorem, allows for estimating the influence tensors. Therefore, (3.24) and (3.26) can be rewritten in the form,

$$\begin{aligned} \boldsymbol{\Sigma} &= \mathbb{C}_{hom} : \boldsymbol{E} \\ &+ (1 - f_{pore}) \int_{\theta=0}^{\pi} \int_{\phi=0}^{2\pi} \boldsymbol{\pi}_{\theta\phi} : \mathbb{A}_{\theta\phi} \frac{\sin\theta}{4\pi} d\theta d\phi \end{aligned} \tag{3.38}$$

On the other hand, the combination of the stress average rule (3.16) with constitutive equations (3.18) and (3.19), as well as with the scale transition relations (3.34) and (3.35), while considering the expression (3.25) for the homogenized stiffness, results in

$$\begin{aligned} \boldsymbol{\Sigma} = {} & f_{pore}\mathbb{C}_{pore} : \left\{ \mathbb{A}_{pore} : \left\{ \boldsymbol{E} + \boldsymbol{E}^{\pi}_{0} \right\} - \mathbb{A}^{\infty}_{pore} : \mathbb{P}_{sph} : \left(-\boldsymbol{\Pi}^{0} \right) \right\} \\ & + (1 - f_{pore}) \int_{\theta=0}^{\pi} \int_{\phi=0}^{2\pi} \left\{ \mathbb{C}_{solid} : \left\{ \mathbb{A}_{\theta\phi} : \left(\boldsymbol{E} + \boldsymbol{E}^{\pi}_{0} \right) \right. \right. \\ & \left. \left. - \mathbb{A}^{\infty}_{\theta\phi} : \mathbb{P}_{cyl}(\theta,\phi) : \left(\boldsymbol{\pi}_{\theta\phi} - \boldsymbol{\Pi}^{0} \right) \right\} + \boldsymbol{\pi}_{\theta\phi} \right\} \frac{\sin\theta}{4\pi} d\theta d\phi \end{aligned} \tag{3.39}$$

Setting the macroscopic stress relations (3.38) and (3.39) equal and solving the resulting expression for $\boldsymbol{\Pi}^{0}$ delivers

$$\begin{aligned} \boldsymbol{\Pi}^{0} = {} & \left\{ (\mathbb{C}_{hom} - \mathbb{C}_{pore}) : f_{pore}\mathbb{A}^{\infty}_{pore} : \mathbb{P}_{sph} \right. \\ & \left. + (\mathbb{C}_{hom} - \mathbb{C}_{solid}) : (1 - f_{pore}) \int_{\theta=0}^{\pi} \int_{\phi=0}^{2\pi} \mathbb{A}^{\infty}_{\theta\phi} : \mathbb{P}_{cyl}(\theta,\phi) \frac{\sin\theta}{4\pi} d\theta d\phi \right\}^{-1} : \\ & \left\{ (1 - f_{pore}) \int_{\theta=0}^{\pi} \int_{\phi=0}^{2\pi} \left[\boldsymbol{\pi}_{\theta\phi} : [\mathbb{I} - \mathbb{A}_{\theta\phi}] \right. \right. \\ & \left. \left. + (\mathbb{C}_{hom} - \mathbb{C}_{solid}) : \mathbb{A}^{\infty}_{\theta\phi} : \mathbb{P}_{cyl}(\theta,\phi) : \boldsymbol{\pi}_{\theta\phi} \right] \frac{\sin\theta}{4\pi} d\theta d\phi \right\} \end{aligned} \tag{3.40}$$

Finally, inserting (3.40) into (3.34) and (3.35) and comparing the resulting expressions to (3.22) and (3.23) yield the eigenstress influence tensors $\mathbb{D}_{pore,\Theta\Phi}$, $\mathbb{D}_{\theta\phi,\Theta\Phi}$, and $\mathbb{D}_{\theta\phi,\theta\phi}$. They read as

$$
\begin{aligned}
\mathbb{D}_{pore,\Theta\Phi} = \Bigg\{ & -\mathbb{A}_{pore}(1-f_{pore}) : \mathbb{A}^{\infty}_{\Theta\Phi} : \mathbb{P}_{cyl}(\Theta,\Phi) \\
& + \left[\mathbb{A}_{pore} f_{pore} : \mathbb{A}^{\infty}_{pore} : \mathbb{P}_{sph} \right. \\
& + \mathbb{A}_{pore}(1-f_{pore}) : \int_{\chi=0}^{\pi} \int_{\psi=0}^{2\pi} \mathbb{A}^{\infty}_{\chi\psi} : \mathbb{P}_{cyl}(\chi,\psi) \frac{\sin\chi}{4\pi} d\chi d\psi \\
& \left. - \mathbb{A}^{\infty}_{pore} : \mathbb{P}_{sph} \right] : \\
& \left[(1-f_{pore})(\mathbb{C}_{hom}-\mathbb{C}_{solid}) : \int_{\chi=0}^{\pi} \int_{\psi=0}^{2\pi} \mathbb{A}^{\infty}_{\chi\psi} : \mathbb{P}_{cyl}(\chi,\psi) \frac{\sin\chi}{4\pi} d\chi d\psi \right. \\
& \left. + f_{pore}(\mathbb{C}_{hom}-\mathbb{C}_{pore}) : \mathbb{A}^{\infty}_{pore} : \mathbb{P}_{sph} \right]^{-1} : \\
& (1-f_{pore}) \big[[\mathbb{I}-\mathbb{A}_{\Theta\Phi}]^{T} \\
& + (\mathbb{C}_{hom}-\mathbb{C}_{solid}) : \mathbb{A}^{\infty}_{\Theta\Phi} : \mathbb{P}_{cyl}(\Theta,\Phi) \Bigg\} : \mathbb{C}_{solid}
\end{aligned}
\tag{3.41}
$$

$$
\begin{aligned}
\mathbb{D}_{\theta\phi,\Theta\Phi} = \Bigg\{ & -\mathbb{A}_{\theta\phi} : (1-f_{pore}) \mathbb{A}^{\infty}_{\Theta\Phi} : \mathbb{P}_{cyl}(\Theta,\Phi) \\
& + \left[\mathbb{A}_{\theta\phi} : (1-f_{pore}) \int_{\chi=0}^{\pi} \int_{\psi=0}^{2\pi} \mathbb{A}^{\infty}_{\chi\psi} : \mathbb{P}_{cyl}(\chi,\psi) \frac{\sin\chi}{4\pi} d\chi d\psi \right. \\
& \left. + \mathbb{A}_{\theta\phi} : f_{pore} : \mathbb{A}^{\infty}_{pore} : \mathbb{P}_{sph} - \mathbb{A}^{\infty}_{\theta\phi} : \mathbb{P}_{cyl}(\theta,\phi) \right] : \\
& \left[(1-f_{pore}) \, (\mathbb{C}_{hom}-\mathbb{C}_{solid}) : \int_{\chi=0}^{\pi} \int_{\psi=0}^{2\pi} \mathbb{A}^{\infty}_{\chi\psi} : \mathbb{P}_{cyl}(\chi,\psi) \frac{\sin\chi}{4\pi} d\chi d\psi \right. \\
& \left. + f_{pore} \, (\mathbb{C}_{hom}-\mathbb{C}_{pore}) : \mathbb{A}^{\infty}_{pore} : \mathbb{P}_{sph} \right]^{-1} : \\
& (1-f_{pore}) \big[[\mathbb{I}-\mathbb{A}_{\Theta\Phi}]^{T} \\
& + (\mathbb{C}_{hom}-\mathbb{C}_{solid}) : \mathbb{A}^{\infty}_{\Theta\Phi} : \mathbb{P}_{cyl}(\Theta,\Phi) \big] \Bigg\} : \mathbb{C}_{solid}
\end{aligned}
\tag{3.42}
$$

$$\begin{aligned}
\mathbb{D}_{\theta\phi,\theta\phi} = \Bigg\{ & [\mathbb{I} - (1-f_{pore})\mathbb{A}_{\theta\phi}] : \mathbb{A}^{\infty}_{\theta\phi} : \mathbb{P}_{cyl}(\theta,\phi) \\
& + \Bigg[\mathbb{A}_{\theta\phi} : (1-f_{pore}) \int_{\chi=0}^{\pi}\int_{\psi=0}^{2\pi} \mathbb{A}^{\infty}_{\chi\psi} : \mathbb{P}_{cyl}(\chi,\psi)\frac{\sin\chi}{4\pi} d\chi d\psi \\
& + \mathbb{A}_{\theta\phi} : f_{pore}\mathbb{A}^{\infty}_{pore} : \mathbb{P}_{sph} - \mathbb{A}^{\infty}_{\theta\phi} : \mathbb{P}_{cyl}(\theta,\phi)\Bigg] : \\
& \Bigg[(1-f_{pore})\left(\mathbb{C}_{hom} - \mathbb{C}_{solid}\right) : \int_{\chi=0}^{\pi}\int_{\psi=0}^{2\pi} \mathbb{A}^{\infty}_{\chi\psi} : \mathbb{P}_{cyl}(\chi,\psi)\frac{\sin\chi}{4\pi} d\chi d\psi \\
& + f_{pore}\left(\mathbb{C}_{hom} - \mathbb{C}_{pore}\right) : \mathbb{A}^{\infty}_{pore} : \mathbb{P}_{sph}\Bigg]^{-1} : \\
& (1-f_{pore})\big[\,[\mathbb{I} - \mathbb{A}_{\theta\phi}]^{T} \\
& + \left(\mathbb{C}_{hom} - \mathbb{C}_{solid}\right) : \mathbb{A}^{\infty}_{\theta\phi} : \mathbb{P}_{cyl}(\theta,\phi)\big]\Bigg\} : \mathbb{C}_{solid}
\end{aligned} \tag{3.43}$$

3.5 Algorithmic treatment of multiscale elastoplasticity

Numerical computations of plastic evolutions within the solid phases of the RVE depicted in Figure 3.1, as a function of arbitrary macroscopic loading in terms of macroscopic stresses $\boldsymbol{\Sigma}$ or macroscopic strains $\boldsymbol{E}$, requires temporal and spatial discretization of the elastoplastic relations (3.22)-(3.26), together with (3.41)-(3.43), and with average rules (3.16)-(3.17); as well as solution of the resulting algebraic equations. This will be dealt with in the following subsection.

3.5.1 Spatial discretization of governing equations

As regards spatial discretization, all integrals over the unit sphere are approximated through weighted sums of the integrands being evaluated at a particular set $\mathcal{S}$ of Gaussian points on the unit sphere (labelled by the two Euler angles $\{\theta_i,\phi_i\}_{i\in\mathcal{S}}$) with the associated Gaussian weights $\omega_i|_{i\in\mathcal{S}}$. Accordingly, the integral over an arbitrary function $a(\Theta,\Phi)$ is approximated by the weighted sum over this function evaluated at particular Gaussian points labelled by index i; i.e. by the following discrete expression

$$\iint_{\Theta,\Phi} a\left(\Theta,\Phi\right)\frac{\sin\Theta}{4\pi} d\Theta d\Phi = \sum_{i\in\mathcal{S}} \omega_i a(\Theta_i,\Phi_i) = \sum_{i\in\mathcal{S}} \omega_i\, a_i \tag{3.44}$$

This leads to the following discretized versions of the governing equations:

- the (spatially discretized) stress and strain average rules

$$\boldsymbol{\Sigma} = f_{pore}\boldsymbol{\sigma}_{pore} + \sum_{i\in\mathcal{S}}(1-f_{pore})\omega_i\boldsymbol{\sigma}_i \tag{3.45}$$

$$\boldsymbol{E} = f_{pore}\boldsymbol{\varepsilon}_{pore} + \sum_{i\in\mathcal{S}}(1-f_{pore})\omega_i\boldsymbol{\varepsilon}_i \tag{3.46}$$

- the (spatially discretized) concentration-influence relations

$$\forall i \in \mathcal{S} \qquad \boldsymbol{\varepsilon}_i = \mathbb{A}_i : \boldsymbol{E} + \sum_{j\in\mathcal{S}}\omega_j\mathbb{D}_{ij} : \boldsymbol{\varepsilon}^p_j \tag{3.47}$$

$$\boldsymbol{\varepsilon}_{pore} = \mathbb{A}_{pore} : \boldsymbol{E} + \sum_{j\in\mathcal{S}}\omega_j\mathbb{D}_{pore,j} : \boldsymbol{\varepsilon}^p_j \tag{3.48}$$

whereby the discretized influence tensors $\mathbb{D}_{pore,j}$, $\mathbb{D}_{ij}$, and $\mathbb{D}_{ii}$ read as

$$\begin{aligned}\mathbb{D}_{pore,j} = \Bigg\{ & -\mathbb{A}_{pore} : (1-f_{pore})\mathbb{A}^{\infty}_j : \mathbb{P}_{cyl,j} + \Bigg[f_{pore}\mathbb{A}_{pore} : \mathbb{A}^{\infty}_{pore} : \mathbb{P}_{sph} \\ & + (1-f_{pore})\mathbb{A}_{pore} : \sum_{k\in\mathcal{S}}\omega_k\mathbb{A}^{\infty}_k : \mathbb{P}_{cyl,k} - \mathbb{A}^{\infty}_{pore} : \mathbb{P}_{sph}\Bigg] \\ & : \Big[f_{pore}\left(\mathbb{C}_{hom}-\mathbb{C}_{pore}\right) : \mathbb{A}^{\infty}_{pore} : \mathbb{P}_{sph} \\ & + (1-f_{pore})\left(\mathbb{C}_{hom}-\mathbb{C}_{solid}\right) : \sum_{k\in\mathcal{S}}\omega_k\mathbb{A}^{\infty}_k : \mathbb{P}_{cyl,k}\Bigg]^{-1} \\ & : (1-f_{pore})\left[\left(\mathbb{I}-\mathbb{A}_j\right)^T + \left(\mathbb{C}_{hom}-\mathbb{C}_{solid}\right) : \mathbb{A}^{\infty}_j : \mathbb{P}_{cyl,j}\right]\Bigg\} : \mathbb{C}_{solid}\end{aligned} \tag{3.49}$$

$$\begin{aligned}\mathbb{D}_{ij} = \Bigg\{ & -\mathbb{A}_i : (1-f_{pore})\mathbb{A}^{\infty}_j : \mathbb{P}_{cyl,j} \\ & + \Bigg[f_{pore}\mathbb{A}_i : \mathbb{A}^{\infty}_{pore} : \mathbb{P}_{sph} + (1-f_{pore})\mathbb{A}_i : \sum_{k\in\mathcal{S}}\omega_k\mathbb{A}^{\infty}_k : \mathbb{P}_{cyl,k} - \mathbb{A}^{\infty}_i : \mathbb{P}_{cyl,i}\Bigg] \\ & : \Big[f_{pore}\left(\mathbb{C}_{hom}-\mathbb{C}_{pore}\right) : \mathbb{A}^{\infty}_{pore} : \mathbb{P}_{sph} \\ & + (1-f_{pore})\left(\mathbb{C}_{hom}-\mathbb{C}_{solid}\right) : \sum_{k\in\mathcal{S}}\omega_k\mathbb{A}^{\infty}_k : \mathbb{P}_{cyl,k}\Bigg]^{-1} \\ & : (1-f_{pore})\left[\left(\mathbb{I}-\mathbb{A}_j\right)^T + \left(\mathbb{C}_{hom}-\mathbb{C}_{solid}\right) : \mathbb{A}^{\infty}_j : \mathbb{P}_{cyl,j}\right]\Bigg\} : \mathbb{C}_{solid}\end{aligned} \tag{3.50}$$

$$\begin{aligned}\mathbb{D}_{ii} =\Big\{ & \left[\mathbb{I} - (1-f_{pore})\mathbb{A}_i\right] : \mathbb{A}_i^{\infty} : \mathbb{P}_{cyl,i} \\ & + \left[f_{pore}\mathbb{A}_i : \mathbb{A}_{pore}^{\infty} : \mathbb{P}_{sph} + (1-f_{pore})\mathbb{A}_i : \sum_{k\in\mathcal{S}} \omega_k \mathbb{A}_k^{\infty} : \mathbb{P}_{cyl,k} - \mathbb{A}_i^{\infty} : \mathbb{P}_{cyl,i} \right] \\ & : \Big[f_{pore} \left(\mathbb{C}_{hom} - \mathbb{C}_{pore}\right) : \mathbb{A}_{pore}^{\infty} : \mathbb{P}_{sph} \\ & + (1-f_{pore}) \left(\mathbb{C}_{hom} - \mathbb{C}_{solid}\right) : \sum_{k\in\mathcal{S}} \omega_k \mathbb{A}_k^{\infty} : \mathbb{P}_{cyl,k} \Big]^{-1} \\ & : (1-f_{pore}) \left[\left(\mathbb{I} - \mathbb{A}_i\right)^T + \left(\mathbb{C}_{hom} - \mathbb{C}_{solid}\right) : \mathbb{A}_i^{\infty} : \mathbb{P}_{cyl,i} \right] \Big\} : \mathbb{C}_{solid}\end{aligned} \tag{3.51}$$

- the microscopic state equation for the solid needle phases

$$\forall i \in \mathcal{S} \qquad \boldsymbol{\sigma}_i = \mathbb{C}_{solid} : \left(\boldsymbol{\varepsilon}_i - \boldsymbol{\varepsilon}_i^p\right) \tag{3.52}$$

- the flow rule

$$\forall i \in \mathcal{S} \qquad \dot{\boldsymbol{\varepsilon}}_i^p = \sum_{\alpha=1}^{N_{Fact,max}} \dot{\lambda}_i^{(\alpha)} \frac{\partial \mathcal{G}^{(\alpha)}}{\partial \boldsymbol{\sigma}_i} \left(\boldsymbol{\sigma}_i\right) \tag{3.53}$$

  associated to the Melan-Kuhn-Tucker conditions

$$\forall \alpha \in \{1, 2, \ldots, N_{Fact,max}\} \qquad \begin{aligned} & \dot{\lambda}_i^{(\alpha)} \geq 0 \\ & \mathcal{F}^{(\alpha)}\left(\boldsymbol{\sigma}_i\right) \leq 0 \\ & \dot{\lambda}_i^{(\alpha)} \times \mathcal{F}^{(\alpha)}\left(\boldsymbol{\sigma}_i\right) = 0 \end{aligned} \tag{3.54}$$

- the macroscopic (homogenized) stiffness tensor

$$\mathbb{C}_{hom} = f_{pore}\mathbb{C}_{pore} : \mathbb{A}_{pore} + (1-f_{pore}) \sum_{i\in\mathcal{S}} \omega_i \mathbb{C}_{solid} : \mathbb{A}_i \tag{3.55}$$

- and the macroscopic plastic strains

$$\boldsymbol{E}^p = (1-f_{pore})\mathbb{C}_{hom}^{-1} : \sum_{i\in\mathcal{S}} \omega_i \mathbb{A}_i^T : \mathbb{C}_{solid} : \boldsymbol{\varepsilon}_i^p \tag{3.56}$$

More precisely, we here employ two different sets $\mathcal{S}$ of Gaussian points:

- the Stroud's integration formulas [Stroud, 1971], comprising 15 or 28 points (see Tables 3.1 and 3.2)

Table 3.1: 15 different needle orientations according to integration formulas of Stroud [1971]

$j =$	1	2	3	4	5	6	7	8	9	10	11	12	13	14	15
$\sin(\theta_j)\cos(\phi_j) =$	$+r$	$+r$	$-r$	$-r$	$+t$	$+t$	$-t$	$-t$	$+s$	$+s$	$-s$	$-s$	1	0	0
$\sin(\theta_j)\sin(\phi_j) =$	$+s$	$-s$	$+s$	$-s$	$+r$	$-r$	$+r$	$-r$	$+t$	$-t$	$+t$	$-t$	0	1	0
$\cos(\theta_j) =$	$+t$	$+t$	$+t$	$+t$	$+s$	$+s$	$+s$	$+s$	$+r$	$+r$	$+r$	$+r$	0	0	1
$\omega(\theta_j, \phi_j) =$	$\frac{1}{15}$	$\frac{1}{15}$	$\frac{1}{15}$	$\frac{1}{15}$	$\frac{1}{15}$	$\frac{1}{15}$	$\frac{1}{15}$	$\frac{1}{15}$	$\frac{1}{15}$	$\frac{1}{15}$	$\frac{1}{15}$	$\frac{1}{15}$	$\frac{1}{15}$	$\frac{1}{15}$	$\frac{1}{15}$
	with $r = 1/2$, $s = \left(\sqrt{5}+1\right)/4$, and $t = \left(\sqrt{5}-1\right)/4$														

- the centroids and areas of triangles meshing the unit sphere, as described in [Badel and Leblond, 2004]. The triangular mesh of the unit sphere is obtained from the refinement of a semi-dodecahedron, splitting each pentagon into five triangles; further refinement can then be achieved by dividing each triangle into four smaller triangles. The centroids of the triangles are chosen as Gaussian points, while the ratio between the areas of the triangle and of the unit sphere is chosen as Gaussian weight. We use 120 integration points.

3.5.2 Temporal discretization of governing equations

As the spatially discretized temporal differential equations (3.45)-(3.56) cannot be solved analytically, approximative solutions will be obtained in an iterative process, which is described in greater detail in Sections 6 and 7. This process relates to discrete time instants t^n and corresponding stresses and strains, such as $E(t^n) = E^n$. Respective evaluations of (3.45)-(3.52) and (3.56) yield

$$\boldsymbol{\Sigma}^n = f_{pore}\boldsymbol{\sigma}^n_{pore} + \sum_{i\in\mathcal{S}}(1 - f_{pore})\,\omega_i\boldsymbol{\sigma}^n_i \tag{3.57}$$

$$\boldsymbol{E}^n = f_{pore}\boldsymbol{\varepsilon}^n_{pore} + \sum_{i\in\mathcal{S}}(1 - f_{pore})\,\omega_i\boldsymbol{\varepsilon}^n_i \tag{3.58}$$

$$\boldsymbol{\varepsilon}^n_i = \mathbb{A}_i : \boldsymbol{E}^n + \sum_{j\in\mathcal{S}}\omega_j\mathbb{D}_{ij} : \boldsymbol{\varepsilon}^{p,n}_j \tag{3.59}$$

$$\boldsymbol{\varepsilon}^n_{pore} = \mathbb{A}_{pore} : \boldsymbol{E}^n + \sum_{i\in\mathcal{S}}\omega_i\mathbb{D}_{pore;i} : \boldsymbol{\varepsilon}^{p,n}_i \tag{3.60}$$

$$\boldsymbol{E}^{p,n} = (1 - f_{pore})\mathbb{C}^{-1}_{hom} : \sum_{i\in\mathcal{S}}\omega_i\mathbb{A}^T_i : \mathbb{C}_{solid} : \boldsymbol{\varepsilon}^{p,n}_i \tag{3.61}$$

$$\boldsymbol{\sigma}^n_i = \mathbb{C}_{solid} : [\boldsymbol{\varepsilon}^n_i - \boldsymbol{\varepsilon}^{p,n}_i] \tag{3.62}$$

$$\boldsymbol{\sigma}^n_{pore} = \mathbb{C}_{pore} : \boldsymbol{\varepsilon}^n_{pore} \tag{3.63}$$

Table 3.2: 28 different needle orientations according to integration formulas of Stroud [1971]

$j =$	1	2	3	4	5	6	7	8	9	10	11	12	13	14
$\sin(\theta_j)\cos(\phi_j) =$	$+t$	$+t$	$-t$	$-t$	$+s$	$+s$	$-s$	$-s$	$+r$	$+r$	$-r$	$-r$	$+r$	$+r$
$\sin(\theta_j)\sin(\phi_j) =$	$+t$	$-t$	$+t$	$-t$	$+r$	$-r$	$+r$	$-r$	$+s$	$-s$	$+s$	$-s$	$+r$	$-r$
$\cos(\theta_j) =$	$+t$	$+t$	$+t$	$+t$	$+r$	$+r$	$+r$	$+r$	$+r$	$+r$	$+r$	$+r$	$+s$	$+s$
$\omega(\theta_j,\phi_j) =$	a	a	a	a	b	b	b	b	b	b	b	b	b	b
$j =$	15	16	17	18	19	20	21	22	23	24	25	26	27	28
$\sin(\theta_j)\cos(\phi_j) =$	$-u$	$+v$	$+v$	$-v$	$-v$	$+v$	$+v$	$-v$	$-v$	$-r$	$-r$	$+u$	$+u$	$-u$
$\sin(\theta_j)\sin(\phi_j) =$	$-v$	$+u$	$-u$	$+u$	$-u$	$+v$	$-v$	$+v$	$-v$	$+r$	$-r$	$+v$	$-v$	$+v$
$\cos(\theta_j) =$	$+v$	$+v$	$+v$	$+v$	$+v$	$+u$	$+u$	$+u$	$+u$	$+s$	$+s$	$+v$	$+v$	$+v$
$\omega(\theta_j,\phi_j) =$	c	c	c	c	c	c	c	c	c	b	b	c	c	c

with $r = \sqrt{\left(9 - 4\sqrt{3}\right)/33}$, $s = \sqrt{\left(15 + 8\sqrt{3}\right)/33}$, $t = \sqrt{1/3}$,

$u = \sqrt{\left(15 - 8\sqrt{3}\right)/33}$, $v = \sqrt{\left(9 + 4\sqrt{3}\right)/33}$,

and $a = 9/280$, $b = \left(122 + 9\sqrt{3}\right)/3360$, $c = \left(122 - 9\sqrt{3}\right)/3360$

Changes of stresses and strains during time interval $\Delta t^{n+1} = t^{n+1} - t^n$ are quantified in terms of increments

$$\Delta\mathbf{E}^{n+1} = \mathbf{E}^{n+1} - \mathbf{E}^n \tag{3.64}$$

$$\Delta\mathbf{\Sigma}^{n+1} = \mathbf{\Sigma}^{n+1} - \mathbf{\Sigma}^n \tag{3.65}$$

$$\Delta\boldsymbol{\sigma}_i^{n+1} = \boldsymbol{\sigma}_i^{n+1} - \boldsymbol{\sigma}_i^n \tag{3.66}$$

$$\Delta\boldsymbol{\varepsilon}_i^{p,n+1} = \boldsymbol{\varepsilon}_i^{p,n+1} - \boldsymbol{\varepsilon}_i^{p,n} \tag{3.67}$$

The latter increments, relating to microscopic plastic strains, need to be related to the temporal derivatives in the evolution equations (3.53). Therefore, we employ a backward Euler integration scheme: Except for time derivatives, we hold all functional values fixed at time t^{n+1}, and we then integrate the flow rule (3.53) between time instant t^n and t^{n+1}, yielding

$$\begin{aligned}
&\forall i \in \mathcal{S} \\
&\int_{t^n}^{t^{n+1}} \dot{\boldsymbol{\varepsilon}}_i^p dt = \sum_{\alpha=1}^{N_{Fact,max}} \int_{t^n}^{t^{n+1}} \dot{\lambda}^{(\alpha)} dt \frac{\partial \mathcal{G}^{(\alpha)}}{\partial \boldsymbol{\sigma}_i}\left(\boldsymbol{\sigma}_i^{n+1}\right) \\
&= \Delta\boldsymbol{\varepsilon}_i^{p,n+1} = \sum_{\alpha=1}^{N_{Fact,max}} \Delta\lambda_i^{(\alpha),n+1} \frac{\partial \mathcal{G}^{(\alpha)}}{\partial \boldsymbol{\sigma}_i}\left(\boldsymbol{\sigma}_i^{n+1}\right)
\end{aligned} \tag{3.68}$$

with the corresponding Melan-Kuhn-Tucker conditions reading as

$$\forall \alpha \in \{1,2,\dots,N_{Fact,max}\} \qquad \begin{aligned} &\Delta\lambda_i^{(\alpha),n+1} \geq 0 \\ &\mathscr{F}^{(\alpha)}\left(\boldsymbol{\sigma}_i^{n+1}\right) \leq 0 \\ &\Delta\lambda_i^{(\alpha),n+1} \times \mathscr{F}^{(\alpha)}\left(\boldsymbol{\sigma}_i^{n+1}\right) = 0 \end{aligned} \tag{3.69}$$

3.5.3 Iterative solution process I: macro-to-micro scale transitions

Inspired by the standard procedure in computational elastoplasticity [Hellmich et al., 1999, Morin et al., 2011a,b, Simo and Hughes, 1998, Simo and Taylor, 1985], a macroscopic strain history is presented in terms of finite strain increments $\Delta\mathbf{E}^{n+1}$, with corresponding totally attained strains reading as

$$\mathbf{E}^{n+1} = \mathbf{E}^n + \Delta\mathbf{E}^{n+1} \tag{3.70}$$

These strains can be prescribed directly (displacement-driven situation), or be the result of equilibrium considerations at the RVE or structural level (force-driven situation). Given the full set of state variables at the end of the n-th load step, $\boldsymbol{\Sigma}^n$, $\mathbf{E}^n$, $\mathbf{E}^{p,n}$; we are left with computing the same full set of variables for the end of the $(n+1)$-st step, based on the prescribed strain increment $\Delta\mathbf{E}^{n+1}$. Therefore, these macroscopic strains are first downscaled from the macro to the microlevel, under the assumption of the absence of any additional plastic events ("trial state"), on the basis of (3.59) and (3.62)

$$\boldsymbol{\sigma}_i^{n+1,trial} = \mathbb{C}_{solid} : \left\{ \mathbb{A}_i : \mathbf{E}^{n+1} + \sum_{j\in\mathcal{S}} \left[\mathbb{D}_{ij} - \delta_{ij}\mathbb{I}\right] : \boldsymbol{\varepsilon}_j^{p,n} \right\} \tag{3.71}$$

Thereafter, it is checked whether this assumption of purely elastic behavior of all solid phases is actually valid, by inserting the trial state of the microscopic solid microstresses, $\boldsymbol{\sigma}_i^{n+1,trial}$, into the yield criterion $(3.69)_2$, yielding respective trial values

$$\forall i \in \mathcal{S}, \forall \alpha \in \{1,2,\dots,N_{Fact,max}\} \qquad \mathscr{F}_i^{(\alpha),n+1,trial} = \mathscr{F}^{(\alpha)}\left(\boldsymbol{\sigma}_i^{n+1,trial}\right) \tag{3.72}$$

with $N_{Fact,max}$ as the maximum number of potentially active yield surfaces per solid phase. These values allow for discrimination between plasticizing and purely elastic phases; as well as between active and non-active yield surfaces associated to these plasticizing phases: all solid phases with $\mathscr{F}_i^{(\alpha),n+1,trial} \leq 0$ holding for all $N_{Fact,max}$ yield surfaces associated to these solid phases, behave purely elastically during time step Δt^{n+1}. On the other hand, those with $\mathscr{F}_i^{(\alpha),n+1,trial} > 0$, for at least one of the $N_{Fact,max}$ yield surfaces defining the multisurface criterion of each solid phase, define the set of plasticizing needle-shaped solid phases, $\mathcal{S}_{cyl,plast}$. This set has $N_{cyl,plast}$ elements, $i = 1, .., N_{cyl,plast}$. Each element of this set is associated to a number of active yield surfaces, $N_{Fact,i}$; always fulfilling $\mathscr{F}_i^{(\alpha),n+1,trial} > 0$. These plasticizing phases exhibit non-zero plastic strain increments $\Delta\boldsymbol{\varepsilon}_i^{p,n+1}$ according to flow rule (3.68), which are determined from fulfillment of the Melan-Kuhn-Tucker conditions (3.69), while considering state equation (3.62) evaluated at load step $(n+1)$ and the definition of the trial state according to (3.71),

$$\begin{aligned}&\forall i \in \mathcal{S}_{cyl,plast}, \forall \alpha \in \{1, 2, \ldots, N_{Fact,i}\}\\ &\mathscr{F}^{(\alpha)}\left(\boldsymbol{\sigma}_i^{n+1,trial} + \mathbb{C}_{solid} : \left\{\sum_{j \in \mathcal{S}_{cyl,plast}} \sum_{\beta=1}^{N_{Fact,j}} \left[\mathbb{D}_{ij} - \delta_{ij}\mathbb{I}\right] \Delta\lambda_j^{(\beta),n+1} \frac{\partial \mathscr{G}^{(\beta)}}{\partial \boldsymbol{\sigma}_j}(\boldsymbol{\sigma}_j^{n+1})\right\}\right) = 0\end{aligned} \tag{3.73}$$

Due to the nonlinear dependence of the phase-specific plastic flow directions $\frac{\partial \mathscr{G}^{(\beta)}}{\partial \boldsymbol{\sigma}_j}$ on the phase stresses $\boldsymbol{\sigma}_j$, a solution for $\Delta\lambda_j^{(\beta),n+1}$ cannot be directly gained from (3.73). Therefore, we solve (3.73) in an iterative manner, with iteration steps labelled by k. Thereby, the approximations of the first iteration step $(k = 1)$ relate to the trial state and therefore read as

$$\Delta\boldsymbol{\varepsilon}_i^{p,n+1,1} = 0 \tag{3.74}$$

$$\Delta\lambda_i^{(\alpha),n+1,1} = 0 \tag{3.75}$$

$$\boldsymbol{\sigma}_i^{n+1,1} = \boldsymbol{\sigma}_i^{n+1,trial} \tag{3.76}$$

They are used for approximating the plastic flow direction, as the basis for obtaining an improved estimate for the plastic multiplier $\Delta\lambda_j^{(\alpha),n+1,k+1}$, according to the approximation scheme

$$\begin{aligned}&\forall i \in \mathcal{S}_{cyl,plast}, \forall \alpha \in \{1, 2, \ldots, N_{Fact,i}\}\\ &\mathscr{F}^{(\alpha)}\Bigg(\boldsymbol{\sigma}_i^{n+1,trial}\\ &+ \mathbb{C}_{solid} : \left\{\sum_{j \in \mathcal{S}_{cyl,plast}} \sum_{\beta=1}^{N_{Fact,j}} \left[\mathbb{D}_{ij} - \delta_{ij}\mathbb{I}\right] \Delta\lambda_j^{(\beta),n+1,k+1} \frac{\partial \mathscr{G}^{(\beta)}}{\partial \boldsymbol{\sigma}_j}(\boldsymbol{\sigma}_j^{n+1,k})\right\}\Bigg) = 0\end{aligned} \tag{3.77}$$

Solution of this non-linear equation (3.77) requires yet another iteration scheme (described in the next section), providing new (improved) approximative solutions $\Delta\lambda_i^{(\beta),n+1,k+1}$, $i = 1, \ldots, N_{cyl,plast}$, $\beta = 1, \ldots, N_{Fact,i}$ with corresponding (improved) plastic strains

$$\begin{aligned} &\forall i \in \{1, \ldots, N_{cyl,plast}\} \\ &\Delta\boldsymbol{\varepsilon}_i^{p,n+1,k+1} = \sum_{\alpha=1}^{N_{Fact,i}} \Delta\lambda_i^{(\alpha),n+1,k+1} \frac{\partial\mathcal{G}^{(\alpha)}}{\partial\boldsymbol{\sigma}_i}(\boldsymbol{\sigma}_i^{n+1,k}) \end{aligned} \tag{3.78}$$

Update of the corresponding microscopic stresses requires another downscaling process from the macro to the microlevel, according to

$$\begin{aligned} &\forall i \in \{1, \ldots, N_{cyl,plast}\} \\ &\boldsymbol{\sigma}_i^{n+1,k+1} = \boldsymbol{\sigma}_i^{n+1,trial} \\ &+ \mathbb{C}_{solid} : \left\{ \sum_{j\in\mathcal{S}_{cyl,plast}} \sum_{\alpha=1}^{N_{Fact,j}} [\mathbb{D}_{ij} - \delta_{ij}\mathbb{I}]\, \Delta\lambda_j^{(\alpha),n+1,k+1} \frac{\partial\mathcal{G}^{(\alpha)}}{\partial\boldsymbol{\sigma}_j}(\boldsymbol{\sigma}_j^{n+1,k}) \right\} \end{aligned} \tag{3.79}$$

Thereafter, iteration step $(k+1)$ is completed by checking whether the alterations in the plastic flow stemming from the update of $\boldsymbol{\sigma}_i^{n+1}$ from iteration step k to iteration step $(k+1)$ become negligible, i.e. lower than a prescribed tolerance value TOL,

$$\begin{aligned} &\forall i \in \{1, \ldots, N_{cyl,plast}\}, \forall\alpha \in \{1, 2, \ldots, N_{Fact,i}\} \\ &\left\| \frac{\partial\mathcal{G}^{(\alpha)}}{\partial\boldsymbol{\sigma}_i}\left(\boldsymbol{\sigma}_i^{n+1,k+1}\right) - \frac{\partial\mathcal{G}^{(\alpha)}}{\partial\boldsymbol{\sigma}_i}\left(\boldsymbol{\sigma}_i^{n+1,k}\right) \right\| \leq \text{TOL} \end{aligned} \tag{3.80}$$

If this is not the case yet, the $(k+1)$-st approximations are used as input for the next (i.e. $(k+2)$-nd) iteration, which is characterized by replacement of k by $(k+1)$, and of $(k+1)$ by $(k+2)$, in (3.77), (3.78), (3.79) and (3.80).

3.5.4 Iterative process II: plastic flow - "return map"

In each iteration step k described in the preceding section, the non-linear equation

$$\begin{aligned}
&\forall i \in \mathcal{S}_{cyl,plast}, \forall \alpha \in \{1,2,\ldots,N_{Fact,i}\}\\
&\mathscr{F}^{(\alpha)}\Bigg(\tilde{\boldsymbol{\sigma}}_i^{n+1} = \boldsymbol{\sigma}_i^{n+1,trial} +\\
&+ \mathbb{C}_{solid} : \left\{ \sum_{j \in \mathcal{S}_{cyl,plast}} \sum_{\beta=1}^{N_{Fact,j}} \left[\mathbb{D}_{ij} - \delta_{ij}\mathbb{I}\right] \Delta\lambda_j^{(\beta),n+1,k+1} \frac{\partial \mathscr{G}^{(\beta)}}{\partial \boldsymbol{\sigma}_j}\left(\boldsymbol{\sigma}_j^{n+1,k}\right)\right\}\Bigg) = 0
\end{aligned} \tag{3.81}$$

needs to be solved. This is done by a Newton iteration scheme, with iteration steps labelled by l, reading as

$$\mathbf{R}^{n+1,k+1,l} + \frac{d\mathbf{R}^{n+1,k+1,l}}{d(\Delta\boldsymbol{\lambda}^{n+1,k+1})} \cdot \Delta\left(\Delta\boldsymbol{\lambda}\right)^{n+1,k+1,l+1} = 0 \tag{3.82}$$

Thereby, the vectorial terms in (3.82) are defined as follows: The plastic multiplier vector reads as

$$\Delta\boldsymbol{\lambda}^{n+1,k+1} = \left\{ \begin{array}{c} \Delta\lambda_1^{(1),n+1,k+1} \\ \Delta\lambda_1^{(2),n+1,k+1} \\ \vdots \\ \Delta\lambda_1^{(N_{Fact,1}),n+1,k+1} \\ \Delta\lambda_2^{(1),n+1,k+1} \\ \vdots \\ \Delta\lambda_2^{(N_{Fact,2}),n+1,k+1} \\ \vdots \\ \Delta\lambda_{N_{cyl,plast}}^{(N_{Fact,N_{cyl,plast}}),n+1,k+1} \end{array} \right\} \tag{3.83}$$

The residual vector reads as

$$\mathbf{R}^{n+1,k+1,l}=\left\{\begin{array}{rl}
R_1^{(1),n+1,k+1,l} & =\mathscr{F}^{(1)}\left[\tilde{\boldsymbol{\sigma}}_1\left(\Delta\boldsymbol{\lambda}^{n+1,k+1,l}\right)\right]\\
R_1^{(2),n+1,k+1,l} & =\mathscr{F}^{(2)}\left[\tilde{\boldsymbol{\sigma}}_1\left(\Delta\boldsymbol{\lambda}^{n+1,k+1,l}\right)\right]\\
 & \vdots\\
R_1^{(N_{Fact,1}),n+1,k+1,l} & =\mathscr{F}^{(N_{Fact,1})}\left[\tilde{\boldsymbol{\sigma}}_1\left(\Delta\boldsymbol{\lambda}^{n+1,k+1,l}\right)\right]\\
R_2^{(1),n+1,k+1,l} & =\mathscr{F}^{(1)}\left[\tilde{\boldsymbol{\sigma}}_2\left(\Delta\boldsymbol{\lambda}^{n+1,k+1,l}\right)\right]\\
R_2^{(2),n+1,k+1,l} & =\mathscr{F}^{(2)}\left[\tilde{\boldsymbol{\sigma}}_2\left(\Delta\boldsymbol{\lambda}^{n+1,k+1,l}\right)\right]\\
 & \vdots\\
R_2^{(N_{Fact,2}),n+1,k+1,l} & =\mathscr{F}^{(N_{Fact,2})}\left[\tilde{\boldsymbol{\sigma}}_2\left(\Delta\boldsymbol{\lambda}^{n+1,k+1,l}\right)\right]\\
 & \vdots\\
R_{N_{cyl,plast}}^{(1),n+1,k+1,l} & =\mathscr{F}^{(1)}\left[\tilde{\boldsymbol{\sigma}}_{N_{cyl,plast}}\left(\Delta\boldsymbol{\lambda}^{n+1,k+1,l}\right)\right]\\
R_{N_{cyl,plast}}^{(2),n+1,k+1,l} & =\mathscr{F}^{(2)}\left[\tilde{\boldsymbol{\sigma}}_{N_{cyl,plast}}\left(\Delta\boldsymbol{\lambda}^{n+1,k+1,l}\right)\right]\\
 & \vdots\\
R_{N_{cyl,plast}}^{(N_{Fact,N_{cyl,plast}}),n+1,k+1,l} & =\mathscr{F}^{(N_{Fact,N_{cyl,plast}})}\left[\tilde{\boldsymbol{\sigma}}_{N_{cyl,plast}}\left(\Delta\boldsymbol{\lambda}^{n+1,k+1,l}\right)\right]
\end{array}\right\} \tag{3.84}$$

with $N_{Fact,i}$ as the number of active surfaces of phase i; and its derivatives

$$\frac{d\mathbf{R}^{n+1,k+1,l}}{d(\boldsymbol{\lambda}^{n+1,k+1})}=$$

$$\left\{\begin{array}{c}
\frac{\partial R_1^{(1)}}{\partial(\Delta\lambda)_1^{(1),n+1,k+1}},\cdots,\frac{\partial R_1^{(1)}}{\partial(\Delta\lambda)_{N_{cyl,plast}}^{(1),n+1,k+1}},\cdots,\frac{\partial R_1^{(1)}}{\partial(\Delta\lambda)_1^{(N_{Fact,1}),n+1,k+1}},\cdots,\frac{\partial R_1^{(1)}}{\partial(\Delta\lambda)_{N_{cyl,plast}}^{(N_{Fact,1}),n+1,k+1}}\\
\frac{\partial R_2^{(1)}}{\partial(\Delta\lambda)_1^{(1),n+1,k+1}},\cdots,\frac{\partial R_2^{(1)}}{\partial(\Delta\lambda)_{N_{cyl,plast}}^{(1),n+1,k+1}},\cdots,\frac{\partial R_2^{(1)}}{\partial(\Delta\lambda)_1^{(N_{Fact,2}),n+1,k+1}},\cdots,\frac{\partial R_2^{(1)}}{\partial(\Delta\lambda)_{N_{cyl,plast}}^{(N_{Fact,2}),n+1,k+1}}\\
\vdots\\
\frac{\partial R_{N_{cyl,plast}}^{(1)}}{\partial(\Delta\lambda)_1^{(1),n+1,k+1}},\cdots,\frac{\partial R_{N_{cyl,plast}}^{(1)}}{\partial(\Delta\lambda)_{N_{cyl,plast}}^{(1),n+1,k+1}},\cdots,\frac{\partial R_{N_{cyl,plast}}^{(1)}}{\partial(\Delta\lambda)_1^{(N_{Fact,1}),n+1,k+1}},\cdots,\frac{\partial R_{N_{cyl,plast}}^{(1)}}{\partial(\Delta\lambda)_{N_{cyl,plast}}^{(N_{Fact,N_{cyl,plast}}),n+1,k+1}}\\
\frac{\partial R_1^{(2)}}{\partial(\Delta\lambda)_1^{(1),n+1,k+1}},\cdots,\frac{\partial R_1^{(2)}}{\partial(\Delta\lambda)_{N_{cyl,plast}}^{(1),n+1,k+1}},\cdots,\frac{\partial R_1^{(2)}}{\partial(\Delta\lambda)_1^{(N_{Fact,1}),n+1,k+1}},\cdots,\frac{\partial R_1^{(2)}}{\partial(\Delta\lambda)_{N_{cyl,plast}}^{(N_{Fact,N_{cyl,plast}}),n+1,k+1}}\\
\vdots\\
\frac{\partial R_{N_{cyl,plast}}^{(N_{Fact,N_{cyl,plast}})}}{\partial(\Delta\lambda)_1^{(1),n+1,k+1}},\cdots,\frac{\partial R_{N_{cyl,plast}}^{(N_{Fact,N_{cyl,plast}})}}{\partial(\Delta\lambda)_{N_{cyl,plast}}^{(1),n+1,k+1}},\cdots,\frac{\partial R_{N_{cyl,plast}}^{(N_{Fact,N_{cyl,plast}})}}{\partial(\Delta\lambda)_1^{(N_{Fact,1}),n+1,k+1}},\cdots,\frac{\partial R_{N_{cyl,plast}}^{(N_{Fact,N_{cyl,plast}})}}{\partial(\Delta\lambda)_{N_{cyl,plast}}^{(N_{Fact,N_{cyl,plast}}),n+1,k+1}}
\end{array}\right\} \tag{3.85}$$

whereby

$$\begin{aligned}\frac{\partial R_1^{(\beta)}}{\partial(\Delta\lambda_i^{(\alpha),n+1,k+1})} &= \frac{\partial \mathscr{F}^{(\beta)}}{\partial \tilde{\boldsymbol{\sigma}}_1^{n+1}}(\tilde{\boldsymbol{\sigma}}_1^{n+1}) : \frac{\partial \tilde{\boldsymbol{\sigma}}_1}{\partial(\Delta\lambda)_i^{(\alpha),n+1,k+1}} \\ &= \frac{\partial \mathscr{F}^{(\beta)}}{\partial \tilde{\boldsymbol{\sigma}}_1^{n+1}}(\tilde{\boldsymbol{\sigma}}_1^{n+1}) : \mathbb{C}_{solid} : [\mathbb{D}_{1i} - \delta_{1i}\mathbb{I}] : \frac{\partial \mathscr{G}^{(\alpha)}}{\partial \tilde{\boldsymbol{\sigma}}_i}(\boldsymbol{\sigma}_i^{n+1,k})\end{aligned} \tag{3.86}$$

The solution vector of iteration $(l+1)$ reads as

$$\Delta\left(\Delta\boldsymbol{\lambda}^{n+1,k+1,l+1}\right) = \begin{Bmatrix} \Delta\left(\Delta\lambda\right)_1^{(1)} \\ \vdots \\ \Delta\left(\Delta\lambda\right)_1^{(N_{Fact,1})} \\ \Delta\left(\Delta\lambda\right)_2^{(1)} \\ \vdots \\ \Delta\left(\Delta\lambda\right)_2^{(N_{Fact,2})} \\ \vdots \\ \Delta\left(\Delta\lambda\right)_{N_{cyl,plast}}^{(1)} \\ \vdots \\ \Delta\left(\Delta\lambda\right)_{N_{cyl,plast}}^{(N_{Fact,N_{cyl,plast}})} \end{Bmatrix} \tag{3.87}$$

and the updated plastic multiplier vector as

$$\Delta\boldsymbol{\lambda}^{n+1,k+1,l+1} = \Delta\boldsymbol{\lambda}^{n+1,k+1,l} + \Delta\left(\Delta\boldsymbol{\lambda}\right)^{n+1,k+1,l+1} \tag{3.88}$$

If the converged solutions $\Delta(\Delta\lambda)_i^{(\alpha),n+1}$ are all positive, the original guess of active phases and surfaces according to the trial state definition (3.71) and (3.72) was correct. If any $\Delta(\Delta\lambda)_i^{(\alpha),n+1}$ are negative, the corresponding yield surfaces are discarded from the sets $\mathcal{S}_{cyl,plast}$ and $\{1, 2, \ldots, N_{Fact,i}\}$ and the process (3.73) to (3.88) is repeated as long as all plastic multipliers are non-negative.

3.6 Exemplification of multiscale elastoplasticity through upscaling of Mohr-Coulomb criterion

We here exemplify the developments of Section 3.5 by assigning, to all needle-shaped solid phases of Figure 3.1, a Mohr-Coulomb criterion in the form

$$\mathscr{F}\left(\boldsymbol{\sigma}\right) = \tau - \left(c_{solid} - \sigma \tan \varphi_{solid}\right) \leq 0 \tag{3.89}$$

with $\tau = \sigma_{nt}$ and $\sigma = \sigma_{nn}$ as the components of the traction vector $\mathbf{T} = \boldsymbol{\sigma} \cdot \mathbf{n}$ in the so-called Mohr plane, which is spanned by the vectors $\mathbf{n}$ and $\mathbf{t}$. $\mathbf{t}$ is in this Mohr plane as well, arising from rotating $\mathbf{n}$ by $(\pi/2)$; i.e. orthogonal to $\mathbf{n}$. Upon fulfillment of (3.89), plastic strains may occur only in terms of shear components ε_{nt}^p, i.e. only such strain components which are energetically conjugated to $\tau = \sigma_{nt}$. According to the general flow rule of (3.53), this may be expressed by a plastic potential $\mathscr{G}$ which does not depend on the normal stress component σ, hence being of the form

$$\mathscr{G}(\boldsymbol{\sigma}) = \tau \tag{3.90}$$

so that $\partial \mathscr{G}/\partial \sigma = 0$ and $\partial \mathscr{G}/\partial \tau = 1$. In the principle stress state, (3.89) represents a pyramid with six faces, six edges and an apex; while (3.90) represents a prism with six faces and edges, being oriented parallel to the hydrostatic axis. Back-projection of trial stress states on these edges and faces of the pyramid, along directions orthogonal to the edges and faces of the prism can be conveniently performed on the basis of the following multisurface representation of (3.89) and (3.90) in the principal stress space; comprising three yield functions

$$\begin{aligned} \mathscr{F}^{(1)} &= \beta\sigma_{i,I} - \sigma_{i,III} - \sigma_y \\ \mathscr{F}^{(2)} &= \beta\sigma_{i,I} - \sigma_{i,II} - \sigma_y \\ \mathscr{F}^{(3)} &= \beta\sigma_{i,II} - \sigma_{i,III} - \sigma_y \end{aligned} \tag{3.91}$$

with the friction parameter β and the compressive yield stress σ_y being related to the cohesion c_{solid} and the angle of internal friction φ_{solid} through

$$\sigma_y = \frac{2c_{solid} \cos \varphi_{solid}}{1 - \sin \varphi_{solid}} \tag{3.92}$$

and

$$\beta = \frac{1 + \sin \varphi_{solid}}{1 - \sin \varphi_{solid}} \tag{3.93}$$

and the plastic potential functions

$$\begin{aligned} \mathscr{G}^{(1)} &= \sigma_{i,I} - \sigma_{i,III} \\ \mathscr{G}^{(2)} &= \sigma_{i,I} - \sigma_{i,II} \\ \mathscr{G}^{(3)} &= \sigma_{i,II} - \sigma_{i,III} \end{aligned} \tag{3.94}$$

whereby $\sigma_{i,I} \geq \sigma_{i,II} \geq \sigma_{i,III}$ are the principal stresses of stress tensor $\boldsymbol{\sigma}_i$. (3.91) and (3.94) can be readily inserted into the general form of the algorithm (3.70)-(3.88).

We explicitly note that the yield and potential functions (3.91) and (3.94) appear as linear in the principal stress state, but that the corresponding principal directions do change during the loading and back-projection steps, which renders the problem as fully non-linear. Depending on the degree of nonlinearity, the accuracy of the trial state in correctly targeting the actually plastically active solid phases and yield surfaces may reduce, which then prolongs the computation time. In this context, the introduction of plastic stress regions according to Clausen et al. [2007] turns out as helpful: These regions are defined on the basis of two expressions, which relate to the delimiting lines of semi-infinite triangular plane (to which the Mohr-Coulomb criterion degenerates in the principical stress space, once the principal stresses are ordered according to $\sigma_I \geq \sigma_{II} \geq \sigma_{III}$). They are

$$\begin{aligned} p_{I-II}(\boldsymbol{\sigma}) = \frac{1}{\beta+1}\left(\sigma_I - \frac{\sigma_y}{\beta-1}\right) - \left(\sigma_{II} - \frac{\sigma_y}{\beta-1}\right) \\ + \frac{1}{\beta+1}\left(\sigma_{III} - \frac{\sigma_y}{\beta-1}\right) \end{aligned} \tag{3.95}$$

$$\begin{aligned} p_{I-III}(\boldsymbol{\sigma}) = \frac{\beta}{\beta+1}\left(\sigma_I - \frac{\sigma_y}{\beta-1}\right) - \left(\sigma_{II} - \frac{\sigma_y}{\beta-1}\right) \\ + \frac{\beta}{\beta+1}\left(\sigma_{III} - \frac{\sigma_y}{\beta-1}\right) \end{aligned} \tag{3.96}$$

The aforementioned stress regions for categorization of the trial stress states are:

- Stress region I relates to $p_{I-II}\left(\boldsymbol{\sigma}_i^{n+1,trial}\right) \geq 0$ and $p_{I-III}\left(\boldsymbol{\sigma}_i^{n+1,trial}\right) \leq 0$: if the trial stress resides in this region, then we choose $\mathscr{F}^{(1)}$ according to (3.91) as active yield surface.

- Stress region II relates to $p_{I-II}\left(\boldsymbol{\sigma}_i^{n+1,trial}\right) < 0$ and $p_{I-III}\left(\boldsymbol{\sigma}_i^{n+1,trial}\right) < 0$: if the trial stress resides in this region, then we choose $\mathscr{F}^{(1)}$ and $\mathscr{F}^{(2)}$ according to (3.91) as active yield surfaces.

- Stress region III relates to $p_{I-II}\left(\boldsymbol{\sigma}_i^{n+1,trial}\right) > 0$ and $p_{I-III}\left(\boldsymbol{\sigma}_i^{n+1,trial}\right) > 0$: if the trial stress resides in this region, then we choose $\mathscr{F}^{(1)}$ and $\mathscr{F}^{(3)}$ according to (3.91) as active yield surfaces.

- Stress region IV relates to all other cases, where we choose all three yield surfaces as active.

Finally, the actually active yield surfaces are idenfitied as described at the end of Section 3.5.3. Next, we show the application of the algorithm described in Section 3.5 and applied to Mohr-Coulomb plasticity earlier in the present chapter, for computing the behavior of the RVE shown in Figure 3.1 with material properties collected in Table 3.3, under pure shear, $\boldsymbol{\Sigma} = \Sigma_{23}\left(\mathbf{e}_2 \otimes \mathbf{e}_3 + \mathbf{e}_3 \otimes \mathbf{e}_2\right)$, under uniaxial tension, $\boldsymbol{\Sigma} = \Sigma_{33}\,\mathbf{e}_3 \otimes \mathbf{e}_3$, $\Sigma_{33} > 0$, and under uniaxial compression,

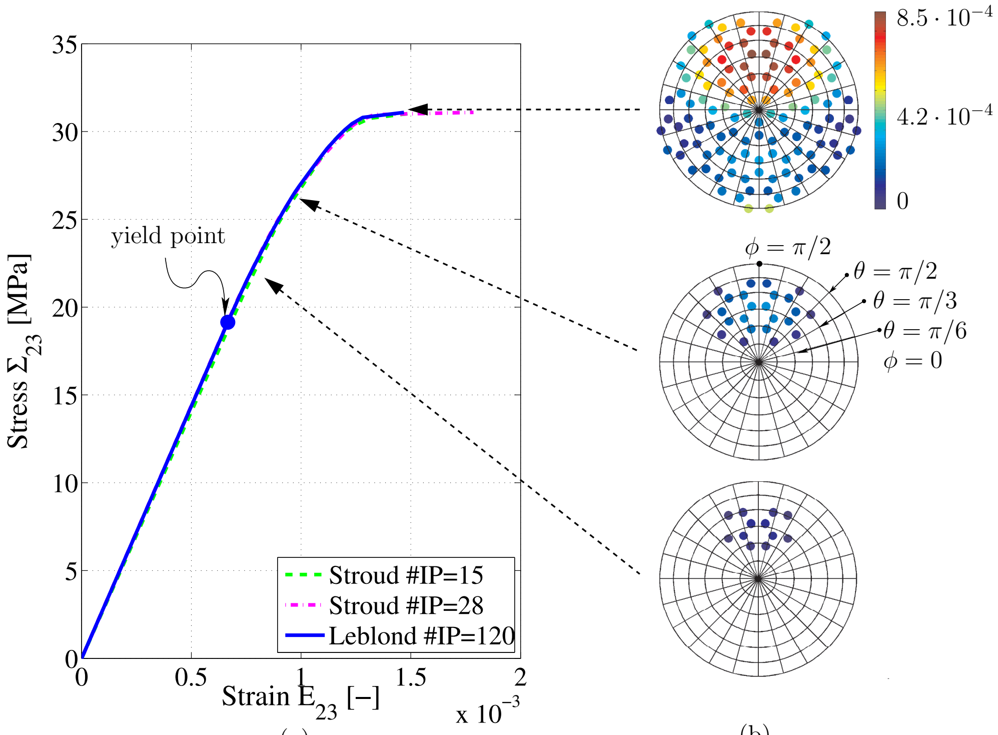

(a) (b)

Figure 3.4: (a) Macroscopic stress-strain relation under pure shear, for different discretizations according to Stroud [1971] and Badel and Leblond [2004], IP... integration point; (b) distribution of the norm of the plastic microstrains over the solid needle phase orientations, at selected macroscopic stress levels

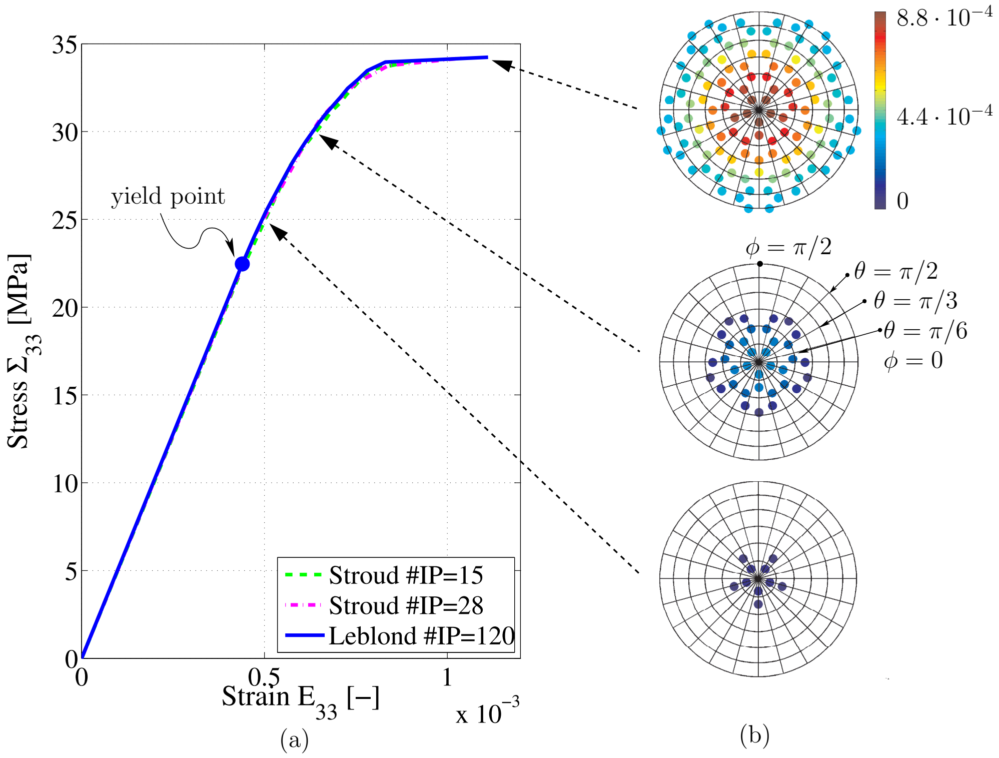

Figure 3.5: (a) Macroscopic stress-strain relation under uniaxial tension (depicted from the onset of plastic events), for different discretizations according to Stroud [1971] and Badel and Leblond [2004], IP... integration point; (b) distribution of the norm of the plastic microstrains over the solid needle phase orientations, at selected macroscopic stress levels

$\mathbf{\Sigma} = \Sigma_{33}\, \mathbf{e}_3 \otimes \mathbf{e}_3$, $\Sigma_{33} < 0$.

Table 3.3: Properties of solid and pore material phases, for the case of porous hydroxyapatite polycrystals, see Section 3.7 for experimental details

Property	Solid phases	Pore phase
Bulk modulus	$k_{solid} = 82.6\,\mathrm{GPa}$	$k_{pore} = 2.3\,\mathrm{GPa}$
Shear modulus	$\mu_{solid} = 44.9\,\mathrm{GPa}$	$\mu_{pore} = 0\,\mathrm{GPa}$
Cohesion	$c_{solid} = 82.3\,\mathrm{MPa}$	
Friction angle	$\varphi = 57.8°$	
Volume fraction	$f_{HA} = 0.68$	$f_{pore} = 0.32$

First of all, it is interesting to study the effect of different discretization schemes on the model predictions, see Figures 3.4(a), 3.5(a), and 3.6(a). Two realizations of the integration scheme of Stroud [1971], with 15 and 28 integration points, respectively, as well as the method of Badel and Leblond [2004] with 120 integration points, deliver very similar results - indicating the converged nature of the reported computational results (see also Table 3.4). For all investigated load cases, plasticity

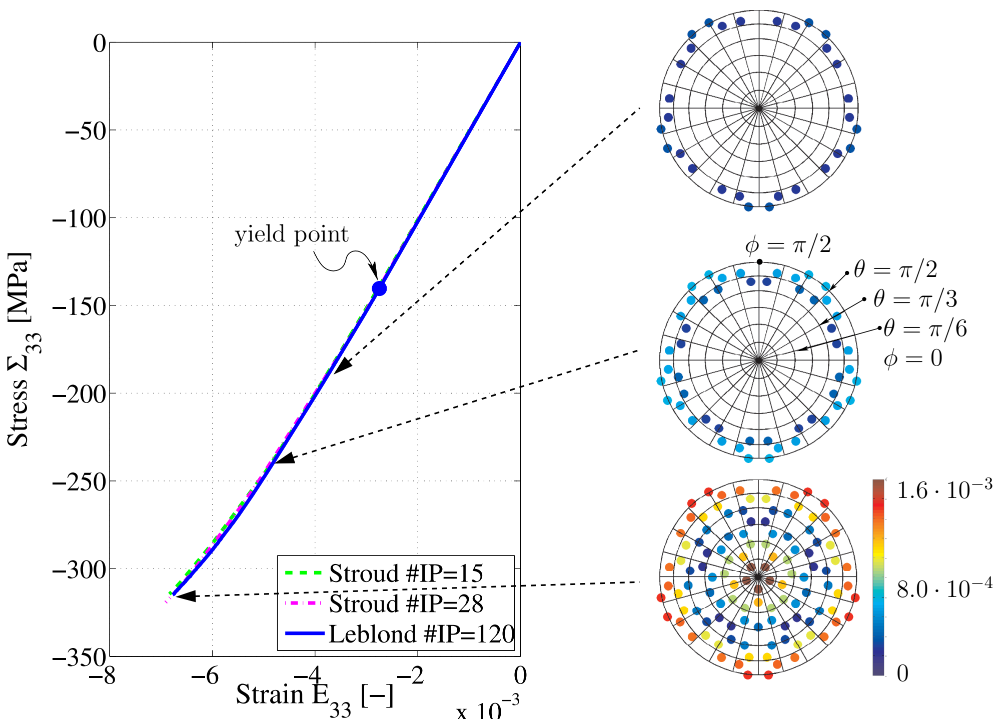

(a) (b)

Figure 3.6: (a) Macroscopic stress-strain relation under uniaxial compression (depicted from the onset of plastic events), for different discretizations according to Stroud [1971] and Badel and Leblond [2004], IP... integration point; (b) distribution of the norm of the plastic microstrains over the solid needle phase orientations, at selected macroscopic stress levels

Table 3.4: Yield and ultimate macroscopic stresses [in MPa] computed for uniaxial tension, uniaxial compression, and pure shear: based on different discretization schemes and different numbers of integration points (#IP)

Discretization	Load case		Yield stress	Ultimate stress
Stroud #IP=15	uniaxial tension	$\Sigma_{33} =$	21.61	34.04
	uniaxial compression	$\Sigma_{33} =$	-131.50	-314.50
	pure shear	$\Sigma_{23} =$	20.87	31.05
Stroud #IP=28	uniaxial tension	$\Sigma_{33} =$	23.77	34.20
	uniaxial compression	$\Sigma_{33} =$	-151.77	-319.16
	pure shear	$\Sigma_{23} =$	20.01	31.10
Leblond #IP=120	uniaxial tension	$\Sigma_{33} =$	22.46	34.23
	uniaxial compression	$\Sigma_{33} =$	-140.36	-314.85
	pure shear	$\Sigma_{23} =$	19.14	31.09

leads to non-linear macroscopic stress-strain curves, and this non-linearity is associated with the propagation of plasticity throughout the solid needle phases. As all solid needle phases exhibit ideal plastic behavior, they cannot undergo any unloading processes under macroscopic loading states. With increasing macroscopic stress, an increasing fraction of the solid needle phases plasticize, as illustrated in

Figures 3.4(b), 3.5(b), and 3.6(b). The orientation of these increasing number of plasticizing phases, quantified in terms of the angles θ and ϕ given in Figure 3.2, can be illustrated on the stereographic projection of a unit sphere onto a plane parallel to the base vectors $\mathbf{e}_1$ and $\mathbf{e}_2$, see Figures 3.4(b), 3.5(b), and 3.6(b) for three such projections each, relating to characteristic macroscopic stress states beyond the yield point. In the aforementioned circular projections, different values for the co-latitudinal coordinate θ are associated with different concentric circles, the outermost circle being related to $\theta = \pi/2$; and different values for the longitudinal coordinate ϕ are associated with different straight lines oriented orthogonal to the aforementioned circles. The plastic strains occuring in differently oriented needle-shaped phases are indicated in terms of their norm, $||\boldsymbol{\varepsilon}^p|| = \sqrt{\sum_i \sum_j \varepsilon^p_{ij}\varepsilon^p_{ij}}$ given as colored circles relating to the 120 integration point orientations employed in the context of the Badel-Leblond discretization scheme, as described in Section 3.5.1. Out of these 120 orientations, only those relating to plasticized phases are indicated. Hence, once all 120 orientations are marked by a colored circle, all solid phases plasticize, and the RVE would fail under a macroscopic stress-driven test. Naturally, the evolution of the aforementioned plastic regions in Figures 3.4(b), 3.5(b), and 3.6(b) give interesting insights into the microstructural events arising under macroscopic loading of the types pure shear, uniaxial tension, and uniaxial compression: In pure shear (see Figure 3.4(b)), plasticity starts in needles belonging to the shear plane and inclined by $\pi/4$ to the $\mathbf{e}_2$-$\mathbf{e}_3$-axes, respectively, and propagates towards needles oriented off-plane, but also less inclined from the axes $\mathbf{e}_2$ and $\mathbf{e}_3$. Under macroscopic uniaxial tensile loading in $\mathbf{e}_3$-direction ($\theta = 0$), the needle-shaped phases oriented in loading directions are the first to plastify, and the subsequent plastification process spreads axisymmetrically around $\mathbf{e}_3$, see Figure 3.5(b). In uniaxial compression (see Figure 3.6(b)), plasticity starts in needles orthogonal to the load direction, and while this plastic region on the unit sphere projection area spreads, a second, independent non-contiguous plastic region emerges around $\theta = 0$, i.e. needles oriented in the loading direction start to plasticize as well. Finally, plastification events affect also the needle-shaped phases inclined by $\pi/4$ from the loading direction, see Figure 3.6(b).

3.7 Application: Push-out test on osteonal bone

Bone tissue is a hierarchically organized material composed of three elementary components governing its mechanical behavior: mineral, collagen, and water with non-collageneous organics. These elementary components are arranged in different microstructures, from the nanometer scale up to that of milimeters [Katz et al., 1984, Weiner and Wagner, 1998], see Figure 3.7. The seemingly "compact", so-called cortical shell surrounding the macroscopic organ [see Figure 3.7(a)] appears, under greater magnification, as a porous material itself, with cylindrical pores (called Haversian canals) being surrounded by concentric layers of lamellar bone matrix (see Figure 3.7(b) for the corresponding microstructural unit called "osteon"). Each osteon consists of one Haversian canal surrounded by alternating collagen-rich and collagen-poor layers of extravascular bone matrix [Marotti et al., 1994, 2013], and such an osteon is bounded by a so-called cement line with up to 5 microns thickness [Skedros et al., 2005]. This cement line is collagen-free, as was experimentally evidenced by staining tests [Skedros et al., 2005, Sokoloff, 1973, Weidenreich, 1930, Weinmann and Sicher, 1955]. Conclusively, cement lines contain hydroxyapatite and water with noncollageneous organics, these components making up a polycrystalline material as seen in Figure 3.7(c). This material can be suitably represented by the RVE of Figure 3.1, see Figure 3.7(d). Such an RVE has been extensively used for the micromechanical modeling of the extrafibrillar spaces within the bone ultrastructure [Fritsch et al., 2009b, Morin and Hellmich, 2014, Vuong and Hellmich, 2011].

The microscopic strength properties of the osteon can be determined through push-out tests, first carried out by Ascenzi and Bonucci [1972] on bone from human femoral shafts, and later by Bigley et al. [2006] on bone from the third metapcarpal of a racehorse. During such tests, a punch with a diameter of about 150 μm applies a compressive load on the osteon until its complete debonding. The absence of collagen in the cement lines makes them comparatively weak, and renders them as preferred locations of osteon debonding in the course of push-out tests.

Such a push-out test produces a pure shear stress in the cement line, which we prescribe in the form $\mathbf{\Sigma} = \Sigma_{23}(\mathbf{e}_2 \otimes \mathbf{e}_3 + \mathbf{e}_3 \otimes \mathbf{e}_2)$ on the RVE of Figure 3.1 with solid phases following a Mohr-Coulomb criterion; by using the algorithm described in Section 3.5. As model input parameters, we need (i) the elastic properties of of the needle-shaped phases and of the pores, (ii) the strength properties of the

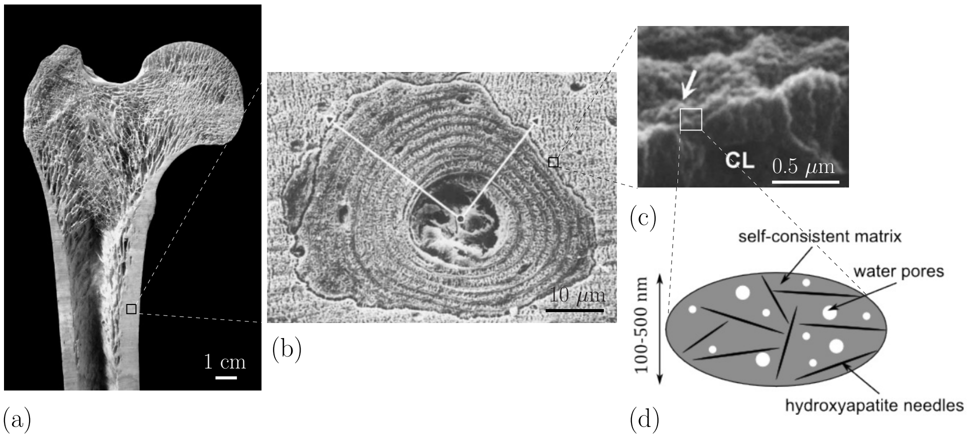

Figure 3.7: Hierarchical organization of bone: (a) photograph of a whole bone; (b) scanning electron micrograph of an osteon, being composed of alternating thick (dense, collagen-rich) and thin (loose, collagen-poor) lamellae, and delineated by a collagen-free cement line [Marotti, 1993], (c) scanning electron micrograph of the isolated cement line [Davies, 2007], (d) micromechanical representation of collagen-free compartment of bone ultrastructure, also referred to as “extrafibrillar space” [Prostak and Lees, 1996]; permission for image reproduction requested (a) from Paul Crompton, University of Wales College of Medicine, (b) from Springer-Verlag New York Inc. for Figures 1 of [Marotti, 1993], and (c) from Elsevier for Figure 2B of [Davies, 2007]

plastic solid phases, and (iii) the volume fractions of pores (filled by water and non-collageneous organic matter) and solid phases (made of hydroxyapatite, abbreviated as HA).

The elastic properties of the constituents were determined by experiments performed on pure constituents: ultrasonic measurements on hydroxyapatite allowed to identify the following isotropic properties [Gilmore and Katz, 1982, Katz and Ukraincik, 1971]

$$\mathbb{C}_{HA} = 3k_{HA}\mathbb{I}^{vol} + 2\mu_{HA}\mathbb{I}^{dev} \tag{3.97}$$

with $k_{HA} = 82.6$ GPa and $\mu_{HA} = 44.9$ GPa, $\mathbb{I}^{vol}$ as the volumetric part of the identity tensor $\mathbb{I}$ with components

$$I^{vol}_{ijkl} = \frac{1}{3}\delta_{ij}\delta_{kl} \tag{3.98}$$

and $\mathbb{I}^{dev}$ as the deviatoric part of the identity tensor defined by $\mathbb{I}^{dev} = \mathbb{I} - \mathbb{I}^{vol}$. The elastic properties of the (undrained) pore fluid are approximated by that of the water: $\mathbb{C}_{pore} = 3k_{H_2O}\mathbb{I}^{vol}$, with $k_{H_2O} = 2.3$ GPa.

The strength properties of hydroxyapatite, as defined through the two parameters of the Mohr-Coulomb criterion, are gained from tension and compression experiments on different HA biomaterials [Akao et al., 1981, Peelen et al., 1978, Shareef et al., 1993], as given in greater detail in [Fritsch et al., 2009b]. The Mohr-Coulomb parameters are chosen so as to minimize the mean square error between model predictions (as functions of porosity) and corresponding experimental results. They amount to: $\beta = 12$ and $\sigma_y = 570$ MPa, or, according to Eq. (3.92) and (3.93), $c_{solid} = 82.3\,\text{MPa}$ and $\varphi_{solid} = 57.8°$.

Finally, the volume fractions are determined from mass, volume, and light microscopy measurements performed by McCarthy et al. [1990] on bone samples from the third equine metacarpus. McCarthy et al. [1990] report 35 values each for the macroscopic mass densities ρ_{macro}, and for the vascular porosities f_{vas}, giving access to the extravascular mass densities as

$$\rho_{exvas} = \frac{\rho_{macro} - \rho_{H_2O} \times f_{vas}}{1 - f_{vas}} \tag{3.99}$$

see Table 3.5 for corresponding numerical results. Then, recent microCT investigations revealing a lacunar-canalicular porosity per extravascular space of $f^{exvas}_{lac+can} = 2.06\,\%$ are considered [Schneider et al., 2007, 2011], so as to transform these extravascular mass densities to the extracellular level, yielding the extracellular mass densities according to

$$\rho_{excel} = \frac{\rho_{exvas} - \rho_{H_2O} \times f^{exvas}_{lac+can}}{1 - f^{exvas}_{lac+can}} \tag{3.100}$$

see Table 3.5 for corresponding numerical results. These ultrastructural mass densities then enter the "universal" composition rules of Vuong and Hellmich [2011], who showed that the composition of the extracellular bone matrix, in terms of mineral, organics and fluid, follows bilinear laws, as became evident from a wide variety of bone tissues tested in over 80 years of research [Biltz and Pellegrino, 1969, Burns, 1929, Gong et al., 1964, Hammet, 1925, Lees, 1987, 2003, Lees and Page, 1992, Lees et al., 1979a, 1983, 1995]. These rules are depicted in Figure 3.8, where the macroscopic-to-ultrastructural mass density transition was based on vascular porosities of 3 % [Lees et al., 1979a], and lacunar-canalicular porosities of 2 % [Schneider et al., 2007, 2011] in the case of mammalian bone tissues, while the absence of such pores in the case of tendons and otic bone tissues does not require discrimination between macroscopic and ultrastructural density and concentration properties. The extracellular bone matrix is made up by an arrangement of collageneous fibrils and collagen-deficient extrafibrillar space, these two compartments being characterized by the same extracollageneous mineral concentration [Hellmich and Ulm, 2003]. This distribution rule, together with the rules identified by Morin et al. [2013] and Morin and Hellmich [2013] for fibrillar swelling and shrinkage due to hydration and mineralization, finally allows for quantification of the intercrystalline porosity and the mineral volume fractions inside an RVE of extrafibrillar space, the one depicted in Figure 3.7(d); see Table 3.5 for corresponding results.

Use of these volume fractions for such an RVE subjected to pure shear until full plastification, yields the shear strength values given in the last column of Table 3.5. Their mean value of 31 MPa virtually perfectly agrees with the mean experimental value of 30.7 MPa given by Bigley et al. [2006] for debond shear strength of cement lines.

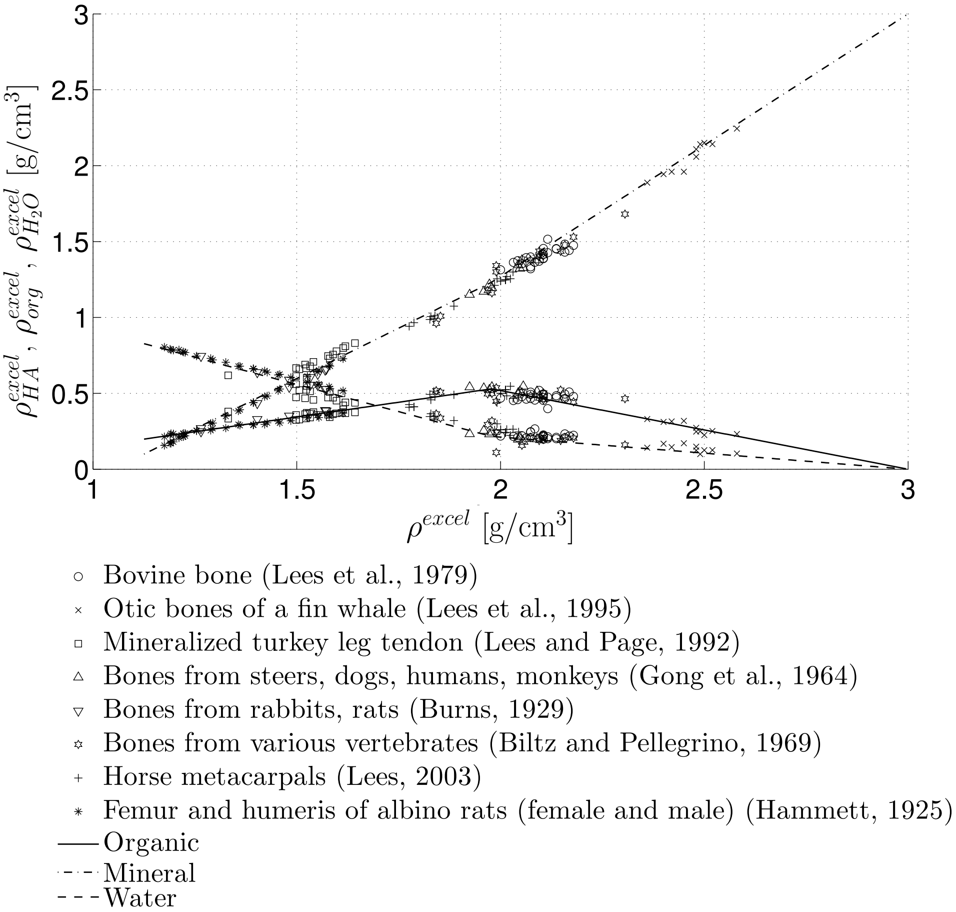

Figure 3.8: Apparent mass densities (per volume of extracellular space) of water, hydroxyapatite, and organic matter, versus overall mass density of extracellular bone matrix, across different species, organs, and ages; in the line of Vuong and Hellmich [2011]

While this impressively confirms our modeling approach, we wish to also base the experimental validation of the model-predicted values of Table 3.5 on a more profound statistical argument. Therefore, we consider the aforementioned strength predictions as validated if and only if the following statistical question is anwered with “yes”. The question is: Does the statistical sample of 35 model-predicted shear strength values belong to the same statistical population of shear strength values as the statistical sample of 66 strength values which were experimentally obtained by Bigley et al. [2006]? If we reconstruct the latter statistical sample of Bigley et al. [2006] through log-normally distributed random variables with a mean value of 30.7 MPa and a standard deviation of 3.9 MPa, i.e. with the characteristics given explicitly by Bigley et al. [2006], then an ANOVA test clearly provides a clear “yes” to the aforementioned question (for 5 randomly reconstructed experimental samples, the corresponding F-values, with a mean of 0.49, stays very clearly below the critical F-value of 3.94). Consequently, we regard our micromechanical model of plastic porous polycrystals as validated for cement lines in osteonal bone.

3.8 Summary and conclusions

While multiscale elastoplasticity remains a veritable challenge in the mechanics and physics of solids, the present paper contains several original contributions providing a computationally efficient way to compute plastic phenomena in porous hydrated polycrystals:

- The influence tensor concept pioneered by Dvorak and colleagues [Dvorak, 1992, Dvorak and Benveniste, 1992, Dvorak et al., 1994] has been extended to infinitely many, mutually interacting, needle-shaped phases oriented in all space directions. This appears as a valuable solution for elastoplastic upscaling in polycrystals; which overcomes the elastoplastic stiffness overestimation associated with traditional micromechanics approaches comprising typically only a few (such as two) phases with (assumedly) uniform plastic strains; see e.g. the discussions in [Chaboche et al., 2001, 2005, Shojaei and Li, 2013]. Similarly effective solutions have been already proposed in the context of the so-called NTFA - non-uniform transformation field analysis [Fritzen and Böhlke, 2011, Jiang et al., 2013, Michel and Suquet, 2003, 2004, Roussette et al., 2009]; however, the latter approaches have all been related

Table 3.5: Characterization of equine cortical bone samples of McCarthy et al. [1990]: experimentally determined macroscopic mass densities and vascular porosities; extravascular and extracellular mass densities according to Eq. (3.99) and (3.100); volume fractions of hydroxyapatite crystal needle phase and of pore phase according to "universal" composition rules reported in [Hellmich and Ulm, 2003, Morin and Hellmich, 2013, Morin et al., 2013, Vuong and Hellmich, 2011]; and shear strength values predicted by the micromechanics model from Section 3.6, based on the material properties of Table 3.3.

ρ_{macro} [g/cm^3]	f_{vas} [-]	ρ_{exvas} [g/cm^3]	ρ_{excel} [g/cm^3]	f_{HA} [-]	f_{pore} [-]	Σ_{23}^{ult} [MPa]
2.03	0.10	2.14	2.17	0.74	0.26	32.5
2.02	0.08	2.11	2.13	0.72	0.28	31.7
2.01	0.11	2.13	2.16	0.74	0.26	32.2
2.01	0.07	2.09	2.11	0.71	0.29	31.2
2.00	0.09	2.10	2.12	0.72	0.28	31.5
2.00	0.07	2.08	2.10	0.71	0.29	31.0
2.00	0.06	2.06	2.09	0.70	0.30	30.7
1.98	0.12	2.11	2.14	0.73	0.27	31.8
1.98	0.12	2.11	2.14	0.73	0.27	31.8
1.98	0.10	2.09	2.11	0.71	0.29	31.3
1.98	0.10	2.09	2.11	0.71	0.29	31.3
1.97	0.10	2.08	2.10	0.71	0.29	31.0
1.97	0.12	2.10	2.13	0.72	0.28	31.6
1.96	0.11	2.08	2.10	0.71	0.29	31.0
1.96	0.10	2.07	2.09	0.70	0.30	30.8
1.95	0.14	2.10	2.13	0.72	0.28	31.6
1.95	0.09	2.04	2.07	0.69	0.31	30.3
1.95	0.12	2.08	2.10	0.71	0.29	31.1
1.95	0.18	2.16	2.18	0.75	0.25	32.7
1.95	0.11	2.07	2.09	0.70	0.30	30.8
1.95	0.14	2.10	2.13	0.72	0.28	31.6
1.93	0.12	2.06	2.08	0.70	0.30	30.6
1.93	0.09	2.02	2.04	0.67	0.33	29.5
1.93	0.13	2.07	2.09	0.70	0.30	30.9
1.92	0.12	2.05	2.07	0.69	0.31	30.4
1.92	0.10	2.02	2.04	0.67	0.33	29.6
1.92	0.12	2.05	2.07	0.69	0.31	30.4
1.92	0.11	2.03	2.06	0.69	0.31	30.0
1.91	0.12	2.03	2.06	0.69	0.31	30.0
1.91	0.22	2.17	2.19	0.75	0.25	32.9
1.91	0.18	2.11	2.13	0.72	0.28	31.7
1.90	0.25	2.20	2.23	0.77	0.23	33.5
1.90	0.12	2.02	2.04	0.68	0.32	29.6
1.82	0.09	1.90	1.92	0.57	0.43	24.9
1.76	0.30	2.09	2.11	0.71	0.29	31.2

to periodic (rather than polycrystalline) microstructures, and the determination of associated plastic modes (replacing uniform plastic strain fields) typically requires the introduction of coupled plastic flow rules and auxiliary numerical simulations, based on the Finite Element, or the Fast Fourier Transform Method. As with the Finite Element Method, also our present approach needs consideration of discretization issues (related, however, to the proper evaluation of integrals over the unit sphere), while it is based on classical multisurface plasticity (with no need to introduce additional "plastic couplings").

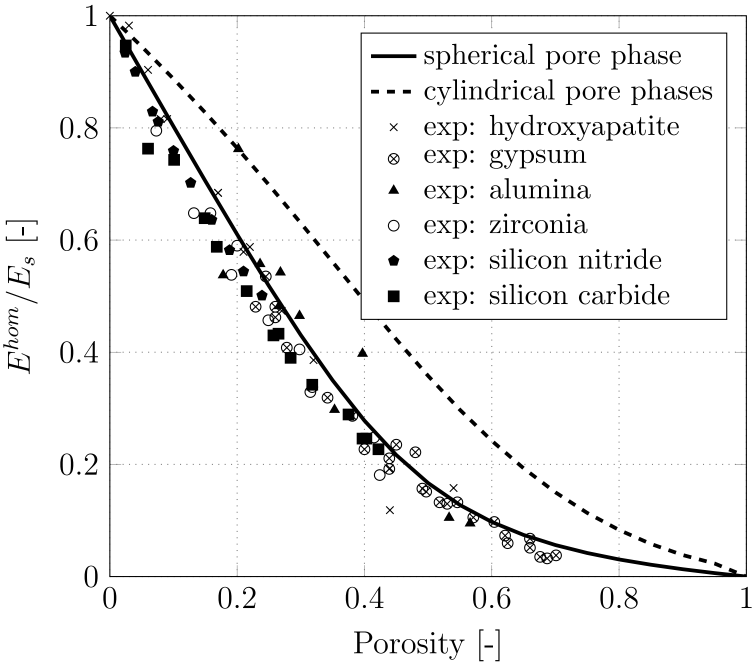

Figure 3.9: Comparison of spherical and cylindrical pore shape representation in micromechanical model for porous polycrystal; and comparison with experiments, see [Fritsch et al., 2013b] for experimental sources.

- The morphology depicted in Figure 3.1 is particularly well suited for a wide class of porous polycrystals. This was shown by Fritsch et al. [2009c, 2013b], Sanahuja et al. [2009]; reporting that the homogenized Young's modulus normalized by the Young's modulus of the solid needle phases turned out to exclusively depend on the porosity, and that this dependence was very well confirmed by experimental data on hydroxyapatite [Charrière et al., 2001, de With et al., 1981, Gilmore and Katz, 1982, Liu, 1998], gypsum [Ali and Singh, 1975, Colak, 2006, Meille, 2001, Phani, 1986, Tazawa, 1998], piezoelectric ceramics [Craciun et al., 1998], alumina [Coble and Kingery, 1956, Pabst et al., 2004], zirconia [Pabst et al., 2004], silicon carbide [Reynaud et al., 2005], and silicon nitride [Díaz and Hampshire, 2004]. In addition, such homogenized elasticity predictions were shown to be in excellent agreement with Finite Element simulations of "real" gypsum microstructures [Sanahuja et al., 2009]. By comparison, approaches which may seem similarly adequate on the first sight, such as the use of uniformly oriented acircular pore phases instead of one spherical pore phase, yield remarkably worse predictions, namely a significant overestimation of experimental data, see Figure 3.9. Further confirming the choice of one spherical pore phase, the micromechanical representation of Figure 3.1 also turned out as very relevant for quasi-brittle strength predictions [Fritsch et al., 2009c, Sanahuja et al., 2009]; and the present paper shows an equally sound capacity of this micromechanical representation when it comes to the realm of elastoplastic property upscaling. Extension of the method from uniformly oriented needle-shaped phases to preference of certain orientations, as encountered e.g. in the case of clay [Wenk et al., 2008] is quite straightforward. As was shown for axisymmetrically oriented needle phases in the context of elasticity [Fritsch et al., 2006], and would be reflected by adding probability density functions inside the spherical integrals appearing in Eqs. (3.16), (3.17), (3.22), (3.23), (3.25), (3.26), (3.31), (3.32), (3.33), (3.34), (3.35), (3.38), (3.39), (3.40), (3.41), (3.42), (3.43) as well as in their discretized counterparts. This is beyond the scope of the present manuscript.

- Involving infinitely many phases as part of the basic concept, our approach requires discretization down to an approriate number of phases, for which we employ two different concepts, namely Stroud's integration [Stroud, 1971] as well as the discretization method described in [Badel and Leblond, 2004]. The results related to all three choices of discretization are in satisfactory agreement. In this context, we reiterate that the consideration of different orientations is one of the keys to the succcess of our new method, a feature which this method shares with the so-called microplane models, as developed extensively by Bažant and colleagues [Bažant and Oh, 1985, Bažant and Prat, 1988, Bažant et al., 2000]. The latter models are also based on the principle of virtual work, however, they restrict corresponding energetical considerations to tangential planes on a unit hemisphere; rather than to a 3D RVE as is typically done in continuum micromechanics and described in Section 3.2.

- Upscaling of the elastoplastic constitutive relations from the solid phase to the porous polycrystal scale is performed by adaptation of the well-known return map algorithm originating from the nonlinear elastoplastic Finite Element analysis [Simo and Hughes, 1998, Simo and Taylor, 1985], based on an incremental load apposition. What is adopted from the original algorithm is the trial state computed from a fictitiously purely elastic deformation in the load step under investigation; this trial step giving a first indication on which solid phases might actually undergo plastic deformations. Whether this is actually the case, is checked via implicit solution of the elastic constitutive equation in combination with fulfillment of the active yield criteria. In contrast to the case encountered in the nonlinear Finite Element analysis, computation of elastoplastic (consistent) tangent is not required, as the concentration-influence relations are explicitly known. We regard this adoption of classical plasticity algorithms for micromechanics approaches as original in the context of polycrystalline materials, while we are aware of similar approaches for metal-ceramic composites with periodic microstructures [Vena et al., 2007]; but also for self-consistent homogenization based on spherical phase representations [Zeng et al., 2014]. The latter reference, however, rests on the use of suitably chosen elastoplastic tangents, while our concept explicitly accounts for the effects of geometrically incompatible non-elastic strains at the microscale, on the overall homogenized material behavior. This new concept extends the transformation field analysis [Dvorak and Benveniste, 1992, Dvorak et al., 1994], based on more recent work of Pichler and Hellmich [2010], towards infinitely many, needle-shaped eigenstressed phases. Realization of a return map algorithm for Mohr-Coulomb plasticity is a quite peculiar undertaking. Our corresponding developments described in Section 3.6 are somewhat inspired by the work of Clausen et al. [2007]. However, the latter work considers cases where the principal stress directions stay unaltered during the back projection of the trial stress state (which is related to one point of the simulated structure), onto the corresponding yield surface. Hence, this return mapping algorithm, which is performed stress state per stress state, is associated with the solution of a linear system of equations. With respect to this situation, our solution described in Section 3.5.4 is original with respect to two features: (i) all trial stress states in all (active) needle phases are back projected simultaneously,

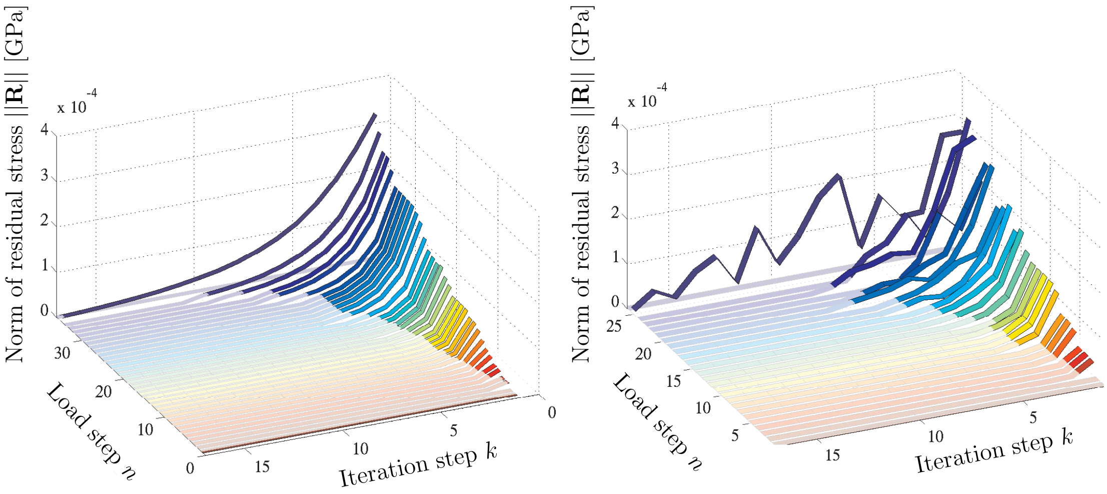

(a) under pure shear

(b) under uniaxial tension

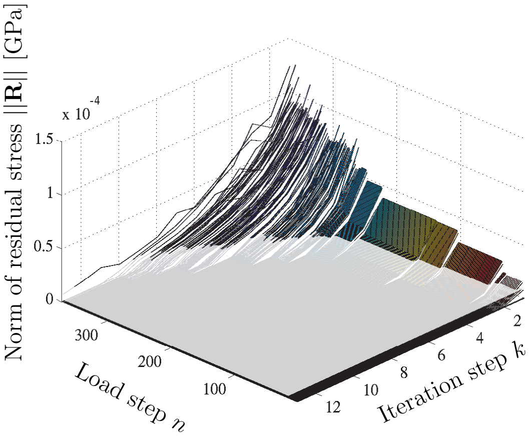

(c) under uniaxial compression

Figure 3.10: Convergence behavior during return map of trial states onto Mohr-Coulomb surfaces related to 120 solid needle phases arising from Badel-Leblond discretization; residual vector $\mathbf{R}$ is defined through Eq. (3.84)

leading finally to a much larger system of equations involving all plastic multipliers from all yield surfaces related to all (active) needle phases; and (ii) the principal stress directions *change* upon back projection of the trial stress states onto the plastic yield surfaces; accordingly the aforementioned system of equations becomes *nonlinear*, and it is hence solved according to the iteration scheme given by Eq. (3.82) - (3.88). Depending on macroscopic loading type and loading level, i.e. on the number of active needle-shaped solid phases, between one and ten iteration steps are typically needed in order to back-project all trial stress states onto the phase-specific yield surfaces, see Figures 3.10(a)-(c).

- As a rule the microstructural plastic events start in crystal phases oriented in the direction of the dominant macroscopic tensile stress; in the case of the latter being absent, the plasticity affects solid phases being oriented perpendicular to the dominant macroscopic compressive direction. Thereafter, the micro-plasticity spreads over all solid phase needle directions. Ultimate loads refer to all solid needle plasticizing, and when applied to the collagen-poor lamellae of osteonal bone, the presented micromechanical concept predicts well the ultimate loads attained in osteon push-out tests. Corresponding Mohr-Coulomb plasticity of the hydroxypatite crystal phases thereby may represent either sliding of hydrated interfaces situated within these phases as repeatedly discussed in material mechanics [Bhowmik et al., 2007, 2009, Qu et al., 2015a,b, Shahidi et al., 2014] or intrinsic dislocation phenomena in hydroxyapatite [Ievlev et al., 2013, Saka et al., 2008, Viswanath et al., 2007].

- As regards model validation, there are two principal options: comparison of micromechanics model results with Finite Element simulations resolving the material microstructures down to minute detail; or with experimental results. Generation of trustworthy Finite Element models requires very detailed knowledge on the geometrical characteristics of the object to be simulated. As regards the extrafibrillar space of bone, the material system investigated in Section 3.7, transmission electron micrographs [Lees and Prostak, 1988, Lees et al., 1994b, McNally et al., 2012, Prostak and Lees, 1996, Su et al., 2003, Zylberberg et al., 1998] have revealed microstructural details down to the several nanometer scale, over ranges spanning several hundreds of nanometers. However, full 3D quantification of structural features, e.g. by means of X-ray-based Computed Tomography techniques which have proved as particularly useful for the generation of trustworthy Finite Element models [Dejaco et al., 2012], is still out of reach. This is why we here compare our homogenization results of Table 3.5 directly to the experimental results of Bigley et al. [2006] for debonding shear strength of cement lines: Model predictions and experiments agree virtually perfectly, as reported in the last paragraph of Section 3.7. From a more qualitative viewpoint, it is interesting that the seamless transition from elastic to elastoplastic regimes in the stress-strain curves of bone at the single micron scale, where polycrystals as the one depicted in Figure 3.1 largely affect the material behavior, is indeed observed experimentally, as recent compressive tests on single micron-sized pillars have impressively shown [Luczynski et al., 2015, Schwiedrzik et al., 2014].

- For the sake of completeness, we may state that our approach targets at capturing the development of micro-plastic strains stemming from non-associated plasticity, and their macroscopic effects. This may be seen as an interesting complement to the popular plastic homogenization approaches based on limit analysis and variational methods; considering, as a rule, microscopic strength criteria, equilibrium at the micro and macro-scale, maximization of dissipation, and sometimes associated plasticity. Corresponding recent developments are reported in [Bignonnet et al., 2016, Cheng et al., 2014, Shen et al., 2015]. Other approaches [Qi et al., 2016] use the additive nature of the macroscopic strains resulting from particular microstructures, such as frictional cracks embedded in an elastic matrix. The macroscopic strains arising from the frictional cracks are directly introduced as macroscopic plastic strains, without any explicit micro-to-macro upscaling.

- Potential future work may aim at going beyond the constraints of ideal plasticity at the solid needle phase level, so as to extend the modeling approach towards catastrophic failure, such as it is eventually seen, for example, in the osteon push-out tests of Bigley et al. [2006]. This would imply careful study of so-called softening plasticity formulations, considering valuable knowledge from nonlocal and gradient plasticity theory [de Sciarra, 2004, 2008a,b, 2009].

Acknowledgments

Financial support in the framework of project ERC-2010-StG-257023-MICROBONE is gratefully acknowledged. The cooperation between TU Wien and EMSE was facilitated by the bilateral Hubert Curien - Amadeus travel grant FR02/2015 of OEAD - Austrian Agency for International Cooperation in Education and Research and Campus France - French Agency for International Cooperation in Education and Research.

3.9 Nomenclature

$\mathbb{A}_i$	fourth-order strain concentration tensor of phase i
$\mathbb{A}_{pore}$	fourth-order strain concentration tensor of pore phase
$\mathbb{A}_{pore}^{\infty}$	matrix-inclusion problem-related strain concentration tensor of the pore phase
$\mathbb{A}_{\theta\phi}$	fourth-order strain concentration tensor of solid needle phase with orientation (θ, ϕ)
$\mathbb{A}_{\theta\phi}^{\infty}$	matrix-inclusion problem-related strain concentration tensor of the solid needle phase oriented in direction (θ, ϕ)
c_{solid}	cohesion of solid phases
$\mathbb{C}_0$	stiffness tensor of matrix in matrix-inclusion problem
$\mathbb{C}_{HA}$	stiffness tensor of hydroxyapatite
$\mathbb{C}_{hom}$	homogenized stiffness tensor (of porous polycrystal)
$\mathbb{C}_{pore}$	stiffness tensor of pore phase
$\mathbb{C}_{solid}$	stiffness tensor of solid needle phases
d	characteristic length of the inhomogeneities within the RVE
$\mathbb{D}_{ij}$	fourth-order influence tensor linking eigenstrains in integration point j to total strains in integration point i
$\mathbb{D}_{pore,\Theta\Phi}$	fourth-order influence tensor linking eigenstrains in (Θ, Φ)-oriented solid needle phase to total strains in the pore phase
$\mathbb{D}_{\theta\phi,\Theta\Phi}$	fourth-order influence tensor linking eigenstrains in (Θ, Φ)-oriented solid needle phase to total strains in (θ, ϕ)-oriented solid needle phase
$\mathbb{D}_{pore,j}$	fourth-order influence tensor linking eigenstrains in phase j to total strains in pore phase
$\mathbf{E}$	macroscopic strain tensor
$\mathbf{E}^n, \mathbf{E}^{n+1}$	macroscopic strain tensor at load steps n and $(n+1)$, respectively
$\Delta\mathbf{E}^{n+1}$	$(n+1)$-st macroscopic strain increment
$\mathbf{E}_0$	homogeneous strains at the infinite boundary of the matrix-inclusion problem
$\mathbf{E}_0^{\pi}$	strain-like quantity according to (3.33)
$\mathbf{E}^p$	macroscopic plastic strain tensor
$\mathbf{E}^{p,n}, \mathbf{E}^{p,n+1}$	macroscopic plastic strains at load steps n and $(n+1)$, respectively
$\mathbf{e}_1, \mathbf{e}_2, \mathbf{e}_3$	unit base vectors of Cartesian reference base frame
$\mathbf{e}_\theta, \mathbf{e}_\phi, \mathbf{e}_r$	unit base vectors of spherical base frame attached to the solid needle phase
f_{HA}	volume fraction of hydroxyapatite
f_{pore}	volume fraction of (intercrystalline) pore space; i.e. (intercrystalline) porosity
f_{vas}	volume fraction of vascular pores; i.e. vascular porosity

$\mathscr{F}^{(\alpha)}$	α-th yield function of the multisurface yield criterion
$\mathscr{F}_i^{(\alpha),n+1,trial}$	trial state in phase i at load step $(n+1)$, of yield function $\mathscr{F}^{(\alpha)}$
$\mathscr{G}^{(\alpha)}$	plastic flow potential related to activity of the α-th yield function in multisurface yield criterion
i, j	indices numbering integration points chosen for evaluation of integrals over the unit sphere (the latter representing the set of all spatial orientations of solid needle-shaped phases)
$\mathbb{I}$	fourth-order identity tensor
$\mathbb{I}^{dev}$	deviatoric part of $\mathbb{I}$
$\mathbb{I}^{vol}$	volumetric part of $\mathbb{I}$
k_{HA}	bulk modulus of hydroxyapatite
k_{H_2O}	bulk modulus of water
l	characteristic length of the RVE
$l_{\theta\phi}$	length of all needle-shaped crystals oriented in (θ, ϕ)-direction
$\mathscr{L}$	characteristic structural length
$\mathbf{n}$	unit normal vector at microscopic scale
$N_{cyl,plast}$	number of plasticizing needle-shaped (cylindrical) solid phases
$N_{Fact,i}$	number of active yield surfaces in (plasticizing) solid needle phase i
$N_{Fact,max}$	maximum number of potentially active yield surfaces per solid needle phase
p_{I-II}, p_{I-III}	planes defining regions in stress space representations of Mohr-Coulomb criterion
$\mathbb{P}_{cyl}$	Hill (or morphology) tensor of cylindrical inclusion embedded in matrix with stiffness $\mathbb{C}_{hom}$
$\mathbb{P}_{sph}$	Hill (or morphology) tensor of spherical inclusion embedded in matrix with stiffness $\mathbb{C}_{hom}$
RVE	Representative Volume Element
$\mathbf{R}^{n+1,k+1,l}$	residual vector in Newton iteration scheme, related to load step $(n+1)$, to the $(k+1)$-st macro-micro transition, and to return mapping iteration l

$\mathcal{S}$	set of Gaussian points over the unit sphere
$\mathcal{S}_{cyl,plast}$	set of plasticizing needle-shaped (cylindrical) solid phases
t^n, t^{n+1}	time instants at load steps n and $(n+1)$, respectively
$\mathbf{t}$	vector orthogonal to $\mathbf{n}$, within the Mohr plane spanned by $\mathbf{n}$ and $\mathbf{T}$
$\mathbf{T}$	(microscopic) traction vector
V_{pore}	volume of pore phase
V_{RVE}	volume of the RVE
∂V_{RVE}	surface of the RVE
W^{ext}	work of external forces acting on the RVE
W^{int}	work of internal forces acting within the RVE
$\mathbf{x}$	position vector inside the RVE
β	ratio between uniaxial tensile strength and shear strength of hydroxyapatite
δ	Kronecker delta
$\boldsymbol{\varepsilon}$	microscopic strain
$\boldsymbol{\varepsilon}_i$	average microscopic strain in phase i
$\boldsymbol{\varepsilon}_i^n, \boldsymbol{\varepsilon}_i^{n+1}$	average microscopic strains in phase i, at load steps n and $(n+1)$, respectively
$\boldsymbol{\varepsilon}_i^p$	average microscopic plastic strains in phase i
$\Delta\boldsymbol{\varepsilon}_i^{p,n+1}$	$(n+1)$-st increment of microscopic plastic strain tensor of phase i
$\boldsymbol{\varepsilon}_{pore}$	average pore strains
$\boldsymbol{\varepsilon}_{pore}^n, \boldsymbol{\varepsilon}_{pore}^{n+1}$	average pore strains at load steps n and $(n+1)$, respectively
$\boldsymbol{\varepsilon}_{\theta\phi}$	average microscopic strains in solid needle phase with orientation (θ, ϕ)
$\boldsymbol{\varepsilon}_{\theta\phi}^p$	average plastic strains in solid needle phase with orientation (θ, ϕ)
θ	spherical (co-latitudinal) coordinate
$\dot{\lambda}_{\theta\phi}^{(\alpha)}$	plastic multiplier related to the α-th yield surface associated to the solid needle phase oriented in (θ, ϕ)-direction
$\Delta\boldsymbol{\lambda}^{n+1,k+1,l}$	plastic multiplier vector in Newton iteration scheme, related to load step $(n+1)$, to the $(k+1)$-st macro-micro transition, and to return mapping iteration l
$\Delta(\Delta\boldsymbol{\lambda})^{n+1,k+1,l}$	plastic multiplier vector update in Newton iteration scheme, related to load step $(n+1)$, to the $(k+1)$-st macro-micro transition, and to return mapping iteration l
$\Delta\lambda_i^{(\alpha),n+1}$	$(n+1)$-st increment of plastic multiplier related to the α-th yield surface associated to phase i
μ_{HA}	shear modulus of hydroxyapatite
$\boldsymbol{\xi}$	microscopic displacement field
$\boldsymbol{\pi}_{\theta\phi}$	eigenstress of solid needle phase oriented in (θ, ϕ)-direction
$\boldsymbol{\Pi}^0$	eigenstress acting in the infinite matrix of the matrix-inclusion problem

ρ_{excel}	extracellular bone tissue mass density
ρ_{exvas}	extravascular bone tissue mass density
ρ_{macro}	macroscopic mass density
ϕ	spherical (longitudinal) coordinate
φ_{solid}	angle of internal friction
$\sigma_{i,j}$	ordered principal stresses of phase i, $j = I, II, III$
$\sigma_{y,HA}$	compressive yield strength of hydroxyapatite
$\boldsymbol{\sigma}$	microscopic stress
$\boldsymbol{\sigma}_i$	average stress in phase i
$\boldsymbol{\sigma}_i^n, \boldsymbol{\sigma}_i^{n+1}$	average stress in phase i at load steps n and $(n+1)$, respectively
$\Delta\boldsymbol{\sigma}_i^{n+1}$	$(n+1)$-st microscopic stress increment of phase i
$\boldsymbol{\sigma}_i^{n+1,trial}$	trial stress in phase i, at load step $(n+1)$
$\tilde{\boldsymbol{\sigma}}_i^{n+1}$	average stress in phase i, at load step $(n+1)$, as defined in (3.81)
$\sigma_{nn} = \sigma$	normal component of traction vector
$\sigma_{nt} = \tau$	shear component of traction vector
$\boldsymbol{\sigma}_{pore}$	average pore stress
$\boldsymbol{\sigma}_{\theta\phi}$	average stress in solid needle phase with orientation (θ, ϕ)
$\boldsymbol{\Sigma}$	macroscopic stress tensor
$\boldsymbol{\Sigma}^n, \boldsymbol{\Sigma}^{n+1}$	macroscopic stress tensor at load steps n and $(n+1)$, respectively
$\Delta\boldsymbol{\Sigma}^{n+1}$	$(n+1)$-st macroscopic stress increment
ω_i	Gaussian weight
∇^s	symmetric gradient operator
$\langle(.)\rangle$	spatial average of quantity (.), over the RVE
div	divergence operator
$(.)^T$	transpose of tensorial quantity (.)
$(.)^{-1}$	inverse of tensorial quantity (.)
$\otimes$	dyadic product
$\dot{(.)}$	rate (temporal derivative) of quantity (.)

Chapter 4

Frictionally sliding micro-interfaces as source of kinematic hardening plasticity: a continuum micromechanics approach

Authored by: Viktoria Vass, Claire Morin, Vikas Tomar, and Christian Hellmich

In preparation for submission to: *European Journal of Mechanics A-Solids*

Contribution: Christian Hellmich set up the overall research strategy (motivated by molecular dynamics studies of Vikas Tomar), supervised the research progress, and checked the key results. Viktoria Vass implemented the Matlab code, ran computations, and documented the results. Claire Morin supported Viktoria Vass during model implementation, code verification, and documentation of research results. All authors contributed to the discussion processes and helped proof reading the paper.

Abstract

Plasticity is standardly considered to arise from dislocation processes at the microscale. We here propose a corresponding continuum micromechanics model, where 2D frictional interfaces which slide as soon as a traction threshold is reached, are embedded in a 3D purely elastic matrix. Therefore, we combine concentration-influence relations linking the macroscopic strains to the interface tractions and the interface dislocations, with flow rule-type evolution laws for the latter quantities. In combination with the classical stress average rule and Hill's lemma (principle of virtual power), this results in a macroscopic material behavior showing features of kinematic hardening plasticity. However, a thermodynamic analysis shows that the strain and the hardening variables (i.e. the interface dislocations) are energetically coupled so that the classical decoupling hypothesis for the frozen energy does not hold. The ideal frictional behavior assigned to the interfaces can be motivated from recent molecular dynamics simulations.

4.1 Introduction

Some ten years ago, a new variant of the self-consistent method [Fritsch et al., 2006], namely one involving one spherical pore phase and infinitely many non-spherical solid phases oriented in all space directions, allowed for gaining new grounds concerning the application range of continuum micromechanics. These applications concern poroelasticity and strength upscaling of porous polycrystals, such as hydroxyapatite [Fritsch et al., 2009b, 2010b], gypsum [Sanahuja et al., 2010], or a variety of alumina, circonia, and silica-based ceramics [Fritsch et al., 2010b]. Based on concepts which are often referred to as transformation field analysis [Dvorak and Benveniste, 1992, Pichler and Hellmich, 2010], these formulations have been recently extended to full elastoplasticity. With a Mohr-Coulomb criterion applied to the solid phases, the corresponding return map algorithms allowed for predicting the sliding failure of the cement line in push-out tests performed on osteonal bone [Morin et al., 2017]. Such a Mohr-Coulomb criterion somehow naturally accounts for sliding process *within* the solid phases (a modeling approach which repeatedly turned out as valuable concerning hydroxyapatite strength in bone [Fritsch et al., 2009c, Tai et al., 2008]). On the other hand, the Mohr-Coulomb criterion does not further resolve the internal sliding processes.

The latter have probably to do with “ice-like-fluid”-filled interfaces, as studied in the framework of molecular dynamics studies of bone mineral [Bhowmik et al., 2007, 2009, Devendra and Tomar, 2009, Qu et al., 2015a, Zahn and Hochrein, 2003], and also in terms of continuum creep deformations they may cause [Qu et al., 2015b, Shahidi et al., 2014, 2016a,b,c]. Deepening this discussion on interface-to-bulk upscaling of inelastic properties, the present contribution focuses on the transition of frictional sliding at the interface scale, to elastoplasticity at the scale of a representative volume element consisting of an elastic solid phase and fluid-filled interfaces (with comparatively negligible volume fractions).

The paper is organized as follows: first, the continuum micromechanics of materials with a matrix-interface type morphology is introduced within a Representative Volume Element (RVE), and material phases are defined: (i) a solid elastic matrix, with (ii) parallel interfaces as 2D objects hosting eventually the “ice-like” fluid layers embedded into the elastic solid matrix. Homogeneous macroscopic strains are prescribed at the boundary of the RVE, and eigentractions are prescribed “inside” the interfaces. These tractions enter the frictional laws, which, thanks to the knowledge of concentration and influence tensors derived from the limit cases of infinitely thin oblate spheroids [Eshelby, 1957, Pichler and Hellmich, 2010, Shahidi et al., 2014], are then upscaled to the homogenized behavior of the RVE. The latter is of the kinematic hardening type, which is explicitly confirmed by a dissipation analysis.

4.2 Separation of scales, stress and strain average rules

In continuum micromechanics [Hashin, 1983, Hill, 1963, Zaoui, 1997, 2002], the material is considered as the macro homogeneous, but micro heterogeneous matter filling a Representative Volume Element (RVE) with volume V_{RVE}, which satisfies the standard separation-of-scales requirement [Drugan and Willis, 1996, Huet, 1990]: the material volume (with characteristic size ℓ) needs to be much smaller than the structure built up by this material (with characteristic size $\mathscr{L}$), and much larger than the inhomogeneities within the material (with characteristic size $\mathscr{d}$)

$$\mathscr{d} \ll \ell \ll \mathscr{L} \tag{4.1}$$

Thereby, the first inequality sign in Eq. (4.1) refers to a factor of 2-3 [Drugan and Willis, 1996], while the second one refers to a factor of 5-50 [Kohlhauser and Hellmich, 2013]. Due to the complexity of the microstructure within one RVE, we do not resolve each and every detail within the material volume, but introduce quasi-homogeneous subdomains, called material phases, with known physical quantities.

We here consider a homogeneous material containing frictional interfaces: the RVE, as depicted on Figure 4.1, consists of one solid matrix phase labelled by index m, and one interface phase representing $\mathcal{N}$ interfaces of identical size and shape; i.e. with a circular cross section of radius a, aligned normal to $\underline{e}_z$. The inter-

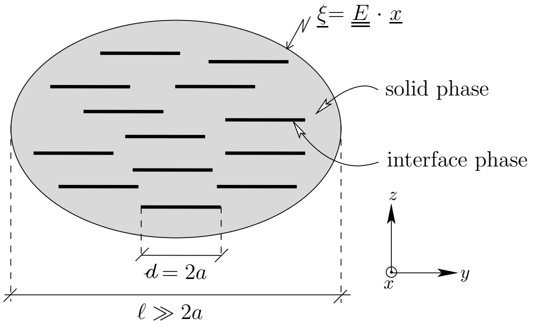

Figure 4.1: RVE of an isotropic solid matrix hosting $\mathcal{N}$ flat, parallel interfaces of identical shape and size, represented as one interface phase

face phase is charaterized by an interface density d, which according to Budiansky and O'Connell [1976] reads as

$$d = \frac{\mathcal{N} a}{V_{RVE}} \tag{4.2}$$

At its boundary S_{RVE}, the RVE is subjected to homogeneous linearized macroscopic strains [Hashin, 1983], prescribed in terms of displacements

$$\underline{\xi}\left(\underline{x}\right) = \underline{\underline{E}} \cdot \underline{x} \qquad \forall \underline{x} \in S_{RVE} \tag{4.3}$$

with $\underline{x}$ as the location vector labeling points within the RVE and on its boundary; and to internal dislocations, quantified in terms of displacement jumps

$$\underline{\xi}^{+}\left(\underline{x}\right) - \underline{\xi}^{-}\left(\underline{x}\right) = \left[\underline{\xi}\right]\left(\underline{x}\right) \qquad \underline{x} \in A_{\delta} \tag{4.4}$$

which are recorded whenever crossing points belonging to the interface phase, the entity of these points making up the total interface domain, which is of two-dimensional nature, with area $A_\delta = \mathcal{N} \times a^2\pi$. The two-dimensional nature of the interface phase implies vanishing of its volume, so that the solid matrix fills the entire volume of the composite, hence $V_{RVE} = V_m$. Boundary conditions of the format (4.3) together with a displacement field comprising discontinuities, imply a strain average rule of the following format [Dormieux et al., 2007, Fritsch and Hellmich, 2007, Hashin, 1983, Shahidi et al., 2016a]

$$\underline{\underline{E}} = \frac{1}{V_{RVE}} \int_{V_{RVE}} \underline{\underline{\varepsilon}}(\underline{x}) dV + \int_{A_\delta} [\underline{\xi}](\underline{x}) \overset{s}{\otimes} \underline{n}(\underline{x}) dS \tag{4.5}$$

where $\underline{n}(\underline{x})$ stands for the unit normal vector at position $\underline{x}$. The RVE is subjected to traction forces at its boundary

$$\begin{aligned} &\underline{T}(\underline{x}) = \underline{\underline{\sigma}}(\underline{x}) \cdot \underline{n}(\underline{x}) && \forall \underline{x} \in S_{RVE},\ \underline{x} \in A_\delta \\ &\text{div } \underline{\underline{\sigma}}(\underline{x}) = 0 && \forall \underline{x} \in V_{RVE} \end{aligned} \tag{4.6}$$

The external power performed by these traction forces is

$$\begin{aligned} P^{ext} &= \int_{S_{RVE}} \underline{T}(\underline{x}) \cdot \underline{\dot{\xi}}(\underline{x})\, dS \\ &= \int_{S_{RVE}} \left(\underline{\underline{\dot{E}}} \cdot \underline{x}\right) \cdot \left(\underline{\underline{\sigma}}(\underline{x}) \cdot \underline{n}(\underline{x})\right)\, dS \\ &= \underline{\underline{\dot{E}}} : \int_{V_{RVE}} \underline{\underline{\sigma}}(\underline{x})\, dV \end{aligned} \tag{4.7}$$

Hence, the force quantity performing power on the macroscopic strain rates $\underline{\underline{\dot{E}}}$ is the volume integral over the microscopic stress. This integral is independent of microscopic position, and of dimension "stress times volume". This induces the existence of the macroscopic stress in the form

$$\underline{\underline{\Sigma}} = \frac{1}{V_{RVE}} \int_{V_{RVE}} \underline{\underline{\sigma}}(\underline{x})\, dV, \tag{4.8}$$

On the other hand, the power of external forces acting on the elastic matrix only comprises an additional term which considers the interface traction forces performing power on the internal surfaces of the RVE,

$$P^{ext,m} = \underline{\underline{\Sigma}} : \underline{\underline{\dot{E}}} - \int_{A_\delta} \underline{T}(\underline{x}) \cdot \underline{\dot{\xi}}(\underline{x})\, dS \tag{4.9}$$

The power expression for the interface phase in Eq. (4.9) can be derived from considering the interface phase as the limit case of an infinitely thin eigenstressed inclusion phase [Pichler and Hellmich, 2010, Shahidi et al., 2014, 2016b]

$$\int_{A_\delta} \underline{T}(\underline{x}) \cdot \dot{\underline{\xi}}(\underline{x})\, dS = \frac{2\pi d}{a} \underline{T}_\delta \, [\underline{\xi}]_\delta \tag{4.10}$$

with $\underline{T}_\delta$ as the traction vector related to the inclusion stresses

$$\underline{T}_\delta = \underline{\underline{\sigma}}_{inc} \cdot \underline{e}_z \tag{4.11}$$

and interface phase-specific dislocation $[\underline{\xi}]_\delta$ stemming from averaging over each of the spherical interfaces

$$[\underline{\xi}]_\delta = \frac{1}{a\pi} \int_0^a [\underline{\xi}](r)\, 2\pi\, r\, dr \tag{4.12}$$

with the radial coordinate r measuring the radial distance from the center of each of the interfaces which altogether make up the interface phase.

Finally, the mechanical state of the matrix phase is characterized by its averages of microstress and microstrain, in the following form:

$$\underline{\underline{\sigma}}_m = \frac{1}{V_{RVE}} \int_{V_{RVE}} \underline{\underline{\sigma}}\,(\underline{x})\, dx \tag{4.13}$$

$$\underline{\underline{\varepsilon}}_m = \frac{1}{V_{RVE}} \int_{V_{RVE}} \underline{\underline{\varepsilon}}\,(\underline{x})\ dV \tag{4.14}$$

From Eqs. (4.13) and (4.8), it follows that

$$\underline{\underline{\sigma}}_m = \underline{\underline{\Sigma}} \tag{4.15}$$

4.3 Behavior of material phases: linear elastic matrix and frictionally sliding interfaces

We consider a linear elastic matrix fulfilling

$$\underline{\underline{\sigma}}_m = \underline{\underline{\underline{\underline{C}}}}_m : \underline{\underline{\varepsilon}}_m \tag{4.16}$$

with $\underline{\underline{\underline{\underline{C}}}}_m$ as the isotropic fourth-order stiffness tensor of the matrix phase

$$\underline{\underline{\underline{\underline{C}}}}_m = 3k_m \underline{\underline{\underline{\underline{I}}}}_{vol} + 2\mu_m \underline{\underline{\underline{\underline{I}}}}_{dev} \tag{4.17}$$

where $\underline{\underline{\underline{I}}}_{vol} = \frac{1}{3}\underline{\underline{1}} \otimes \underline{\underline{1}}$ and $\underline{\underline{\underline{I}}}_{dev} = \underline{\underline{\underline{I}}} - \underline{\underline{\underline{I}}}_{vol}$, respectively, denote the volumetric and deviatoric part of the symmetric fourth-order identity tensor $\underline{\underline{\underline{I}}}$, with components $I_{ijkl} = 1/2\,(\delta_{ik}\delta_{jl} + \delta_{il}\delta_{kj})$, and with δ_{ij} denoting the Kronecker delta being equal to 1 if $i = j$ and 0 otherwise, and $\underline{\underline{1}}$ as a second-order identity tensor. In (4.17), k_m and μ_m denote the bulk modulus and the shear modulus of the matrix phase, respectively.

The open literature on the continuum micromechanics of so-called frictional cracks [Barthélémy et al., 2003, Zhu et al., 2008], and molecular dynamics simulations of lubricating fluid-filled interfaces [Tao et al., 2015], see Appendix for further details, motivate us to characterize the interfaces by a perfectly frictional behavior, which is mathematically described through relations between the components of the interfacial displacement jumps $[\underline{\xi}]_\delta$ quantifying the displacement jumps across the interfaces, and the interfacial traction vectors $\underline{T}_\delta$ acting on the interface planes; as follows:

- The interfaces do not "open"; this is also referred to as "glueing condition", and implies
$$[\xi]_{\delta,z} = 0 \tag{4.18}$$
- As for the in-plane behavior, the tangential components of the displacement jumps are of exclusively frictional nature; which can be expressed by a formulation resembling a plastic flow rule;
$$[\dot{\xi}]_{\delta,\alpha} = \begin{cases} 0, & \text{if } \mathscr{F}(\underline{T}_\delta) \leq 0, \\ \dot{\lambda}_\delta \frac{\partial \mathscr{F}}{\partial T_{\delta,\alpha}}, & \text{if } \mathscr{F}(\underline{T}_\delta) = 0 \text{ and } \dot{\mathscr{F}}(\underline{T}_\delta) \geq 0; \text{ with } \alpha \in \{x, y\} \end{cases} \tag{4.19}$$
with a frictional (plastic) multiplier $\dot{\lambda}_\delta$, and with $\mathscr{F}(\underline{T}_\delta)$ as Mohr-Coulomb-type yield criterion, governing the initiation and the propagation of plasticity
$$\mathscr{F}(\underline{T}_\delta) = |\tau_\delta| + \sigma_\delta \tan\phi - c \leq 0 \tag{4.20}$$
with $\tau_\delta = \underline{T}_\delta \cdot \underline{t}$ and $\sigma_\delta = \underline{T}_\delta \cdot \underline{n}$ as the norm of the shear and normal components of the traction vector, respectively, ϕ as the friction angle, and c as the cohesion.
The sliding activity is then governed by the so-called Melan-Kuhn-Tucker

conditions [Melan, 1938, Ortiz and Popov, 1985], and the consistency condition restricted to the interface plane; altogether reading as

$$\dot{\lambda}_\delta \geq 0\,, \quad \mathscr{F}(\underline{T}_\delta) \leq 0\,, \quad \dot{\lambda}_\delta \times \mathscr{F}(\underline{T}_\delta) = 0\,, \quad \text{and} \quad \dot{\lambda}_\delta \times \dot{\mathscr{F}}(\underline{T}_\delta) = 0 \tag{4.21}$$

4.4 Scale transition: concentration-influence relations

For an RVE with kinematics and equilibrium conditions as given in Section 4.2, and with a linear elastic matrix according to Eq. (4.16) and (4.17), the mean displacement jumps across interfaces, defined through Eq. (4.12), are related to the macroscopic strains and the interface tractions according to the so-called concentration-influence relations [Dvorak and Benveniste, 1992]. The latter read for the investigated material system as [Shahidi et al., 2014]

$$[\underline{\xi}]_\delta = \underline{\underline{\underline{A}}}_\delta : \underline{\underline{E}} + \underline{\underline{D}}_{\delta\delta} \cdot \underline{T}_\delta \tag{4.22}$$

whereby $\underline{\underline{\underline{A}}}_\delta$ denotes the third-order strain concentration tensor describing the influence of macroscopic strain on the average displacement jump encountered when crossing any portion of the interface phase; and $\underline{\underline{D}}_{\delta\delta}$ stands for the second-order influence tensor describing the influence of interfacial eigentraction on the average displacement jump of the interface phase, see the Appendix for the components of these tensors. In addition, the strains in solid matrix can be related to the macroscopic strains and the traction forces, by adapting the case of pore pressures as described in Fritsch et al. [2013b], to that of interface tractions,

$$\underline{\underline{\varepsilon}}_m = \underline{\underline{\underline{\underline{A}}}}_m : \underline{\underline{E}} + \underline{\underline{\underline{D}}}_{m\delta} \cdot \underline{T}_\delta \tag{4.23}$$

Combination of (4.23) with elasticity law (4.16) and stress average (4.13) yields

$$\underline{\underline{\Sigma}} = \underline{\underline{\underline{\underline{C}}}}_{hom} : \underline{\underline{E}} + \underline{\underline{\underline{B}}}_\delta \cdot \underline{T}_\delta \tag{4.24}$$

with

$$\underline{\underline{\underline{\underline{C}}}}_{hom} = \underline{\underline{\underline{\underline{C}}}}_m : \underline{\underline{\underline{\underline{A}}}}_m = \underline{\underline{\underline{\underline{C}}}}_m : \left[\underline{\underline{\underline{\underline{I}}}} + \frac{4\pi d}{3}\underline{\underline{\underline{\underline{T}}}}_\delta\right] \tag{4.25}$$

as the homogenized stiffness tensor, d as the interface density, and $\underline{\underline{\underline{B}}}_\delta = \underline{\underline{\underline{C}}}_m : \underline{\underline{\underline{D}}}_{m\delta}$ as the Biot-type tensor relating interface tractions to overall macroscopic stresses, see the Appendix for the components of $\underline{\underline{\underline{T}}}_\delta$ (4-th order tensor) and $\underline{\underline{\underline{B}}}_\delta$.

4.5 Analytical solution of the problem

4.5.1 Elastic domain

In the elastic domain, interface displacement jumps have not yet occurred,

$$[\xi]_{\delta,\alpha} = 0 \qquad \text{with } \alpha = (x, y) \tag{4.26}$$

and also their rate remains zero. Traction forces $\underline{T}_\delta$ are fully transmitted over the not yet recognizable interfaces, and accordingly, only the elastic matrix intervenes in the overall material behavior; a macroscopic stress provokes a macroscopic strain via

$$\underline{\underline{E}} = \underline{\underline{\underline{C}}}_m^{-1} : \underline{\underline{\Sigma}} \tag{4.27}$$

As the interfacial traction forces $\underline{T}_\delta$ are the governing factors for eventual sliding processes under increasing macroscopic stress, it is convenient to express the former as functions of the latter. For this purpose, influence relation (4.22) is specified for vanishing displacement jumps, and is then used in order to express the interface traction vector as a function of the macroscopic strains, which, in combination with (4.27), yields

$$\underline{T}_\delta = \underline{\underline{D}}_{\delta\delta}^{-1} : \underline{\underline{\underline{A}}}_\delta : \underline{\underline{\underline{C}}}_m^{-1} : \underline{\underline{\Sigma}} \tag{4.28}$$

According to Eq. (4.28), the non-zero components of interface tractions $\underline{T}_\delta$ in a base frame $\underline{e}_x$, $\underline{e}_y$, $\underline{e}_z$, which is aligned with the interface phase, see Figure 4.1, read as

$$\begin{aligned}
T_{\delta,x} &= D_{xx}^{-1} A_{xxz} (C_m^{-1})_{xzxz} \Sigma_{xz} \\
T_{\delta,y} &= D_{yy}^{-1} A_{yyz} (C_m^{-1})_{yzyz} \Sigma_{yz} \\
T_{\delta,z} &= D_{zz}^{-1} \sum_j \sum_k A_{zjj} \left(C_m^{-1}\right)_{jjkk} \Sigma_{kk} \quad \text{with} \quad j,k = \{x,y,z\}
\end{aligned} \tag{4.29}$$

Insertion of (4.29) into the yield criterion (4.20) gives access to the elastic domain in terms of the macroscopic stress components

$$\sqrt{\sum_j \left(D_{jj}^{-1} A_{jjz} \, (C_m^{-1})_{jzjz} \, \Sigma_{jz}\right)^2} + \tan\phi \, D_{zz}^{-1} \sum_k \sum_l A_{zkk} \left(C_m^{-1}\right)_{kkll} \Sigma_{ll} - c \leq 0 \tag{4.30}$$

Re-formulation of (4.30) towards

$$\frac{\Sigma_{xz}^2}{\left(\frac{c - \tan\phi \, D_{zz}^{-1} \sum_k \sum_l A_{zkk}\left(C_m^{-1}\right)_{kkll} \Sigma_{ll}}{D_{xx}^{-1} A_{xxz} (C_m^{-1})_{xzxz}}\right)^2} + \frac{\Sigma_{yz}^2}{\left(\frac{c - \tan\phi \, D_{zz}^{-1} \sum_k \sum_l A_{zkk}\left(C_m^{-1}\right)_{kkll} \Sigma_{ll}}{D_{yy}^{-1} A_{yyz} (C_m^{-1})_{yzyz}}\right)^2} = 1$$
$$\text{with } j = \{x, y\}, \; k, l = \{x, y, z\} \tag{4.31}$$

evidences that the elastic domain exhibits the shape of an ellipse in the Σ_{xz}- Σ_{yz} plane, with its center at the point ($\Sigma_{xz} = 0; \Sigma_{yz} = 0$) and with semi-axes measuring

$$\left(c - \tan\phi \, D_{zz}^{-1} \sum_k \sum_l A_{zkk} \left(C_m^{-1}\right)_{kkll} \Sigma_{ll}\right) / \left(D_{jj}^{-1} A_{jjz} \, (C_m^{-1})_{jzjz} \, \Sigma_{jz}\right) \tag{4.32}$$

whereby j is a semi-axis-specific index, $j = \{x, y\}$. Specification of the elastic domain in the format (4.30) for pure shear loading in the interface plane yields

$$\sqrt{\sum_j \left(D_{jj}^{-1} A_{jjz} \, (C_m^{-1})_{jzjz} \, \Sigma_{jz}\right)^2} - c \leq 0 \qquad \text{with} \qquad j = \{x, y\} \tag{4.33}$$

The re-formulation

$$\frac{\Sigma_{xz}^2}{\left(\frac{c}{D_{xx}^{-1} A_{xxz} (C_m^{-1})_{xzxz}}\right)^2} + \frac{\Sigma_{yz}^2}{\left(\frac{c}{D_{yy}^{-1} A_{yyz} (C_m^{-1})_{yzyz}}\right)^2} = 1 \tag{4.34}$$

indicates an ellipse in the Σ_{xz}- Σ_{yz} plane, with semi-axes measuring

$$(c) \, / \, \left(D_{jj}^{-1} A_{jjz} \, (C_m^{-1})_{jzjz} \, \Sigma_{jz}\right) \tag{4.35}$$

whereby j is a semi-axis-specific index, $j = \{x, y\}$.

4.5.2 Elasto-plastic domain

Beyond the yield limit, dissipative interfacial sliding events occur according to Eq. (4.19)-(4.21), quantified in terms of non-zero dislocation vector components $[\xi]_{\delta,\alpha}$, $\alpha = \{x, y\}$, i.e. in terms of dislocation vectors of the form

$$[\underline{\xi}]_\delta = [\xi]_{\delta,x}\underline{e}_x + [\xi]_{\delta,y}\underline{e}_y \tag{4.36}$$

The latter call for an extension of macro-to-micro relation (4.28); namely through solving Eq. (4.24) for the macroscopic strains $\underline{\underline{E}}$, and inserting the result into concentration-influence relation Eq. (4.22), finally yielding

$$\underline{T}_\delta = \underline{\underline{\Delta}}_{\delta\delta}^{-1} \cdot \left\{ \underline{\underline{\underline{A}}}_\delta : \underline{\underline{\underline{\underline{C}}}}_{hom}^{-1} : \underline{\underline{\Sigma}} - [\underline{\xi}]_\delta \right\} = \underline{\underline{\underline{\Gamma}}}_\delta : \underline{\underline{\Sigma}} - \underline{\underline{\Delta}}_{\delta\delta}^{-1} \cdot [\underline{\xi}]_\delta \tag{4.37}$$

with $\underline{\underline{\Delta}}_{\delta\delta}$ as a stress influence-like second order diagonal tensor defined as

$$\underline{\underline{\Delta}}_{\delta\delta} = \underline{\underline{\underline{A}}}_\delta : \underline{\underline{\underline{\underline{C}}}}_{hom}^{-1} : \underline{\underline{\underline{B}}}_\delta - \underline{\underline{D}}_{\delta\delta} \tag{4.38}$$

and $\underline{\underline{\underline{\Gamma}}}_\delta$ being a stress concentration-like third-order tensor defined as

$$\underline{\underline{\underline{\Gamma}}}_\delta = \underline{\underline{\Delta}}_{\delta\delta}^{-1} \cdot \underline{\underline{\underline{A}}}_\delta : \underline{\underline{\underline{\underline{C}}}}_{hom}^{-1} \tag{4.39}$$

with $\Gamma_{jkz} \neq 0$ if $j = k; j, k = \{x, y, z\}$.

Due to the non-zero components of the tensors $\underline{\underline{\underline{\Gamma}}}_\delta$ and $\underline{\underline{\Delta}}_{\delta\delta}$, it follows from Eq. (4.37) that the in-plane components of the traction vector depend on the corresponding shear components of the macroscopic stress tensor and those of the displacement jump, while the out-of-plane component of the traction vector is a function of all three normal components of the macroscopic stress tensor; mathematically, this reads as

$$\begin{aligned}
T_{\delta,x} =& \Delta_{xx}^{-1} A_{xxz} (C_{hom}^{-1})_{xzxz} \Sigma_{xz} - \Delta_{xx}^{-1} [\xi]_{\delta,x} \\
T_{\delta,y} =& \Delta_{yy}^{-1} A_{yyz} (C_{hom}^{-1})_{yzyz} \Sigma_{yz} - \Delta_{yy}^{-1} [\xi]_{\delta,y} \\
T_{\delta,z} =& \Delta_{zz}^{-1} \sum_j \sum_k A_{zjj} \left(C_{hom}^{-1}\right)_{jjkk} \Sigma_{kk} \text{ with } j, k = \{x, y, z\}
\end{aligned} \tag{4.40}$$

In the plastic regime, the traction forces as given in (4.40) also need to fulfill the yield criterion (4.20), reading for $\underline{t} = \underline{e}_y$ as

$$\mathscr{F}(\underline{T}_\delta) = 0 \qquad \rightarrow \qquad |T_{\delta,y}| = c - T_{\delta,z} \tan\phi \tag{4.41}$$

In case of pure shear loading in the y-z-plane, the load dependency relation (4.40) implies that only the corresponding in-plane component of the traction vector differs from zero, $T_{\delta,y} \neq 0$, while $T_{\delta,x} = T_{\delta,z} = 0$. As a consequence, the Mohr-Coulomb-type criterion (4.41) degenerates into a Tresca-type yield criterion giving access to the unknown in-plane component $T_{\delta,y}$ as

$$|T_{\delta,y}| = c \tag{4.42}$$

Eq. (4.42) implies that once the plastic zone is reached, additional load increments have no further effect on the in-plane component of the traction vector: it remains constant, $\dot{\underline{T}}_\delta = 0$, i.e. $\partial \underline{T}_\delta / \partial \underline{\underline{E}} = 0$ in case of strain-driven loading.
However, in case of combined loading, the changes in the traction vector components are directly related to each other, as seen in Eq. (4.41): in order to fulfill the yield condition, an increase in the normal component has to be compensated by a decrease in the in-plane component, requiring the following restriction $c - T_{\delta,z} \tan\phi \geq 0$. Having the traction vector in hand, allows for computing the corresponding displacement jump

$$[\underline{\xi}]_\delta = \underline{\underline{\underline{A}}}_\delta : \underline{\underline{\underline{\underline{C}}}}_{hom}^{-1} : \underline{\underline{\Sigma}} - \underline{\underline{\Delta}}_{\delta\delta} \cdot \underline{T}_\delta \tag{4.43}$$

which in pure shear evolves in the following fashion

$$\Delta[\underline{\xi}]_\delta = \underline{\underline{\underline{A}}}_\delta : \underline{\underline{\underline{\underline{C}}}}_{hom}^{-1} : \Delta\underline{\underline{\Sigma}} \tag{4.44}$$

see Figure 4.2.

Plastic slope in pure shear Considering that the traction vector remains constant in the plastic range, i.e. $\Delta\underline{T}_\delta = 0$, together with the homogenized constitutive relation (4.24), the relation between the macroscopic stress and strain increments reads as follows

$$\Delta\Sigma_{ij} = C_{hom,ijij}\, \Delta E_{ij} \tag{4.45}$$

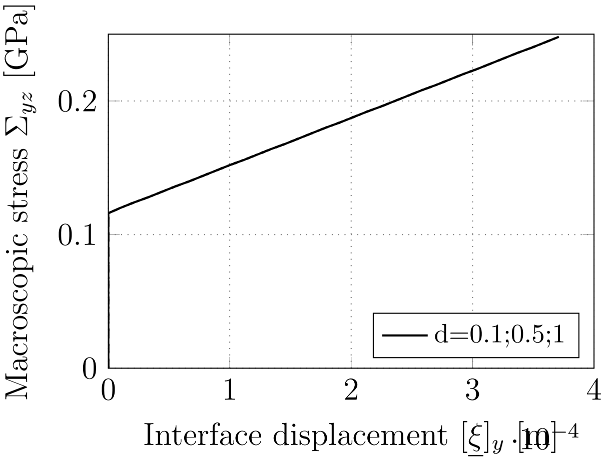

Figure 4.2: Macroscopic stress-interface displacement relation under pure shear, in dependency of the interface density d; for an elastic matrix with Young's modulus of $E_m = 114\,\text{GPa}$ and Poisson's ratio of $\nu_m = 0.27$; relating to hydroxyapatite [Gilmore and Katz, 1982, Katz and Ukraincik, 1971]

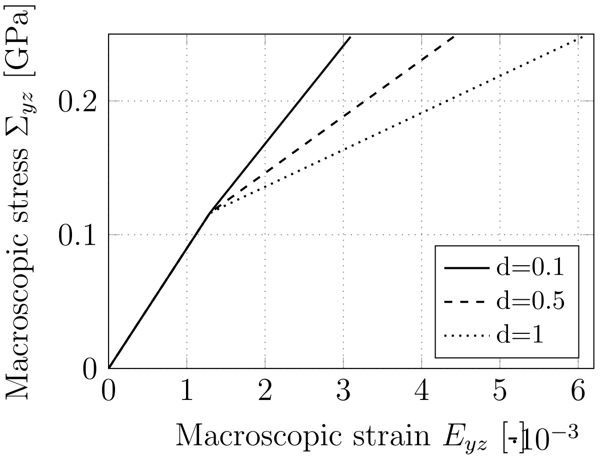

Figure 4.3: Macroscopic stress-strain relation under pure shear, in dependency of the interface density d; for an elastic matrix with Young's modulus of $E_m = 114\,\text{GPa}$ and Poisson's ratio of $\nu_m = 0.27$; relating to hydroxyapatite [Gilmore and Katz, 1982, Katz and Ukraincik, 1971]

for $\{ij\} = \{yz, xz, xy\}$ so that the homogenized stiffness components play the role of an “elastoplastic” modulus $\mathscr{H}$ appearing in the macroscopic stress-strain relations, see Figures 4.3 and 4.4. It should be noted that this modulus is different from the hardening modulus, which will be introduced in Section 4.6.

Plastic slope in case of combined loading Given interfaces with normals pointing in $\underline{e}_z$-direction, the RVE is susceptible to plastic behavior when subjected to shear aligned with the interface orientation, i.e. if shear is applied in the $\underline{e}_x$-$\underline{e}_z$

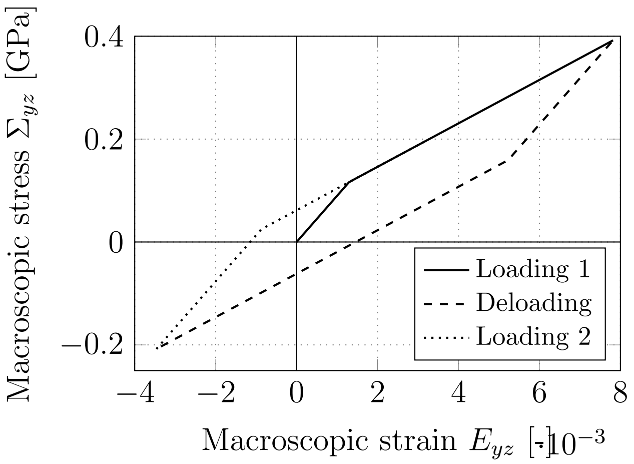

Figure 4.4: Macroscopic stress-strain relation under pure shear showing kinematic hardening, for an interface density of $d = 0.5$, and an elastic matrix with Young's modulus of $E_m = 114\,\text{GPa}$ and Poisson's ratio of $\nu_m = 0.27$; relating to hydroxyapatite [Gilmore and Katz, 1982, Katz and Ukraincik, 1971]

and/or in the $\underline{e}_y$-$\underline{e}_z$-plane; arbitrarily combined with tension and/or compression in any direction. For the sake of simplicity here we restrict the macroscopic loading to one of the shear components, Σ_{yz}, but with all normal components. Glueing condition (4.18), combined with solving the general concentration-influence relation Eq. (4.22) with respect to the macroscopic strain, yields the normal interface traction vector component as

$$T_{\delta,z} = -D_{zz}^{-1} \sum_j A_{zjj} E_{jj} \quad \text{with} \quad j = \{x, y, z\} \tag{4.46}$$

Insertion of (4.46) into (4.41) yields, for $\underline{t} = \underline{e}_y$

$$|T_{\delta,y}| = c + \tan\phi D_{zz}^{-1} \sum_j A_{zjj} E_{jj} \quad \text{with} \quad j = \{x, y, z\} \tag{4.47}$$

while $T_{\delta,x} = 0$ due to the load dependency relation (4.40). Insertion of the traction vector components into Eq. (4.24) yields the following relationship for the components of the macroscopic stress, as functions of the macroscopic strain components, with $T_{\delta,x} = 0$, $T_{\delta,y}$ according to (4.47), $T_{\delta,z}$ according to (4.46); reading in Kelvin-Mandel notation as

$$\left\{\begin{matrix} \Sigma_{xx} \\ \Sigma_{yy} \\ \Sigma_{zz} \\ \sqrt{2}\Sigma_{yz} \\ 0 \\ 0 \end{matrix}\right\} = \mathscr{M} \cdot \left\{\begin{matrix} E_{xx} \\ E_{yy} \\ E_{zz} \\ \sqrt{2}E_{yz} \\ 0 \\ 0 \end{matrix}\right\} + \left\{\begin{matrix} 0 \\ 0 \\ 0 \\ \sqrt{2}c \cdot B_{yzy} \\ 0 \\ 0 \end{matrix}\right\} \tag{4.48}$$

whereby the 6 × 6 matrix representation of $\mathscr{M}$ read as

$$\left\{\begin{matrix} C_{hom,xxxx} - B_{xxz}D_{zz}^{-1}A_{zxx} & C_{hom,xxyy} - B_{xxz}D_{zz}^{-1}A_{zyy} & C_{hom,xxzz} - B_{xxz}D_{zz}^{-1}A_{zzz} & 0 & 0 & 0 \\ C_{hom,yyxx} - B_{yyz}D_{zz}^{-1}A_{zxx} & C_{hom,yyyy} - B_{yyz}D_{zz}^{-1}A_{zyy} & C_{hom,yyzz} - B_{yyz}D_{zz}^{-1}A_{zzz} & 0 & 0 & 0 \\ C_{hom,zzxx} - B_{zzz}D_{zz}^{-1}A_{zxx} & C_{hom,zzyy} - B_{zzz}D_{zz}^{-1}A_{zyy} & C_{hom,zzzz} - B_{zzz}D_{zz}^{-1}A_{zzz} & 0 & 0 & 0 \\ \sqrt{2}B_{yzy}\tan\phi D_{zz}^{-1}A_{zxx} & \sqrt{2}B_{yzy}\tan\phi D_{zz}^{-1}A_{zyy} & \sqrt{2}B_{yzy}\tan\phi D_{zz}^{-1}A_{zzz} & \sqrt{2}C_{hom,yzyz} & 0 & 0 \\ 0 & 0 & 0 & 0 & 0 & 0 \\ 0 & 0 & 0 & 0 & 0 & 0 \end{matrix}\right\} \tag{4.49}$$

Yield surface Due to the non-zero components of the third-order tensor $\underset{\equiv\delta}{\Gamma}$ and the second-order tensor $\underset{=\delta\delta}{\Delta}$, the components of the traction vector read as

$$\begin{aligned} T_{\delta,x} &= \Gamma_{xxz}\Sigma_{xz} - \Delta_{xx}^{-1}[\xi]_{\delta,x} \\ T_{\delta,y} &= \Gamma_{yyz}\Sigma_{yz} - \Delta_{yy}^{-1}[\xi]_{\delta,y} \\ T_{\delta,z} &= \sum_j \Gamma_{zjj}\Sigma_{jj} \qquad\qquad \text{with} \quad j = \{x, y, z\} \end{aligned} \tag{4.50}$$

Having that in hand, the yield surface can be given as

$$\sqrt{\left\{\Gamma_{xxz}\Sigma_{xz} - \Delta_{xx}^{-1}[\xi]_{\delta,x}\right\}^2 + \left\{\Gamma_{yyz}\Sigma_{yz} - \Delta_{yy}^{-1}[\xi]_{\delta,y}\right\}^2} = c - \tan\phi \sum_j \Gamma_{zjj}\Sigma_{jj} \tag{4.51}$$

(4.51) has the format of a yield criterion with linear kinematic hardening, i.e. in the $(\Sigma_{xz}, \Sigma_{yz})$-plane an ellipse with half-axes measuring

$$\left(c - \tan\phi \sum_j \Gamma_{zjj}\Sigma_{jj}\right) / \left(\Gamma_{kkz}\right) \qquad \text{with } j = \{x, y, z\},\ k = \{x, y\} \tag{4.52}$$

is moving as the components of its center point $\left(\Delta_{xx}^{-1}[\xi]_{\delta,x}; \Delta_{yy}^{-1}[\xi]_{\delta,y}\right)$, evolve with the sliding dislocation vector.

In case of pure shear loading, the out-of-plane traction vector component vanishes, such that the yield surface is given by

$$\sqrt{\left\{\Gamma_{xxz}\Sigma_{xz} - \Delta_{xx}^{-1}[\xi]_{\delta,x}\right\}^2 + \left\{\Gamma_{yyz}\Sigma_{yz} - \Delta_{yy}^{-1}[\xi]_{\delta,y}\right\}^2} = c \tag{4.53}$$

4.6 Discussion, from a thermodynamics viewpoint

As the developments of the last subsection evidenced similarities of the upscaled macroscopic yield surfaces with the notion of kinematic hardening plasticity, it is interesting to check whether the upscaled macroscopic equations fall into the respective thermodynamic framework [Coleman and Noll, 1963, Coussy, 1995, 2004, Halphen and Nguyen, 1975, Mandel, 1973]. This check comprises the derivation of a free energy function related to our frictional sliding system: In fact, the entire work done on the elastic matrix is converted into free energy, as this matrix is purely elastic. Mathematically, this reads as

$$\dot{\psi} = P^{ext,m} = \underline{\underline{\Sigma}} : \dot{\underline{\underline{E}}} - \frac{2\pi d}{a}\underline{T}_\delta \cdot [\dot{\underline{\xi}}]_\delta \tag{4.54}$$

Insertion of this expression into the Clausius-Duhem equation yields the dissipation as

$$\mathscr{D} = \underline{\underline{\Sigma}} : \dot{\underline{\underline{E}}} - \dot{\psi} = \frac{2\pi d}{a}\underline{T}_\delta \cdot [\dot{\underline{\xi}}]_\delta \geq 0 \tag{4.55}$$

From (4.55), it follows that the elastic energy depends on the macroscopic strains and on the interface dislocation vector,

$$\psi = \psi\left(\underline{\underline{E}}, [\underline{\xi}]_\delta\right) \tag{4.56}$$

Use of (4.56) in (4.55) yield the state equations

$$\underline{\underline{\Sigma}} = \frac{\partial\psi}{\partial\underline{\underline{E}}} \qquad \text{and} \qquad \underline{T}_\delta = -\frac{\partial\psi}{\partial[\underline{\xi}]_\delta} \tag{4.57}$$

Corresponding explicit expressions follow from solving Eq. (4.22) for $\underline{T}_\delta$, yielding

$$\underline{T}_\delta = -\underline{\underline{D}}_{\delta\delta}^{-1} \cdot \underline{\underline{\underline{A}}}_\delta : \underline{\underline{E}} + \underline{\underline{D}}_{\delta\delta}^{-1} \cdot [\underline{\xi}]_\delta \tag{4.58}$$

and from inserting (4.58) into Eq. (4.24) yielding

$$\underline{\underline{\Sigma}} = \left(\underline{\underline{\underline{\underline{C}}}}_{hom} - \underline{\underline{\underline{B}}}_{\delta} \cdot \underline{\underline{D}}_{\delta\delta}^{-1} \cdot \underline{\underline{\underline{A}}}_{\delta}\right) : \underline{\underline{E}} + \underline{\underline{\underline{B}}}_{\delta} \cdot \underline{\underline{D}}_{\delta\delta}^{-1} \cdot [\underline{\xi}]_{\delta} \tag{4.59}$$

Hence, at complete macroscopic unloading after the occurrence of plastic events, $\underline{\underline{E}} = 0$, we observe a so-called frozen energy of the form

$$\psi\left(\underline{\underline{E}} = 0, [\underline{\xi}]\right) = U\left([\underline{\xi}]\right) = \frac{1}{2}[\underline{\xi}]_{\delta} \cdot \underline{\underline{D}}_{\delta\delta}^{-1} \cdot [\underline{\xi}]_{\delta} \tag{4.60}$$

However, this frozen energy is not fully decoupled from the rest of the free energy (as often assumed in hardening plasticity), as the effects of $\underline{\underline{E}}$ and $[\underline{\xi}]$, on ψ, are coupled, see Eq. (4.57), (4.58), and (4.59)

$$\psi \neq \hat{\psi}(\underline{\underline{E}}) + U\left([\underline{\xi}]\right) \tag{4.61}$$

4.7 Appendix A: Extension to multiple interface families

4.7.1 Elastic domain

When dealing with N interface phases, differing in size and in interface density, i.e. characterized by interface radii a_i and interface densities d_i, the concentration-influence relation (4.22) and the homogenized macroscopic relation (4.24) take the following format

$$[\underline{\xi}]^{i} = \underline{\underline{\underline{A}}}^{i} : \underline{\underline{E}} + \sum_{j=1}^{N} \underline{\underline{D}}^{ij} \cdot \underline{T}^{j} \tag{4.62}$$

$$\underline{\underline{\Sigma}} = \underline{\underline{\underline{\underline{C}}}}_{hom} : \underline{\underline{E}} + \sum_{i=1}^{N} \underline{\underline{\underline{B}}}^{i} \cdot \underline{T}^{i} \tag{4.63}$$

In the elastic case, the solution is derived based on Eq. (4.28), with $\underline{T}$ is now an assembly of N, 3×1 traction vectors belonging to the interface families i, $\underline{\underline{\underline{B}}}$ becomes a $6 \times 3N$ matrix, and $\underline{\underline{D}}$ takes the form of a $3N \times 3N$ matrix; $i = 1 \ldots N$.

The components of the traction vector for interface family i read as

$$\begin{aligned}
T_x^i &= \left(\sum_{j=1}^{N} D_{xx}^{-1,ij} A_{xxz}^j\right)(C_m^{-1})_{xzxz}\Sigma_{xz}\\
T_y^i &= \left(\sum_{j=1}^{N} D_{yy}^{-1,ij} A_{yyz}^j\right)(C_m^{-1})_{yzyz}\Sigma_{yz}\\
T_z^i &= \sum_l \left\{\sum_k \left[\sum_{j=1}^{N} D_{zz}^{-1,ij} A_{zkk}^j\right](C_m^{-1})_{kkll}\right\}\Sigma_{ll}\\
&\text{with } l,k=\{x,y,z\}
\end{aligned}\tag{4.64}$$

Insertion of (4.64) into the yield criterion (4.20) gives access to the elastic domain in terms of the macroscopic stress components

$$\begin{aligned}
&\sqrt{\left[\left(\sum_{j=1}^{N} D_{xx}^{-1,ij} A_{xxz}^j\right)(C_m^{-1})_{xzxz}\Sigma_{xz}\right]^2+\left[\left(\sum_{j=1}^{N} D_{yy}^{-1,ij} A_{yyz}^j\right)(C_m^{-1})_{yzyz}\Sigma_{yz}\right]^2}+\\
&+\tan\phi\sum_l\left\{\sum_k\left[\sum_{j=1}^{N} D_{zz}^{-1,ij} A_{zkk}^j\right](C_m^{-1})_{kkll}\right\}\Sigma_{ll}-c\le 0
\end{aligned}\tag{4.65}$$

Re-formulation of (4.65) towards

$$\begin{aligned}
&\frac{\Sigma_{xz}^2}{\frac{c-\tan\phi\sum_l\left\{\sum_k\left[\sum_{j=1}^{N} D_{zz}^{-1,ij} A_{zkk}^j\right](C_m^{-1})_{kkll}\right\}\Sigma_{ll}}{\left(\sum_{j=1}^{N} D_{xx}^{-1,ij} A_{xxz}^j\right)(C_m^{-1})_{xzxz}}}+\\
&+\frac{\Sigma_{yz}^2}{\frac{c-\tan\phi\sum_l\left\{\sum_k\left[\sum_{j=1}^{N} D_{zz}^{-1,ij} A_{zkk}^j\right](C_m^{-1})_{kkll}\right\}\Sigma_{ll}}{\left(\sum_{j=1}^{N} D_{yy}^{-1,ij} A_{yyz}^j\right)(C_m^{-1})_{yzyz}}}=1
\end{aligned}\tag{4.66}$$

evidences that the elastic domain exhibits the shape of an ellipse in the Σ_{xz}-Σ_{yz} plane, with its center at the point $(\Sigma_{xz}=0;\Sigma_{yz}=0)$ and with semi-axes measuring

$$\frac{c-\tan\phi\sum_l\left\{\sum_k\left[\sum_{j=1}^{N} D_{zz}^{-1,ij} A_{zkk}^j\right](C_m^{-1})_{kkll}\right\}\Sigma_{ll}}{\left(\sum_{j=1}^{N} D_{xx}^{-1,ij} A_{xxz}^j\right)(C_m^{-1})_{xzxz}}\tag{4.67}$$

and

$$\frac{c-\tan\phi\sum_l\left\{\sum_k\left[\sum_{j=1}^{N} D_{zz}^{-1,ij} A_{zkk}^j\right](C_m^{-1})_{kkll}\right\}\Sigma_{ll}}{\left(\sum_{j=1}^{N} D_{yy}^{-1,ij} A_{yyz}^j\right)(C_m^{-1})_{yzyz}}\tag{4.68}$$

Specification of the elastic domain in the format (4.65) for pure shear loading in the interface plane yields

$$\sqrt{\left[\left(\sum_{j=1}^{N} D_{xx}^{-1,ij} A_{xxz}^{j}\right)(C_m^{-1})_{xzxz}\Sigma_{xz}\right]^2+\left[\left(\sum_{j=1}^{N} D_{yy}^{-1,ij} A_{yyz}^{j}\right)(C_m^{-1})_{yzyz}\Sigma_{yz}\right]^2}-c\leq 0 \tag{4.69}$$

The re-formulation

$$\frac{\Sigma_{xz}^2}{\frac{c}{\left(\sum_{j=1}^{N} D_{xx}^{-1,ij} A_{xxz}^{j}\right)(C_m^{-1})_{xzxz}}}+\frac{\Sigma_{yz}^2}{\frac{c}{\left(\sum_{j=1}^{N} D_{yy}^{-1,ij} A_{yyz}^{j}\right)(C_m^{-1})_{yzyz}}}=1 \tag{4.70}$$

indicates an ellipse in the Σ_{xz}-Σ_{yz} plane, with semi-axes measuring

$$\frac{c}{\left(\sum_{j=1}^{N} D_{xx}^{-1,ij} A_{xxz}^{j}\right)(C_m^{-1})_{xzxz}} \tag{4.71}$$

and

$$\frac{c}{\left(\sum_{j=1}^{N} D_{yy}^{-1,ij} A_{yyz}^{j}\right)(C_m^{-1})_{yzyz}} \tag{4.72}$$

4.7.2 Elasto-plastic domain

In the elasto-plastic domain, the out-of-plane component of the traction vector of interface family i can be determined from the glueing condition (4.18), and mathematically reads as

$$\begin{aligned} T_z^i &= \sum_l \left\{\sum_k \left[\sum_{j=1}^{N} \Delta_{zz}^{-1,ij} A_{zkk}^{j}\right](C_{hom}^{-1})_{kkll}\right\}\Sigma_{ll} \\ &\text{with } l,k=\{x,y,z\} \end{aligned} \tag{4.73}$$

which gives access to the non-zero in-plane traction vector component when inserted into the yield condition (4.20)

$$T_y^i = c-\tan\phi\sum_l \left\{\sum_k \left[\sum_{j=1}^{N} \Delta_{zz}^{-1,ij} A_{zkk}^{j}\right](C_{hom}^{-1})_{kkll}\right\}\Sigma_{ll} \tag{4.74}$$

whereby the $\underline{\underline{\Delta}}$ tensor, as defined in (4.38), has now the format of a $3N \times 3N$ matrix made up of 3×3 diagonal submatrices $\underline{\underline{\Delta}}^{ij}$ with components

$$\begin{aligned}
&\Delta^{ij}_{xx} = A^i_{xxz}(C^{-1}_{hom})_{xzxz}B^j_{xzx} - D^{ij}_{xx} \\
&\Delta^{ij}_{yy} = A^i_{yyz}(C^{-1}_{hom})_{yzyz}B^j_{yzy} - D^{ij}_{yy} \\
&\Delta^{ij}_{zz} = \sum_l \left(\sum_k A^i_{zkk}(C^{-1}_{hom})_{kkll} \right) B^j_{llz} - D^{ij}_{zz} \\
&\text{with } i,j = 1 \dots N;\ \ l,k = \{x,y,z\}
\end{aligned} \tag{4.75}$$

Extension of Eq. (4.43) for multiple interface families yields the displacement jump of interface family i as

$$[\underline{\xi}]^i = \underline{\underline{\underline{A}}}^i : \underline{\underline{\underline{\underline{C}}}}^{-1}_{hom} : \underline{\underline{\Sigma}} - \sum_{j=1}^{N} \underline{\underline{\Delta}}^{ij} \cdot \underline{T}^j \tag{4.76}$$

and its evolution in pure shear as follows

$$\Delta[\underline{\xi}]^i = \underline{\underline{\underline{A}}}^i : \underline{\underline{\underline{\underline{C}}}}^{-1}_{hom} : \Delta\underline{\underline{\Sigma}} \tag{4.77}$$

Yield surface In analogy with Eq. (4.50), the components of the traction vector for family i read as

$$\begin{aligned}
&T^i_x = \Gamma^i_{xxz}\Sigma_{xz} - \sum_{j=1}^{N} \Delta^{-1,ij}_{xx}[\xi]^j_x \\
&T^i_y = \Gamma^i_{yyz}\Sigma_{yz} - \sum_{j=1}^{N} \Delta^{-1,ij}_{yy}[\xi]^j_y \\
&T^i_z = \sum_k \Gamma^i_{zkk}\Sigma_{kk} \\
&\text{with } k = \{x,y,z\}
\end{aligned} \tag{4.78}$$

Insertion of (4.78) into the yield criterion (4.20) yields the yield surface as

$$\begin{aligned}
&\sqrt{\left\{ \Gamma^i_{xxz}\Sigma_{xz} - \sum_{j=1}^{N} \Delta^{-1,ij}_{xx}[\xi]^j_x \right\}^2 + \left\{ \Gamma^i_{yyz}\Sigma_{yz} - \sum_{j=1}^{N} \Delta^{-1,ij}_{yy}[\xi]^j_y \right\}^2} = \dots \\
&\dots = c - \tan\phi \sum_k \Gamma_{zkk}\Sigma_{kk}
\end{aligned} \tag{4.79}$$

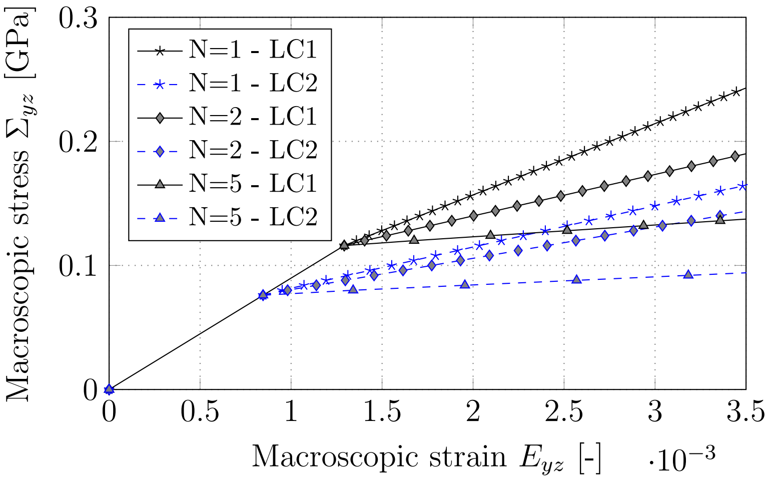

Figure 4.5: Macroscopic stress-strain relation in dependency of the number of interfaces N, under pure shear loading (LC1), and under combined shear and tension (LC2), for interface densities $d_1 = 0.25$, $d_2 = 0.5$, $d_3 = 0.75$, $d_4 = 1$, $d_5 = 1.25$

(4.79) has the format of a yield criterion with linear kinematic hardening, i.e. in the $(\Sigma_{xz}, \Sigma_{yz})$-plane an ellipse with half-axes measuring

$$\left(c - \tan\phi \sum_k \Gamma_{zkk}\Sigma_{kk}\right) / \left(\Gamma^i_{llz}\right) \qquad \text{with } k = \{x, y, z\},\ l = \{x, y\} \tag{4.80}$$

is moving as the components of its center point $\left(\sum_{j=1}^N \Delta_{xx}^{-1,ij}[\xi]^j_x ; \sum_{j=1}^N \Delta_{yy}^{-1,ij}[\xi]^j_y\right)$, evolve with the sliding dislocation vector. In case of pure shear loading, the out-of-plane traction vector component vanishes, such that the yield surface is given by

$$\sqrt{\left\{\Gamma^i_{xxz}\Sigma_{xz} - \sum_{j=1}^N \Delta_{xx}^{-1,ij}[\xi]^j_x\right\}^2 + \left\{\Gamma^i_{yyz}\Sigma_{yz} - \sum_{j=1}^N \Delta_{yy}^{-1,ij}[\xi]^j_y\right\}^2} = c \tag{4.81}$$

Concluding remarks As evidenced in Figure 4.5, the number of interface phases plays a significant role in the macroscopic material behavior. With increasing amount of interface phases the overall material behavior tends towards perfect plasticity.

4.8 Appendix B: Molecular dynamics simulations

Qu et. al quantified the interface stress in hydroxyapatite-water-hydroxyapatite (HAP-WT-HAP) supercells using a combination of classical non-equilibrium molecular dynamics (NEMD) simulations with steered molecular dynamics (SMD) simulations. NEMD is used to reveal interface stress as a function of applied strain based on the virial stress formulation, while SMD is used to understand interface separation mechanism and to calculate interfacial shear stress based on a viscoplastic interfacial sliding model.

Crystal geometry The crystallographic form of HAP is hexagonal with space group $P2_1/b$. The unit cell dimensions are $a = 9,4214\,\text{Å}$, $b = 2a$, $c = 6,8814\,\text{Å}$, $\alpha = 90°$, $\beta = 90°$, $\gamma = 120°$ with 88 atoms. One HAP supercell consists of 40 unit cells.

Methods A NAMD package is used to perform both NEMD and SMD simulations. Water molecules are added to the interface region using 'SOLVATE' module in the visual molecular dynamics (VMD) software. An inorganic force field for HAP is used to model atomistic interactions. The particle mesh Ewald method is used to calculate electrostatic interactions with a cut off of 12 Å. The simulations are performed with periodic boundary conditions.

In SMD simulations, external force is applied to selected atom or atoms. SMD simulations were performed in constant speed mode: the upper HAP crystals were pulled with velocity 0.4 Å/ps from the substrate HAP crystals. The force was applied to the center of mass of the upper HAP crystals in two loading directions: (i) along the molecule length, (ii) transverse to the molecule length. Water molecules in the interface region remained unconstraint, i.e. free to move. The force in constant velocity SMD is calculated as

$$F = k(vt - x) \tag{4.82}$$

where k is the virtual spring constant taken as $100\,\text{kcal/mol/Å}^2$ acting between pulled atoms and the virtual point, t is the time and x is the displacement. The interfacial sliding process can be described in four stages (see Figure 4.6)

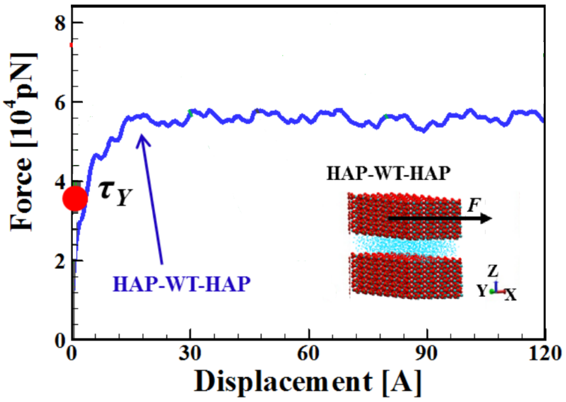

Figure 4.6: SMD force as a function of displacement

- During $t < t_{sliding}$, there is no sliding, the interfacial shear stress is monotonously increasing,
- At $t = t_{sliding}$, the yield stress τ_Y is reached initiating slipping,
- During $t_{sliding} < t < t_{transition}$, the shear stress converges to a constant value,
- During $t > t_{transition}$, a steady state sliding process is obtained.

It is remarkable that the initial "elastic" region in Figure 4.6 reflects a "Young's modulus" of around 100 GPa, which is close to the elastic modulus of hydroxyapatite alone, i.e. 120 GPa [Ching et al., 2009]. This is a strong motivation to study systems where the elasticity is fully ascribed to an extended solid phase, while the dissipative processes are fully ascribed to liquid-crystal-type interfaces. This is exactly the focus of the present paper.

4.9 Appendix: Derivation of homogenized stiffness tensor, of interface morphology tensor, as well as of the concentration and influence tensors

The quantification of concentration and influence tensors requires an additional mathematical step for the case of flat interfaces [Shahidi et al., 2014]; inspired by the strategy for "sharp cracks" presented by Pensée et al. [2002]: In order to derive the aforementioned concentration and influence tensors, we consider the slits as limit cases of oblate spheroids with aspect ratio ω, for which analytical solutions are available. The tensors are derived from their generally defined fourth-order counterparts [Zaoui, 2002] through the transition from oblate spheroids to flat interfaces ($\lim \omega \to 0$), and by taking the non-vanishing tensor components into account [Shahidi et al., 2014]. The third-order concentration tensor, describing the influence of macroscopic strain $\underline{\underline{E}}$ on the average displacement jumps $[\underline{\xi}]_\delta$, is defined as

$$\underline{\underline{\underline{A}}}_{\delta} = \lim_{\omega \to 0} \omega \underline{\underline{\underline{\underline{A}}}}_{\delta} = \lim_{\omega \to 0} \omega \left\{ \underline{\underline{\underline{\underline{A}}}}^{\infty}_{\delta} : \left[f_m \underline{\underline{\underline{\underline{I}}}} + f_\delta \underline{\underline{\underline{\underline{A}}}}^{\infty}_{\delta} \right] \right\} \tag{4.83}$$

with components

$$\begin{aligned} A_{\delta,xxz} &= A_{\delta,yyz} = \frac{8(1-\nu_m)a}{\pi[3(2-\nu_m)+16d(1-\nu_m)]} \\ A_{\delta,zxx} &= A_{\delta,zyy} = \frac{16\nu_m(1-\nu_m)a}{\pi[3(1-2\nu_m)+16d(1-\nu_m)^2]} \\ A_{\delta,zzz} &= \frac{16\nu_m(1-\nu_m)^2 a}{\pi\nu_m[3(1-2\nu_m)+16d(1-\nu_m)^2]} \end{aligned} \tag{4.84}$$

Analogously, the second-order influence tensor is defined as

$$\underline{\underline{D}}_{\delta\delta} = \lim_{\omega \to 0} \omega \underline{\underline{\underline{\underline{D}}}}_{\delta\delta} = \lim_{\omega \to 0} \omega \left\{ f_m \underline{\underline{\underline{\underline{A}}}}_{m} : \underline{\underline{\underline{\underline{A}}}}^{\infty}_{\delta} : \underline{\underline{\underline{\underline{P}}}}_{\delta} \right\} \tag{4.85}$$

with its components reading as

$$\begin{aligned} D_{\delta\delta,xx} &= D_{\delta\delta,yy} = -\frac{16(1-\nu_m^2)a}{E_m\pi[3(2-\nu_m)+16d(1-\nu_m)]} \\ D_{\delta\delta,zz} &= -\frac{16\nu_m(1-\nu_m)^2(1-2\nu_m)a}{E_m\pi[3(1-2\nu_m)+16d(1-\nu_m)^2]} \end{aligned} \tag{4.86}$$

with $\underline{\underline{\underline{\underline{P}}}}_i$ as the fourth-order Hill-tensor of an oblate spheroid [Hill, 1963], and $\underline{\underline{\underline{\underline{A}}}}_\delta^\infty$ as the fourth-order strain concentration of oblate inclusion phase in an Eshelby-type matrix-inclusion problem [Eshelby, 1957]

$$\underline{\underline{\underline{\underline{A}}}}_\delta^\infty = \left[\underline{\underline{\underline{\underline{I}}}} - \underline{\underline{\underline{\underline{P}}}}_\delta : \underline{\underline{\underline{\underline{C}}}}_m\right]^{-1} \tag{4.87}$$

In the macroscopic state equation (4.24), $\underline{\underline{\underline{B}}}_\delta$ denotes the third-order influence tensor describing the influence of interfacial eigentractions on the macroscopic stress,

$$\underline{\underline{\underline{B}}}_\delta = \lim_{\omega\to 0}\left[\frac{4\pi d}{3}\omega \underline{\underline{\underline{A}}}_\delta^t\right] \tag{4.88}$$

with its components reading as

$$\begin{aligned}
B_{\delta,zxx} = B_{\delta,zyy} &= \frac{16d(1-\nu_m)}{3(2-\nu_m)+16d(1-\nu_m)}\\
B_{\delta,xxz} = B_{\delta,yyz} &= \frac{16d\nu_m(1-\nu_m)}{3(1-2\nu_m)+16d(1-\nu_m)^2}\\
B_{\delta,zzz} &= \frac{16d(1-\nu_m)^2}{3(1-2\nu_m)+16d(1-\nu_m)^2}
\end{aligned} \tag{4.89}$$

and $\underline{\underline{\underline{\underline{C}}}}_{hom}$ denotes the homogenized stiffness tensor in a form

$$\underline{\underline{\underline{\underline{C}}}}_{hom} = \underline{\underline{\underline{\underline{C}}}}_m : \left[\underline{\underline{\underline{\underline{I}}}} + \frac{4\pi d}{3}\underline{\underline{\underline{\underline{T}}}}_\delta\right]^{-1} \tag{4.90}$$

with d as the interface density parameter, and $\underline{\underline{\underline{\underline{T}}}}_\delta$ as the fourth-order morphology tensor for interfaces

$$\underline{\underline{\underline{\underline{T}}}}_\delta = \lim_{\omega\to 0}\omega \underline{\underline{\underline{\underline{A}}}}_\delta^\infty \tag{4.91}$$

with its components reading as

$$\begin{aligned}
T_{\delta,xzxz} = T_{\delta,zxxz} = T_{\delta,xzzx} = T_{\delta,zxzx} &= \frac{2(1-\nu_m)}{\pi(2-\nu_m)}\\
T_{\delta,yzyz} = T_{\delta,zyyz} = T_{\delta,yzzy} = T_{\delta,zyzy} &= \frac{2(1-\nu_m)}{\pi(2-\nu_m)}\\
T_{\delta,zzxx} = T_{\delta,zzyy} &= \frac{4\nu_m(1-\nu_m)}{\pi(1-2\nu_m)}\\
T_{\delta,zzzz} &= \frac{4(1-\nu_m)^2}{\pi(1-2\nu_m)}
\end{aligned} \tag{4.92}$$

4.10 Nomenclature

A_δ	union of all interface surface domains
$\underline{\underline{\underline{A}}}_\delta$	third-order strain concentration tensor of interface phase i describing the influence of macroscopic strain on the average displacement jump of flat interfaces
$\underline{\underline{\underline{A}}}^\infty_\delta$	dilute strain concentration tensor in the matrix-inclusion problem
a	interface radius
a_i	interface radius of interfaces making up interface phase i
$\underline{\underline{\underline{B}}}_\delta$	third-order strain Biot tensor of interface phase δ describing the influence of interfacial eigentractions of flat interfaces on the macroscopic stress
$\underline{\underline{\underline{\underline{C}}}}_{hom}$	homogenized fourth-order stiffness tensor
$\underline{\underline{\underline{\underline{C}}}}_m$	fourth-order stiffness tensor of solid matrix phase
c	cohesion factor
$\underline{\underline{D}}_{\delta\delta}$	second-order influence tensor of phase δ
$\mathscr{D}$	dissipation
đ	characteristic size of the inhomogeneities within the RVE
d	interface density parameter
d_i	interface density of interface phase i
div	divergence operator
$\underline{\underline{E}}$	second-order macroscopic strain tensor
$\underline{\underline{\dot{E}}}$	rate of the second-order macroscopic strain tensor
$\mathscr{E}$	elastic slope tensor
$\underline{e}_x, \underline{e}_y, \underline{e}_z$	unit base vectors of Cartesian reference base frame
$\mathscr{F}$	Mohr-Coulomb yield criterion
f_δ	volume fraction of interface phase δ
f_m	volume fraction of solid matrix phase
$\mathscr{H}$	elastoplastic modulus
$\underline{\underline{\underline{\underline{I}}}}$	fourth-order identity tensor
$\underline{\underline{\underline{\underline{I}}}}_{dev}$	deviatoric part of the fourth-order identity tensor
$\underline{\underline{\underline{\underline{I}}}}_{vol}$	volumetric part of the fourth-order identity tensor
k_m	bulk modulus of solid matrix phase
$\mathscr{L}$	characteristic length of the structure or the loading of the structure
ℓ	characteristic length of the RVE
$\mathscr{M}$	matrix relating the macroscopic stresses to macroscopic strains as given in Eq. (48)
m	matrix phase
$\mathscr{N}$	number of interfaces in interface phase
N	number of interface phases within the RVE
$\underline{n}$	unit normal vector

$\underline{\underline{\underline{\underline{P}}}}_{\delta}$	Hill tensor of phase δ
P^{ext}	external power
$P^{ext,m}$	external power performed on interal surfaces
S_{RVE}	boundary of the RVE
$\underline{T}$	surface traction vector
$\underline{T}_{\delta}$	eigentraction vector of interface phase δ
$\underline{\underline{\underline{\underline{T}}}}_{\delta}$	fourth-order morphology tensor for flat inclusions
U	energy term accounting for hardening
V_m	volume of solid matrix phase
V_{RVE}	volume of the RVE
$\underline{x}$	position vector inside the RVE

$\underline{\underline{\underline{\Gamma}}}_{\delta}$	third order tensor as given in Eq. (39)
$\underline{\underline{\Delta}}_{\delta\delta}$	second-order tensor as given in Eq. (38)
$\Delta\underline{\underline{E}}$	increment of macroscopic strain tensor
$\Delta\underline{\underline{\Sigma}}$	increment of macroscopic stress tensor
$\Delta[\underline{\xi}]_{\delta}$	increment of average displacement jump of interface phase δ
δ	interface phase
$\underline{\underline{\varepsilon}}$	microscopic strain field
$\underline{\underline{\varepsilon}}_{m}$	average microscopic strain field in solid matrix phase
λ_{δ}	plastic multiplier of interface phase δ
μ_m	shear modulus of solid matrix phase
$\underline{\xi}$	microscopic displacement field
$[\underline{\xi}]$	interface dislocation vector
$[\underline{\xi}]_{\delta}$	average displacement jump of interface phase δ
$[\dot{\underline{\xi}}]_{\delta}$	rate of average displacement jump of interface phase δ
$\underline{\underline{\Sigma}}$	second-order macroscopic stress tensor
$\underline{\underline{\sigma}}$	microscopic stress field
$\underline{\underline{\sigma}}_{inc}$	microscopic inclusion stress
$\underline{\underline{\sigma}}_{m}$	average microscopic stress in solid matrix phase
σ_{δ}	normal component of the traction vector acting on interface phase δ
τ_{δ}	shear component of the traction vector acting on interface phase δ
ϕ	friction angle
ψ	free Helmholtz energy
$\dot{\psi}$	rate of free Helmholtz energy
ω	aspect ratio

Chapter 5

Coupling multiscale X-ray physics and micromechanics for bone tissue composition and elasticity determination from micro-CT data, by example of femora from OVX and sham rats

Authored by: Patricia Hasslinger, Viktoria Vass, Alexander Dejaco, Romane Blanchard, Gissur Örlygsson, Paolo Gargiulo, and Christian Hellmich

Published in: *International Journal for Computational Methods in Engineering Science and Mechanics*, 17(3), p. 222-244, http://dx.doi.org/10.1080/15502287.2016.1145762, 2016

Contribution: This paper results from a collaboration among the Institute for Mechanics of Materials and Structures of TU Wien, the Department of Materials, Biotechnology and Energy of the Innovation Center Iceland, the Institute of Biomedical and Neural Engineering of Reykjavík University, and the Department of Science of Landspítali University Hospital, Iceland. Christian Hellmich set up the overall research strategy, supervised the research progress, and checked the key results. Gissur Örlygsson and Paolo Gargiulo provided the CT-scans serving as a basis for the computations. Patricia Hasslinger performed the image reconstruction, improved the Matlab code originally conceived by Alexander Dejaco, ran computations, and documented the results. Viktoria Vass supported Patricia Hasslinger during model implementation, code verification, and documentation of research results. All authors contributed to the discussion processes and helped proof reading the paper.

Abstract

Due to its high resolution, micro-CT scanning is the key to assess bone quality of sham and OVX (ovariectomized) rats. Combination of basic X-ray physics, such as the energy- and chemistry-dependence of attenuation coefficients, with results from ashing tests on rat bones, delivers mineral, organic, and water volume fractions within the voxels. Additional use of a micro-elastic model for bone provides voxel-specific elastic properties. The new method delivers realistic bone mass densities, and reveals that OVX protocols may indeed induce some bone mass loss, while the average composition of the bone tissue remains largely unaltered.

5.1 Introduction

Micro-CT imaging has become a key tool in biomedical studies, as they allow for high-resolution, non-destructive investigation of the inner structure of organs, and it has been particularly embraced for studying bone in health, disease, and tissue-engineering-supported regeneration [Buie et al., 2007, Cancedda et al., 2007, Jones et al., 2007, Laib et al., 2000]. Standardly, such images are evaluated on the basis of morphometric measures such as bone volume over total volume (BV/TV), trabecular spacing (Tr.Sp.), trabecular number (Trab.N.), or cortical thickness (Ct.Th.) [Buie et al., 2007]. Alternatively, micro-CT images provide a basis for finite element models (FEM) [Jaecques et al., 2004, Kornhuber et al., 2008]. In this context, the question about the material properties to be assigned to the bone elements arises. The most straightforward approach consists of assigning constant properties to all bone elements [Van Rietbergen et al., 1995, 1999]. On the other hand, more sophisticated approaches account for the dependence of elastic properties on the local material density [Couteau et al., 1998, Rho et al., 1995], Renders2008, [Baca et al., 2008]; the latter being approximated by the X-ray attenuation-related grey values of the voxels making up the three dimensional image stack. Corresponding "CT-density"-versus-elasticity relations, however, stay empirical in nature, depending strongly on the settings of the used instruments. Therefore, numerous formulations rather than a generally agreed-on concept, are discussed in the open literature [Cong et al., 2011, Wirtz et al., 2000]. During the last seven years, a new strategy for deriving CT-elasticity relations has been proposed and continuously refined [Blanchard et al., 2013, Czenek et al., 2014, Dejaco et al., 2012, Hellmich et al., 2008, Scheiner et al., 2009, Vuong and Hellmich, 2011, Yosibash et al., 2008]. Thereby, such relations are not guessed any more, but derived from fundamental laws of X-ray physics and continuum micromechanics, in combination with additional knowledge on the chemistry of the scanned objects. As a common feature of all the aforementioned approaches, the spatial average rule for X-ray attenuation coefficients [Crawley et al., 1988, Jackson and Hawkes, 1981] is employed to retrieve, from the attenuation-related, voxel-specific grey values, voxel-specific compositional information on the matter filling the voxels. Thereafter, this compositional information is used as input for micromechanical models [Fritsch and Hellmich, 2007, Fritsch et al., 2006, 2009c, Hellmich et al., 2004a] which translate material composition into elastic properties. Naturally, these methods appear the more powerful the fewer input informations are needed beyond the standard clinical or micro-CT images themselves. A particularly delicate issue in this context is the normally undisclosed X-ray energy used for scanning, which however, does effect the measurement of X-ray intensities, the basis of the entire suite of processing steps leading in the end to 3D CT images. It is the focus of the present paper, extending a recent contribution in the field of ceramic bone materials to natural bone tissue [Czenek et al., 2014], by example of micro-CT images of femoral bones of OVX (ovariectomized) and sham rats. With the chemically determined OVX- as well as sham-specific mineral-to-organic ratios determined through ashing experiments by Kim et al. [2009], as the only additional input needed, we derive, in the following, from stacks of OVX and sham rat femur micro-CT images, spatial distributions of mineral, organic, and water contents at micrometer-resolution, together with corresponding elastic properties – with the X-ray energy used for these images. The paper is completed by discussing the results with respect to earlier findings, including the potentials and limitations of OVX-treatment for osteoporosis simulation in rat models.

5.2 Materials and Methods

5.2.1 Animal model and sample preparation

The micro-CT images used in the present study visualize femurs of 10 ovariectomized (OVX) female Sprague-Dawley rats, and 10 sham-operated rats serving as controls. At the age of six months, the rats were anaesthetized through an injection of 0.2 ml per 100 g body weight, of Hypnorm and Dormicum diluted in water at volume ratios of 1:1:2. Afterwards, they were subject to a "single midline dorsal skin incision" [Hoegh-Andersen et al., 2004], followed by muscle cutting in order to provide access to the ovaries. Thereafter, both ovaries were removed from the rats belonging to the OVX group, while the ovaries were left within the rats of the control group. Then, the muscles were closed by means of one to two stitches on each side, and the skin was sutured through three to four stitches. Six weeks post surgery, the rats were asphyxiated by carbon dioxide, and sacrificed by exsanguination after at least 14 hours of fasting. In order to check the success of the OVX procedure, the absence of ovaries was checked at necropsy. We anticipate that the operations have been always successful, in each of the investigated rats which underwent OVX treatment. The femurs were then excised, freed from flesh, and wrapped in saline soaked gauze. They were stored in plastic tubes at $-20°C$ for the time period until CT scanning. For the latter, the bones were first thawed in a refrigerator, and then embedded in a watery solution with 0.9 g NaCl and 0.1 g NaN_3 per 100 ml water, enclosed in a plastic cylinder. Thereafter, the samples were X-ray scanned in a Phoenix Nanotom S (General Electric Measurement and Control), at a source voltage of 110 kV and a source current of 150 μA, without employing any X-ray filter. Thereby, the scanning modalities were as follows: magnification: 6.25, voxel size: 8.00 μm, rotation step: 0.36°, exposure time: 2000 ms, tube mode: 0, frame averaging number: 3, 1 frame skipped. The obtained projection images underwent translational motion compensation, guaranteeing perfect matching of the 0° and the 360° shadow images. Thereafter, they were used to reconstruct the investigated three-dimensional objects, by means of the Radon transform as algorithmized in the software datos|x-reconstruction by phoenix|x-ray [Beyerer and Puente León, 2002, Radon, 1917]. VGStudio Max 2.0 from Volume Graphics allowed for extraction of stacks of 800 images slices with identical pixel number, visualizing the space from the distal end of the femur to the knee joint.

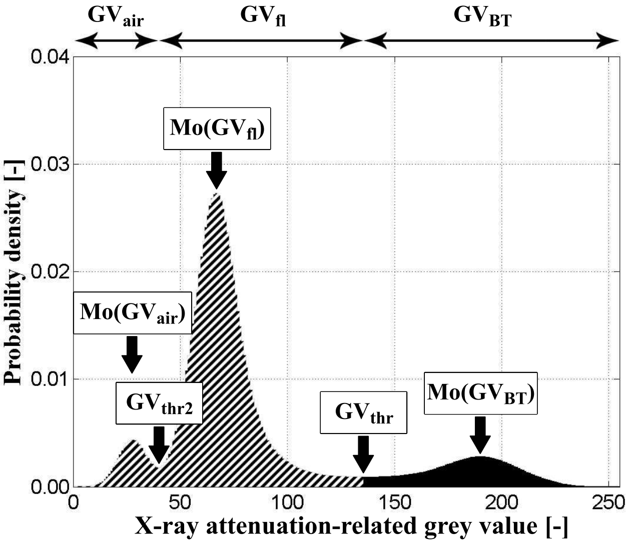

Figure 5.1: Probability density function of attenuation-related grey values of a sham rat femur

5.2.2 Conversion of CT grey values to energy-dependent attenuation coefficients

The X-ray attenuation coefficients μ describe the decrease of X-ray beam intensity per length of pervaded matter. Standardly, they are not directly provided by a CT machine, which rather would give access to X-ray attenuation-related grey values (GV) assigned to the 8 micron sized voxels making up an image stack. Here such attenuation-related grey values visualizing a portion of a femur of one rat, are binned into histograms, which are then normalized, so as to provide probability density functions, as exemplarily shown in Figure 5.1. As a rule, these functions exhibit three maxima or peaks, being related to the voxels which are most frequently occurring in the image stack compartments visualizing air (containing voxels with grey values denoted by GV_{air}), the aforementioned watery (fluid) solution (containing voxels with grey values denoted by GV_{fl}), and bone tissue (containing voxels with grey values denoted by GV_{BT}). Correspondingly, the aforementioned peak values follow as $Mo(GV_{air})$, $Mo(GV_{fl})$, and $Mo(GV_{BT})$, with the function $Mo(.)$ – standing for “mode” – extracting the most probable (resp. the most frequently occurring) values out from a probability density distribution (resp. from a normalized frequency plot). The increasing density of the matter filling the aforementioned compartments implies $Mo(GV_{air}) < Mo(GV_{fl}) < Mo(GV_{BT})$. The minimum value between $Mo(GV_{fl})$ and $Mo(GV_{BT})$, denoted as threshold value (GV_{thr}), is used to distinguish the voxels comprising bone tissue from all other voxels (see Figure 5.1). These bone tissue voxels, fulfilling $GV > GV_{thr}$, will be subject to an "intravoxel" evaluation procedure, which will be described in Section 5.2.3. Before entering the aforementioned "intravoxel" evaluation procedure, we need to specify the linear relation [Blanchard et al., 2013, Fritsch et al., 2011, MITA, 2013] between the voxel-specific grey values and the voxel-specific X-ray attenuation coefficients μ. Since the X-ray attenuation coefficients not only depend on the chemical composition of the matter filling the voxel, but also on the used photon energy ε, the slope a and the intersection b defining the aforementioned linear relation, depend on the photon energy as well [Czenek et al., 2014]

$$\mu(\varepsilon) = a(\varepsilon) \times GV + b(\varepsilon) \tag{5.1}$$

In order to identify $a(\varepsilon)$ and $b(\varepsilon)$, (5.1) is specified for the voxels characterized by $Mo(GV_{air})$ and $Mo(GV_{fl})$, respectively. This leads to the following system of equations for the unknowns $a(\varepsilon)$ and $b(\varepsilon)$

$$\begin{aligned} \mu^{air}(\varepsilon) &= a(\varepsilon) \times Mo(GV_{air}) + b(\varepsilon) \\ \mu^{fl}(\varepsilon) &= a(\varepsilon) \times Mo(GV_{fl}) + b(\varepsilon) \end{aligned} \tag{5.2}$$

whereby the attenuation coefficients for air and fluid, $\mu^{air}(\varepsilon)$ and $\mu^{fl}(\varepsilon)$ (the latter is approximated by that of water H_2O), follow from the respective mass attenuation coefficients μ/ρ available in the database of the National Institute of Standards and Technology (NIST) [Hubbell and Seltzer, 1996] upon input of their chemical compositions (see [Bolz and Tuve, 1973] for air), and from the mass densities ρ_{air}=0.0012 g/cm^3 [Searle, 1934] and ρ_{fl}=1 g/cm^3 (approximated by the mass density ρ_{H_2O} of water), see Figure 5.2. Solving the system of (5.2) for the unknowns $a(\varepsilon)$ and $b(\varepsilon)$ delivers

$$\begin{aligned} a(\varepsilon) &= \frac{\mu^{fl}(\varepsilon) - \mu^{air}(\varepsilon)}{Mo(GV_{fl}) - Mo(GV_{air})} \\ b(\varepsilon) &= \frac{Mo(GV_{fl}) \times \mu^{air}(\varepsilon) - Mo(GV_{air}) \times \mu^{fl}(\varepsilon)}{Mo(GV_{fl}) - Mo(GV_{air})} \end{aligned} \tag{5.3}$$

The coefficient functions $a(\varepsilon)$ and $b(\varepsilon)$ allow for translation of any grey value found in the micro-computer tomographs of the investigated rat femurs into corresponding X-ray attenuation coefficients – provided the photon energy is known. Its identification will be dealt with next.

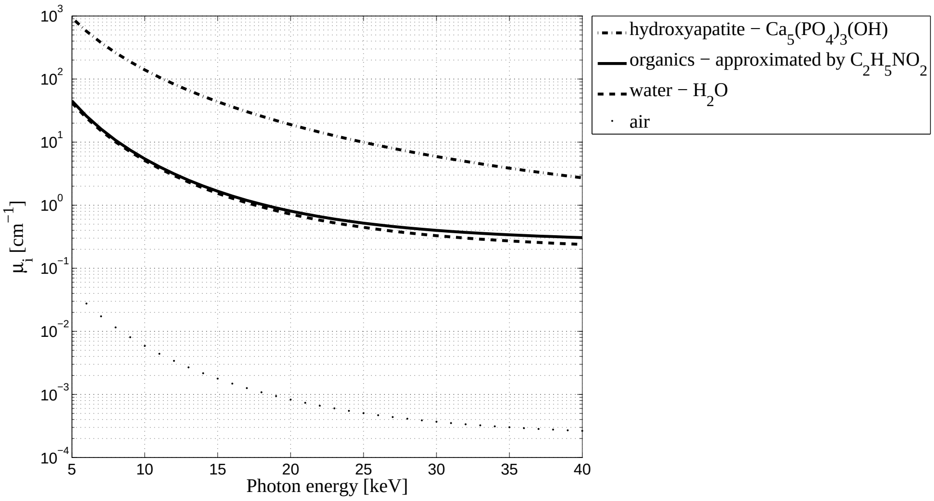

Figure 5.2: X-ray attenuation coefficients of hydroxyapatite, organics, water, and air as functions of the photon energy, according to NIST-database on http://physics.nist.gov/PhysRefData/XrayMassCoef/cover.html [Bolz and Tuve, 1973, Eastoe, 1955, Hubbell and Seltzer, 1996, Lees, 1987, Searle, 1934]

5.2.3 Identification of applied X-ray energy and of extracellular bone mass density

Following the strategy outlined in [Czenek et al., 2014], the photon energy determination rests on an equation which follows from equalizing two independent mathematical expressions for the most frequently occurring X-ray attenuation coefficient in the bone tissue compartments of the investigated images stacks, denoted as μ^{BT}. The first expression for μ^{BT} stems straightforwardly from specification of (5.1) for $Mo(GV_{BT})$ (see Figure 5.1), resulting in

$$\mu^{BT}(\varepsilon) = a(\varepsilon) \times Mo(GV_{BT}) + b(\varepsilon) \tag{5.4}$$

The second expression is derived from the average rule for the attenuation coefficient μ [Crawley et al., 1988, Hellmich et al., 2008, Jackson and Hawkes, 1981]

$$\mu(\varepsilon) = \sum_{i}^{N_c} \mu_i(\varepsilon) \times f_i \tag{5.5}$$

whereas μ_i represents the X-ray attenuation coefficient of material constituent i, and f_i stands for the corresponding volume; index i runs from 1 through N_C, the total number of constituents within the voxel characterized by attenuation coefficient μ. The 8x8x8 μm^3-sized bone tissue voxels contain the three elementary components of bone tissue [Buckwalter et al., 1995]: hydroxyapatite (HA), organics (denoted by suffix "org" – mainly collagen), and water. Specification of (5.5) for these particular constituents yields [Blanchard et al., 2013]

$$\begin{aligned}
&\forall\, GV_{BT}(> GV_{thr}) : \\
&\mu_{BT}^{voxel}(\varepsilon) = \mu_{HA}(\varepsilon) \times f_{HA}^{voxel} + \mu_{org}(\varepsilon) \times f_{org}^{voxel} + \mu_{H_2O}(\varepsilon) \times f_{H_2O}^{voxel} \\
&\text{with} \quad f_{HA}^{voxel} + f_{org}^{voxel} + f_{H_2O}^{voxel} = 1
\end{aligned} \tag{5.6}$$

where the superscript "*voxel*" indicates voxel-specificity. Similar to what we did for air and the fluid solution in Section 5.2.2, the attenuation coefficients $\mu_i(\varepsilon)$ of the elementary constituents of the bone tissue are retrieved from the NIST data base [Hubbell and Seltzer, 1996]. To begin with, using the chemical formulae of hydroxyapatite and water, $Ca_5(PO_4)_3(OH)$ [Clarke, 2008, Fritsch and Hellmich, 2007, Landis, 1995] and H_2O, as input to this NIST data base delivers, as output, the mass attenuation coefficients $(\mu(\varepsilon)/\rho)_i$, $i = HA, H_2O$. Combination of these mass attenuation coefficients with the corresponding mass densities of ρ_{HA}=3 g/cm^3 [Gong et al., 1964, Lees, 1987] and of ρ_{H_2O}=1 g/cm^3 yields the functions depicted in Figure 5.2. Next, we approximate the mass density of the complex organic matter in the extracellular bone matrix by that of collagen which amounts to ρ_{org}=1.43 g/cm^3 [Harley et al., 1977]. The latter, in turn, makes up 90 % of the organic matter in bone [Buckwalter et al., 1995, Lees, 1987, Urist et al., 1983]. Furthermore, we approximate the attenuation coefficient of the organics by that of the amino acid glycine, $C_2H_5NO_2$, which is representative for collagen [Eastoe, 1955, Lodish et al., 2000] (see Figure 5.2).

The aforementioned volume fractions f_{HA}^{voxel}, f_{org}^{voxel}, and $f_{H_2O}^{voxel}$ are expected to vary from voxel to voxel within the bone tissue compartments of the investigated rats, and except for $(5.6)_2$, no further relation among them can be given. The picture changes, however, if we consider spatial average values over the entire bone tissue compartments rather than local voxel-specific values. In fact, Kim et al. [2009] performed drying experiments on rat femoral bones, giving access to their respective (overall) organic and mineral weight, in combination with ashing experiments at 550 degrees Celsius. According to Gong et al. [1964] ashing at such a high temperature leads to volatilizing of not only the entire organic portion of the bones, but also of a certain portion of the mineral, amounting to 1.8 % of the mineral left after the burning process as ash. Accordingly, the experiments of Kim et al. [2009] yield mineral-to-organic mass ratios $\mathscr{R}$ amounting to 1.680 for sham rats, and to 1.578 for OVX rats. Hence, the mineral and organic volume fractions averaged over all voxels filled by bone tissue, which we denote by f_{HA}^{BT} and f_{org}^{BT}, fulfill

$$f_{HA}^{BT} = \mathfrak{R} \times \frac{\rho_{org}}{\rho_{HA}} \times f_{org}^{BT} \tag{5.7}$$

From a statistical viewpoint, the values averaged over the image domains filled by the bone tissue voxels are equal to the expected values of the statistical distributions of f_{HA}^{voxel} and f_{org}^{voxel}, hence,

$$\begin{aligned} f_{HA}^{BT} &= E(f_{HA}^{voxel}) \\ f_{org}^{BT} &= E(f_{org}^{voxel}) \end{aligned} \tag{5.8}$$

with $E(.)$ extracting the most probable (the most frequently occurring) value from all argument values (here all voxel-specific values) for f_{HA}^{voxel} and f_{org}^{voxel} within a scanned CT image stack. In the following, we approximate the spatial averages over all bone tissue voxels by quantities occurring in the most frequent bone tissue voxels, in mathematical terms,

$$E(f_i^{voxel}) \approx Mo(f_i^{voxel}) \ , \qquad i = HA, org, H_2O \tag{5.9}$$

(5.9) would be an identity rather than an approximation for the case of a Gaussian distribution of bone tissue voxels around the peak $Mo(GV_{BT})$ seen in Figure 5.1, so that (5.7) would also characterize this most frequently occurring bone tissue voxel. (5.7) and (5.9) imply constant volume fractions within the subvolume of the most frequently occurring bone tissue voxel, which is filled by organics and mineral (HA+org),

$$\begin{aligned} f_{HA}^{HA+org} &= \frac{f_{HA}^{BT}}{f_{HA}^{BT} + f_{org}^{BT}} = \mathfrak{R} \times \frac{\rho_{org}}{\rho_{HA}} \times \frac{1}{\mathfrak{R} \times \frac{\rho_{org}}{\rho_{HA}} + 1} \\ f_{org}^{HA+org} &= 1 - f_{HA}^{BT} = \frac{1}{\mathfrak{R} \times \frac{\rho_{org}}{\rho_{HA}} + 1} \end{aligned} \tag{5.10}$$

These volume fractions give access to an only energy-dependent attenuation coefficient $\mu_{HA+org}(\varepsilon)$ of the non-H_2O subvolume found in the most frequently occurring bone tissue voxel, by means of specification of the average rule (5.5) for two constituents, $i = HA, org$

$$\mu_{HA+org}(\varepsilon) = f_{HA}^{HA+org} \times \mu_{HA}(\varepsilon) + \left[1 - f_{HA}^{HA+org}\right] \times \mu_{org}(\varepsilon) \tag{5.11}$$

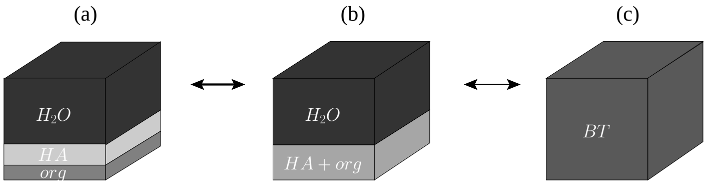

Figure 5.3: Averaging (a-b-c) or splitting up (c-b-a) X-ray attenuation coefficients or volume fractions within a bone tissue voxel: (a) elementary components with voxel-specific volume fractions (subvolumes), and with voxel-invariant attenuation coefficients and corresponding grey values, (b) water and "*solid* - $(HA + org)$ compound" with voxel-specific volume fractions (subvolumes), and with voxel-invariant attenuation coefficients and corresponding grey values, (c) overall bone tissue with voxel-specific attenuation coefficient and corresponding grey value

Applying now the attenuation rule again to the entire voxel considered as a mixture of the aforementioned "mineral-plus-organic compound" $(HA{+}org)$ and of water (see Figure 5.3), we arrive at

$$\mu^{BT}(\varepsilon) = f^{BT}_{H_2O} \times \mu_{H_2O}(\varepsilon) + \left[1 - f^{BT}_{H_2O}\right] \times \mu_{HA+org}(\varepsilon) \tag{5.12}$$

Identification of the latter expression with (5.4) yields a relation giving access to the X-ray energy ε

$$\begin{aligned} a(\varepsilon) \times Mo(GV_{BT}) + b(\varepsilon) \;&=\; f^{BT}_{H_2O} \times \mu_{H_2O}(\varepsilon) + \left[1 - f^{BT}_{H_2O}\right] \times \mu_{HA+org}(\varepsilon) \\ \rightarrow f^{BT}_{H_2O} = \frac{a(\varepsilon) \times Mo(GV_{BT}) + b(\varepsilon) - \mu_{HA+org}(\varepsilon)}{\mu_{H_2O}(\varepsilon) - \mu_{HA+org}(\varepsilon)} & \end{aligned} \tag{5.13}$$

Given the concave nature of this function $f^{BT}_{H_2O} = f^{BT}_{H_2O}(\varepsilon)$ (see Figure 5.4), the inverse relation $\varepsilon(f^{BT}_{H_2O})$ assigns, as a rule, to each value of $f^{BT}_{H_2O}$, none or two values for ε, and there exists only one single value for $f^{BT}_{H_2O}$, which is assigned to precisely one value of ε. As the same photon source and the same photon detector under the same conditions have been used for the production of all micro-CT image stacks, they all refer to only one (average) X-ray energy. Hence, there needs to exist only one value for the average photon energy ε. This implies that the maximum in the function $(5.13)_2$ defines the water volume fraction which actually occurs on average (or most frequently) throughout all voxels representing bone tissue. The value for ε related to this maximum is the sought, actually used X-ray energy, denoted as $\bar{\varepsilon}$.

This value gives access to the constituent volume fractions occurring in the "average" bone tissue voxel: the "average" volume fraction of water follows from

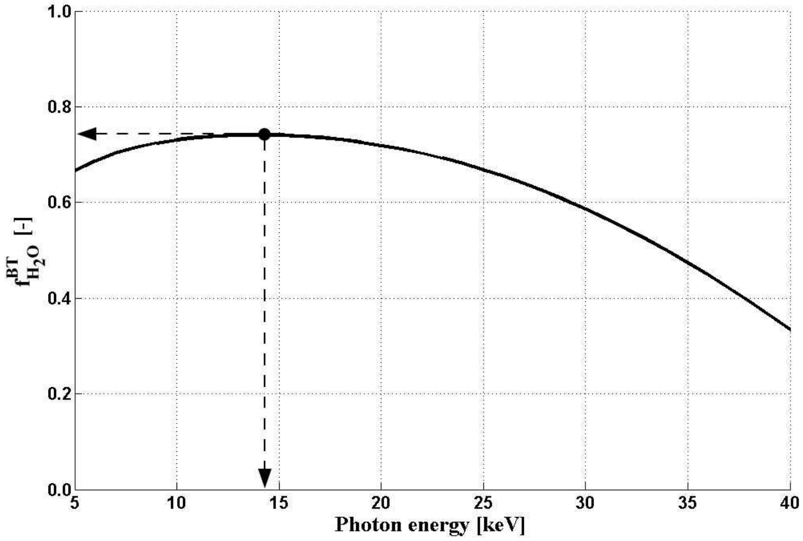

Figure 5.4: Identification of the applied X-ray energy and of its role as argument in the concave function for the water volume fraction in the "average" bone tissue voxel, as given in (5.13)

evaluation of $(5.13)_2$ for $\varepsilon = \bar{\varepsilon}$; the remaining voxel volume is filled by mineral and organics, see $(5.6)_2$, so that simultaneous use of $(5.10)_2$ yields

$$\begin{aligned} f_{org}^{BT}(\bar{\varepsilon}) &= f_{org}^{HA+org} \times \left[1 - f_{H_2O}^{BT}(\bar{\varepsilon})\right] \\ f_{HA}^{BT}(\bar{\varepsilon}) &= 1 - f_{org}^{BT}(\bar{\varepsilon}) - f_{H_2O}^{BT}(\bar{\varepsilon}) \end{aligned} \qquad (5.14)$$

These compositional characteristics of the "average" bone tissue voxel holds the key to determination of the properties of any voxel belonging to the bone tissue of the investigated micro-CT image stack: In this context, we follow earlier contributions [Roschger et al., 2008] considering that variations in the attenuation coefficients from one voxel to its neighbors reflect changes in mineralization degree; and that mineral precipitation consumes the ions from the watery solution while not affecting the organic matter within the voxels [Lees, 2003, Morin et al., 2013]. Accordingly, we set the organic volume fraction equal to the average organic volume fraction throughout all bone tissue voxels ($f_{org} = f_{org}^{BT}$), and determine the voxel-specific mineral and water volume fractions from specialization of (5.1) for bone tissue ($GV = GV_{BT}$), and of $(5.6)_1$ for the identified photon energy ($\varepsilon = \bar{\varepsilon}$), yielding

$$
\begin{aligned}
f_{HA}^{voxel}(\bar{\varepsilon}) &= \frac{a(\bar{\varepsilon}) \times GV_{BT} + b(\bar{\varepsilon}) - f_{org}^{BT}(\bar{\varepsilon}) \times \mu_{org}(\bar{\varepsilon}) - \left[1 - f_{org}^{BT}(\bar{\varepsilon})\right] \times \mu_{H_2O}(\bar{\varepsilon})}{\mu_{HA}(\bar{\varepsilon}) - \mu_{H_2O}(\bar{\varepsilon})} \\
f_{H_2O}^{voxel}(\bar{\varepsilon}) &= \frac{a(\bar{\varepsilon}) \times GV_{BT} + b(\bar{\varepsilon}) - f_{org}^{BT}(\bar{\varepsilon}) \times \mu_{org}(\bar{\varepsilon}) - \left[1 - f_{org}^{BT}(\bar{\varepsilon})\right] \times \mu_{HA}(\bar{\varepsilon})}{\mu_{H_2O}(\bar{\varepsilon}) - \mu_{HA}(\bar{\varepsilon})} \\
f_{org}^{voxel}(\bar{\varepsilon}) &= f_{org}^{BT}(\bar{\varepsilon})
\end{aligned}
\tag{5.15}
$$

see also Appendix A. These voxel-specific volume fractions then also allow for voxel-specific determination of the bone tissue mass density, according to

$$
\rho_{BT}^{voxel}(\bar{\varepsilon}) = \rho_{HA} \times f_{HA}^{voxel}(\bar{\varepsilon}) + \rho_{org} \times f_{org}^{voxel}(\bar{\varepsilon}) + \rho_{H_2O} \times f_{H_2O}^{voxel}(\bar{\varepsilon}) \tag{5.16}
$$

5.2.4 Translation of voxel-specific composition into voxel-specific elastic properties

Next, the voxel-specific volume fractions (5.15) serve as input for an experimentally validated poro-micro-elastic model for extracellular bone matrix [Morin and Hellmich, 2013], cast within the framework of continuum micromechanics [Dormieux et al., 2006b, Zaoui, 2002] (see Appendix B for derivation). According to this framework, the elasticity of a piece of matter, located in a material volume called representative volume element (RVE), depends on the elasticity of more or less homogeneous subvolumes within the RVE, called material phases, as well as on their shapes, interactions, and volume fractions. In this line, every voxel is regarded as RVE, with mechanically relevant microstructural characteristics as depicted in Figure 5.5. In more detail, each bone tissue voxel hosts two material phases with elongated cylindrical shape: "mineralized collagen fibrils" and "porous polycrystal in extrafibrillar space". According to the separation-of-scales principle [Drugan and Willis, 1996, Zaoui, 2002], the lineal dimensions of these phases, i.e. their diameters amounting to some hundred nanometers, need to be much smaller then those of the RVE, namely 8 μm, as described in Section 5.2.1. These phases are entangled and intertwined so that the mathematical relations between phase volume fractions, phase stiffnesses; and the (voxel-specific) elastic properties of the overall (voxel-specific) RVEs follow from a self-consistent homogenization scheme

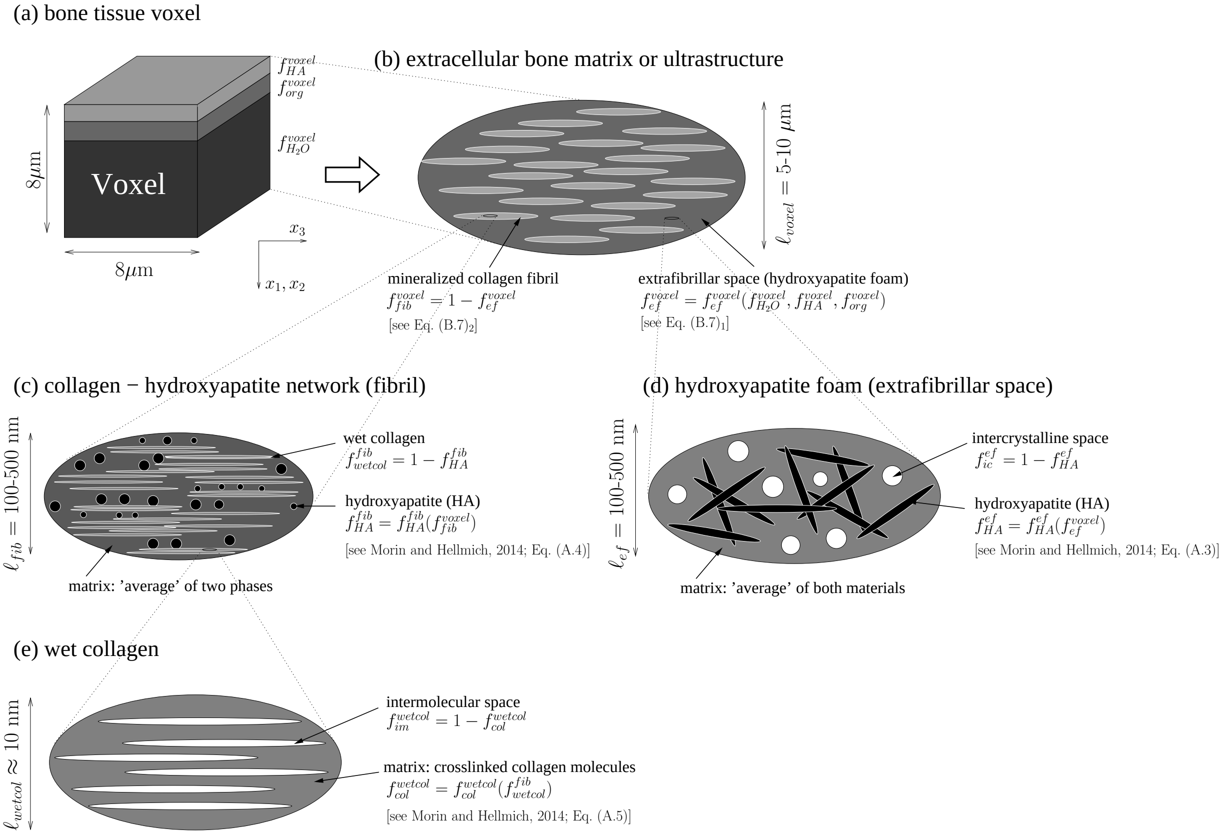
(a) bone tissue voxel
f_{HA}^{voxel}
f_{org}^{voxel}
$f_{H_2O}^{voxel}$
Voxel
8μm
8μm
x_3
x_1, x_2
(b) extracellular bone matrix or ultrastructure
$\ell_{voxel} = 5\text{-}10\ \mu m$
mineralized collagen fibril
$f_{fib}^{voxel} = 1 - f_{ef}^{voxel}$
[see Eq. (B.7)$_2$]
extrafibrillar space (hydroxyapatite foam)
$f_{ef}^{voxel} = f_{ef}^{voxel}(f_{H_2O}^{voxel}, f_{HA}^{voxel}, f_{org}^{voxel})$
[see Eq. (B.7)$_1$]
(c) collagen − hydroxyapatite network (fibril)
$\ell_{fib} = 100\text{-}500$ nm
wet collagen
$f_{wetcol}^{fib} = 1 - f_{HA}^{fib}$
hydroxyapatite (HA)
$f_{HA}^{fib} = f_{HA}^{fib}(f_{fib}^{voxel})$
[see Morin and Hellmich, 2014; Eq. (A.4)]
matrix: 'average' of two phases
(d) hydroxyapatite foam (extrafibrillar space)
$\ell_{ef} = 100\text{-}500$ nm
intercrystalline space
$f_{ic}^{ef} = 1 - f_{HA}^{ef}$
hydroxyapatite (HA)
$f_{HA}^{ef} = f_{HA}^{ef}(f_{ef}^{voxel})$
[see Morin and Hellmich, 2014; Eq. (A.3)]
matrix: 'average' of both materials
(e) wet collagen
$\ell_{wetcol} \approx 10$ nm
intermolecular space
$f_{im}^{wetcol} = 1 - f_{col}^{wetcol}$
matrix: crosslinked collagen molecules
$f_{col}^{wetcol} = f_{col}^{wetcol}(f_{wetcol}^{fib})$
[see Morin and Hellmich, 2014; Eq. (A.5)]

Figure 5.5: Mechanical characterization of a bone tissue voxel by means of a four-step micromechanics model [Morin and Hellmich, 2014]: (a) bone tissue voxel with indication of volume fractions of mineral, organics, and water; (b) RVE of extracellular bone matrix – bone ultrastructure; (c) RVE of mineralized fibril; (d) RVE of extrafibrillar space; (e) RVE of wet collagen; (x$_1$, x$_2$: transverse material directions; x$_3$: axial material direction)

[Hershey, 1954, Morin and Hellmich, 2013]

$$\begin{aligned}\mathbb{C}^{voxel} =& \Big\{ f_{fib}^{voxel}\mathbb{C}_{fib}\Big[\mathbb{I} + \mathbb{P}_{cyl}^{ec} : (\mathbb{C}_{fib} - \mathbb{C}^{voxel})\Big]^{-1} + \\ & f_{ef}^{voxel}\mathbb{C}_{ef}\Big[\mathbb{I} + \mathbb{P}_{cyl}^{ec} : (\mathbb{C}_{ef} - \mathbb{C}^{voxel})\Big]^{-1}\Big\} : \\ & \Big\{ f_{fib}^{voxel}\Big[\mathbb{I} + \mathbb{P}_{cyl}^{ec} : (\mathbb{C}_{fib} - \mathbb{C}^{voxel})\Big]^{-1} + \\ & f_{ef}^{voxel}\Big[\mathbb{I} + \mathbb{P}_{cyl}^{ec} : (\mathbb{C}_{ef} - \mathbb{C}^{voxel})\Big]^{-1}\Big\}^{-1}\end{aligned} \tag{5.17}$$

where f_{fib}^{voxel} and f_{ef}^{voxel} denote the voxel-specific volume fractions of the fibrils and the extrafibrillar space (they can be determined from the voxel-specific volume fractions of mineral, organics, and water, as detailed further below), $\mathbb{I}$ denotes the fourth-order identity tensor, with components $I_{ijkl} = 1/2 \times (\delta_{ik}\delta_{jl} + \delta_{il}\delta_{jk})$, whereas the Kronecker delta δ_{ij} is 1 for $i = j$ and zero otherwise, and P^{ec}_{cyl} is the morphology or Hill tensor, accounting for the cylindrical shape of the phases embedded in a fictitious matrix with the elastic properties of the extracellular (voxel-specific) RVE; and $\mathbb{C}_{fib}$ and $\mathbb{C}_{ef}$ are the elasticity tensors of the fibrillar and the extrafibrillar space, respectively. They follow from yet additional homogenization steps related to RVEs at lower scales, as depicted in Figure 5.5. At these lower scales, "universal", i.e. tissue-independent, phase properties [Fritsch and Hellmich, 2007, Hellmich et al., 2004a,b, Morin and Hellmich, 2014, Morin et al., 2013] are encountered at the level of the mechanical elementary constituents: hydroxyapatite, collagen, and water with non-collageneous organics. The elasticity of the hydroxyapatite phase follows from ultrasonic tests of Katz and Ukraincik [1971] and of Gilmore and Katz [1982]; that of molecular collagen can be retrieved from Brillouin light scattering tests of Cusack and Miller [1979]; while the elasticity of water is known from acoustic tests, such as the ones of Del Grosso and Mader [1972]. The phase volume fractions within all these RVEs can be retrieved, on the basis of general bone composition rules described elsewhere [Hellmich and Ulm, 2002b, Morin and Hellmich, 2013, Morin et al., 2013, Vuong and Hellmich, 2011] from the extracellular volume fractions of collagen, mineral, and bone fluid. Thereby, the mineral volume fraction follows $(5.15)_1$, the volume fraction of collagen amounts to 90 % of the organic volume fraction of $((5.15)_3$ [Urist et al., 1983], and the rest of the voxel is filled by bone fluid - water with non-collageneous organic components (see Appendix B). In this contribution, we present the voxel-specific stiffness tensors in terms of the engineering components called Young's and shear moduli, and Possion's ratios [Vuong and Hellmich, 2011]. They are based on the compliance tensor, which is the inverse of the stiffness tensor,

$$\mathbb{D}^{voxel} = \mathbb{C}^{voxel,-1} \tag{5.18}$$

The compliance tensor components then give access to the Young's moduli in transverse and longitudinal directions according to

$$E_1^{voxel} = D_{1111}^{voxel,-1} \qquad \text{and} \qquad E_3^{voxel} = D_{3333}^{voxel,-1} \tag{5.19}$$

to the Poisson's ratios according to

$$\nu_{12}^{voxel} = -D_{1122}^{voxel} \times E_1^{voxel} \qquad \text{and} \qquad \nu_{13}^{voxel} = -D_{1133}^{voxel} \times E_3^{voxel} \tag{5.20}$$

and to the shear modulus according to

$$G_{12}^{voxel} = \frac{E_1^{voxel}}{2 \times (1 + \nu_{12}^{voxel})} \tag{5.21}$$

5.2.5 Statistical Analysis

The results in Section 5.3 are given in a rat-specific manner, together with the mean values and standard deviations (SD) across all rats of either the sham or the OVX group. Potential differences between OVX and sham rat-specific quantities were investigated by means of a one-way ANOVA (analysis of variance). The corresponding null hypothesis was: Quantity X does not differ between the OVX and the sham population, and the investigated quantities were: GV_{thr}, $Mo(GV_{BT})$, μ^{BT}, f_{HA}^{BT}, $E_1^{voxel}\big[Mo(GV_{BT})\big]$, $E_3^{voxel}\big[Mo(GV_{BT})\big]$, $G_{12}^{voxel}\big[Mo(GV_{BT})\big]$, $\nu_{12}^{voxel}\big[Mo(GV_{BT})\big]$, $\nu_{13}^{voxel}\big[Mo(GV_{BT})\big]$. The homoscedasticity and normality requirements for ANOVA were checked by means of the Brown-Forsythe test [Brown and Forsythe, 1974] and the D'Agostino-Pearson omnibus test [D'Agostino, 1986]; we here anticipate that these requirements are met for the data sets documented in the Results section.

5.3 Results

All histograms derived from the 20 investigated micro-CT stacks exhibit clearly three peaks, related to air, fluid, and "average" bone tissue, respectively, see Figure 5.6. The histogram-based evaluation of the 10 sham rat micro-CT image stacks delivered air-related grey values between 29 and 33, water-related values between 66 and 71, and "average" bone-related values between 185 and 193, see Table 5.1. The histogram-based evaluation of the 10 OVX rat micro-CT image stacks delivered air-related grey values between 29 and 33, water-related values between 65 and 72, and "average" bone-related values between 183 and 193, see Table 5.2. Obviously, there are some variations between the most frequently occurring grey values $Mo(.)$ from one image stack to another within the respective group, but those are relatively small as indicated through the standard deviation (SD). In addition, we investigated the potential difference between OVX- and sham rat-related images, through testing the null hypothesis that the statistical populations, built up by the image-stack-specific values for GV_{thr} and $Mo(GV_{BT})$ would not differ

Table 5.1: Most frequently occurring grey values of air, fluid and bone tissue, and threshold grey values of the sham rats

Samples	**1**	**2**	**3**	**4**	**5**	**6**	**7**	**8**	**9**	**10**	**mean**	**SD**
$Mo(GV_{air})$	29	32	29	33	30	32	29	33	31	30	31	1.62
$Mo(GV_{fl})$	68	69	69	67	70	66	68	70	69	71	69	1.49
$Mo(GV_{thr})$	134	139	136	134	135	133	128	134	135	138	135	2.99
$Mo(GV_{BT})$	191	188	192	185	186	190	188	187	193	190	189	2.62

Table 5.2: Most frequently occurring grey values of air, fluid and bone tissue, and threshold grey values of the OVX rats

Samples	**1**	**2**	**3**	**4**	**5**	**6**	**7**	**8**	**9**	**10**	**mean**	**SD**
$Mo(GV_{air})$	33	30	31	29	31	30	32	29	31	32	31	1.32
$Mo(GV_{fl})$	71	68	72	65	72	66	68	69	72	72	70	2.68
$Mo(GV_{thr})$	140	132	136	134	137	128	132	133	134	139	135	3.60
$Mo(GV_{BT})$	193	184	187	183	190	188	186	186	185	193	188	3.50

between the OVX and the sham group. According to a corresponding ANOVA, this null hypothesis can indeed be maintained with probabilities being as high as p=94.7 % (for GV_{thr}) and p=29.3 % (for $Mo(GV_{BT})$).

Corresponding reconstructions of X-ray energy-dependent slope and intersect parameter functions a and b according to (5.3) deliver quite similar, yet not identical functions, see Figures 5.7(a) and (b). Similarly small changes are seen in the image-specific functions (5.13), based on (5.12), (5.11), and (5.10), see Figure 5.7(c). The maxima of these functions, identifying the used X-ray energy, however, are even identical: $\overline{\varepsilon}$=14 keV. Hence, virtually no variations in the photon spectrum emitted in the scanner are detectable. This energy value, when used in the functions depicted in Figure 5.7(a,b), allows for identification of image-specific slope and intersect parameters a and b, see Table 5.3 for sham rats, and Table 5.4 for OVX rats.

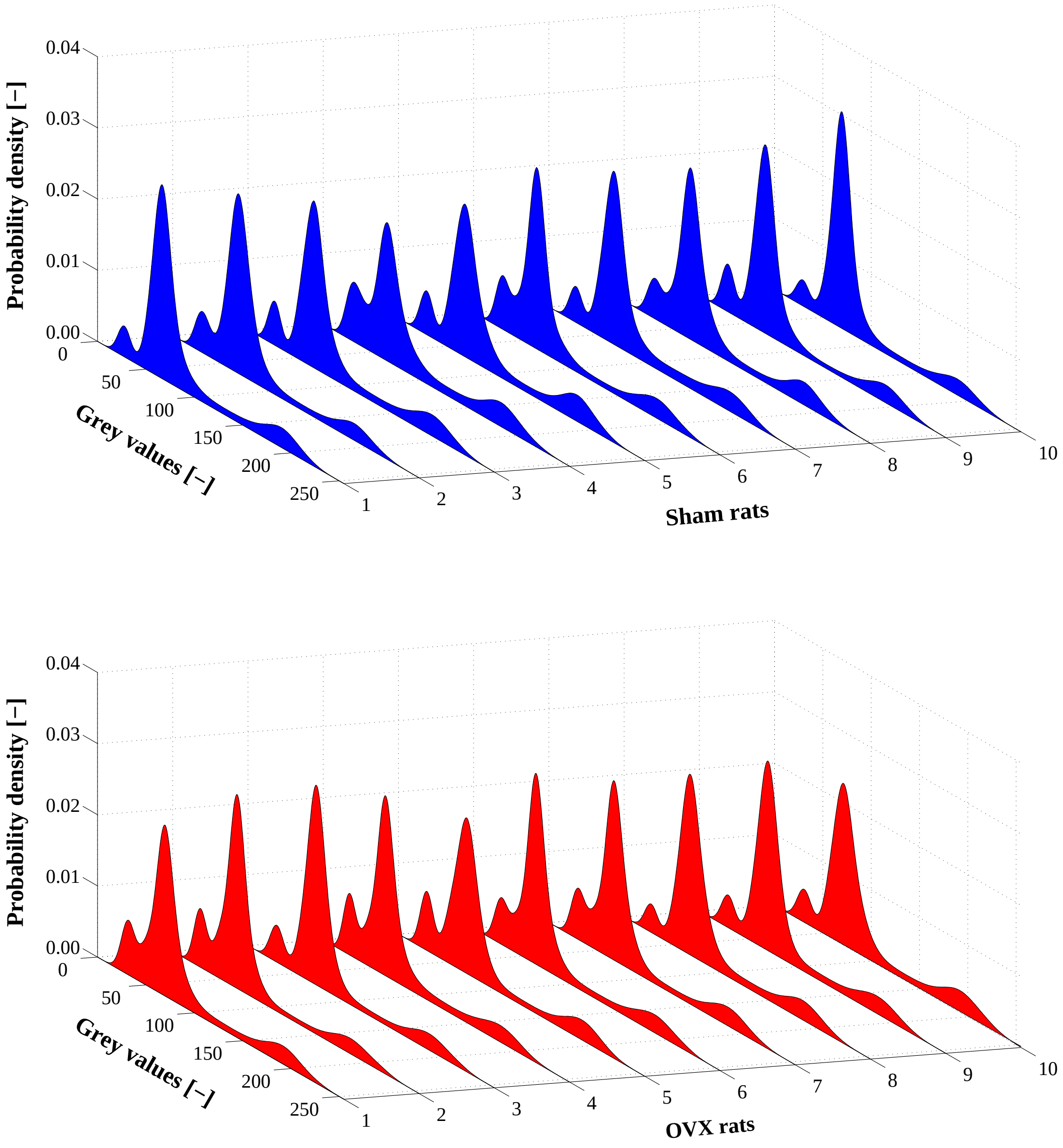

Figure 5.6: Probability density functions of attenuation-related grey values: (a) sham rats, (b) OVX rats

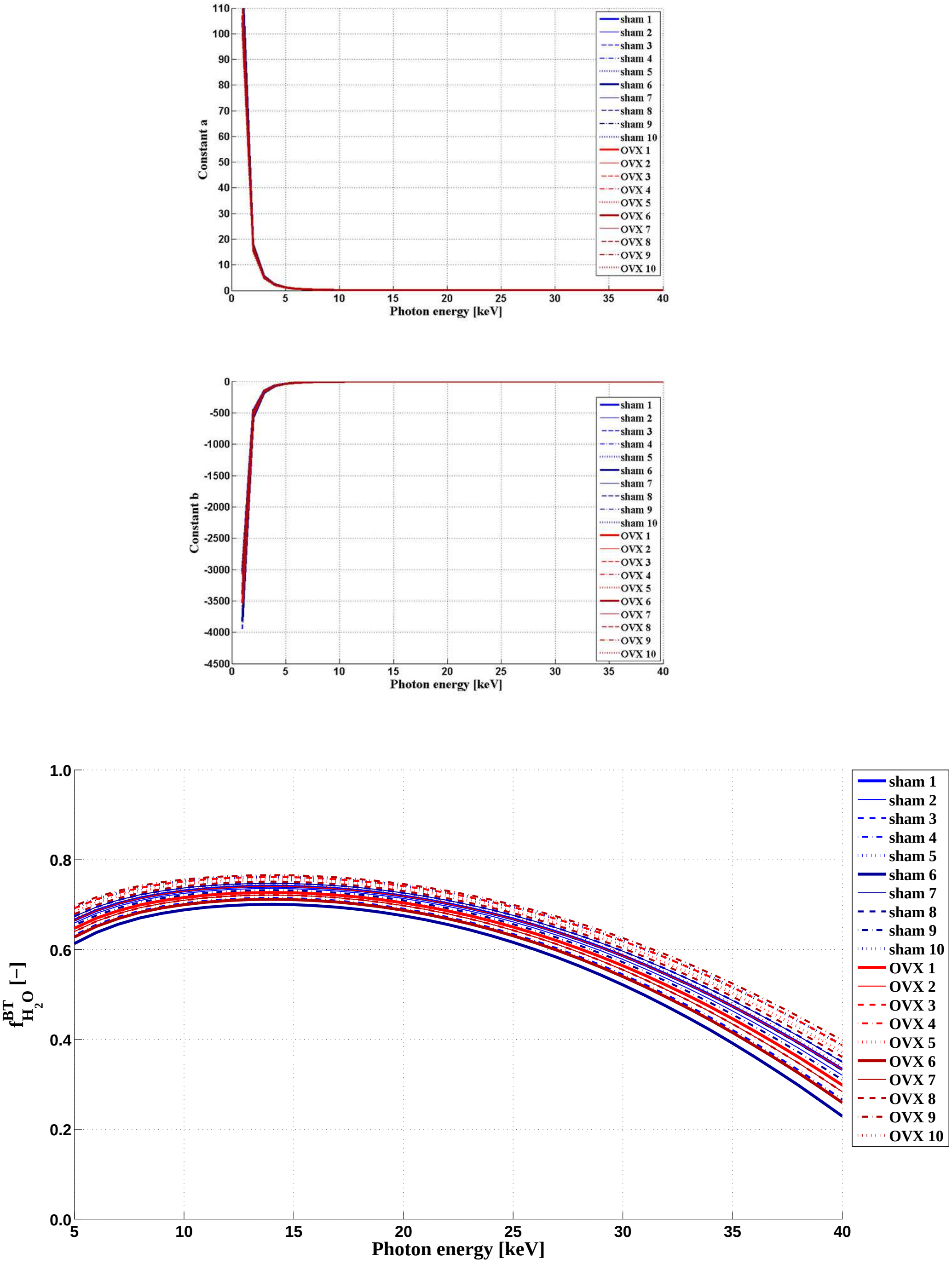

Figure 5.7: (a), (b) Line constants a and b relating grey values to attenuation coefficients, as functions of the photon energy, (c) Water volume fractions in the "average" bone voxel, as functions of the photon energy

Table 5.3: Line constants a and b, volume fractions, as well as attenuation coefficients and densities of the average bone tissue at $\overline{\varepsilon} = 14\,\mathrm{keV}$ of the sham rats

Samples	**1**	**2**	**3**	**4**	**5**	**6**	**7**	**8**	**9**	**10**	**mean**	**SD**
a	0.048	0.051	0.047	0.055	0.047	0.055	0.048	0.051	0.049	0.046	0.050	0.003
$-b$	1.390	1.617	1.355	1.815	1.402	1.760	1.390	1.667	1.525	1.368	1.529	0.174
μ^{BT}	7.778	7.894	7.630	8.370	7.302	8.701	7.634	7.793	7.982	7.307	7.839	0.436
ρ^{BT}	1.288	1.293	1.281	1.317	1.265	1.333	1.281	1.288	1.298	1.265	1.291	0.021
f_{HA}^{BT}	0.114	0.116	0.111	0.126	0.105	0.132	0.111	0.115	0.118	0.105	0.115	0.008
f_{org}^{BT}	0.145	0.148	0.141	0.159	0.133	0.167	0.141	0.145	0.150	0.133	0.146	0.011
$f_{H_2O}^{BT}$	0.741	0.736	0.748	0.715	0.762	0.701	0.748	0.741	0.732	0.762	0.739	0.019

Table 5.4: Line constants a and b, volume fractions, as well as attenuation coefficients and densities of the average bone tissue at $\overline{\varepsilon} = 14\,\mathrm{keV}$ of the OVX rats

Samples	**1**	**2**	**3**	**4**	**5**	**6**	**7**	**8**	**9**	**10**	**mean**	**SD**
a	0.049	0.049	0.046	0.052	0.046	0.052	0.052	0.047	0.046	0.047	0.049	0.003
$-b$	1.623	1.476	1.413	1.506	1.413	1.558	1.662	1.355	1.413	1.495	1.492	0.099
μ^{BT}	7.884	7.588	7.124	8.010	7.261	8.217	8.010	7.349	7.033	7.536	7.601	0.412
ρ^{BT}	1.297	1.282	1.259	1.303	1.266	1.313	1.303	1.270	1.255	1.280	1.283	0.020
f_{HA}^{BT}	0.116	0.111	0.102	0.119	0.104	0.123	0.119	0.106	0.100	0.110	0.111	0.008
f_{org}^{BT}	0.157	0.149	0.137	0.160	0.141	0.165	0.160	0.143	0.135	0.148	0.149	0.011
$f_{H_2O}^{BT}$	0.727	0.741	0.762	0.721	0.755	0.712	0.721	0.751	0.766	0.743	0.740	0.019

Use of these parameters in (5.1) allows for determination of voxel-specific attenuation coefficients, as depicted in the form of histograms in Figure 5.8 for the ten respective sham and OVX rats. The corresponding most frequently occurring attenuation coefficients in the bone tissue compartments of each of the 20 investigated image stacks vary between $7.3\,\mathrm{cm}^{-1}$ and $8.7\,\mathrm{cm}^{-1}$ in sham rats (see Table 5.3) and between $7.0\,\mathrm{cm}^{-1}$ and $8.2\,\mathrm{cm}^{-1}$ in OVX rats (see Table 5.4). According to a one-way ANOVA, the null hypothesis that the average bone tissue attenuation of OVX and sham rat femora do not differ, can be maintained with a probability of p=22.6 %. Hence, there are not only image stack-related variations in user-specific parameters a and b, but also in the actual, user-independent attenuation behavior of the "average" voxels representing different rats, be they within one of the groups (OVX or sham), or across these groups. The same holds true for the "average" volume fractions of mineral, organics, and water, as well as for "average" mass densities found in the bone tissue voxels, as is evident from Tables 5.3 and 5.4 as well.

The grey value dependencies of composition and elasticity are exemplarily shown for a sham rat in Figure 5.9 and for an OVX rat in Figure 5.10. The corresponding elastic properties according to (5.19), (5.20) and (5.21), as well as the volume fractions of the mineral are illustrated as maps in Figures 5.11 and 5.12, while respective average values are given in Tables 5.5 and 5.6. According to respective one-way ANOVA analyses, the null hypotheses that OVX and sham rat femora do not vary can be maintained for the average bone tissue for the mineral volume fraction at p=22.4 %, for the transverse Young's modulus at p=29.7 %, for the axial Young's modulus at p=53.4 %, for the shear modulus at p=32.6 %, and for the axial and transverse Poisson's ratios at p=24.1 %.

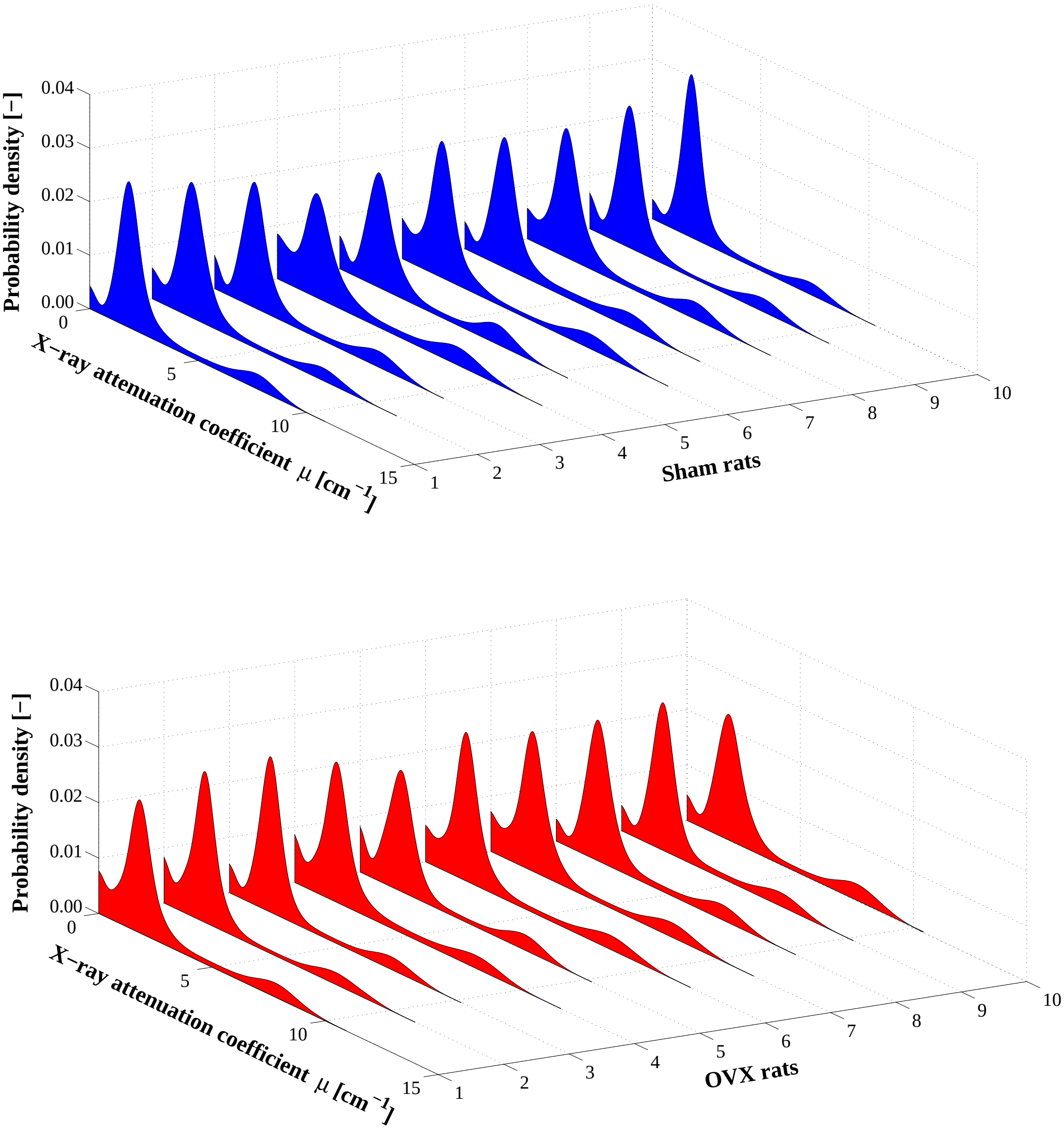

Figure 5.8: Probability density functions of X-ray attenuation coefficients: (a) sham rats, (b) OVX rats

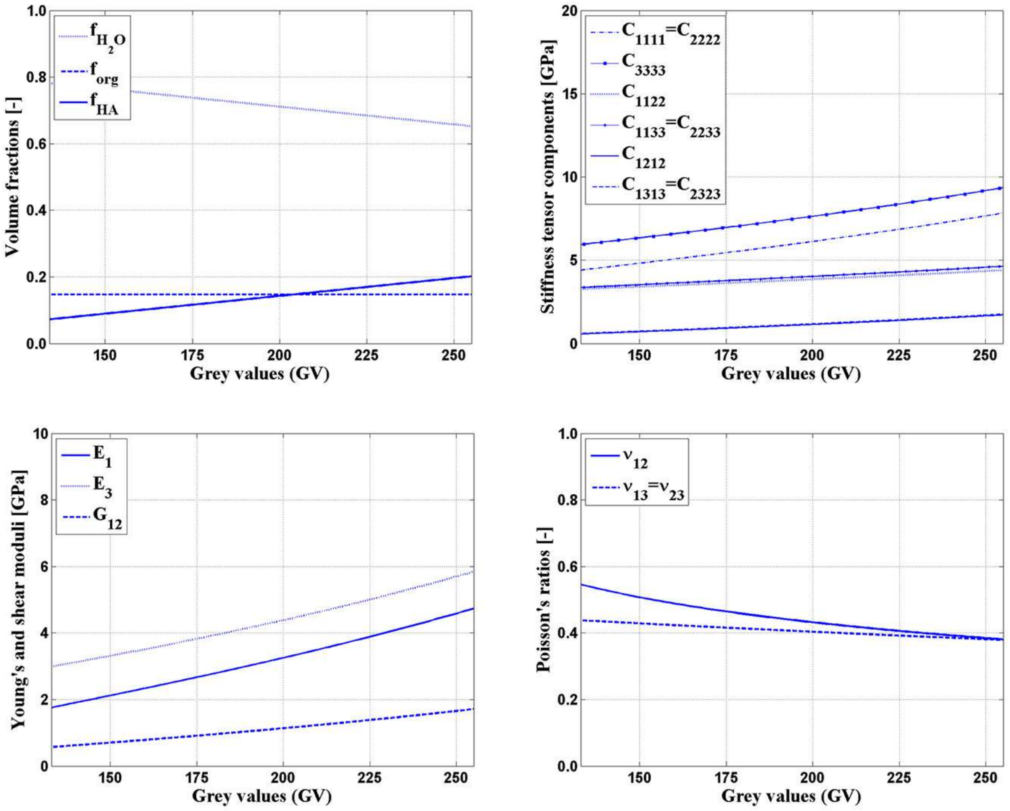

Figure 5.9: Grey value dependencies of composition and elasticity of bone tissue in sham rat #6: (a) volume fractions, (b) stiffness tensor components, (c) Young's and shear moduli, (d) Poisson's ratios

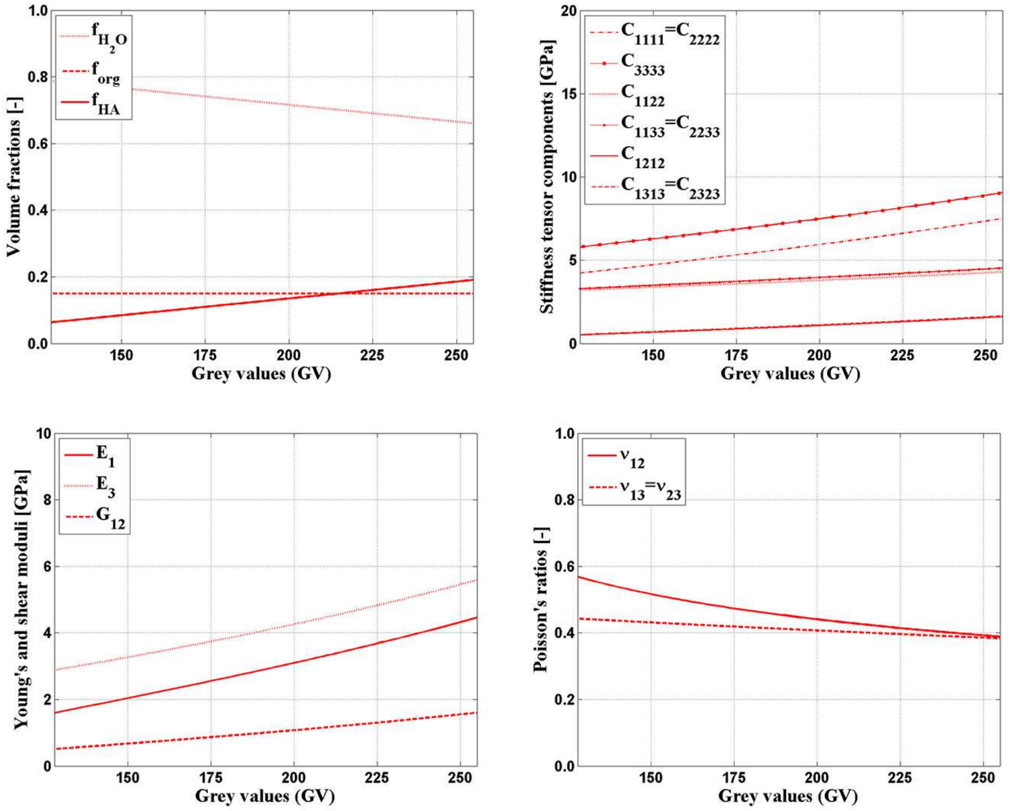

Figure 5.10: Grey value dependencies of composition and elasticity of bone tissue in OVX rat #6: (a) volume fractions, (b) stiffness tensor components, (c) Young's and shear moduli, (d) Poisson's ratios

Table 5.5: Elasticity of extracellular bone tissue: Most frequent, minimum and maximum values for transverse and axial Young's moduli, isotropic shear moduli, and inplane and out-of-plane Poisson's ratios; E_1^{voxel}, E_3^{voxel} and G_{12}^{voxel} in [GPa], ν_{12}^{voxel} and ν_{12}^{voxel} in [–]; given for all 10 image stacks illustrating sham rat femurs

Samples	**1**	**2**	**3**	**4**	**5**	**6**	**7**	**8**	**9**	**10**	**mean**	**SD**
$E_1^{voxel}(GV_{thr})$	1.555	1.699	1.542	1.756	1.506	1.756	1.443	1.582	1.587	1.513	1.594	0.108
$E_1^{voxel}\big[Mo(GV_{BT})\big]$	2.627	2.675	2.567	2.873	2.436	3.012	2.569	2.634	2.711	2.437	2.654	0.180
$E_1^{voxel}(255)$	3.993	4.209	3.861	4.700	3.839	4.730	3.993	4.183	4.085	3.717	4.131	0.344
$E_3^{voxel}(GV_{thr})$	2.821	2.943	2.811	2.992	2.780	2.992	2.729	2.844	2.848	2.786	2.855	0.091
$E_3^{voxel}\big[Mo(GV_{BT})\big]$	3.785	3.830	3.729	4.018	3.605	4.152	3.730	3.791	3.865	3.607	3.811	0.170
$E_3^{voxel}(255)$	5.108	5.321	4.978	5.810	4.956	5.840	5.108	5.296	5.199	4.837	5.245	0.340
$G_{12}^{voxel}(GV_{thr})$	0.495	0.547	0.490	0.568	0.477	0.568	0.454	0.504	0.506	0.479	0.509	0.039
$G_{12}^{voxel}\big[Mo(GV_{BT})\big]$	0.895	0.914	0.872	0.989	0.822	1.043	0.873	0.898	0.927	0.823	0.906	0.069
$G_{12}^{voxel}(255)$	1.424	1.508	1.372	1.701	1.363	1.713	1.424	1.498	1.460	1.316	1.478	0.135
$\nu_{12}^{voxel}(GV_{thr})$	0.572	0.553	0.574	0.546	0.579	0.546	0.588	0.568	0.567	0.578	0.567	0.014
$\nu_{12}^{voxel}\big[Mo(GV_{BT})\big]$	0.467	0.464	0.471	0.452	0.481	0.444	0.471	0.467	0.462	0.481	0.466	0.012
$\nu_{12}^{voxel}(255)$	0.402	0.395	0.407	0.381	0.408	0.381	0.402	0.396	0.399	0.412	0.399	0.011
$\nu_{13}^{voxel}(GV_{thr})$	0.444	0.440	0.444	0.438	0.445	0.438	0.447	0.443	0.443	0.445	0.443	0.003
$\nu_{13}^{voxel}\big[Mo(GV_{BT})\big]$	0.417	0.416	0.418	0.411	0.421	0.409	0.418	0.417	0.415	0.421	0.416	0.004
$\nu_{13}^{voxel}(255)$	0.390	0.387	0.393	0.379	0.393	0.379	0.390	0.387	0.389	0.395	0.388	0.005

Table 5.6: Elasticity of extracellular bone tissue: Most frequent, minimum and maximum values for transverse and axial Young's moduli, isotropic shear moduli, and inplane and out-of-plane Poisson's ratios; E_1^{voxel}, E_3^{voxel} and G_{12}^{voxel} in [GPa], ν_{12}^{voxel} and ν_{12}^{voxel} in [–]; given for all 10 image stacks illustrating OVX rat femurs

Samples	**1**	**2**	**3**	**4**	**5**	**6**	**7**	**8**	**9**	**10**	**mean**	**SD**
$E_1^{voxel}(GV_{thr})$	1.661	1.566	1.476	1.735	1.493	1.593	1.634	1.504	1.440	1.559	1.566	0.092
$E_1^{voxel}\left[Mo(GV_{BT})\right]$	2.692	2.571	2.384	2.744	2.439	2.830	2.744	2.474	2.348	2.550	2.578	0.168
$E_1^{voxel}(255)$	4.062	4.135	3.720	4.477	3.720	4.449	4.395	3.886	3.720	3.819	4.038	0.312
$E_3^{voxel}(GV_{thr})$	2.939	2.859	2.785	3.002	2.799	2.882	2.916	2.808	2.755	2.853	2.860	0.077
$E_3^{voxel}\left[Mo(GV_{BT})\right]$	3.872	3.758	3.584	3.921	3.635	4.003	3.921	3.668	3.550	3.738	3.765	0.157
$E_3^{voxel}(255)$	5.201	5.273	4.864	5.612	4.864	5.585	5.531	5.028	4.864	4.961	5.178	0.308
$G_{12}^{voxel}(GV_{thr})$	0.533	0.498	0.465	0.560	0.472	0.508	0.523	0.476	0.453	0.496	0.498	0.033
$G_{12}^{voxel}\left[Mo(GV_{BT})\right]$	0.919	0.873	0.802	0.939	0.823	0.972	0.939	0.836	0.788	0.865	0.876	0.064
$G_{12}^{voxel}(255)$	1.450	1.479	1.317	1.613	1.317	1.602	1.581	1.381	1.317	1.355	1.441	0.122
$\nu_{12}^{voxel}(GV_{thr})$	0.559	0.572	0.585	0.550	0.583	0.569	0.563	0.581	0.591	0.573	0.573	0.013
$\nu_{12}^{voxel}\left[Mo(GV_{BT})\right]$	0.464	0.472	0.486	0.461	0.482	0.456	0.461	0.479	0.489	0.474	0.472	0.012
$\nu_{12}^{voxel}(255)$	0.401	0.398	0.413	0.388	0.413	0.387	0.390	0.407	0.413	0.409	0.402	0.010
$\nu_{13}^{voxel}(GV_{thr})$	0.441	0.444	0.446	0.439	0.446	0.443	0.442	0.445	0.447	0.444	0.444	0.003
$\nu_{13}^{voxel}\left[Mo(GV_{BT})\right]$	0.416	0.418	0.423	0.415	0.422	0.413	0.415	0.421	0.424	0.419	0.418	0.004
$\nu_{13}^{voxel}(255)$	0.390	0.388	0.395	0.383	0.395	0.384	0.384	0.393	0.395	0.394	0.390	0.051

5.4 Discussion

While traditional approaches of micro-CT evaluation target at morphometric analysis of the entire image stacks based on a variety of different quantities such as bone mineral density (BMD), bone mineral content (BMC), bone volume over total volume (BV/TV), trabecular separation (Tb.Sp), trabecular number (Tb.N), trabecular thickness (Tb.Th), structure model index (SMI) and connectivity density (ConnD) [Böcker et al., 2014, Borah et al., 2001, Campbell et al., 2008, Donnelly, 2011, Fanti et al., 1998, Francisco et al., 2011, Govindarajan et al., 2014, Laib et al., 2000, Lesclous et al., 2004, Saito et al., 2009, Wang et al., 2001, Yang et al., 2014], the present contribution focussed on the information contained in each and every voxel, beyond a producer- and user-dependent grey value representing a mixture of physical properties and tunable regression parameters. Therefore, the linear relation between grey values and attenuation coefficients, the energy-dependence of the latter, and the average rule they obey to, were appropriately combined with drying and ashing tests on bones similar to those scanned – namely femurs from sham and OVX rats. As results, the average photon energy of the light source was quantified, as were the voxel-dependent mineral, organic and water volume fractions, i.e. the composition of each and every voxel. In this context, the volume fraction of hydroxyapatite increases with increasing X-ray attenuation-related grey value, while the water volume fraction decreases with increasing grey value, and the one of organics remains constant. This is consistent with the view that hydroxyapatite precipitates from a fluid solution, with negligibly little affect of the organic matter [Lees, 2003, Morin and Hellmich, 2013]. Feeding the aforementioned compositional information into a validated micro-elastic model yielded maps of elastic properties across the organ, as valuable source for potential structural analyses (see Figures 5.11 and 5.12).

The corresponding CT-elasticity relationships, as depicted in Figures 5.9(c) and 5.10(c), propose a quasi-linear relation between elastic modulus and attenuation-related grey values, and therefore confirm an earlier postulate of [Shefelbine et al., 2005] for a similar type of images depicting similar bones. We also note that our stiffness values compare very well with stiffness values which were obtained by testing mouse bone samples in three point-bending, four-point bending, and torsion mode [Battaglia et al., 2003, Lowe et al., 2014, Silva et al., 2004]; as well as by testing rat femurs in three-point bending mode [Hogan et al., 2000].

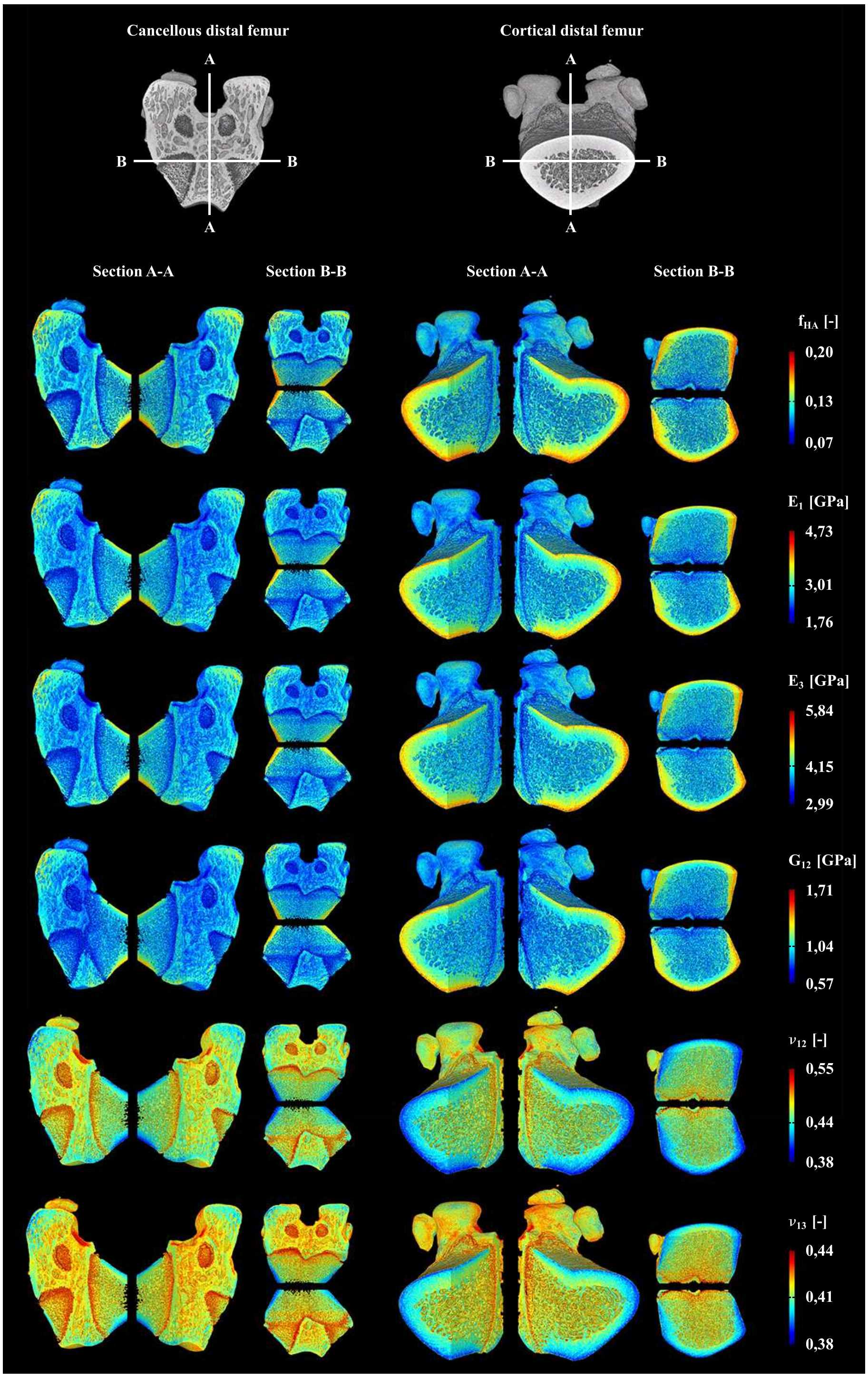
Cancellous distal femur
Cortical distal femur
A
B
B
A
A
B
B
A
Section A-A
Section B-B
Section A-A
Section B-B
f_{HA} [-]
0,20
0,13
0,07
E_1 [GPa]
4,73
3,01
1,76
E_3 [GPa]
5,84
4,15
2,99
G_{12} [GPa]
1,71
1,04
0,57
ν_{12} [-]
0,55
0,44
0,38
ν_{13} [-]
0,44
0,41
0,38

Figure 5.11: Distribution of the mineral volume fraction, f_{HA}^{voxel}, and of the engineering constants – E_1^{voxel}, E_3^{voxel}, G_{12}^{voxel}, ν_{12}^{voxel}, ν_{13}^{voxel} – throughout the bone tissue compartment of the distal femur of sham rat #6; the color bars are labelled by extreme values, as well as by the most frequently occurring one

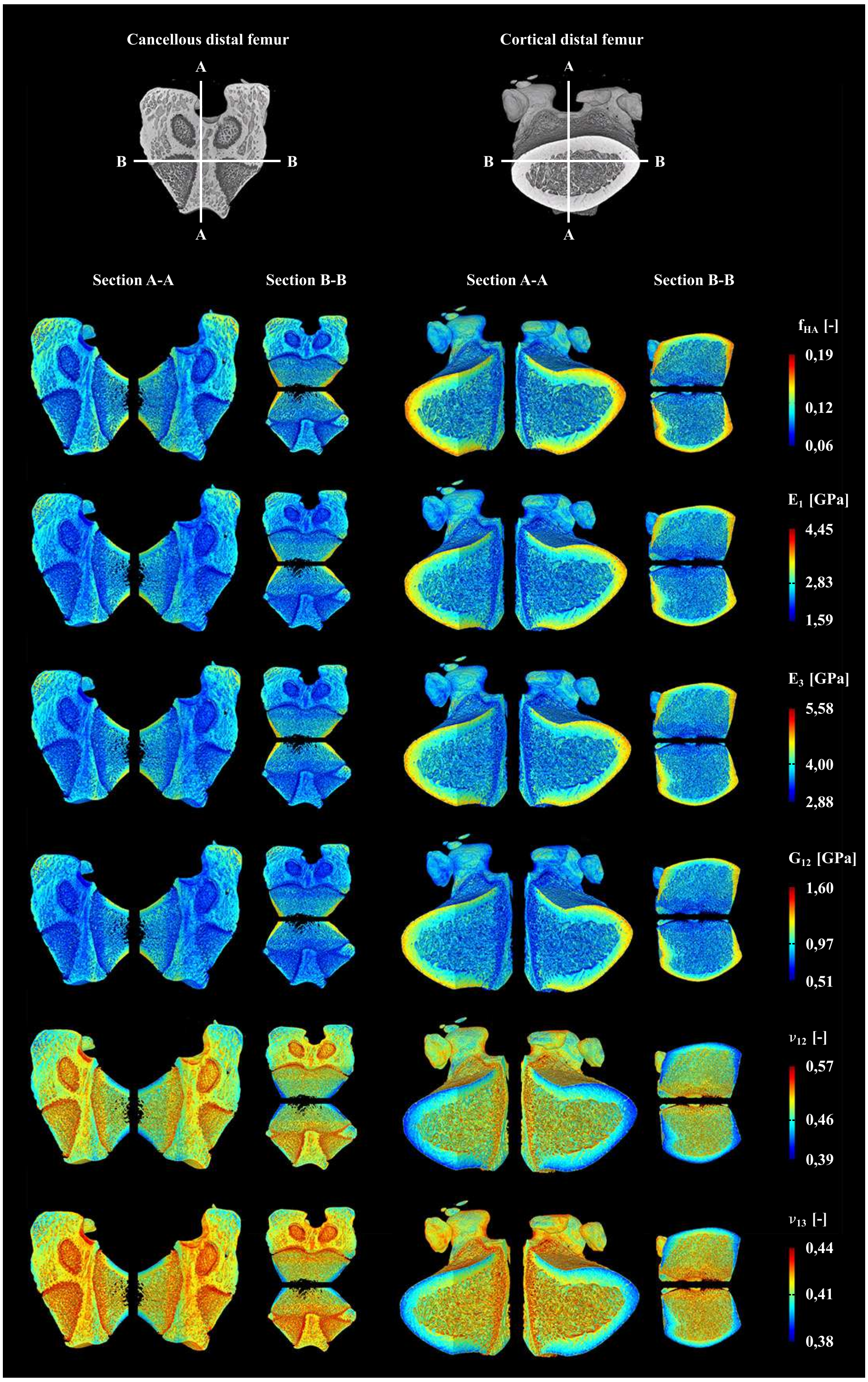
Cancellous distal femur
Cortical distal femur
A
A
B
B
A
A
B
B
Section A-A
Section B-B
Section A-A
Section B-B
f_HA [-]
0,19
0,12
0,06
E_1 [GPa]
4,45
2,83
1,59
E_3 [GPa]
5,58
4,00
2,88
G_12 [GPa]
1,60
0,97
0,51
ν_12 [-]
0,57
0,46
0,39
ν_13 [-]
0,44
0,41
0,38

Figure 5.12: Distribution of the mineral volume fraction, f_{HA}^{voxel}, and of the engineering constants – E_1^{voxel}, E_3^{voxel}, G_{12}^{voxel}, ν_{12}^{voxel}, ν_{13}^{voxel} – throughout the bone tissue compartment of the distal femur of OVX rat #6; the color bars are labelled by extreme values, as well as by the most frequently occurring one

The question may arise whether the value $\bar{\varepsilon}$, determined for the mean photon energy encountered in the investigated bone femur samples, could have been checked by means of a more direct measurement technique. However, it is the unaltered policy of most micro-CT producers to not disclose this information. Their standard market model builds on providing images allowing for appropriate morphometrical image analysis, while leaving aside any quantitative information on the actually retrieved X-ray attenuation coefficients. However, the linear relation (5.1) is confirmed by the producers of the employed CT equipment [MITA, 2013].
Whenever, working with CT data, concerns about ring and beam hardening artifacts may arise: The ring artifact is caused by a misaligned or defective detector, see e.g. Boas and Fleischmann [2012]. As careful observation of our scans (see Figure 5.13 for a representative example) did not suggest the existence of rings centered on the center of rotation, we may conclude the used detector was neither misaligned nor defective. Beam hardening expresses itself in dark streaks between two high attenuation objects, such as metal and bone [Boas and Fleischmann, 2012, Duerinckx and Macovski, 1978]; and/or through cupping artifacts where the inner regions of a uniform cylinder undergo artificial "density reduction" [Barrett and Keat, 2004, Joseph and Spital, 1978]. As the vast majority of our scans neither exhibit such streaks nor significant cupping artifacts, we conclude that beam hardening did not essentially reduce the quality of the used scans. The overall satisfactory quality of our scans may be due to the following precautions: The samples were put into fluid-filled plastic tubes, and the scan optimization compensating translational motion was applied before reconstruction. Furthermore, all samples were treated in exactly the same fashion. At the same time, we wish to clarify that the focus of our approach is the improved exploitation of satisfactorily reconstructed attenuation values, rather than reconstruction issues *per se*. In this sense, successful application of our method is always the more probable the more reliable the used CT device and the *a priori* chosen and employed reconstruction algorithms are. In the present case, the producer calls the used device "closest to synchrotron CT" [GE Measurement and Control, 2014].

The micromechanics approach rests on experimental investigations which give access to the elastic properties of the elementary components of bone: hydroxyapatite mineral, collagen, and water. In the micromechanical context, these elementary components play the role of phases, as illustrated in Figure 5.5. Accordingly, the most straightforward access to these phase properties is the consideration of RVEs

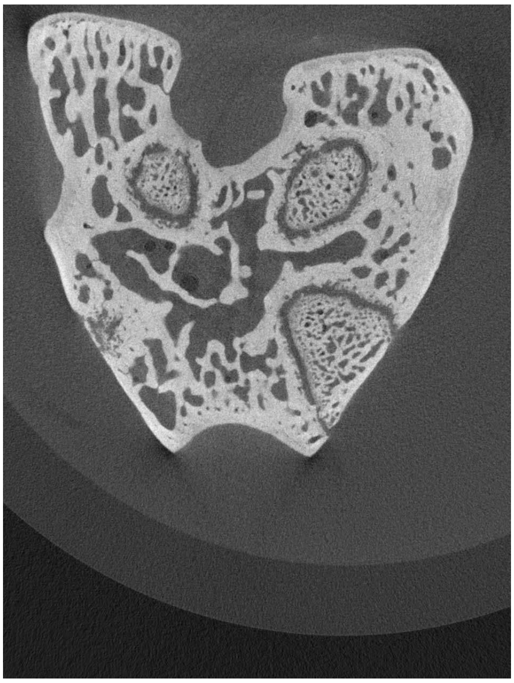

Figure 5.13: Example of a reconstructed micro-CT scan showing a cross section through the distal femur of sham rat #9

which (almost) exclusively consist of one single phase representing one of the aforementioned elementary components, and to corresponding experiments performed on samples which actually represent such RVEs. As regards the mineral phase, the used micromechanics model rests on the ultrasonic tests reported by Katz and Ukraincik [1971] and Gilmore and Katz [1982]; these tests were performed on dense apatite solids. The resulting isotropic elastic constants, namely a bulk modulus of 83 GPa and shear modulus of 45 GPa [Morin and Hellmich, 2014], agree remarkably well with totally independent *ab initio* calculations [Ching et al., 2009] based on the Vienna *ab initio* simulation package (VASP) [Kresse and Hafner, 1993]. The latter simulations deliver a bulk modulus of 84 GPa and a shear modulus of 48 GPa. Accordingly, we conclude that totally different and independent sources lead to key material properties used as input for the herein employed micromechanical model, which do not differ by more than 5 %. Similar arguments hold for the collagen properties derived from Brillouin light scattering tests performed on *stretched* dehydrated samples consisting almost exclusively of type I collagen [Cusack and Miller, 1979, Morin and Hellmich, 2014]. First, the interest in stretched samples is due to the fact that bone cells *stretch* the still unmineralized collagen fibrils before impregnating them with mineral [Engler et al., 2006]; and expanding on the aforementioned argument, we note that the Brillouin scattering-derived stiffness properties as given in Eq. (34) of Morin and Hellmich [2014] compare well to properties obtained either from atomistic simulations of crosslinked collagen [Buehler, 2008], or from microelectromechanical tests [Eppell et al., 2006, Shen et al., 2008]. It is instructive to consider these facts in view of recent stochastic homogenization approaches to estimate bone elastic properties [Sansalone et al., 2014], which came to the main conclusion that "the statistical fluctuations of the (homogenized) elastic coefficients are smaller than those of its elementary constituents." This would imply that the homogenized elastic properties used herein for voxel characterization, are precise up to an error of typically less than 5 %, due to potential variations in the material properties which were assigned to the elementary constituents of bone.

A further independent check of our homogenized, voxel-specific tissue properties might still be desirable. We are not aware of nanoindendation tests on OVX and sham rat femora; however, the nanoindendation campaign of Guo and Goldstein [2000] on vertebral trabecular bone showed that the tissue properties remain unchanged upon ovariectomy, being therefore fully consistent with the results of our present study. As regards absolute numbers, the stiffnesses reported by Guo and Goldstein [2000] are comparable to those of Silva et al. [2004] obtained from dried femoral bone tissue of senescence accelerated mice. On the other hand, corresponding wet mouse tissue properties were determined by Silva et al. [2004] from four-point bending tests: Respective Young's moduli range between 2.8 and 7.4 GPa; and this range largely overlaps with that of Tables 5.5 and 5.6.

The key goal of the present work was to derive, from micro-CT data, voxel-specific composition and elasticity information which is to the largest extend possible, based on tissue- and species-invariant quantities and relations. The latter comprise mass densities and attenuation coefficients of organics, mineral, and water; the linear relation between grey values and attenuation coefficients; as well the average rule for X-ray attenuation coefficients. The only species-specific input to our method is the mineral-to-organic mass ratio provided by [Kim et al., 2009]. The latter researchers tested animals undergoing surgery at 10 weeks age and being sacrificed at 16 weeks age, while the rats investigated here underwent surgery at 24 weeks age and were sacrificed at 30 weeks age. It has been repeatedly stated that the age at ovariectomy and the post OVX time span may affect the outcome of the treatment [Francisco et al., 2011, Liu et al., 2015, Thompson et al., 1995]. On the other hand, it is known that tissue property changes are typically restricted to young age, and are ceasing with adulthood [Akkus et al., 2003, Boivin and Meunier, 2002, Hellmich et al., 2008, Roschger et al., 2003]. Hence, the question arises, whether the 16 weeks old rats of [Kim et al., 2009] may be regarded as equally "adult" as the 30 weeks old rats investigated in the present study. For a rough answer to this question, we consider the chemical tests on rat bones reported by Hammet [1925] from which evolutions of tissue mass density with age can be determined, see Table 5 of Vuong and Hellmich [2011] for corresponding data. Fitting these data by a decaying exponential curve delivers characteristic "growing times" of rats of about 10 weeks. As the age at sacrifice of both the rats reported by Kim et al. [2009] and the presently investigated rats is clearly beyond this "growing time", we may, in a first approximation, consider both as "adult", and therefore, as exhibiting largely age-independent tissue properties.

Our CT-derived compositional data, in combination with the mass densities of mineral, organics, and water, give access to the voxel-specific mass density of bone tissue voxels, and the average value of the latter, amounting to about 1.3 g/cm^3 according to our analysis based on CT images and ashing/drying tests, agrees very well with independent, direct mass density measurements on rat femurs [Hammet, 1925], delivering an average value of 1.3 g/cm^3. This good agreement gives additional confidence in our new method. Secondly, it becomes evident that the intra-group variations (within the OVX and sham rat groups), of all studied variables, such as grey values, attenuation coefficients, volume fractions, and elastic properties, are much larger than the differences between the OVX and the sham group, in particular when considering the corresponding ANOVA results given in the Results Section. Accordingly, only the macroscopic level is left for potential identification of differences between OVX and sham rats. Given roughly the same sizes of femora OVX and sham rats, the overall bone tissue volume emerges as interesting quantity to quantify "OVX-induced osteoporosis". The null hypothesis that also this bone tissue volume would not differ between the OVX and the sham group can be maintained with a probability amounting to only p=11.7 %. Hence, OVX-induced changes at the overall bone organ level are more probable than at the tissue level. Still, the value of 11.7 % exceeds the standard 5 % threshold which is customary for calling a difference "really significant". This reflects certain doubts on the OVX procedure as a means to mimick osteoporosis, as they are expressed in the literature: Reasons for that the lost function of the ovaries in rats does not always provoke similar effects as in humans were reviewed by Kalu [1991]: (i) rats exhibit a stable bone mass, or even gain bone, throughout most of their lifetime (in contrast to humans), and (ii) bone remodeling patterns in rats differ from those in humans, e.g. the former do not exhibit Haversian cortical bone. The remodeling activities can also be traced in terms of mineralization states at the bone tissue scale [Roschger et al., 2008], where higher attenuation would be related to lower remodeling activities (indicating osteoporosis). However, the OVX rats exhibit lower bone attenuation properties (and smaller mineral volume fractions) when compared to the sham rats – and the latter properties can even be more easily distinguished between the OVX and the sham rat groups, relative to Young's modulus and grey values.

These somehow doubtful results on the actual efficiency of OVX-treatment are fully consistent with reports on OVX studies measured through dual X-ray absorptiometry (DXA): Some researchers report no significant difference in BMD between OVX and sham rats [Campbell et al., 2008, Saito et al., 2009], while others observe a decrease of BMD due to oestrogen deprivation [Fanti et al., 1998, Govindarajan et al., 2014, Wang et al., 2001].

5.5 Appendix A. Derivation of the mineral volume fraction of Eq. (5.15)$_1$

Specialization of (5.1) adapted for the bone tissue (BT) and for $\varepsilon = \overline{\varepsilon}$ reads as

$$\mu_{BT}^{voxel}(\overline{\varepsilon}) = a(\overline{\varepsilon}) \times GV_{BT} + b(\overline{\varepsilon}) \tag{5.22}$$

whereas specialization of (5.6) for $f_{org}(\varepsilon) = f_{org}^{BT}(\varepsilon)$ and $\varepsilon = \overline{\varepsilon}$ reads as

$$\mu_{BT}^{voxel}(\overline{\varepsilon}) = \mu_{HA}(\overline{\varepsilon}) \times f_{HA}^{voxel}(\overline{\varepsilon}) + \mu_{org}(\overline{\varepsilon}) \times f_{org}^{BT}(\overline{\varepsilon}) + \mu_{H_2O}(\overline{\varepsilon}) \times \left[1 - f_{HA}^{voxel}(\overline{\varepsilon}) - f_{org}^{BT}(\overline{\varepsilon})\right] \tag{5.23}$$

Setting (5.22) and (5.23) equal to each other, yields

$$\begin{aligned} &a(\overline{\varepsilon}) \times GV_{BT} + b(\overline{\varepsilon}) - \mu_{org}(\overline{\varepsilon}) \times f_{org}^{BT}(\overline{\varepsilon}) - \mu_{H_2O}(\overline{\varepsilon}) \times \left[1 - f_{org}^{BT}(\overline{\varepsilon})\right] = \ldots \\ &\ldots f_{HA}^{voxel}(\overline{\varepsilon}) \times \left[\mu_{HA}(\overline{\varepsilon}) - \mu_{H_2O}(\overline{\varepsilon})\right] \end{aligned} \tag{5.24}$$

and solving (5.24) for f_{HA}^{voxel} finally results in

$$f_{HA}^{voxel}(\overline{\varepsilon}) = \frac{a(\overline{\varepsilon}) \times GV_{BT} + b(\overline{\varepsilon}) - f_{org}^{BT}(\overline{\varepsilon}) \times \mu_{org}(\overline{\varepsilon}) - \left[1 - f_{org}^{BT}(\overline{\varepsilon})\right] \times \mu_{H_2O}(\overline{\varepsilon})}{\mu_{HA}(\overline{\varepsilon}) - \mu_{H_2O}(\overline{\varepsilon})} \tag{5.25}$$

5.6 Appendix B. Derivation of fibrillar and extrafibrillar volume fractions, f_{fib}^{voxel} and f_{ef}^{voxel}, in the line of Morin and Hellmich [2013]

From the voxel-specific volume fractions of mineral, organics, and water, f_{HA}^{voxel}, f_{org}^{voxel}, and $f_{H_2O}^{voxel}$, the volume fractions entering the multiscale micromechanical model of [Morin and Hellmich, 2014] are determined, according to the general bone composition and evolution rules identified by Morin and Hellmich [2013] for precipitation of solid hydroxyapatite from a fluid ionic solution under closed thermodynamic conditions, and by Hellmich and Ulm [2003] for the distribution of mineral between fibrillar and extrafibrillar spaces, while considering the hydration-induced swelling properties of unmineralized collageneous tissues according to Morin et al. [2013]. In more detail, the voxel-specific volume fraction of collagen per (extracellular) bone tissue volume reads as

$$f_{col}^{voxel} = 0.9 \times f_{org}^{voxel} \tag{5.26}$$

as 90 % of the organic matter in bone is known to be type I collagen [Urist et al., 1983]. This implies the volume fracton of the bone fluid phase (consisting mainly of water, but also containing some non-collageneous organics) to read as

$$f_{fl}^{voxel} = 1 - f_{HA}^{voxel} - f_{col}^{voxel} \tag{5.27}$$

During mineralization the density difference between low-density ionic fluid (ρ_{H_2O}=ρ_{fl}=1 g/cm^3) out of which the mineral precipitates and high-density solid hydroxyapatite (ρ_{HA}=3 g/cm^3), implies shrinkage of the tissue, due to "contraction" of the fluid spaces inside and outside the collagen fibrils. This motivates to first determine the fibrillar and extrafibrillar volume fractions in a piece of yet unmineralized (and fully saturated) bone tissue (called osteoid). In such a tissue, the collagen volume fraction within the fibrils is a constant and amounts to (see Eq. (B.1) of [Morin and Hellmich, 2013])

$$f_{col}^{fib,0} = 0.45 \tag{5.28}$$

It gives access to the fibrillar and extrafibrillar volume fractions in unmineralized osteoid, according to Eq. (B.3) of [Morin and Hellmich, 2013]

$$\begin{aligned} f_{fib}^0 =& f_{col}^{fib,0} \times \frac{\rho_{H_2O}}{\mathscr{R}^0 \times \rho_{col} + \rho_{H_2O}} \\ f_{ef}^0 =& 1 - f_{fib}^0 \end{aligned} \tag{5.29}$$

with $\mathscr{R}^0$ as the fluid-to-collagen mass ratio of the unmineralized tissue, which can readily be expressed as

$$\begin{gathered} \mathscr{R}^0 = \frac{f_{fl}^0}{f_{col}^0} \times \frac{\rho_{H_2O}}{\rho_{col}} \\ \text{with} \quad f_{fl}^0 + f_{col}^0 = 1 \end{gathered} \tag{5.30}$$

with f_{fl}^0 and f_{col}^0 as the fluid and collagen volume fractions of the unmineralized (osteoid) tissue. The latter follows from Eq. (B.5) of [Morin and Hellmich, 2013], and reads as

$$f_{col}^0 = \frac{f_{col}^{voxel}}{\frac{\rho_{HA}}{\rho_{H_2O}} \times f_{HA}^{voxel} + f_{fl}^{voxel} + f_{col}^{voxel}} \tag{5.31}$$

Quantities (5.26) to (5.31) give access to the extrafibrillar and fibrillar volume fractions in mineralized tissue, according to Eqs. (C.13) and (10) of [Morin and Hellmich, 2013]

$$\begin{aligned} f_{ef}^{voxel} =& \frac{f_{ef}^0}{1 + \left(\frac{\rho_{HA}}{\rho_{H_2O}} - 1\right) \times f_{HA}^{voxel}} + \frac{f_{ef}^0}{1 - f_{col}^0} \times \left(1 - \frac{\rho_{HA}}{\rho_{H_2O}}\right) \times f_{HA}^{voxel} \\ f_{fib}^{voxel} =& 1 - f_{ef}^{voxel} \end{aligned} \tag{5.32}$$

5.7 Nomenclature

a	slope of the linear relation between X-ray attenuation coefficient and grey value of a micro-Computed Tomograph
b	intersection of the linear relation between X-ray attenuation coefficient and grey value of a micro-Computed Tomograph
$\mathbb{C}_{ef}$	stiffness tensor of the extrafibrillar space (residing in the respective subvolume of the considered voxel)
$\mathbb{C}_{fib}$	stiffness tensor of the fibrillar space (residing in the respective subvolume of the considered voxel)
$\mathbb{C}^{voxel}$	(voxel-specific) micromechanics-derived stiffness tensor of the extracellular bone tissue
C_{ijkl}^{voxel}	(voxel-specific) micromechanics-derived stiffness tensor component of the extracellular bone tissue
$\mathbb{D}^{voxel}$	(voxel-specific) micromechanics-derived compliance tensor of the extracellular bone tissue
D_{ijkl}^{voxel}	(voxel-specific) micromechanics-derived compliance tensor component of the extracellular bone tissue
$E(.)$	expected value of random variable (.)
E_1^{voxel}	(voxel-specific) micromechanics-derived Young's modulus of the extracellular bone matrix in transverse direction
E_3^{voxel}	(voxel-specific) micromechanics-derived Young's modulus of the extracellular bone matrix in axial direction
f_{HA}^{BT}	volume fraction of hydroxyapatite related to the most frequently occurring bone tissue voxel (approximating the "average" bone tissue voxel)
$f_{H_2O}^{BT}$	volume fraction of water related to the most frequently occurring bone tissue voxel (approximating the "average" bone tissue voxel)
f_{org}^{BT}	volume fraction of organics related to the most frequently occurring bone tissue voxel (approximating the "average" bone tissue voxel)
f_{HA}^{ef}	volume fraction of hydroxyapatite in the extrafibrillar space
f_{ic}^{ef}	volume fraction of the intercrystalline pore space in the extrafibrillar space
$f_{col}^{fib,0}$	collagen volume fraction in the fibrils of the unmineralized osteoid
f_{HA}^{fib}	volume fraction of hydroxyapatite in the fibrillar space
f_{wetcol}^{fib}	volume fraction of wet collagen in the fibrillar space
f_{col}^{wetcol}	volume fraction of collagen in the wet collagen space
f_{im}^{wetcol}	volume fraction of the intermolecular pore space in the wet collagen
f_{HA}^{HA+org}	volume fraction of hydroxyapatite per organics- and mineral-filled subvolume of the most frequently occurring bone voxel
f_{org}^{HA+org}	volume fraction of organics per organics- and mineral-filled subvolume of the most frequently occurring bone voxel

f_{col}^{voxel}	(voxel-specific) volume fraction of collagen
f_{ef}^{voxel}	(voxel-specific) volume fraction of the extrafibrillar space
f_{fib}^{voxel}	(voxel-specific) volume fraction of the fibrillar space
f_{fl}^{voxel}	(voxel-specific) volume fraction of bone fluid in intercrystalline and intermolecular pore spaces
f_{HA}^{voxel}	(voxel-specific) volume fraction of hydroxyapatite
$f_{H_2O}^{voxel}$	(voxel-specific) volume fraction of water
f_{org}^{voxel}	(voxel-specific) volume fraction of organics
f_{col}^{0}	volume fraction of collagen in the unmineralized osteoid
f_{ef}^{0}	extrafibrillar volume fraction in the unmineralized osteoid
f_{fib}^{0}	fibrillar volume fraction in the unmineralized osteoid
f_{fl}^{0}	fluid volume fraction in the unmineralized osteoid
GV	(voxel-specific) X-ray attenuation-related grey value
GV_{air}	(voxel-specific) grey values occurring in air compartment of a CT image stack
GV_{BT}	(voxel-specific) grey values occurring in bone tissue compartment of a CT image stack
GV_{fl}	(voxel-specific) grey values occurring in fluid compartment of a CT image stack
GV_{thr}	threshold grey value between bone tissue-related voxels and fluid-filled voxels
GV_{thr2}	threshold grey value between fluid-filled voxels and air-filled voxels
G_{12}^{voxel}	(voxel-specific) micromechanics-derived shear modulus in transverse (isotropic) plane
$\mathbb{I}$	fourth-order identity tensor
$Mo(.)$	mode of random variable (.)
P_{cyl}^{ec}	fourth-order Hill or morphology tensor, accounting for the cylindrical phase shape in a matrix with the elastic properties of extracellular (ec) bone tissue
$\mathscr{R}$	mass ratio between mineral and organics in bony organ, according to [Kim et al., 2009]
$\mathscr{R}^0$	mass ratio between fluid and collagen in the unmineralized (osteoid) tissue, according to [Morin and Hellmich, 2013]
ε	average photon energy related to a CT image stack
$\bar{\varepsilon}$	identified average photon energy (constant)
μ	X-ray attenuation coefficient
μ^{air}	X-ray attenuation coefficient which most frequently occurs within the air compartment of a CT image stack of a rat femur
μ^{BT}	X-ray attenuation coefficient which most frequently occurs within the bone tissue compartment of a CT image stack of a rat femur
μ^{fl}	X-ray attenuation coefficient which most frequently occurs within the fluid compartment of a CT image stack of a rat femur

μ_{HA}	X-ray attenuation coefficient of hydroxapatite
μ_{HA+org}	X-ray attenuation coefficient of the organics- and mineral-filled subvolume of the most frequently occurring bone tissue voxel
μ_{H_2O}	X-ray attenuation coefficient of water
μ_{org}	X-ray attenuation coefficient of organics
μ_{BT}^{voxel}	(voxel-specific) X-ray attenuation coefficient within the bone tissue compartment of a CT image stack of a rat femur
ν_{12}^{voxel}	(voxel-specific) micromechanics-derived Poisson's ratio in transverse (isotropic) plane
ν_{13}^{voxel}	(voxel-specific) micromechanics-derived Poisson's ratio in (any) axial plane
ρ_{air}	mass density of air
ρ_{HA}	mass density of hydroxyapatite
ρ_{H_2O}	mass density of water
ρ_{org}	mass density of organics
ρ_{BT}^{voxel}	(voxel-specific) bone tissue mass density
ρ^{BT}	mass density related to the most frequently occurring bone tissue voxel
BT	bone tissue
cyl	cylindrical
ec	extracellular bone matrix
ef	extrafibrillar space
fib	fibrillar space
fl	fluid
HA	hydroxyapatite
$HA+org$	organics and mineral within the bone tissue
H_2O	water
ic	intercrystalline pore space
im	intermolecular pore space
org	organic matter
OVX	ovariectomized
RVE	respective volume element
$voxel$	voxel-specific
$wetcol$	wet collagen
thr	threshold between bone tissue-related voxels and fluid-filled voxels
$thr2$	threshold between fluid-filled voxels and air-filled voxels
0	unmineralized (osteoid) tissue
1	transverse direction
2	axial direction
12	transverse (isotropic) plane
13	(any) axial plane

Chapter 6

X-ray physics-based CT-to-composition conversion applied to a tissue engineering scaffold, enabling multiscale simulation of its elastic behavior

Authored by: Karol Szlazak, Viktoria Vass, Patricia Hasslinger, Jakub Jaroszewicz, Alexander Dejaco, Joanna Idaszek, Stefan Scheiner, Christian Hellmich, and Wojciech Świeszkowszki

Submitted to: *Materials Science and Engineering C*, 2017

Contribution: This paper results from a collaboration between the Institute for Mechanics of Materials and Structures of TU Wien, and the Faculty of Materials Science and Engineering of the Warsaw University of Technology, Poland. Christian Hellmich and Wojciech Świeszkowszki set up the overall research strategy, supervised the research progress, and checked the key results. Karol Szlazak manufactured the investigated scaffolds, took microCT images, and performed the image reconstruction. He modified and improved the Matlab code, ran computations entering Finite Element simulations, and documented the results. Viktoria Vass supported Karol Szlazak during the micromechanical model implementation, and code verification. Stefan Scheiner supervised the documentation process, and together with Patricia Hasslinger, contributed to the scientific discussions, and helped proof reading the paper.

Abstract

Nowadays, the assessment of the mechanical competence of tissue engineering scaffolds based on computer simulations is a well-accepted technology. Typically, such simulations are performed by means of the Finite Element (FE) method, with the underlying structural model being created based on micro-computed tomography (microCT). Here, this analysis modality is applied to a new, ternary composite, consisting of PHBV, i.e. poly(3-hydroxybutyrate-co-3-hydroxyvalerate), PLGA, i.e. poly(lactic-co-glycolide), as well as of TCP, i.e. tricalcium phosphate hydrate. The here studied scaffold structure is made up by fibers of this new composite material, manufactured by means of the rapid prototyping method. The data collected from microCT will be additionally utilized for adequately defining the mechanical properties of the FE model. In particular, the three-dimensional field of grey values is interpreted in terms of the underlying field of attenuation coefficients, taking into account the photon energy employed in microCT imaging, eventually allowing for calculation of the three-dimensionally distributed, voxel-specific composition of the studied material. For the sake of keeping the FE simulations as efficient as possible, groups of voxels are combined into one finite element; the grey value of the latter is obtained by averaging. Employing a two-step micromechanical homogenization scheme, the experimentally accessible stiffness of the three constituents (PHBV, PLGA, and TCP) is then, finite element by finite element, upscaled to the composition-dependent stiffness of the composite material. The plausibility and adequacy of the FE model is demonstrated by simulating the effects of uniaxial compression on scaffold structure, in terms of resulting stress and strain fields, highlighting the importance of the fiber junctions (as they are the mechanically most stressed regions), and that neglecting the material heterogeneity would lead to potentially significant underestimation of stresses and strains. Finally, a comparison is made of the employed analysis modality of microCT data with a previously pursued, simplified analysis strategy, highlighting the conceptual superiority of the former, and pointing out the application limits of the latter.

6.1 Introduction

Bone tissue engineering scaffolds must fulfil diverse requirements [Hollister, 2005, Hutmacher, 2000, Rezwan et al., 2006, Williams, 2008]. Firstly, they must be biocompatible, that is they must not cause any harm to the targeted physiological environment. Then, such scaffolds must also stimulate the regeneration of bone tissue, by being suitable hosts of bone growth-promoting cells and growth factors, and by being porous enough in order to provide enough space for substantial ingrowth of bone tissue. Ideally, once new bone tissue has accumulated to a sufficient extent, the scaffold structure degrades and eventually disappears, as it has fulfilled the purpose of providing temporary support and is no longer needed. And, finally, since bone is often concerned with bearing mechanical loads, bone tissue engineering scaffolds must feature suitable mechanical properties.

The range of materials that have been developed to meet the aforementioned requirements is extremely widespread, including materials that are particularly biodegradable [Castilla Bolaños et al., 2017, Di Luca et al., 2016, Gupta et al., 2017, Szlazak et al., 2016] or metallic alloys [Wang et al., 2017, Wysocki et al., 2016, Yazdimamaghani et al., 2017]. However, conventional materials often lack at least one of the aforementioned features, therefore exhibiting limited applicability in bone tissue engineering. In this paper, we present a new ternary composite material, consisting of two types of polymers, namely PHBV, i.e. poly(3-hydroxybutyrate-co-3-hydroxyvalerate), PLGA, i.e. poly(lactic-co-glycolide), as well as of TCP, i.e. tricalcium phosphate hydrate. PHBV, a thermoplastic polyester produced by many bacteria as an intracellular reservoir of carbon and energy [Zinn et al., 2001], is biodegradable, biocompatible, piezoelectric, and exhibits mechanical properties which render PHBV as suitable for application as scaffold material in bone tissue engineering [Fukada and Ando, 1986]. However, PHBV is not bioactive, thus it does not promote bone regeneration [Li and Chang, 2004] and may instead lead to fibrous encapsulation [James et al., 1999, Kokubo et al., 1990]. Furthermore, PHBV degrades rather slowly [Idaszek et al., 2013], and is difficult to process by means of extrusion, owing to a comparably low viscosity [Kublik et al., 2012] (leading to a correspondingly high mass flow rate). Merging organic particles, such as TCP, into PHBV improves the bioactivity of the resulting composite, as compared to PHBV alone [Chen and Wang, 2002]. The viscosity of the compound consisting of PHBV and TCP is also higher than the one of PHBV, and is further reduced by including PLGA, a polymer with high molecular weight, as third constituent [Kublik et al., 2012]. Additionally, PLGA leads to an increased degradation rate of the polymer matrix [Idaszek et al., 2013, 2015a,b, 2016]. Thus, the presented three-phase composite material made up by PHBV, PLGA, and TCP unites supreme characteristics in terms of processability, bioactivity, and biodegradability, and therefore promises to be a very interesting complement to the range of already existing materials.

The aforementioned requirement concerning the mechanical behavior of the bone tissue engineering scaffold has to be fulfilled on two different levels, that is both on the material level, ensured by an appropriate composite mixture, and on the structural level. As for the latter, collecting as many insights into the exact mechanical behavior of the scaffold structure as possible, before implantation, is certainly preferable over the often-pursued trial-and-error strategy (which is potentially ineffective and patient-unfriendly). In this paper, we present a computational method, combining X-ray physics, averaging rules, continuum micromechanics, and large-scale Finite Element (FE) simulations, for studying the structural mechanical behavior. In particular, after defining the constituents of the scaffold material, and describing how it is manufactured (in Section 6.2), acquiring the material's microstructure by means of micro-computed tomography (microCT) will be dealt with in Section 6.3.1. Over the past decade, substantial progress has been made in terms of "translating" the spatial arrangement of grey values resulting from CT scanning, into corresponding volume fraction maps quantifying the material's composition [Czenek et al., 2014, Hasslinger et al., 2016, Hellmich et al., 2008, Luczynski et al., 2012, Scheiner et al., 2009]. Here, we will tie in with these works, by back-analyzing the photon energy applied in the CT studies performed on the aforementioned ternary composite material (i.e. an information which is standardly not provided by manufacturers of tomographs), based on which the volume fractions of the polymers (PHBV and PLGA) and of the TCP inclusions can be calculated (see Section 6.3.2). These volume fractions serve as input for Finite Element simulations of the structural behavior of the scaffold, with the underlying constants resulting from continuum micromechanical homogenization (see Section 6.4). After clarifying the required accuracy of the Finite Element mesh, numerical simulations of uniaxial compressive loading demonstrate how important thorough consideration of the heterogeneous distribution of the composite material's composition is (see Section 6.5). The paper is concluded with a brief discussion (see Section 6.6).

6.2 Material characterization and processing

The ingredients of the composite material presented in this paper are PHBV, i.e. poly(3-hydroxybutyrate-co-3-hydroxyvalerate), PLGA, i.e. poly(L-lactide-co-glycolide), and TCP, i.e. tricalcium phosphate hydrate. PHBV (with a 3-hydroxyvalerate content of 12 wt%) was purchased from Sigma-Aldrich, USA. PLGA (in particular Resomer LG 855S, with a GA content of 15 mol%, and an inherent viscosity of 2.5 to 3.5 dl/g) was ordered from Boehringer Ingelheim, Germany. TCP nanopowder (with a particle size of less than 200 nm, according to BET) was bought from Aldrich, USA. Furthermore, methylene chloride was obtained from Chempur, Poland.

The composites were prepared utilizing the solvent casting technique. PHBV and PLGA (with a mass ratio of 7:3) were dissolved in methylene chloride ($c = 20\,\mathrm{w/v\%}$). Subsequently, 5 wt% of TCP powder was added and mixed by means of a magnetic stirrer, in order to ensure a homogenous particle distribution. The resulting slurry, with volume fractions $f_{\mathrm{PHBV}} = 0.7127$, $f_{\mathrm{PLGA}} = 0.2657$, and $f_{\mathrm{TCP}} = 0.0216$, was then cast into a Petri dish and dried, first overnight in a fume hood, and then, for several days, in a vacuum dryer at a temperature of 45°C and a pressure of 50 mbar. The resulting film was cut into small pieces and used to fabricate composite scaffolds using the rapid prototyping device BioScaffolder (Syseng, Germany). The composite was extruded through a G23-nozzle (with an inner diameter of 330 μm), at a temperature of 165°C and a pressure of approximately 2 bar. The movement of the printing head was set to 100 mm/min, while the screw was set to approximately 200 rpm. The samples were produced in form of cylinders with a diameter of 6 mm, a height of 2 mm and a lay-down pattern of 0/90°, see Figure 6.1. The spacing between fibers in each layer was set to 0.657 mm, ensuring a pore size in the xy-plane larger than 300 μm, and to 0.24 mm in neighboring layers, ensuring sufficient adhesion between the fibers in z-direction. Furthermore, for the sake of comparison (see Sections 6.3.1 and 6.3.2), a sample of pure PHBV was also scanned by microCT.

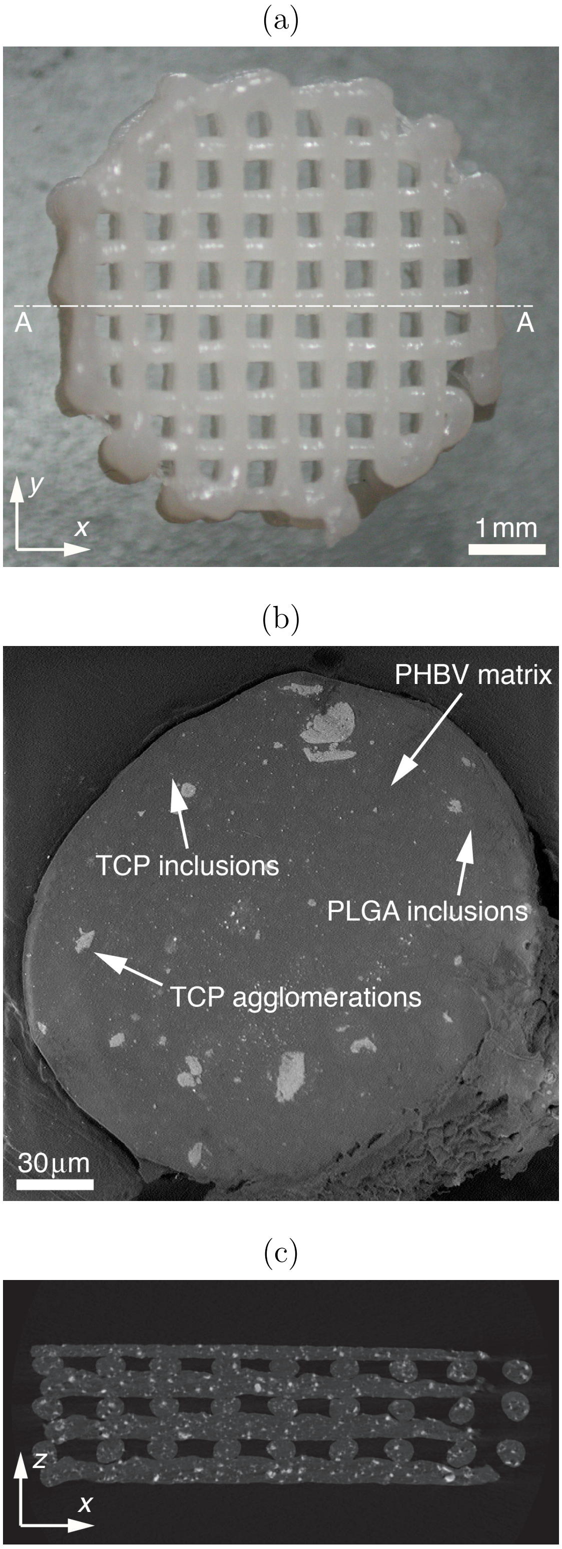
(a)
A
A
y
x
1 mm
(b)
PHBV matrix
TCP inclusions
PLGA inclusions
TCP agglomerations
30μm
(c)
z
x

Figure 6.1: (a) Photograph of one of the produced scaffolds, obtained by means of stereomicroscopy; (b) cross section of one fiber, acquired by means of scanning electron microscopy, showing the distribution of PLGA and TCP inclusions, as well as large TCP agglomerations, within the PHBV matrix; and (c) one layer of the image stack obtained by means of microCT, relating to cross-section A-A indicated in (a)

6.3 Acquisition of the scaffold microstructure by means of micro-computed tomography

6.3.1 Definition of imaging modality

After production, micro-computed tomography (microCT) was performed on the scaffold structure by means of a Zeiss Xradia MicroXCT-400, in order to ascertain its exact (macroscopic) geometry, and to investigate the microstructural distribution of material constituents. For this purpose, source voltage and source current were set to 40 kV and 250 μA. The obtained resolution was 6 μm. The scanning procedure was carried out by performing a rotation of the emitted X-ray by 180°, with a step size of 0.15°, and an exposure time of 15 s per projection.

From a conceptual point of view, CT imaging is based on sending X-rays through the studied object, and measuring the resulting attenuation of the X-ray intensity. This procedure is repeated many times, varying the position of the X-ray source and the direction of the X-ray. Making use of the Radon transform [Radon, 1917], the collected information is then processed such that a three-dimensional distribution of attenuation coefficients emerges. In order to illustrate this distribution, the attenuation coefficients are usually translated into corresponding grey values. In particular, the studied object is compartmentalized into so-called voxels, which are essentially cubic domains whose side length corresponds to the CT resolution; thus, in the present study the size of the voxels is $6 \times 6 \times 6\,\mu$m. To each voxel i, one constant grey value GV^i is assigned, being proportional to attenuation coefficient μ^i, i.e. the attenuation coefficient of the material contained in this voxel. Figure 6.1(c) shows the thereby obtained field of grey values (on an 8 bit-scale) across one specific cross-section of the microCT-scanned domain. Furthermore, for the sake of comparison, a so-called phantom, i.e. a pure PHBV granule (provided by the manufacturer), was also placed in the scanned domain.

6.3.2 Analysis of microCT data for determination of the voxel-specific scaffold composition

The aforementioned proportionality between GV^i and μ^i can be mathematically expressed by means of a linear relation [Blanchard et al., 2013, Czenek et al., 2014, Fritsch et al., 2011, Hasslinger et al., 2016],

$$\mu^i(\epsilon) = a(\epsilon) \times \mathrm{GV}^i + b(\epsilon)\,. \tag{6.1}$$

Thus, the voxel-specific attenuation coefficient, as well as constants a and b are functions of the photon energy ϵ used for the CT imaging. Finding eventually a relation between the voxel-specific grey values provided by a CT scan and the corresponding, voxel-specific constituent volume fractions is described next.

We start with considering the frequency distributions of the grey values resulting from the microCT scans of both the scaffold structure and the PHBV phantom, see Figure 6.2. In this plot, several peaks can be identified, two of which are particularly useful. On the one hand, the leftmost peak unambiguously relates to air, i.e. to the voxels not containing any composite material, occurring at $\mathrm{GV}_{\mathrm{air}}^{\mathrm{peak}} = 3.29$. On the other hand, right of the peak relating to air, the second-highest peak relates to the PHBV phantom, at $\mathrm{GV}_{\mathrm{PHBV}}^{\mathrm{peak}} = 23.97$. Specifying Eq. (6.1) for the air and PHBV phases yields the following two equations:

$$\mu_{\mathrm{air}}(\epsilon) = a(\epsilon) \times \mathrm{GV}_{\mathrm{air}}^{\mathrm{peak}} + b(\epsilon) \tag{6.2}$$

and

$$\mu_{\mathrm{PHBV}}(\epsilon) = a(\epsilon) \times \mathrm{GV}_{\mathrm{PHBV}}^{\mathrm{peak}} + b(\epsilon)\,. \tag{6.3}$$

Knowing the chemical compositions of air and PHBV, the National Institute of Standards and Technology (NIST) of the United States of America readily provides the photon energy-dependent attenuation coefficients $\mu_{\mathrm{air}}(\epsilon)$ and $\mu_{\mathrm{PHBV}}(\epsilon)$ [Hubbel and Seitzer, 2004], allowing to solve Eqs. (6.2) and (6.3) for $a(\epsilon)$ and $b(\epsilon)$, yielding

$$a(\epsilon) = \frac{\mu_{\mathrm{air}}(\epsilon) - \mu_{\mathrm{PHBV}}(\epsilon)}{\mathrm{GV}_{\mathrm{air}}^{\mathrm{peak}} - \mathrm{GV}_{\mathrm{PHBV}}^{\mathrm{peak}}} \tag{6.4}$$

and

$$b(\epsilon) = \frac{\mu_{\mathrm{air}}(\epsilon)\mathrm{GV}_{\mathrm{PHBV}}^{\mathrm{peak}} - \mu_{\mathrm{PHBV}}(\epsilon)\mathrm{GV}_{\mathrm{air}}^{\mathrm{peak}}}{\mathrm{GV}_{\mathrm{PHBV}}^{\mathrm{peak}} - \mathrm{GV}_{\mathrm{air}}^{\mathrm{peak}}}\,. \tag{6.5}$$

Next, the photon energy used for the particular CT data studied here is considered. For this purpose, we consider the third peak visible in Figure 6.2, representing the scaffold material, at $\mathrm{GV}_{\mathrm{scaff}}^{\mathrm{peak}} = 28.99$. Again, Eq. (6.1) is accordingly specified:

$$\mu_{\mathrm{scaff}}^{\mathrm{peak}}(\epsilon) = a(\epsilon) \times \mathrm{GV}_{\mathrm{scaff}}^{\mathrm{peak}} + b(\epsilon)\,. \tag{6.6}$$

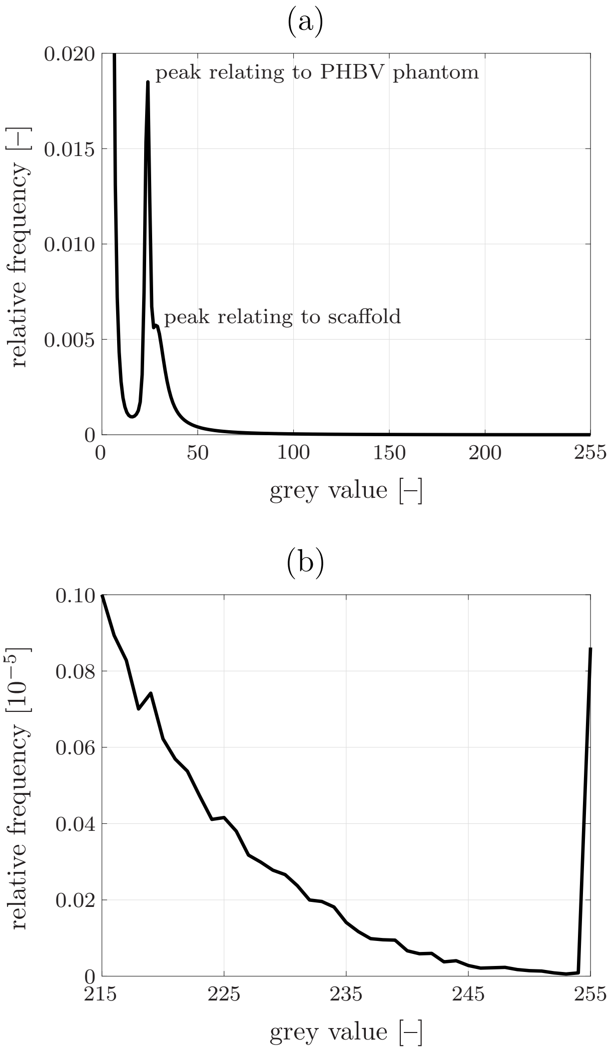

Figure 6.2: Relative frequency distribution of the grey values obtained from microCT scanning of the scaffold depicted in Figure 6.1, together with the PHBV phantom; (b) relates to a zoom-out from (a)

Additionally, we take into account that the attenuation coefficient of a composite material follows from volume averaging, thus

$$\mu_{\text{scaff}}^{\text{peak}}(\epsilon) = \sum_j \mu_j(\epsilon) f_j \,, \tag{6.7}$$

where index j represents PHBV, PLGA, and TCP, and where f_j are the volume fractions of the constituents (related here to the composition which is most frequently occurring in the voxels making up the scaffold material domain of the microCT image). Then, we plot $\mu_{\text{scaff}}^{\text{peak}}(\epsilon)$ based on Eq. (6.6), on the one hand, by inserting the coefficients according to Eqs. (6.4) and (6.5), and based on Eq. (6.7), on the other hand, by considering the attenuation coefficients following from the NIST-database as well as the constituent volume fractions following from the

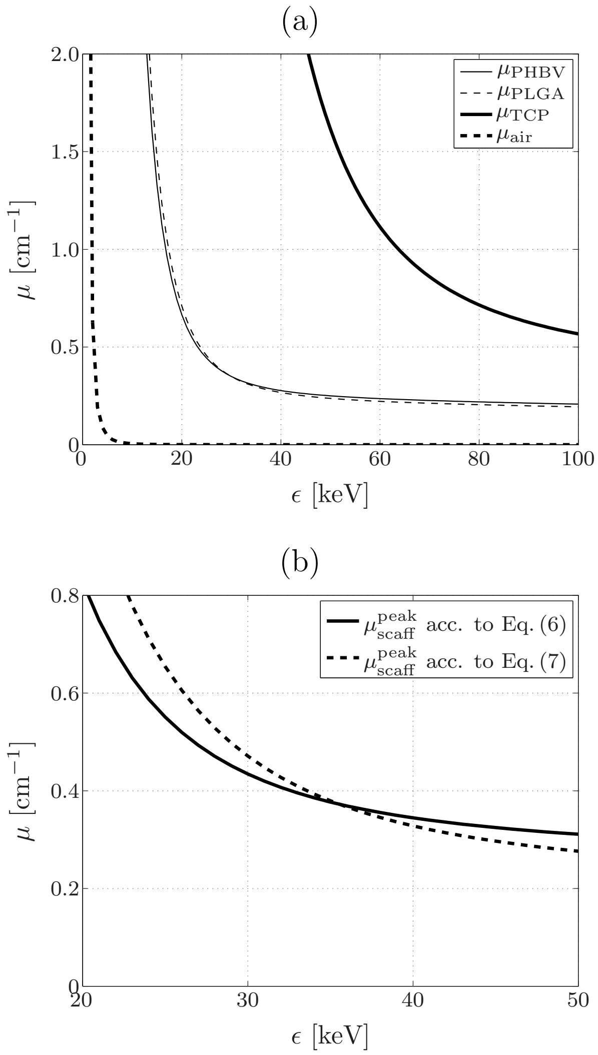

Figure 6.3: (a) X-ray attenuation coefficients of PHBV, PLGA, TCP, and air, as functions of the photon energy, according to the NIST-database [Hubbel and Seitzer, 2004]; (b) $\mu_{\text{scaff}}^{\text{peak}}(\epsilon)$ according to both Eqs. (6.6) and (6.7), exhibiting an intersection at $\epsilon = 35.55\,\text{keV}$

mixture of the composite material, see Section 6.2, and consider the intersection of the two graphs, see Figure 6.3. This intersection gives then access to the photon energy that is required in order to reach equality between Eqs. (6.6) and (6.7), $\epsilon = 35.55\,\text{keV}$, and, via Eqs. (6.4) and (6.5) to $a = 0.0145\,\text{cm}^{-1}$ and $b = -0.0330\,\text{cm}^{-1}$.

Finally, for calculating the voxel-specific material composition from the CT-data, we consider the simplification that in the CT data, due the very similar attenuation behavior of PHBV and PLGA, the polymers can be hardly distinguished. Thus, Eq. (6.7) is accordingly reformulated, for quantifying the attenuation coefficient of a composite material in voxel i, yielding

$$\mu^i = \mu_{\text{poly}} \left(1 - f^i_{\text{TCP}}\right) + \mu_{\text{TCP}} f^i_{\text{TCP}} \,, \tag{6.8}$$

where μ_{poly} is the attenuation coefficient of the polymer, $\mu_{\text{poly}} = (\mu_{\text{PHBV}} f_{\text{PHBV}} + \mu_{\text{PLGA}} f_{\text{PLGA}})/(f_{\text{PHBV}} + f_{\text{PLGA}})$, with the attenuation coefficients of PHBV and PLGA quantified for a photon energy of 35.55 keV, and respective volume fractions according to the composite mixture, and f^i_{TCP} is the volume fraction of TCP within voxel i. Specifying then again Eq. (6.1) for such a voxel, considering the voxel-specific grey value GV^i, and setting the resulting equation equal to Eq. (6.8) allows us to eventually derive the sought-after relation which gives access to the voxel-specific volume fraction of TCP:

$$f^i_{\text{TCP}} = \frac{\mu_{\text{poly}} - a \times \text{GV}^i - b}{\mu_{\text{poly}} - \mu_{\text{TCP}}} \,. \tag{6.9}$$

6.4 Computation of strain and stress fields across the scaffold when subjected to uniaxial compression

6.4.1 Finite Element model of scaffold structure

In order to study the structural behavior of the scaffold made up by the ternary composite consisting of PHBV, PLGA, and TCP, see Section 6.2, large-scale numerical computations, by means of the Finite Element (FE) method are performed. For this purpose, a FE model is built from the three-dimensional distribution of grey values obtained from CT scanning, see Figure 6.4. In order to minimize computation time, one finite element actually represents a group of voxels; in this work, we have considered grouping of $8\times8\times8$, $7\times7\times7$, $6\times6\times6$, $5\times5\times5$, $4\times4\times4$, $3\times3\times3$, and $2\times2\times2$ voxels into one finite element, yielding FE meshes consisting of 39757, 59443, 98898, 166058, 318306, 761631 and 2575100 elements (i.e. cubic elements with tri-linear shape functions, each element consisting of eight nodes).

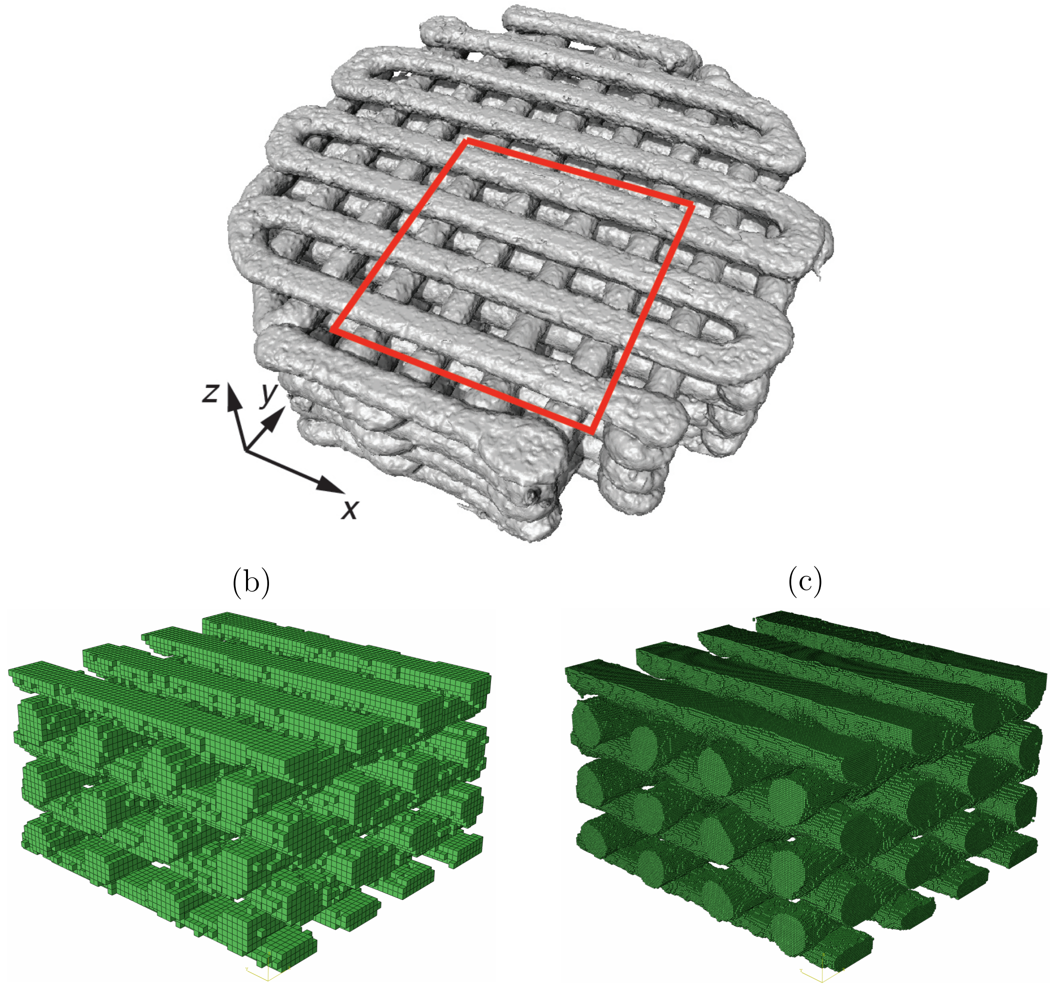
(a)

(b)

(c)

Figure 6.4: (a) Three-dimensional reconstruction of the scaffold structure based on the data obtained from microCT imaging, with indication of the rectangular prism cut out of the reconstructed scaffold structure serving as basis for the FE models; FE models with varying accuracy, i.e. consisting of (b) 59443 elements (with 7 × 7 × 7 voxels combined into one element), and of (c) 2575100 elements (with 2 × 2 × 2 voxels combined into one element)

Notably, the grey values of all voxels making up one finite element are averaged,

$$\mathrm{GV}^k = \frac{1}{N_k} \sum_{i}^{N_k} \mathrm{GV}^i \,, \tag{6.10}$$

and the resulting three-dimensional field of finite element-specific grey values is translated into a corresponding distribution of TCP and polymer matrix volume fractions, as described in detail in Section 6.3.2.

6.4.2 Microstructure-based elastic constants by means of micromechanical homogenization

Elastic constants have to be assigned to each finite element, in order to mechanically characterize the simulated material. In the present case, this task is not straightforward since each finite element potentially contains more than one constituent. Provided that the so-called "separation of scales"-requirement is fulfilled, continuum micromechanical homogenization can be employed for that purpose [Hill, 1965a,b, Zaoui, 2002]. In particular, the aforementioned requirement relates to the characteristic lengths of a representative volume element (RVE), denoted as ℓ_{RVE} – in our case this is the side length of a finite element – and of the heterogeneities found within the RVE, denoted as d_{RVE}, $d_{\text{RVE}} \ll \ell_{\text{RVE}}$. It could be shown that the condition $\ll$ is already adequately fulfilled if ℓ_{RVE} is approximately twice as large as d_{RVE} [Drugan and Willis, 1996]. In general, the microstructure within one RVE is so complicated that it cannot be described in complete detail. Therefore, quasi-homogeneous subdomains with known physical properties are reasonably chosen. They are called material phases, typically comprising solid and pore phases. The homogenized (upscaled) elastic behavior of the material on the observation scale of the RVE, i.e. the relation between homogeneous deformations acting on the boundary of the RVE and the resulting macroscopic (average) stresses can then be estimated from the elastic behavior of the material phases, their volume fractions within the RVE, their characteristic shapes, and their interactions. If a single phase exhibits a heterogeneous microstructure itself, its mechanical behavior can be estimated by introduction of an RVE within this phase, with dimensions $\ell_{\text{RVE},2} \leq d_{\text{RVE}}$, comprising again smaller phases with characteristic length $d_{\text{RVE},2} \ll \ell_{\text{RVE},2}$, and so on. This leads to a multistep homogenization scheme. In the present context, we perform a two-step homogenization scheme. First, PHBV and PLGA are homogenized into one polymer material. Thereafter, the latter and TCP are homogenized into the scaffold material appearing in a voxel-specific manner in the microCT image.

In homogenization step I, we consider the two polymer phases, PHBV and PLGA, as one polymer matrix, with quasi-spherical PLGA inclusions distributed uniformly throughout the PHBV matrix. This calls for a Mori-Tanaka-type scheme for homogenizing the stiffness of the polymer matrix [Benveniste, 1987, Mori and

Tanaka, 1973], reading as

$$\mathbb{C}_{\mathrm{poly}} = \left\{ f_{\mathrm{PHBV}} \mathbb{C}_{\mathrm{PHBV}} + f_{\mathrm{PLGA}} \mathbb{C}_{\mathrm{PLGA}} \times \left[\mathbb{I} + \mathbb{P}^{\mathrm{PHBV}}_{\mathrm{sph}} : (\mathbb{C}_{\mathrm{PLGA}} - \mathbb{C}_{\mathrm{PHBV}}) \right]^{-1} \right\} : \left\{ f_{\mathrm{PHBV}} \mathbb{I} + f_{\mathrm{PLGA}} \left[\mathbb{I} + \mathbb{P}^{\mathrm{PHBV}}_{\mathrm{sph}} : (\mathbb{C}_{\mathrm{PLGA}} - \mathbb{C}_{\mathrm{PHBV}}) \right]^{-1} \right\}^{-1} \tag{6.11}$$

where $\mathbb{c}_{\mathrm{PHBV}}$ and $\mathbb{c}_{\mathrm{PLGA}}$ are the stiffness tensors of the PHBV matrix and of the PLGA inclusions, $\mathbb{I}$ is the fourth-order unit tensor, and $\mathbb{P}^{\mathrm{PHBV}}_{\mathrm{sph}}$ is the fourth-order Hill tensor relating to spherical inclusions embedded in a matrix of isotropic stiffness $\mathbb{c}_{\mathrm{PHBV}}$. As both polymer phases are isotropic, their stiffness tensors are each fully defined by two elastic constants, through

$$\mathbb{c}_{\mathrm{PHBV}} = 3k_{\mathrm{PHBV}} \mathbb{K} + 2G_{\mathrm{PHBV}} \mathbb{J} = \frac{E_{\mathrm{PHBV}}}{1 - 2\nu_{\mathrm{PHBV}}} \mathbb{K} + \frac{E_{\mathrm{PHBV}}}{1 + \nu_{\mathrm{PHBV}}} \mathbb{J} \tag{6.12}$$

and

$$\mathbb{c}_{\mathrm{PLGA}} = 3k_{\mathrm{PLGA}} \mathbb{K} + 2G_{\mathrm{PLGA}} \mathbb{J} = \frac{E_{\mathrm{PLGA}}}{1 - 2\nu_{\mathrm{PLGA}}} \mathbb{K} + \frac{E_{\mathrm{PLGA}}}{1 + \nu_{\mathrm{PLGA}}} \mathbb{J} \,. \tag{6.13}$$

In Eqs. (6.12) and (6.13), k_j, G_j, E_j, and ν_j are the bulk modulus, the shear modulus, the Young's modulus, and the Poisson's ratio of phase j, $j = \mathrm{PHBV}, \mathrm{PLGA}$; accessible from experiments, see Table 6.1. Furthermore, $\mathbb{K}$ is the volumetric part of the fourth-order unit tensor, with components $K_{ijkl} + 1/3\delta_{ij}$, δ_{ij} being the Kronecker-delta, and $\mathbb{J}$ is the deviatoric part of the fourth-order unit tensor, $\mathbb{J} = \mathbb{I} - \mathbb{K}$. $\mathbb{P}^{\mathrm{PHBV}}_{\mathrm{sph}}$ is defined via the fourth-order Eshelby-tensor, $\mathbb{S}^{\mathrm{PHBV}}_{\mathrm{sph}}$ [Eshelby, 1957], through

$$\mathbb{P}^{\mathrm{PHBV}}_{\mathrm{sph}} = \mathbb{S}^{\mathrm{PHBV}}_{\mathrm{sph}} : (\mathbb{c}_{\mathrm{PHBV}})^{-1} \,, \tag{6.14}$$

while for spherical inclusions embedded in an isotropic matrix made up by PHBV $\mathbb{S}^{\mathrm{PHBV}}_{\mathrm{sph}}$ reads as

$$\mathbb{S}^{\mathrm{PHBV}}_{\mathrm{sph}} = \frac{3k_{\mathrm{PHBV}}}{3k_{\mathrm{PHBV}} + 4G_{\mathrm{PHBV}}} \mathbb{K} + \frac{6(k_{\mathrm{PHBV}} + 2G_{\mathrm{PHBV}})}{5(3k_{\mathrm{PHBV}} + 4G_{\mathrm{PHBV}})} \mathbb{J} \,. \tag{6.15}$$

In homogenization step II, we deal with the scaffold materialcontained in finite element k, which is also considered to exhibit a matrix-inclusion morphology, with TCP inclusions of approximately spherical shape embedded in the polymer matrix.

Table 6.1: Young's moduli and Poisson's ratios of the constituents of the composite material studied in this paper

Material	Young's modulus [GPa]	Poisson's ratio [–]
PHBV	4.70 [Luczynski et al., 2012]	0.35 [Simbara et al., 2015]
PLGA	2.00 [Gentile et al., 2014]	0.25 [Brady et al., 2015]
TCP	114.04 [Kublik et al., 2012]	0.27 [Kublik et al., 2012]

Accordingly, the homogenized stiffness $\mathbb{C}^i_{\text{scaff}}$ follows as well from a Mori-Tanaka-type scheme, of the format

$$\begin{aligned}\mathbb{C}^k_{\text{scaff}} =& \left\{ (1 - f^k_{\text{TCP}})\mathbb{c}_{\text{poly}} + f^k_{\text{TCP}}\mathbb{c}_{\text{TCP}} \times \left[\mathbb{I} + \mathbb{P}^{\text{poly}}_{\text{sph}} : (\mathbb{c}_{\text{TCP}} - \mathbb{c}_{\text{poly}}) \right]^{-1} \right\} : \\ & \left\{ 1 - f^k_{\text{TCP}})\mathbb{I} + f^k_{\text{TCP}} \left[\mathbb{I} + \mathbb{P}^{\text{poly}}_{\text{sph}} : (\mathbb{c}_{\text{TCP}} - \mathbb{c}_{\text{poly}}) \right]^{-1} \right\}^{-1} ,\end{aligned} \tag{6.16}$$

where $\mathbb{c}_{\text{poly}}$ is the stiffness tensor of the polymer matrix following from Eq. (6.11), $\mathbb{P}^{\text{poly}}_{\text{sph}}$ is the Hill tensor relating to spherical inclusions embedded in an isotropic matrix of stiffness $\mathbb{c}_{\text{poly}}$, and $\mathbb{c}_{\text{TCP}}$ is the stiffness tensor of TCP. While $\mathbb{P}^{\text{poly}}_{\text{sph}}$ is defined analogously to $\mathbb{P}^{\text{PHBV}}_{\text{sph}}$, see Eqs. (6.14) and (6.15), $\mathbb{c}_{\text{TCP}}$ is again defined via the respective elastic constants,

$$\mathbb{c}_{\text{TCP}} = 3k_{\text{TCP}}\mathbb{K} + 2G_{\text{TCP}}\mathbb{J} = \frac{E_{\text{TCP}}}{1 - 2\nu_{\text{TCP}}}\mathbb{K} + \frac{E_{\text{TCP}}}{1 + \nu_{\text{TCP}}}\mathbb{J} \tag{6.17}$$

see Table 6.1 for experimentally obtained Young's modulus E_{TCP} and Poisson's ration ν_{TCP}. The finite element-specific, grey value-dependent isotropic stiffness tensor of the scaffold material, following from evaluation of Eq. (6.16), is again fully defined by two elastic constants, e.g. by Young's modulus E^k_{scaff},

$$E^k_{\text{scaff}} = \frac{1}{D^k_{\text{scaff},1111}} , \tag{6.18}$$

and Poisson's ratio ν^k_{scaff},

$$\nu^k_{\text{scaff}} = -\frac{D^k_{\text{scaff},1122}}{D^k_{\text{scaff},1111}} , \tag{6.19}$$

where $D^k_{\text{scaff},1111}$ and $D^k_{\text{scaff},1122}$ are components of compliance tensor $\mathbb{D}^k_{\text{scaff}}$, $\mathbb{D}^k_{\text{scaff}} = (\mathbb{C}^k_{\text{scaff}})^{-1}$, see Figures 6.5(b) and (c) for the heterogeneous distribution of Young's modulus and Poisson's ratio across the scaffold, following from the described analysis modality.

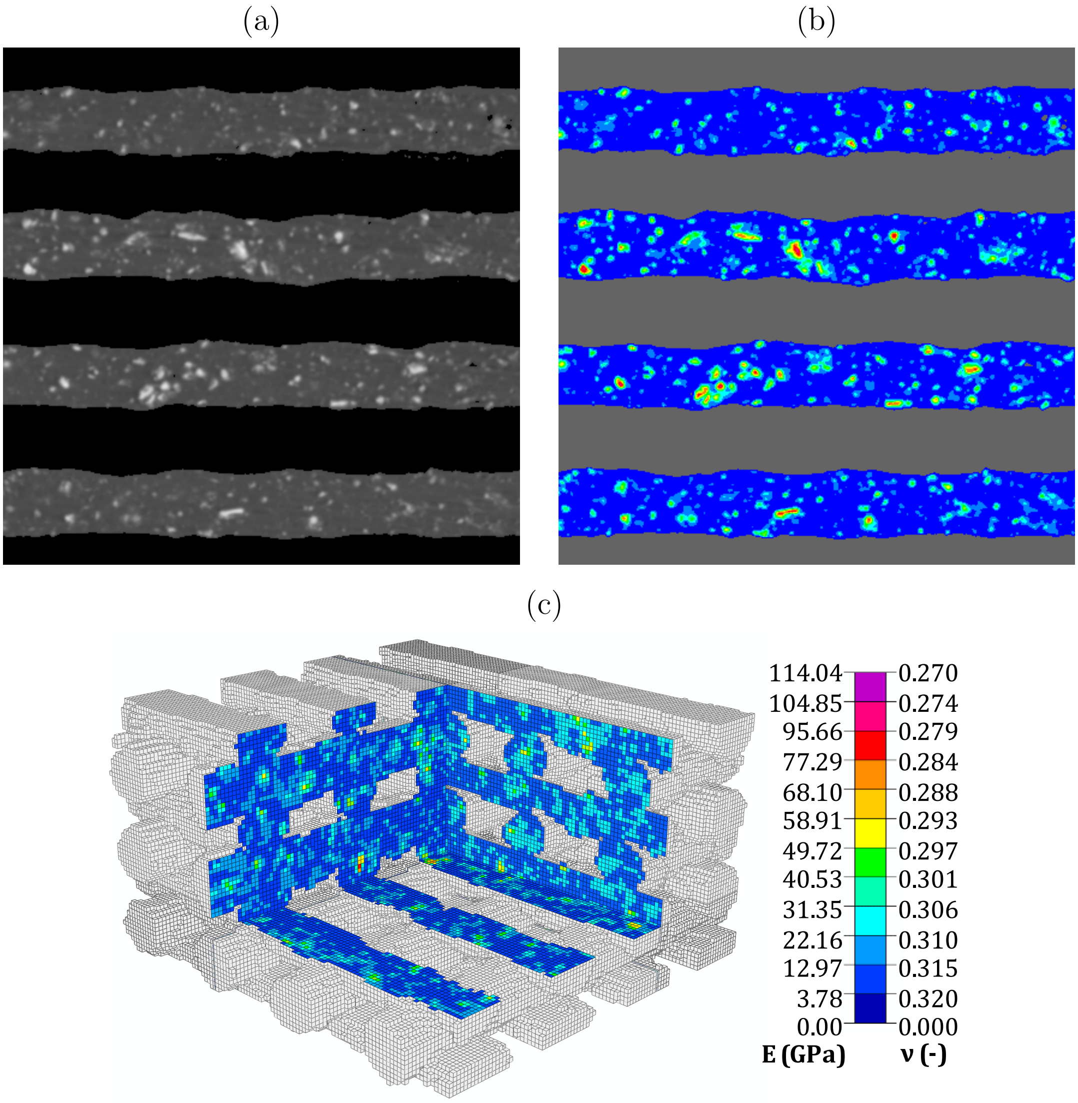
(a)
(b)
(c)
114.04
104.85
95.66
77.29
68.10
58.91
49.72
40.53
31.35
22.16
12.97
3.78
0.00
E (GPa)
0.270
0.274
0.279
0.284
0.288
0.293
0.297
0.301
0.306
0.310
0.315
0.320
0.000
ν (-)

Figure 6.5: Distribution of elastic Young's modulus and Poisson's ratio across the scaffold; (a) underlying CT-derived distribution of grey values in specific cross-section, and (b) corresponding distribution of Young's modulus and Poisson's ratio; (c) three-dimensional distribution of these elastic constants; one finite element follows from merging of $3 \times 3 \times 3$ voxels, with grey value averaging according to Eq. (6.10)

6.4.3 Boundary and loading conditions

The FE simulations were implemented by means of the commercial FE software Abaqus, version 6.14. The bottom surface of FE models, see Figure 6.4(c), were fixed in z-direction, allowing there displacements only in x- and y-direction. The lateral surfaces were allowed to deform without any constraints, and thus stress-free. The top surfaces were subjected to a displacement of 5 % of the scaffold height, implying uniaxial compressive loading in z-direction.

6.5 Numerical results

First, it was made sure that a sufficiently fine FE mesh was considered. For this purpose, FE meshes with varying fineness, see Section 6.4.1, were subjected to uniaxial compression (as described in Section 6.4.3). The simulation results were evaluated in terms of elastic strain energy, and it turned out that a merging factor of 3 – i.e., one finite element consists of $3 \times 3 \times 3 = 27$ voxels – is adequate; thus, the change in total elastic strain energy due to further refinement of the FE mesh is negligible.

Next, the effect of the scaffold heterogeneity on the strain and stress distributions during elastic deformations was studied, see Figure 6.6 for the distributions of minimum principal strains and minimum principal stresses, for both heterogeneously distributed polymer and TCP volume fractions, and an (average) homogeneous scaffold composition. The simulations have revealed that neglecting the heterogeneities in the scaffold material that become apparent from microCT scanning would lead to underestimation of strains and stresses, at least at specific locations. Moreover, the simulations confirm that the fiber junctions are the parts of the scaffold which must sustain the highest mechanical loads.

6.6 Discussion

In this paper, a previously developed analysis modality for microCT scans of polymer-based scaffold materials [Luczynski et al., 2012] has been successfully extended from a two-phase to a three-phase composite, thereby considering an improved physical foundation. In particular, in the aforementioned work [Luczynski et al., 2012] translation of grey values into corresponding constituent volume fractions relied on an educated guess concerning the grey value relating to the TCP inclusions. On this conceptual basis, the following relation between grey value and TCP volume fraction could be derived:

$$f^i_{\mathrm{TCP}} = \frac{\mathrm{GV}^i - \mathrm{GV}_{\mathrm{poly}}}{\mathrm{GV}^{\mathrm{est}}_{\mathrm{TCP}} - \mathrm{GV}_{\mathrm{poly}}}\,, \tag{6.20}$$

where $\mathrm{GV}^{\mathrm{est}}_{\mathrm{TCP}}$ is an estimate for the grey value relating to pure TCP. Here, we have instead taken into account the linear, photon energy-dependent relation between grey values and attenuation coefficients, see Eq. (6.1), eventually leading to

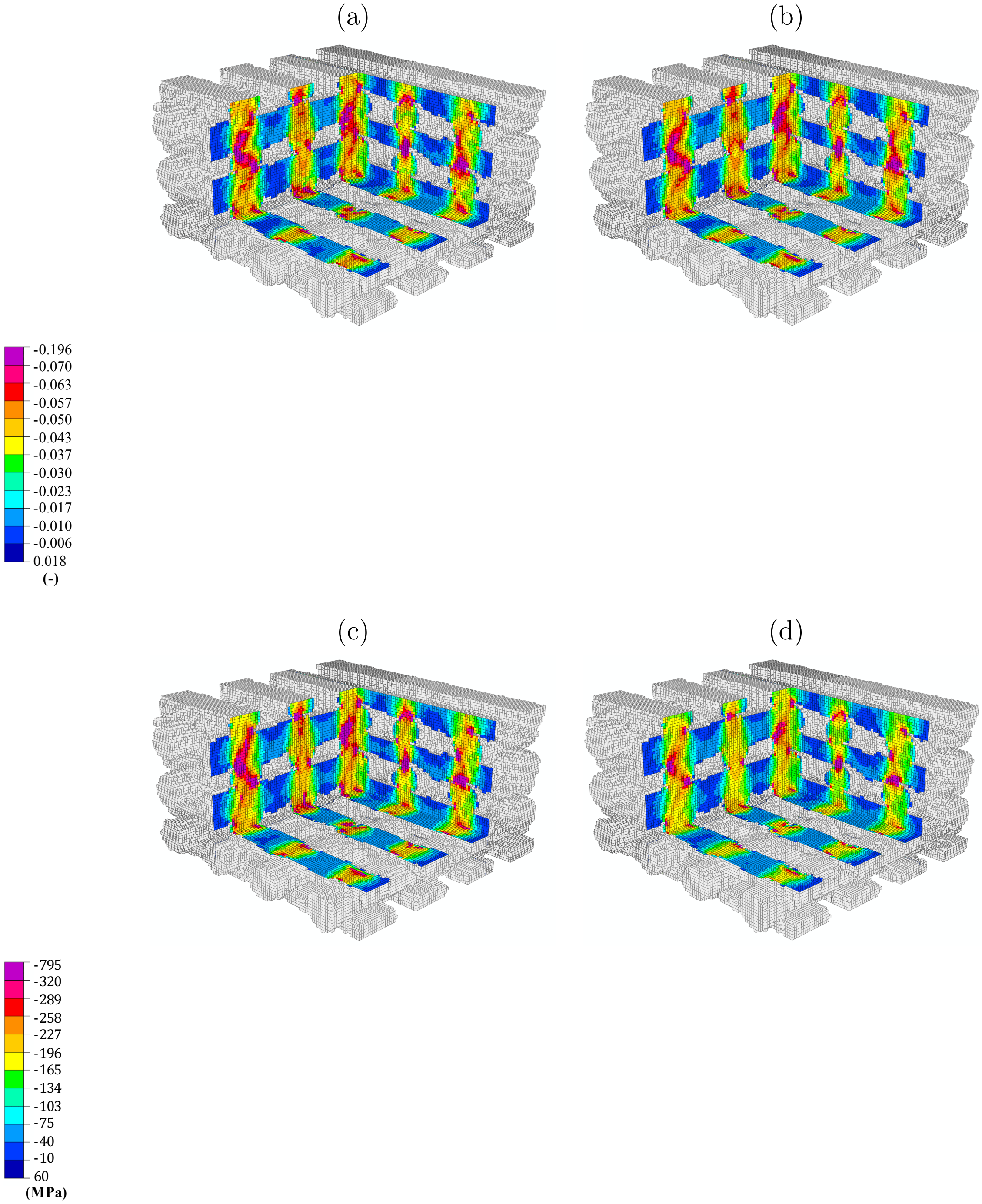
(a)
(b)
-0.196
-0.070
-0.063
-0.057
-0.050
-0.043
-0.037
-0.030
-0.023
-0.017
-0.010
-0.006
0.018
(-)
(c)
(d)
-795
-320
-289
-258
-227
-196
-165
-134
-103
-75
-40
-10
60
(MPa)

Figure 6.6: Distributions of minimum principal strains (a) and (b), as well as minimum principal stresses (c) and (d) across the scaffold when subjected to uniaxial compression; based on a heterogeneously distributed scaffold composition (a) and (c), as well as on a homogeneous scaffold composition (b) and (d); the FE model has been built by merging $3 \times 3 \times 3$ voxels into one finite element, leading to 761631 elements

Eq. (6.9). It is now instructive to compare the two approaches. Eq. (6.9) gives access to the true grey value representing pure TCP, namely $\mathrm{GV}_{\mathrm{TCP}}^{\mathrm{true}} = 261.8$. In the work of Luczynski et al. [2012], on the other hand, $\mathrm{GV}_{\mathrm{TCP}}^{\mathrm{est}}$ was simply assumed to be the brightest voxel in the CT data, thus $\mathrm{GV}_{\mathrm{TCP}}^{\mathrm{est}} = 255$. The small difference between $\mathrm{GV}_{\mathrm{TCP}}^{\mathrm{true}}$ and $\mathrm{GV}_{\mathrm{TCP}}^{\mathrm{est}}$ implies that the difference between f_{TCP}^{i} according to Eq. (6.9) and f_{TCP}^{i} according to Eq. (6.20) is negligibly small as well, amounting at most to only a few percent. This finding confirms the assumption concerning $\mathrm{GV}_{\mathrm{TCP}}^{\mathrm{est}}$ that was made in [Luczynski et al., 2012], but at the same time clarifies that this assumption would fail dramatically for a larger CT resolution; namely, in the latter case, the brightest voxel would most likely not adequately represent pure TCP.

In summary, the here presented results confirm the adequacy of the proposed analysis modality applicable to CT scans of composite materials, providing adequate input data for simulation of the structural behavior of such materials, e.g. by means of the Finite Element method. In the future, in order to provide even more insights, the present approach may be extended towards micromechanical estimation of the material's strength, thereby paving the way for a computational fracture risk assessment tool.

Acknowledgments

The authors gratefully acknowledge COST action NEWGEN – New Generation Biomimetic and Customized Implants for Bone Engineering (MP1301), in the framework of which the first author of this paper could undertake a short-term scientific mission (STSM) at Vienna University of Technology. Moreover, this work has been supported by the National Centre for Research and Development of Poland (Pol-Nor/202132/68/2013), and by the National Science Centre of Poland (DEC-2012/07/D/ST8/02606).

6.7 Nomenclature

a, b	coefficients for determination of the attenuation coefficients
$\mathbb{c}_j$	stiffness tensor of material phase j, j representing PHBV, PLGA, the polymer matrix, or TCP
$\mathbb{C}^k_{\text{scaff}}$	stiffness tensor of scaffold material in finite element k
d_{RVE}	characteristic length of heterogeneities within in RVE
$\mathbb{D}^k_{\text{scaff}}$	compliance tensor of scaffold material in finite element k
$D^k_{\text{scaff},ijkl}$	$ijkl$-th component of $\mathbb{D}^k_{\text{scaff}}$
E^k_{scaff}	Young's modulus of the scaffold material in finite element k
E_j	Young's modulus of material phase j, j representing PHBV, PLGA, or TCP
f_j	volume fraction of material phase j, j representing PHBV or PLGA
f^i_{TCP}	volume fraction of TCP in voxel i
f^k_{TCP}	volume fraction of TCP in finite element k
FE	Finite Element
G_j	shear modulus of material phase j, j representing PHBV, PLGA, or TCP
GV^i	grey value in voxel i
GV^k	grey value in finite element k
$\text{GV}^{\text{peak}}_{\text{air}}$	grey value peak relating to air
$\text{GV}^{\text{peak}}_{\text{PHBV}}$	grey value peak relating to PHBV
GV_{poly}	grey value peak relating to polymer matrix
$\text{GV}^{\text{est}}_{\text{TCP}}$	estimate of the grey value relating to pure TCP
$\text{GV}^{\text{true}}_{\text{TCP}}$	true grey value relating to pure TCP
$\mathbb{I}$	fourth-order unit tensor
$\mathbb{J}$	deviatoric part of $\mathbb{I}$
$\mathbb{K}$	volumetric part of $\mathbb{I}$
k_j	bulk modulus of material phase j, j representing PHBV, PLGA, or TCP
ℓ_{RVE}	characteristic length of RVE
N_k	number of voxels which are combined into one finite element
$\mathbb{P}^{\text{PHBV}}_{\text{sph}}$	Hill-tensor relating to spherical inclusions embedded in matrix with stiffness $\mathbb{c}_{\text{PHBV}}$
$\mathbb{P}^{\text{poly}}_{\text{sph}}$	Hill-tensor relating to spherical inclusions embedded in matrix with stiffness $\mathbb{c}_{\text{poly}}$
PHBV	poly(3-hydroxybutyrate-co-3-hydroxyvalerate)
PLGA	poly(lactic-co-glycolide)
RVE	representative volume element
$\mathbb{S}^{\text{PHBV}}_{\text{sph}}$	Eshelby-tensor relating to spherical inclusions embedded in matrix with stiffness $\mathbb{c}_{\text{PHBV}}$
TCP	tricalcium phosphate hydrate

δ_{ij}	Kronecker-delta, $\delta_{ij} = 1$ if $i = j$, and $\delta_{ij} = 0$ if $i \neq j$
ϵ	photon energy
μ^i	attenuation coefficient of voxel i
μ_j	attenuation coefficient of material phase j, j representing air, PHBV, PLGA, the polymer matrix, or TCP
$\mu_{\text{scaff}}^{\text{peak}}$	attenuation coefficient of scaffold material at the respective grey value peak
ν_{scaff}^k	Poisson's ratio of the scaffold material in finite element k
ν_j	Poisson's ration of material phase j, j representing PHBV, PLGA, or TCP

Chapter 7

A continuum micromechanics approach to the elasticity of planar fiber networks and its application to paper

Authored by: Pedro Miguel J.S. Godinho, Leopold Wagner, Viktoria Vass, Josef Eberhardsteiner, and Christian Hellmich

Published in: *CD-ROM Proceedings for the World Conference on Timber Engineering (WCTE 2016)*, ISBN: 978-3-903039-00-1, Paper ID 1074, 8 pages, 2016

Contribution: Christian Hellmich and Josef Eberhardsteiner set up the overall research strategy. Christian Hellmich supervised the research progress, and checked the key results. Pedro Miguel J.S. Godinho developed the Matlab code, carried out model validation based on the experimental data he found in the literature. Leopold Wagner and Viktoria Vass supported Pedro Miguel J.S. Godinho during model implementation, code verification, contributed to all the scientific discussions, and to the documentation of research results.

Abstract

Given the eminent role of structure-property relations in paper production, it is not surprising that various mathematical models for the mechanical interaction of pulp fibers within the overall material "paper" have been proposed. However, all these approaches did not explicitly account for the scale difference between the loads applied to the overall material and those acting on the level of the individual fiber. We here fill this essential conceptual gap by the development of a new micromechanics model: We first recall the fundamental micromechanical concept of the representative volume element (RVE) and the corresponding stress and strain average rules, before we specify these rules for planar networks such as paper material. Then we introduce elastic material behavior at the fiber level, and derive so-called concentration relations for upscaling this behavior to the planar network level. Combination of these relations with matrix-inclusion problems of the Eshelby-Laws type yields closed-form semianalytical expressions for the paper stiffness tensor, as function of fiber stiffness and porosity. The model, which is confirmed by various experimental data and which highlights the importance of the fiber's anisotropy for the overall elastic behavior, is deemed as a new support tool in the design of paper production processes.

7.1 Introduction

The elastic properties of any micro-heterogeneous material depend on its inherent microstructure. One class of micro-heterogeneous materials are so-called fibrous materials. Their microstructure is made up of fiber networks where the individual fibers are connected via fiber-fiber bonds. In the majority of cases, the fibers are more or less parallel to one plane; then one speaks of planar fibrous materials. Planar fibrous materials find numerous applications, which range from thermal and sound insulators, tissue templates, as well as gas and fluid fillers, to various paper product applications, including healthcare applications [Wu and Dzenis, 2005]. One particularly widespread planar fibrous material is paper, a network of mechanically and/ or chemically treated wood fibers, so-called pulp fibers (see Figure 7.1). In all the aforementioned applications, as well as in paper production, the mechanical properties, such as elasticity and strength of the planar networks, are of crucial importance. Therefore, it is not surprising that numerous mathematical models for the mechanical behavior ofpaper and paper-like materials have been proposed. Various researchers [Harrysson and Ristinmaa, 2008, Mäkelä and Östlund, 2003] have developed anisotropic elasto-plastic models relating stresses and strains directly at the paper material level. In such approaches, heuristic "anisotropy factors" need to be introduced, and to be tuned according to data from experiments on the fiber networks, such as homogeneously loaded paper sheets. However, it is the arrangement of the fibers and their mechanical properties, which actually govern the mechanical properties of the overall paper-like material, both in terms of magnitude and of (transversely isotropic or orthotropic) symmetry [Mann et al., 1980, Mark et al., 2002, Uesaka et al., 1980]. This has motivated more profound modeling approaches, which explicitly refer to microstructural details: A straightforward approach was given by Cox [1952], who first of all proposed that the fibers are deformed primarily in tension (so that shear and bending deformations can be neglected). Then, he partitioned, on a purely geometrical basis, the strains acting on a planar mat of fibers, i.e. on the paper-like material, into components relating to the orientation of individual fibers; and assumed that these new strain components would satisfactorily describe the deformation state at the microstructural level of the fiber. From a strict physical viewpoint, this would mean that all fibers would span throughout the entire mat, which is not necessarily the case. Hence, the Cox model has been modified, in order to account for more realistic "stress transfer mechanisms" [Åström et al., 1994]. Other researchers [Schulgasser, 1981, Wu and Dzenis, 2005] extended the Cox model from the case of tensile deformations of the fibers, to that of tension, shear, and/ or bending. What counts in the end, is whether such models predict reasonably well the experimentally tested material at the paper sheet level; and in this context, the Cox model and its extension to fiber shear deformations [Cox, 1952] do quite well, while - to the knowledge of the authors - no remarkable improvement of model predictions related to fiber bending deformations could be shown so far. This motivates us to focus on tensile/ shear fiber deformation characteristics, and to invest into a rigorous theoretical formulation which explicitly differentiates between a micro-scale (where micro-strains and micro-stresses relate to fiber characteristics) and a macro-scale (where macro-strains and macro-stresses relate to the behavior of the fibrous material, which is e.g. tested by deforming paper sheets). Our formulation is cast within the framework of continuum micromechanics [Suquet, 1997a, Zaoui, 2002], which has been recently adapted for 3D (spatial) networks of solid fibers (or needles) [Fritsch et al., 2006, 2009a, 2010a, 2013a, Pichler et al., 2009, Sanahuja et al., 2009]. Given the excellent experimental validation of the aforementioned mathematical models, we here tackle the development of a similar theoretical concept for planar networks. The remainder of the present paper is organized as follows: We first recall the fundamental micromechanical concept of the representative volume element (RVE) and the corresponding stress and strain average rules (Section 2.1), before we specify these rules for planar networks such as paper material (Section 7.2.2). Then we introduce elastic material behavior at the fiber level, and derive so-called concentration relations for upscaling this behavior to the planar network level (Sections 7.2.3). Combination of these relations with matrix-inclusion problems of the Eshelby-Laws type yield closed-form semi-analytical expressions for the paper stiffness tensor, as function of fiber stiffness and porosity (Section 7.2.4). Characteristics of these expressions are presented in the Results and Discussion section (Section 7.3), as is the experimental validation of our new micromechanics model.

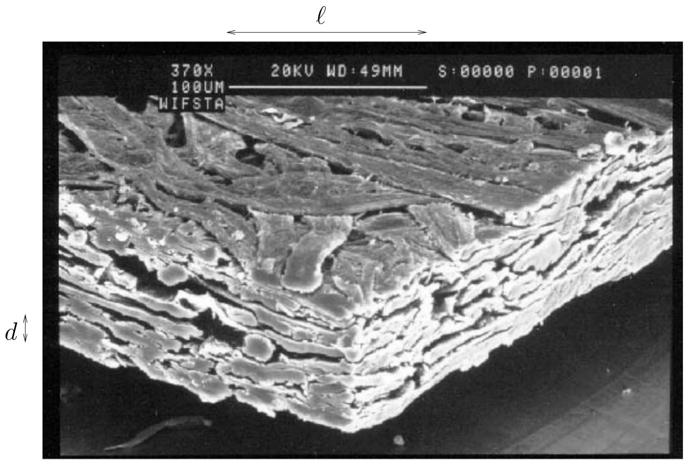

Figure 7.1: SEM micrograph of paper exhibiting a porous pulp fiber network predominantly oriented within the paper plane, permission for reproduction granted by Tryding [1996].

7.2 Micromechanics model

7.2.1 Representative volume element - stress and strain average rules

The starting point for any continuum micromechanics model is the consideration of a representative volume element (hereafter: RVE) with characteristic length ℓ fulfilling the separation of scale conditions [Zaoui, 2002], i.e. $\mathscr{L} \gg \ell \gg d$, whereby $\mathscr{L}$ stands for the characteristic lengths of the geometry or loading of a structure built up by the solid material defined on the RVE, and d stands for the characteristic length of inhomogeneities within the RVE, respectively (see Figures 7.1 and 7.2). In the case of paper, the approximate sizes of ℓ and d are 100 μm and 20 μm, respectively (see Figure 7.1). For the subsequent mathematical derivations, the RVE is considered as a continuum itself, and any location within this RVE is quantified through the position vector $\mathbf{x}$. Furthermore, the RVE is loaded by

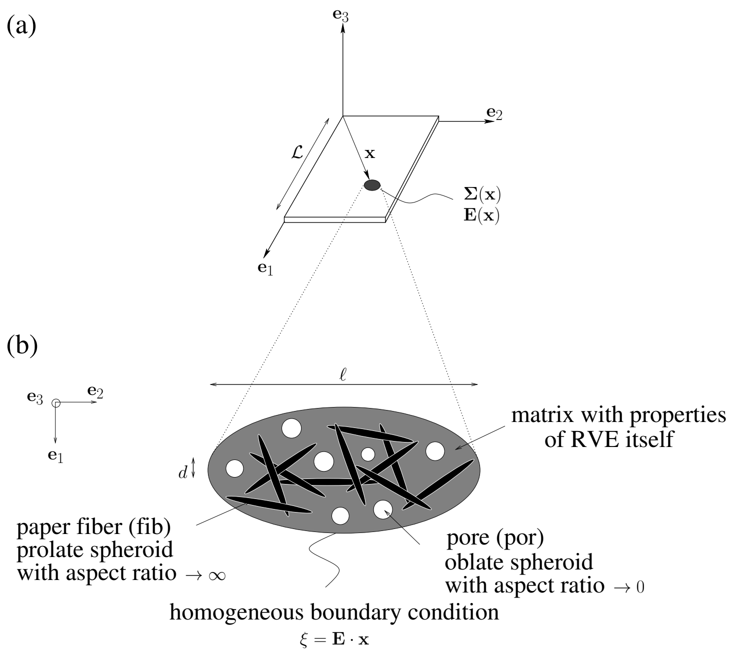
(a)
e3
e2
ℒ
x
Σ(x)
E(x)
e1
(b)
e3
e2
e1
ℓ
d
matrix with properties of RVE itself
paper fiber (fib) prolate spheroid with aspect ratio → ∞
pore (por) oblate spheroid with aspect ratio → 0
homogeneous boundary condition
ξ = E · x

Figure 7.2: (a) Planar sheet of length L, made of fibrous material (e.g. paper); $\mathbf{x}$ stands for the position vector labelling "material points", and $\mathbf{\Sigma}$ and $\mathbf{E}$ for (position-dependent, "macroscopic") stress and strain tensors prevailing at these material points; ($\mathbf{e}_1$, $\mathbf{e}_2$, $\mathbf{e}_3$) is an orthonormal base frame aligned with the sheet plane; (b) zooming out one material point, appearing as "representative volume element - RVE" at a length scale $\ell \ll \mathscr{L}$; the latter is made up of cylindrical fibers oriented in all planar directions, and of oblate spheroidal pores, which are aligned with the paper plane as well

traction forces, $\mathbf{T}(\mathbf{x})$, on its boundary, where homogeneous linearized macroscopic strains, $\mathbf{E}$, are prescribed in terms of compatible displacements (see Figure 7.2):

$$\forall \mathbf{x} \in \partial V_{RVE} : \qquad \boldsymbol{\xi}(\mathbf{x}) = \mathbf{E} \cdot \mathbf{x} \tag{7.1}$$

Compatibility of microscopic strains defined within the RVE imply the so-called strain average rule [Hashin, 1983]:

$$\mathbf{E} = \langle \boldsymbol{\varepsilon}(\mathbf{x}) \rangle = \frac{1}{V_{RVE}} \int_{V_{RVE}} \boldsymbol{\varepsilon}(\mathbf{x}) dV \tag{7.2}$$

Moreover, we apply the Principle of Virtual Power [Salençon, 2001], which considers simultaneously kinematic compatibility and equilibrium, to the aforementioned RVE material system, which yields the so-called stress average rule [Germain, 1973]:

$$\boldsymbol{\Sigma} = \langle \boldsymbol{\sigma}(\mathbf{x}) \rangle = \frac{1}{V_{RVE}} \int_{V_{RVE}} \boldsymbol{\sigma}(\mathbf{x}) dV \tag{7.3}$$

7.2.2 Morphological representation of planar fiber networks: material phases

The microstructure within an RVE of typical size ℓ as seen in Figure 7.1 is so complex that it cannot be described in full detail. Accordingly, the description of the RVE needs to be reduced to mechanically relevant details. This is standardly done by partitioning the RVE into sub-volumes with more or less homogeneous mechanical properties; these sub-volumes being called material phases. The mechanical state of these phases is then characterized by micro-stresses and micro-strains averaged over the aforementioned sub-volumes. In the case of paper, we choose an RVE which consists of a pore space, while the remaining space is filled by (one-dimensional) solid fibers which are characterized by orientation angles ϑ and φ, i.e. by the classical spherical coordinates. Then, pore strains and pore stresses, i.e. the strains and stresses averaged over the pore space, read as

$$\boldsymbol{\sigma}_{por} = \frac{1}{V_{por}} \int_{V_{por}} \boldsymbol{\sigma}(\mathbf{x}) dV \tag{7.4}$$

$$\boldsymbol{\varepsilon}_{por} = \frac{1}{V_{por}} \int_{V_{por}} \boldsymbol{\varepsilon}(\mathbf{x}) dV \tag{7.5}$$

while the stresses and strains characterizing the mechanical state in the solid (one-dimensional) fiber phase oriented in (ϑ, φ)-direction are given by the averages,

$$\boldsymbol{\sigma}_{fib}\left(\vartheta, \varphi\right) = \frac{1}{L_{fib}\left(\vartheta, \varphi\right)} \int_{L_{fib}(\vartheta,\varphi)} \boldsymbol{\sigma}(\mathbf{x}) dV \tag{7.6}$$

$$\boldsymbol{\varepsilon}_{fib}\left(\vartheta, \varphi\right) = \frac{1}{L_{fib}\left(\vartheta, \varphi\right)} \int_{L_{fib}(\vartheta,\varphi)} \boldsymbol{\varepsilon}(\mathbf{x}) dV \tag{7.7}$$

with $L_{fib}\left(\vartheta, \varphi\right)$ being the overall length of the fiber phase oriented in (ϑ, φ)-direction. Specification of the stress and strain average rules (7.2) and (7.3) for the phase stresses and phase strains according to (7.4)-(7.7) yields

$$\boldsymbol{\Sigma} = \frac{1-\phi}{4\pi} \int\int_{\varphi=0;\vartheta=0}^{2\pi,\pi} \boldsymbol{\sigma}_{fib}\left(\vartheta, \varphi\right) \sin\left(\vartheta\right) p\left(\vartheta, \varphi\right) d\vartheta d\varphi + \phi \boldsymbol{\sigma}_{por} \tag{7.8}$$

$$\mathbf{E} = \frac{1-\phi}{4\pi} \int\int_{\varphi=0;\vartheta=0}^{2\pi,\pi} \boldsymbol{\varepsilon}_{fib}\left(\vartheta, \varphi\right) \sin\left(\vartheta\right) p\left(\vartheta, \varphi\right) d\vartheta d\varphi + \phi \boldsymbol{\varepsilon}_{por} \tag{7.9}$$

with $p\left(\vartheta, \varphi\right)$ as the probability distribution function representing the three-dimensional arrangement of fibers. As all fibers are oriented parallel to the $\mathbf{e}_1$-$\mathbf{e}_2$ plane, where $\vartheta = \pi/2$, the probability distribution function relevant to our case reads as

$$p\left(\vartheta, \varphi\right) = 2\delta\left(\vartheta - \frac{\pi}{2}\right) \tag{7.10}$$

with δ denoting the Dirac distribution, so that (7.10) obviously fulfils the normalization condition:

$$\frac{1}{4\pi} \int\int_{\varphi=0;\vartheta=0}^{2\pi,\pi} \sin\left(\vartheta\right) p\left(\vartheta, \varphi\right) d\vartheta d\varphi = 1 \tag{7.11}$$

Specification of the stress and strain average rules (7.8) and (7.9) for the fiber distribution (7.10) yields:

$$\boldsymbol{\Sigma} = \frac{1-\phi}{2\pi} \int_{\varphi=0}^{2\pi} \boldsymbol{\sigma}_{fib}\left(\varphi\right) d\varphi + \phi \boldsymbol{\sigma}_{por} \tag{7.12}$$

$$\mathbf{E} = \frac{1-\phi}{2\pi} \int_{\varphi=0}^{2\pi} \boldsymbol{\varepsilon}_{fib}\left(\varphi\right) d\varphi + \phi \boldsymbol{\varepsilon}_{por} \tag{7.13}$$

We conclude that in the context of continuum micromechanics, the forms (7.12) and (7.13) of the stress and strain average rules are relevant for planar fibrous materials such as paper.

7.2.3 Elastic concentration problem - Micro-macro transition - Homogenized stiffness tensor

The present analysis is restricted to elasticity. Accordingly, the fiber stresses and strains are linked by a fiber elasticity tensor, $\mathbb{c}_{fib}$, reading as

$$\boldsymbol{\sigma}_{fib}\left(\varphi\right) = \mathbb{c}_{fib}\left(\varphi\right) : \boldsymbol{\varepsilon}_{fib}\left(\varphi\right) \tag{7.14}$$

and an analogous relation is employed for the pore phase,

$$\boldsymbol{\sigma}_{por} = \mathbb{c}_{por} : \boldsymbol{\varepsilon}_{por} \tag{7.15}$$

Linearity of the constitutive relations (7.14) and (7.15), together with the kinematical and equilibrium conditions described in Section 7.2.1, implies applicability of the superposition principle when solving the underlying differential equations, and hence the existence of strain concentration relations between macroscopic and phase-specific microscopic strains

$$\boldsymbol{\varepsilon}_{fib}\left(\varphi\right) = \mathbb{A}_{fib}\left(\varphi\right) : \mathbf{E} \tag{7.16}$$

$$\boldsymbol{\varepsilon}_{por} = \mathbb{A}_{por} : \mathbf{E} \tag{7.17}$$

with $\mathbb{A}_{fib}\left(\varphi\right)$ and $\mathbb{A}_{por}$, as the so-called pore and fiber strain concentration tensors. Insertion of concentration relations (7.16) and (7.17) into the microelastic laws (7.14) and (7.15) yields:

$$\boldsymbol{\sigma}_{fib}\left(\varphi\right) = \mathbb{c}_{fib}\left(\varphi\right) : \mathbb{A}_{fib}\left(\varphi\right) : \mathbf{E} \tag{7.18}$$

$$\boldsymbol{\sigma}_{por} = \mathbb{c}_{por} : \mathbb{A}_{por} : \mathbf{E} \tag{7.19}$$

Averaging stress expressions (7.18) and (7.19) over all phases according to Eq. (7.12), yields the following concentration tensor-based relation between the macroscopic stresses and strains, $\boldsymbol{\Sigma}$ and $\mathbf{E}$, respectively:

$$\boldsymbol{\Sigma} = \left[\frac{1-\phi}{2\pi}\int_{\varphi=0}^{2\pi} \mathbb{c}_{fib}\left(\varphi\right) : \mathbb{A}_{fib}\left(\varphi\right) d\varphi + \phi\mathbb{c}_{por} : \mathbb{A}_{por}\right] : \mathbf{E} \tag{7.20}$$

This gives access to the homogenized macroscopic stiffness tensor $\mathbb{C}^{hom}$, which standardly links $\mathbf{\Sigma}$ and $\mathbf{E}$, through:

$$\mathbf{\Sigma} = \mathbb{C}^{hom} : \mathbf{E} \tag{7.21}$$

Comparison of Eqs. (7.20) and (7.21), yields the following expression for $\mathbb{C}^{hom}$:

$$\mathbb{C}^{hom} = \frac{1-\phi}{2\pi} \int_{\varphi=0}^{2\pi} \mathbb{c}_{fib}\left(\varphi\right) : \mathbb{A}_{fib}\left(\varphi\right) d\varphi + \phi \mathbb{c}_{por} : \mathbb{A}_{por} \tag{7.22}$$

Expression (7.22), however, depends on the concentration tensors $\mathbb{A}_{fib}\left(\varphi\right)$ and $\mathbb{A}_{por}$, which are unknown so far. In the next step, they will be estimated on the basis of matrix-inclusion problems proposed by Eshelby [1957] and Laws [1977a]; in the context of a so-called self-consistent scheme.

7.2.4 Matrix inclusion problem based self consistent estimate for the strain concentration tensors

Each material phase (i.e. the pore phase and the infinitely many solid fiber phases lying in the paper plane) is represented by an ellipsoidal inclusion embedded into a fictitious infinite elastic matrix. The latter is loaded by fictitious strains $\mathbf{E}^{\infty}$ at its infinite boundary, and exhibits the stiffness of the homogenized material, $\mathbb{C}^{hom}$ (see Figure 7.3). This choice of matrix stiffness is a way to model mutual contact of all phases; i.e. a polycrystalline arrangement of theses phases. This will finally

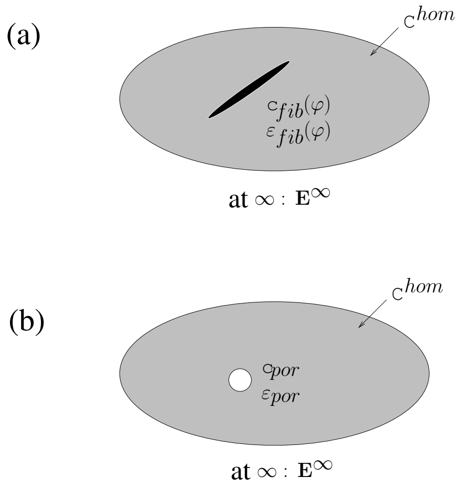
(a)
$\mathbb{c}^{hom}$
$\mathbb{c}_{fib}(\varphi)$
$\varepsilon_{fib}(\varphi)$
at ∞ : $\mathbf{E}^{\infty}$
(b)
$\mathbb{c}^{hom}$
$\mathbb{c}_{por}$
ε_{por}
at ∞ : $\mathbf{E}^{\infty}$

Figure 7.3: Eshelby-Laws inclusion problem representation for (a) infinitely many fiber phases, and (b) one pore phase

lead to a so-called self-consistent homogenization scheme [Zaoui, 2002]. In the case of the fiber phases, the aforementioned inclusion is a circular cylinder, i.e. an ellipsoid with a slenderness ratio going to infinity and an aspect ratio of one. The homogeneous strains in such an inclusion follow as

$$\boldsymbol{\varepsilon}_{fib}\left(\varphi\right) = \left[\mathbb{I} + \mathbb{P}^{hom}_{cyl}\left(\varphi\right) : \left(\mathbb{c}_{fib}\left(\varphi\right) - \mathbb{C}^{hom}\right)\right]^{-1} : \mathbf{E}^{\infty} \tag{7.23}$$

with the fourth-order Hill tensor $\mathbb{P}^{hom}_{cyl}$ depending on the shape of the inclusion and on the stiffness $\mathbb{C}^{hom}$ of the fictitious matrix: its components are given in Laws [1977a]. As regards the pore phase, we consider a circular oblate inclusion (ellipsoid with slenderness ratio equal to one and an aspect ratio going to zero). Thereby, the oblate plane coincides with the overall paper plane, i.e. with the plane $\mathbf{e}_1$-$\mathbf{e}_2$ in Figure 7.2, which is the plane of isotropy of the (yet unknown) homogenized stiffness tensor $\mathbb{C}^{hom}$. The homogeneous strains in such an inclusion follow as

$$\boldsymbol{\varepsilon}_{por} = \left[\mathbb{I} + \mathbb{P}^{hom}_{oblsph} : \left(\mathbb{c}_{por} - \mathbb{C}^{hom}\right)\right]^{-1} : \mathbf{E}^{\infty} \tag{7.24}$$

whereby the components of the fourth-order Hill tensor for an oblate spheroid in a transversely isotropic matrix follow from specification of the expressions given by Sevostianov et al. [2005]. They read as:

$$\begin{aligned} &P_{oblsph3333} = \frac{1}{C_{3333}} \\ &P_{oblsph2323} = P_{oblsph3232} = P_{oblsph2332} = P_{oblsph3223} = \\ &...P_{oblsph1313} = P_{oblsph3131} = P_{oblsph1331} = P_{oblsph3113} = \frac{1}{4C_{1313}} \end{aligned} \tag{7.25}$$

Being representative for the strains arising in the RVE of paper, the phase strain expressions (7.23) and (7.24) need to fulfill the strain average rule (7.13). Insertion of matrix-inclusion-related expressions (7.23) and (7.24) into (7.13) yields the following expression for the fictitious strains $\mathbf{E}^{\infty}$

$$\begin{aligned} \mathbf{E}^{\infty} = &\left[\frac{1-\phi}{2\pi}\int_{\varphi=0}^{2\pi}\left[\mathbb{I} + \mathbb{P}^{hom}_{cyl}\left(\varphi\right) : \left(\mathbb{c}_{fib}\left(\varphi\right) - \mathbb{C}^{hom}\right)\right]^{-1} d\varphi + \right. \\ &\left. ...\phi\left[\mathbb{I} + \mathbb{P}^{hom}_{oblsph} : \left(\mathbb{c}_{por} - \mathbb{C}^{hom}\right)\right]^{-1}\right]^{-1} : \mathbf{E} \end{aligned} \tag{7.26}$$

and insertion of the fictitious-to-RVE strain relation (7.26) into the matrix-inclusion-related expressions (7.23) and (7.24) yields estimates for the fiber and pore strain concentration tensors in the form:

$$\begin{aligned}\mathbb{A}_{fib}\left(\varphi\right) = & \left[\mathbb{I} + \mathbb{P}^{hom}_{cyl}\left(\varphi\right) : \left(\mathbb{c}_{fib}\left(\varphi\right) - \mathbb{C}^{hom}\right)\right]^{-1} : ... \\ & ... \left[\frac{1-\phi}{2\pi}\int_{\varphi=0}^{2\pi}\left[\mathbb{I} + \mathbb{P}^{hom}_{cyl}\left(\varphi\right) : \left(\mathbb{c}_{fib}\left(\varphi\right) - \mathbb{C}^{hom}\right)\right]^{-1} d\varphi + \right. \\ & \left. ...\phi\left[\mathbb{I} + \mathbb{P}^{hom}_{oblsph} : \left(\mathbb{c}_{por} - \mathbb{C}^{hom}\right)\right]^{-1}\right]^{-1}\end{aligned} \tag{7.27}$$

$$\begin{aligned}\mathbb{A}_{por} = & \left[\mathbb{I} + \mathbb{P}^{hom}_{oblsph} : \left(\mathbb{c}_{por} - \mathbb{C}^{hom}\right)\right]^{-1} : ... \\ & ... \left[\frac{1-\phi}{2\pi}\int_{\varphi=0}^{2\pi}\left[\mathbb{I} + \mathbb{P}^{hom}_{cyl}\left(\varphi\right) : \left(\mathbb{c}_{fib}\left(\varphi\right) - \mathbb{C}^{hom}\right)\right]^{-1} d\varphi + \right. \\ & \left. ...\phi\left[\mathbb{I} + \mathbb{P}^{hom}_{oblsph} : \left(\mathbb{c}_{por} - \mathbb{C}^{hom}\right)\right]^{-1}\right]^{-1}\end{aligned} \tag{7.28}$$

Finally, insertion of (7.27) and (7.28) into (7.22) provides an implicit expression for the desired homogenized stiffness of the planar network material, reading as:

$$\begin{aligned}\mathbb{C}^{hom} = & \left[\frac{1-\phi}{2\pi}\int_{\varphi=0}^{2\pi}\mathbb{c}_{fib}\left(\varphi\right) : \left[\mathbb{I} + \mathbb{P}^{hom}_{cyl}\left(\varphi\right) : \left(\mathbb{c}_{fib}\left(\varphi\right) - \mathbb{C}^{hom}\right)\right]^{-1} d\varphi + ... \right. \\ & \left. ...\phi\mathbb{c}_{por} : \left[\mathbb{I} + \mathbb{P}^{hom}_{oblsph} : \left(\mathbb{c}_{por} - \mathbb{C}^{hom}\right)\right]^{-1}\right] : ... \\ & ... \left[\frac{1-\phi}{2\pi}\int_{\varphi=0}^{2\pi}\left[\mathbb{I} + \mathbb{P}^{hom}_{cyl}\left(\varphi\right) : \left(\mathbb{c}_{fib}\left(\varphi\right) - \mathbb{C}^{hom}\right)\right]^{-1} d\varphi + \right. \\ & \left. ...\phi\left[\mathbb{I} + \mathbb{P}^{hom}_{oblsph} : \left(\mathbb{c}_{por} - \mathbb{C}^{hom}\right)\right]^{-1}\right]^{-1}\end{aligned} \tag{7.29}$$

This expression provides a tool also in the case of very high stiffness contrast; so that the case of empty pores with stiffness going to zero can be effectively tackled, without losing the benefits from the particularly simple form of the $\mathbb{P}$ tensor given in Eq. (7.25).

7.3 Results and discussion

Here we investigate fundamental properties of the homogenized stiffness expression (7.29), relating to two fundamental questions:

- Which stiffness contrast between realistically chosen values for the fiber phases and those chosen for the virtually vanishing pore stiffness needs to be chosen, so as to arrive at sufficiently converged homogenized results?

- How does fiber stiffness affect the overall stiffness of the homogenized material?

For investigations related to both questions, we start with a typical Young's modulus in pulp fiber direction of 21.54 GPa, which appears as the expected value of a log-normally distributed large number of experimental results collected from references [Adusumalli et al., 2010, Duncker and Nordman, 1965, Ehrnrooth and Kolseth, 1984, Page et al., 1977] (see Figure 7.4). In order to account for the transversely isotropic nature of pulp fiber, which - to the best knowledge of the authors - has not been explicitly tested yet, we resort to the experimentally validated micromechanics model for wood proposed by Bader et al. [2011], which we evaluate for typical volume fractions of spruce, up to the level of the cell wall material. The corresponding transversely isotropic stiffness tensor is then linearly re-scaled, so as to exhibit the aforementioned Young's modulus of 21.54 GPa. This leads to the following elasticity tensor of softwood pulp fibers, reading in Kelvin-Mandel notation [Cowin and Mehrabadi, 1992, Helbig, 1994, Helnwein, 2001] as

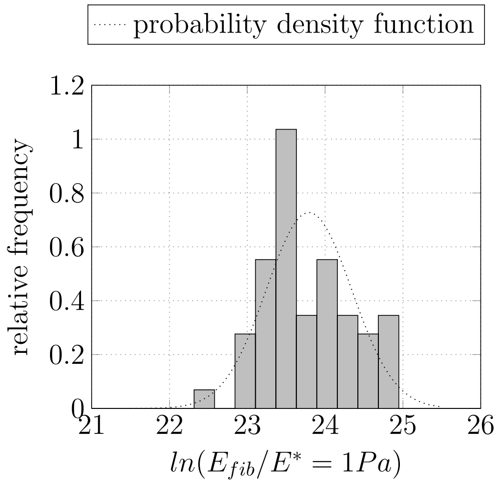

Figure 7.4: Histogram of logarithmic sample of mean softwood pulp fiber Young's moduli in longitudinal direction

$$\mathbb{C}_{fib}^{exp} =$$

$$= \left\{ \begin{matrix} C_{1111,fib} & C_{1122,fib} & C_{1133,fib} & \sqrt{2}C_{1123,fib} & \sqrt{2}C_{1113,fib} & \sqrt{2}C_{1112,fib} \\ C_{2211,fib} & C_{2222,fib} & C_{2233,fib} & \sqrt{2}C_{2223,fib} & \sqrt{2}C_{2213,fib} & \sqrt{2}C_{2212,fib} \\ C_{3311,fib} & C_{3322,fib} & C_{3333,fib} & \sqrt{2}C_{3323,fib} & \sqrt{2}C_{3313,fib} & \sqrt{2}C_{3312,fib} \\ \sqrt{2}C_{2311,fib} & \sqrt{2}C_{2322,fib} & \sqrt{2}C_{2333,fib} & 2C_{2323,fib} & 2C_{2313,fib} & 2C_{2312,fib} \\ \sqrt{2}C_{1311,fib} & \sqrt{2}C_{1322,fib} & \sqrt{2}C_{1333,fib} & 2C_{1323,fib} & 2C_{1313,fib} & 2C_{1312,fib} \\ \sqrt{2}C_{1211,fib} & \sqrt{2}C_{1222,fib} & \sqrt{2}C_{1233,fib} & 2C_{1223,fib} & 2C_{1213,fib} & 2C_{1212,fib} \end{matrix} \right\}_{\mathbf{e}_1,\mathbf{e}_2,\mathbf{e}_3}$$

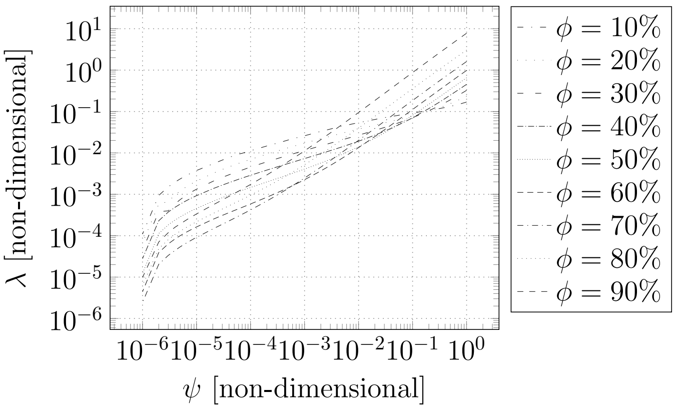

Figure 7.5: Relative approximation error concerning the pore stiffness approaching zero; according to Eq. (7.31), for selected values of the porosity

$$= \begin{Bmatrix} 2.9228 & 1.0329 & 1.2588 & 0 & 0 & 0 \\ 1.0329 & 2.9228 & 1.2588 & 0 & 0 & 0 \\ 1.2588 & 1.2588 & 22.3402 & 0 & 0 & 0 \\ 0 & 0 & 0 & 2.9143 & 0 & 0 \\ 0 & 0 & 0 & 0 & 2.9143 & 0 \\ 0 & 0 & 0 & 0 & 0 & 1.88991 \end{Bmatrix}_{\mathbf{e}_1,\mathbf{e}_2,\mathbf{e}_3} \tag{7.30}$$

For testing the influence of the phase stiffness contrast on the homogenized network stiffness results (fundamental question #1 posed above), we start with the solution for a zero-porosity network, i.e. with Eq. (7.29) evaluated for $\mathbb{C}_{fib}^{exp}$ according to Eq. (7.30) and for $\phi = 0$. The corresponding homogenized stiffness tensor reads in Kelvin-Mandel notation as

$$\mathbb{C}^{hom}\left(\phi = 0\right) = \begin{Bmatrix} 7.9942 & 2.2475 & 1.1034 & 0 & 0 & 0 \\ 2.2475 & 7.9942 & 1.1034 & 0 & 0 & 0 \\ 1.1034 & 1.1034 & 2.9218 & 0 & 0 & 0 \\ 0 & 0 & 0 & 2.3463 & 0 & 0 \\ 0 & 0 & 0 & 0 & 2.3463 & 0 \\ 0 & 0 & 0 & 0 & 0 & 5.7467 \end{Bmatrix}_{\mathbf{e}_1,\mathbf{e}_2,\mathbf{e}_3} \tag{7.31}$$

We use these values to construct a pore stiffness tensor of the format $\mathbb{c}_{por} = \psi \times \mathbb{C}^{hom}\left(\phi = 0\right)$, whereby ψ is a contrast factor, which takes values of decreasing magnitude, approaching zero down to the value of 10^{-6}. For each of these factors, we compute the corresponding stiffness tensors, and we estimate their quality with respect to reliably representing the zero-stiffness limit, by means of a convergence analysis known from the Finite Element Method [Zienkiewicz and Taylor, 1994]. Accordingly, we compute the relative approximation error for the in-plane elastic moduli, $E^{hom}_{in-plane}$, according to

$$\lambda_E(\psi) = \frac{E^{hom}_{in-plane}(\psi) - E^{hom}_{in-plane}(\psi_{min})}{E^{hom}_{in-plane}(\psi_{min})} \tag{7.32}$$

with a minimum value for ψ denoted as ψ_{min}. Then we plot the aforementioned relative errors as function of the contrast factor ψ (see Figure 7.5 for $\psi_{min} = 10^{-6}$, and in dependence of selected values for the porosity, ϕ). We observe that $\psi = 10^{-5}$ is sufficient for arriving at homogenized values with a numerical error of less than 1 %, and that this error can be reduced down to one per mille as well. We also note that the Young's modulus in the out-of-plane direction tends to zero upon ψ going to zero, so that the homogenized elastic behaviour of paper is essentially two-dimensional, i.e. planar, in nature. For the in-plane Young's modulus and Poisson's ratio of the homogenized material, we refer to Figures 7.6 and 7.7.

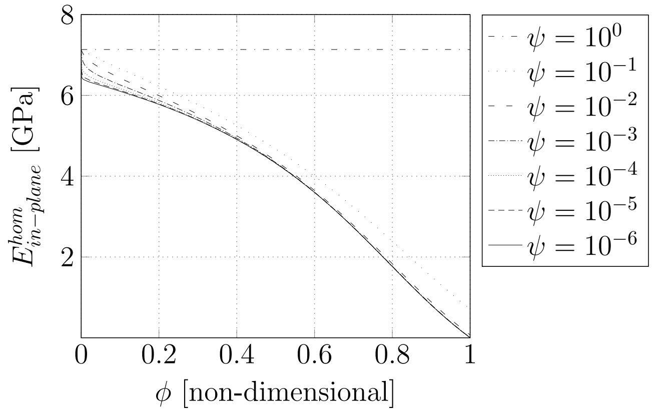

Figure 7.6: Micromechanically predicted in-plane Young's modulus of the planar network, as a function of the porosity of the latter

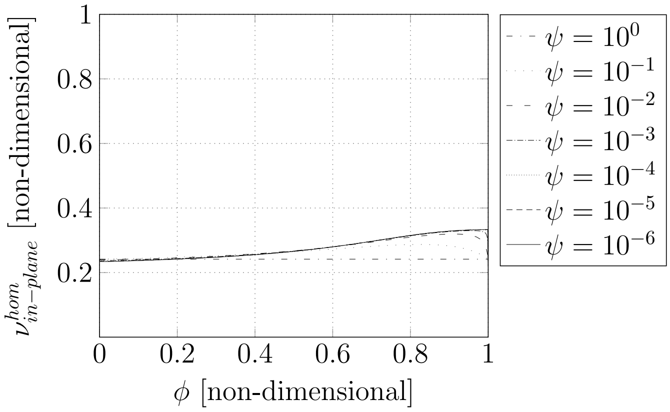

Figure 7.7: Micromechanically predicted in-plane Poisson's ratio of the planar network, as a function of the porosity of the latter

For testing the influence of the fiber stiffness on the overall homogenized network stiffness (fundamental question #2 posed above), we consider fiber stiffness tensors of different magnitude, in the format

$$\mathbb{c}_{fib} = \frac{E_{fib}}{E_{fib}^{exp}} \times \mathbb{c}_{fib}^{exp} \tag{7.33}$$

with a variable fiber modulus E_{fib}, and with E_{fib}^{exp} being the experimentally derived fiber modulus of 21.4 GPa. A dimensional analysis of Eq. (7.29) for fiber stiffnesses according to Eq. (7.30) yields the following relation for the homogenized Young's modulus

$$\frac{E^{hom}}{E_{fib}} = f(\phi) \tag{7.34}$$

and this result can actually be tested by evaluating Eq. (7.29) for a large range of different values of according to (7.33); the dimensionless relation (7.34) is illustrated in Figure 7.8. It is interesting to compare this result with that arising from assuming an isotropic fiber stiffness with Young's modulus E_{fib} and a Poisson's ratio $\nu = 0.31$, which corresponds to the axial Poisson's ratio ν_{31} of $\mathbb{c}_{fib}^{exp}$. The latter assumption yields a gross overestimation of the transversely isotropic case (see Figure 7.6): hence, the transverse isotropy of the pulp fibers is of eminent importance for the overall elastic behavior of paper and paper-like materials.

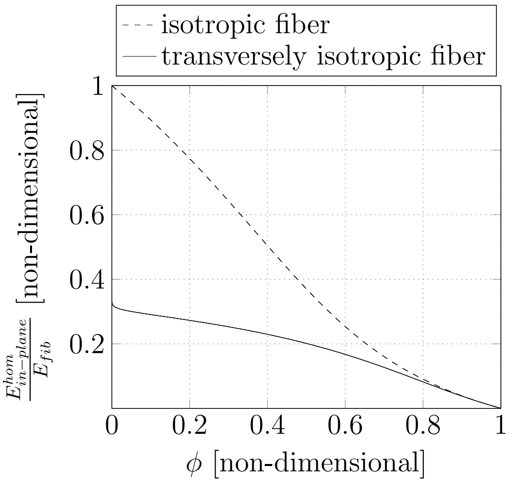

Figure 7.8: Homogenized in-plane Young's modulus of paper normalized with respect to fiber elastic modulus, for isotropic and transversely isotropic fiber phases; as function of porosity

For experimental validation of the presented model, we adapt the statistical method presented by [Pichler et al., 2005] to our present case. From the experimental data base represented in Figure 7.4, we derive 5 % and 95 % percentiles of the fiber Young's modulus. They amount to:

$$E_{fib_{5\,\%}} = 6.35\,\mathrm{GPa}$$
$$E_{fib_{95\,\%}} = 73.07\,\mathrm{GPa}$$

and we plot micromechanical predictions corresponding to these upper and lower bounds for the pulp fiber stiffness found in softwood-based paper materials (see Figure 7.9). These predictions turn out to satisfactorily frame various experimental data concerning softwood paper stiffness, as collected from the open literature [Alexander and Marton, 1968]. Hence, the presented micromechanical model turns out as reliable and efficient means for predicting paper elasticity from fiber stiffness and porosity. Its extension to brittle strength in the line of Fritsch et al. [2013a] is quite straightforward; and this will open the way to theory-based design of paper production processes where the estimation of sudden material failure is essential.

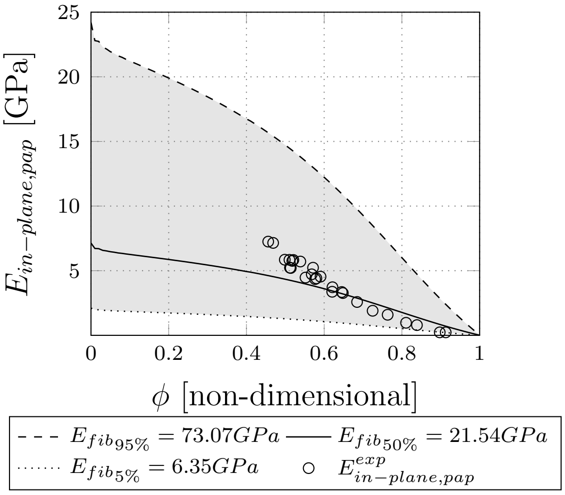

Figure 7.9: Experimental validation of micromechanics model described in Section 2: prediction based on 5 % and 95 % quantiles of the pulp fiber stiffness satisfactorily frame experimental data on the paper level

Acknowledgement

Financial support for this work in the framework of the PhD-School DokIn'Holz, funded by the Austrian Federal Ministry of Science, Research and Ecomomy, as well as by Mondi Frantschach GmbH and Sappi Austria Vertriebs-GmbH & CO KG, is gratefully acknowledged.

7.4 Nomenclature

$\mathbb{A}_{fib}$	fourth-order strain concentration tensor of fiber phase
$\mathbb{A}_{por}$	fourth-order strain concentration tensor of pore phase
$\mathbb{c}_{fib}$	stiffness tensor of fiber phase
$\mathbb{c}_{por}$	stiffness tensor of pore phase
$\mathbb{c}_{fib}^{exp}$	experimentally validated elasticity tensor of softwood fibers
$\mathbb{C}_{hom}$	homogenized stiffness tensor (of porous polycrystal)
d	characteristic length of the inhomogeneities within the RVE
$\mathbf{E}$	macroscopic strain tensor
$\mathbf{E}^{\infty}$	homogeneous strains at the infinite boundary of the matrix-inclusion problem
$E_{fib_{5\,\%}}$	5 % percentile of fiber Young's modulus
$E_{fib_{95\,\%}}$	95 % percentile of fiber Young's modulus
E_{fib}	fiber Young's modulus
E_{fib}^{exp}	experimentally derived Youngs's modulus of paper fibers
E^{hom}	homogenized Young's modulus of fibers
$E_{in-plane}^{hom}$	model-predicted in-plane elastic moduli of paper fibers
$\mathbf{e}_1, \mathbf{e}_2, \mathbf{e}_3$	unit base vectors of Cartesian reference base frame
ℓ	characteristic length of the RVE
$L_{fib}(\vartheta, \varphi)$	overall length of the fiber phase oriented in (ϑ, ϕ)-direction
$\mathscr{L}$	characteristic structural length
$p(\vartheta, \varphi)$	probability distribution function representing the three-dimensional arrangement of fibers
$\mathbb{P}_{cyl}^{hom}$	Hill (or morphology) tensor of cylindrical inclusion embedded in matrix with stiffness $\mathbb{C}_{hom}$
$\mathbb{P}_{oblsph}^{hom}$	Hill (or morphology) tensor of oblate spherical inclusion embedded in matrix with stiffness $\mathbb{C}_{hom}$
RVE	Representative Volume Element
$\mathbf{T}$	(microscopic) traction vector
V_{por}	volume of pore phase
V_{RVE}	volume of the RVE
∂V_{RVE}	surface of the RVE
$\mathbf{x}$	position vector inside the RVE

δ	Kronecker delta
$\boldsymbol{\varepsilon}$	microscopic strain
$\boldsymbol{\varepsilon}_{fib}$	average microscopic strain in fiber phase
$\boldsymbol{\varepsilon}_{pore}$	average microscopic strain in pore phase
λ	relative approximation error
ν	Poisson's ratio
ϑ	spherical (co-latitudinal) coordinate
$\boldsymbol{\xi}$	microscopic displacement field
ϕ	porosity
φ	spherical (longitudinal) coordinate
ψ	contrast factor
$\boldsymbol{\sigma}$	microscopic stress
$\boldsymbol{\sigma}_{fib}$	average stress in fiber phase
$\boldsymbol{\sigma}_{por}$	average stress in pore phase
$\boldsymbol{\Sigma}$	macroscopic stress tensor
$\langle(.)\rangle$	spatial average of quantity (.), over the RVE
$(.)^{-1}$	inverse of tensorial quantity (.)

Chapter 8

Conclusions and outlook

The key objective of the present work is to explain the highly diverse (poro)mechanical properties (in particular strength) of bone materials at different observation scales from the mechanical properties of their elementary constituents, and from the nano- and microstructures thereof. The mechanical behavior of the aforementioned nano- and microstructures has been revealed through the theoretical tool of continuum micromechanics, an approach that is well established for engineering materials, as well as for biomaterials [Fritsch and Hellmich, 2007, Fritsch et al., 2009c, 2013b, Hellmich, 2005, Hellmich and Ulm, 2002a, 2005a, Hellmich et al., 2004a,b, 2009]. Consideration of ductile sliding of hydrated porous polycrystals allowed to predict uniaxial tensile and compressive strengths of various different cortical bones [Fritsch et al., 2009c], and served as a starting point for the present contribution; namely to predict the multiaxial strength of bone (bio)materials. This required major micromechanical developments, in which the realization of the following micromechanical concepts has been encountered:

- In addition to the concentration tensors relating the macroscopic strains at the boundary of the RVE to the strains in all the materials phases within the RVE, the so-called influence tensors relating plastic strains of one material phase inside the considered RVE to the total (micro-)strains in all other material phases of that RVE, were derived and estimated by means of “extended” eigenstressed matrix-inclusion problems [Pichler and Hellmich, 2010].

- In contrast to the elastic case, the loading of the RVEs was done in an incremental manner, representing the load level-dependent plastic processes within the microstructure. Accordingly, the evolution equations of elastoplasticity were discretized by means of an Euler backward integration scheme.

- Involving infinitely many phases required also a spatial discretization down to an appropriate number of phases, which was realized by two different discretization schemes, comprising 15 or 28 points [Stroud, 1971]; or 120 integration points [Badel and Leblond, 2004].

- Efficient and robust algorithms for upscaling the elastoplastic constitutive relations from the solid phase to the porous polycrystal scale were established by means of the well-known return mapping strategy, adapted for non-associated, multi-surface Mohr-Coulomb plasticity.

We proposed a fully multiaxial and multiscale return-mapping procedure to account for the inelastic behavior of mineral crystal. Combination of this non-linear constitutive law at the extrafibrillar scale with a strength criterion (1.39) for molecular collagen at the subfibrillar scale allows for prediction of the strength of bone tissue in any multiaxial load case.

Interfaces were then considered as the origin of plastic sliding events. The mechanical behavior of rigid-plastic interfaces was revealed through the theoretical tool of continuum micromechanics. Here, we aimed at translating the interface behavior into plastic sliding mechanics at the continuum scale of materials. To this end, we considered, at the interface scale, a linear relationship between (i) the rate of relative displacements of neighboring fluid layers and (ii) corresponding interface eigentractions. Recent explicit micromechanical homogenization schemes are used to upscale the liquid crystal behavior confined to 2D interfaces up to the larger observation scale of a matrix-inclusion-type composite material consisting of a homogeneous, isotropic, and linear elastic solid matrix and of interacting, circular, flat interfaces oriented in a parallel fashion. These schemes are based on limit cases of Eshelby-type solution for eigenstressed ellipsoidal inclusions in infinite matrices together with the compatibility requirements fulfilled in so-called Mori-Tanaka schemes. We developed a model describing how the macroscopic loading, the elastic properties of the solid, as well as the size, and the density of the interfaces influence the macroscopic plastic behavior of the composite, which is of kinematic hardening type.

Future work involves the use of the newly developed method in the light of real materials exhibiting polycrystals, such as bone, clay or concrete. A carefully experimentally validated hierarchical micromechanics model for bone is to be complemented by an additional homogenization step: downscaling from the hydroxyapatite mineral crystals found in the extrafibrillar space to the interfaces present in these clusters. Once the developed micromechanical models will have been validated by experiments, they will be implemented into standard Finite Element Software in order to analyze whole bones and skeletal (sub)systems. Thereby, Computer Tomographic (CT) images of whole organs will be translated into fields of dosages of elementary components serving as model input. The micromechanics models will allow for transformation of these fields into fields of inhomogeneous and anisotropic material properties. The FE models would be set in the framework of elastoplasticity, combining, probably for the first time ever, multiscale continuum micro-elastoplasticity with computational plasticity algorithms at the structural scale of the Finite Element discretization. Besides their clinical relevance, such model approaches have the potential to open a new chapter in the scientific communities of computational mechanics and numerical mathematics.

Regarding **paper**, in contrary to previous mathematical models, we proposed a new approach which accounts for the scale difference between the loads applied to the overall material and those acting on the level of the individual paper fiber. By introducing new concentration- and influence relations specified for planar fiber networks, and its combination with common matrix-inclusion problems we can now predict the paper stiffness tensor as a function of fiber stiffness and porosity. The experimentally validated micromechanical model strongly indicates that the elasticity of planar fibrous materials can be accurately predicted from the elasticity of the fibers leading to its formations. This highlights the potential of micromechanical modeling in improving design of such materials, through optimization of key microscopic parameters such as porosity or mechanical and geometrical properties of fibers and pores, in order to achieve the desired macroscopic elastic properties.

Bibliography

J. Aaron. Histology and micro-anatomy of bone. In B. Nordin, editor, *Calcium, Phosphate and Magnesium Metabolism: Clinical Physiology and Diagnostic Procedures*, pages 298–356. Churchill Livingstone, New York, 1971.

R.-B. Adusumalli, W. M. Mook, R. Passas, P. Schwaller, and J. Michler. Nanoindendation of single pulp fibre cell wals. *Journal of Materials Science*, 45(10): 2558–2563, 2010.

M. Akao, H. Aoki, and K. Kato. Mechanical properties of sintered hydroxyapatite for prosthetic applications. *Journal of Materials Science*, 16(3):809–812, 1981.

O. Akkus, A. Polyakova-Akkus, F. Adar, and M. Schaffler. Aging of microstructural compartments in human compact bone. *Journal of Bone and Mineral Research*, 18(6):1012–1019, 2003.

B. Alexander, T. Daulton, G. Genin, J. Lipner, J. Pasteris, B. Wopenka, and S. Thomopoulos. The nanometre-scale physiology of bone: steric modelling and scanning transmission electron microscopy of collagen–mineral structure. *Journal of the Royal Society – Interface*, 9:1774–1786, 2012.

S. D. Alexander and R. Marton. Effect of beating and wet pressing on fiber and sheet properties. II. Sheet properties. *TAPPI Journal*, 51(6):283–288, 1968.

M. Ali and B. Singh. The effect of porosity on the properties of glass fibre-reinforced gypsum plaster. *Journal of Materials Science*, 10(11):1920–1928, 1975.

H. Anderson. The role of matrix vesicles in growth plate development and biomineralization. *Frontiers in Bioscience*, 10:822–837, 2005.

B. Aoubiza, J. Crolet, and A. Meunier. On the mechanical characterization of compact bone structure using the homogenization theory. *Journal of Biomechanics*, 29(12):1539–1547, 1996.

A. Ascenzi and E. Bonucci. The shearing properties of single osteons. *The Anatomical Record*, 172(3):499–510, 1972.

R. Ashman and J. Rho. Elastic modulus of trabecular bone material. *Journal of Biomechanics*, 21(3):177–181, 1988.

R. Ashman, S. Cowin, W. van Buskirk, and J. Rice. A continuous wave technique for the measurement of the elastic properties of cortical bone. *Journal of Biomechanics*, 17(5):349–361, 1984.

J. Åström, S. Saarinen, K. Niskanen, and J. Kurkijärvi. Microscopic mechanics of fiber networks. *Journal of Applied Physics*, 75(5):2383, 1994.

J.-L. Auriault, C. Boutin, and C. Geindreau. *Homogenization of Coupled Phenomena in Heterogenous Media*. Wiley, 2009.

V. Baca, Z. Horak, P. Mikulenka, and V. Dzupa. Comparison of an inhomogeneous orthotropic and isotropic material models used for FE analyses. *Medical Engineering & Physics*, 30(7):924–930, 2008.

P. Badel and J. Leblond. A note on integration schemes for the microplane model of the mechanical behaviour of concrete. *Communications in Numerical Methods in Engineering*, 20(1):75–81, 2004.

T. K. Bader, K. Hofstetter, C. Hellmich, and J. Eberhardsteiner. The poroelastic role of water in cell walls of the hierarchical composite 'softwood'. *Acta Mechanica*, 217(1-2):75–100, 2011.

A. Bailey, R. Paul, and L. Knott. Mechanisms of maturation and ageing of collagen. *Mechanisms of Ageing and Development*, 106(1-2):1–56, 1998.

Y. Bala, D. Farlay, P. Delmas, P. Meunier, and G. Boivin. Time sequence of secondary mineralization and microhardness in cortical and cancellous bone from ewes. *Bone*, 46:1204–1212, 2010.

J. Barrett and N. Keat. Artifacts in CT: Recognition and avoidance. *RadioGraphics*, 24(6):1679–1691, 2004.

J.-F. Barthélémy, L. Dormieux, and D. Kondo. Determination of the macroscopic behavior of a medium with frictional cracks. *Comptes Rendus Mécanique*, 331 (1):77–84, 2003.

T. Battaglia, A.-C. Tsou, E. Taylor, and B. Mikic. Ash content modulation of torsionally derived effective material properties in cortical mouse bone. *Journal of Biomechanical Engineering*, 125(5):615–619, 2003.

G. Baum. The elastic properties of paper: A review. *The Institute for Paper Chemistry, Appleton, WI*, 1984.

Z. Bažant and B. Oh. Microplane model for progressive fracture of concrete and rock. *Journal of Engineering Mechanics*, 111:559–582, 1985.

Z. Bažant and P. Prat. Microplane model for brittle plastic material: I. theory. *Journal of Engineering Mechanics*, 114:1672–1688, 1988.

Z. Bažant, F. Caner, I. Carol, M. Adley, and S. Akers. Microplane model m4 for concrete. i: Formulation with work-conjugate deviatoric stress. *Journal of Engineering Mechanics*, 126:944–953, 2000.

D. Baylink and J. Wergedal. *Bone formation and resorption by osteocytes*, pages 257–289. 1971.

L. Bell, M. Kayser, and C. Jones. The mineralized osteocyte: a living fossil. *American Journal of Physical Anthropolgy*, 137:449–456, 2008.

Y. Benveniste. A new approach to the application of mori-tanaka's theory in composite materials. *Mechanics of Materials*, 6(2):147–157, 1987.

O. Bernard, F. J. Ulm, and E. Lemarchand. A multiscale micromechanics-hydration model for the early-age elastic properties of cement-based materials. *Cement and Concrete Research*, 33(9):1293–1309, 2003.

E. Bertrand and C. Hellmich. Multiscale elasticity of tissue engineering scaffolds with tissue-engineered bone: A continuum micromechanics approach. *Journal of Engineering Mechanics*, 135(5):395–412, 2009.

M. Berveiller and A. Zaoui. An extension of the self-consistent scheme to plastically-flowing polycrystals. *Journal of the Mechanics and Physics of Solids*, 26(5-6):325–344, 1978.

J. Beyerer and F. Puente León. Die Radontransformation in der digitalen Bildverarbeitung. *Automatisierungstechnik (at)*, 50:472–480, 2002.

R. Bhowmik, K. Katti, and D. Katti. Mechanics of molecular collagen is influenced by hydroxyapatite in natural bone. *Journal of Materials Science*, 42(21):8795—-8803, 2007.

R. Bhowmik, K. Katti, and D. Katti. Mechanisms of load-deformation behavior of molecular collagen in hydroxyapatite-tropocollagen molecular system: Steered molecular dynamics study. *Journal of Engineering Mechanics*, 135(5):413—-421, 2009.

R. Bigley, L. Griffin, L. Christensen, and R. Vandenbosch. Osteon interfacial strength and histomorphometry of equine cortical bone. *Journal of Biomechanics*, 39(9):1629–40, 2006.

F. Bignonnet, L. Dormieux, and D. Kondo. A micro-mechanical model for the plasticity of porous granular media and link with the cam clay model. *International Journal of Plasticity*, 79:259–274, 2016.

R. Biltz and E. Pellegrino. The chemical anatomy of bone. i. a comparative study of bone composition in sixteen vertebrates. *The Journal of Bone and Joint Surgery*, 51(3):456–466, 1969.

R. Blanchard, A. Dejaco, E. Bongaers, and C. Hellmich. Intravoxel bone micromechanics for microct-based finite element simulations. *Journal of Biomechanics*, 46:2710–2721, 2013.

R. Blanchard, C. Morin, A. Malandrino, A. Vella, S. Zdenka, and C. Hellmich. Patient-specific fracture risk assessment of vertebrae: A multiscale approach coupling x-ray physics and continuum micromechanics. *Numerical Methods in Biomedical Engineering*, 32(9), 2016.

F. Boas and D. Fleischmann. CT artifacts: Causes and reduction techniques. *Imaging in Medicine*, 4(2):229–240, 2012.

W. Böcker, T. El Khassawna, N. Bauer, K. Brodsky, D. Weisweiler, P. Govindarajan, G. Schlewitz, M. Kampschulte, L. Dürselen, U. Thormann, G. Szalay, R. Schnettler, A. Langheinrich, and C. Heiss. Short-term glucocorticoid treatment causes spinal osteoporosis in ovariectomized rats. *European Spine Journal*, 23(11):2437–2448, 2014.

G. Boivin and P. Meunier. The degree of mineralization of bone tissue measured by computerized quantitative contact microradiography. *Calcified Tissue International*, 70(6):503–511, 2002.

R. Bolz and G. e. Tuve. *CRC Handbook of tables for applied engineering science*, volume Internet Version 2005. CRC Press, Cleveland, Ohio, 2nd edition edition, 1973.

L. Bonar, S. Lees, and H. Mook. Neutron diffraction studies of collagen in fully mineralized bone. *Journal of Molecular Biology*, 181(2):265–270, 1985.

L. Bonewald and M. Johnson. Osteocytes, mechanosensing and wnt signaling. *Bone*, 42(4):606–615, 2008.

E. Bonucci. The osteocyte: the underestimated conductor of the bone orchestra. *Rendiconti Lincei: Scienze Fisiche e Naturali*, 20:237–254, 2009.

B. Borah, G. Gross, T. Dufresne, T. Smith, M. Cockman, P. Chmielewsky, M. Lundy, J. Hartke, and W. Sod. Three-dimensional microimaging (MRμI and μCT), finite element modeling, and rapid prototyping provide unique insights into bone architecture in osteoporosis. *The Anatomical Record*, 265(2): 101–110, 2001.

V. Bousson, C. Bergot, A. Meunier, F. Barbot, C. Parlier-Cuau, A.-M. Laval-Jeantet, and J.-D. Laredo. Ct of the middiaphyseal femur: cortical bone mineral density and relation to porosity. *Radiology*, 217(1):179–187, 2000.

V. Bousson, A. Meunier, C. Bergot, E. Vicaut, M. Rocha, M. Morais, A.-M. Laval-Jeantet, and J.-D. Laredo. Distribution of intracortical porosity in human midfemoral cortex by age and gender. *Journal of Bone and Mineral Research*, 16(7):1308–1317, 2001.

L. Bozec and M. Horton. Topography and mechanical properties of single molecules of type i collagen using atomic force microscopy. *Biophysical Journal*, 88(6): 4223–4231, 2005.

J. Bradley. Interactive Image Display for the X Window System. Version 3.10a, 2nd edn. *Available at http://www.trilon.com/xv/manual/xv-3.10a*, 1994.

M. Brady, A. Renzing, T. Douglas, Q. Liu, S. Wille, M. Parizek, L. Bacakova, A. Kromka, M. Jarosova, G. Godier, and P. Warnkel. Development of composite poly(lactide-co-glycolide)-nanodiamond scaffolds for bone cell growth. *Journal of Nanoscience and Nanotechnology*, 15(2):1060–1069, 2015.

R. Brannon. Geometric insight into return mapping plasticity algorithms. *New Mexico: University of New Mexico*, 2002.

B. Brodsky, E. Eikenberry, and a.-K. Belbruno, K.C. Variations in collagen fibril structure in tendons. *Biopolymers*, 21(5):935–951, 1982.

M. Brown and A. Forsythe. Robust tests for the equality of variances. *Journal of the American Statistical Association*, 69(346):364–367, 1974.

J. Buckwalter, M. Glimcher, R. Cooper, and R. Recker. Bone biology part i: blood supply, cells, matrix, and mineralization. *The Journal of Bone and Joint Surgery*, 77:1256–1275, 1995.

B. Budiansky and R. O'Connell. Elastic moduli of a cracked solid. *International Journal of Solids and Structures*, 12(2):81–97, 1976.

M. Buehler. Nanomechanics of collagen fibrils under varying cross-link densities: Atomistic and continuum studies. *Journal of the Mechanical Behavior of Biomedical Materials*, 1(1):59–67, 2008.

H. Buie, G. Campbell, R. Klinck, J. MacNeil, and S. Boyd. Automatic segmentation of cortical and trabecular compartments based on a dual threshold technique for in vivo micro-CT bone analysis. *Bone*, 41(4):505–515, 2007.

C. Burns. The effect of the continued ingestion of mineral acid on growth of body and bone and on the composition of bone and of the soft tissues. *Biochemical Journal*, 23(5):860–867, 1929.

A. Buxboim, I. Ivanovska, and D. Discher. Matrix elasticity, cytoskeletal forces and physics of the nucleus: How deeply do cells "feel" outside and in? *Journal of Cell Science*, 123(3):297–308, 2010.

G. Campbell, H. Buie, and S. Boyd. Signs of irreversible architectural changes occur early in the development of experimental osteoporosis as assessed by in vivo micro-CT. *Osteoporosis International*, 19:1409–1419, 2008.

R. Cancedda, A. Cedola, A. Giuliani, V. Komlev, S. Lagomarsino, M. Mastrogiacomo, F. Peyrin, and F. Rustichelli. Bulk and interface investigations of scaffolds and tissue-engineered bones by X-ray microtomography and X-ray microdiffraction. *Biomaterials*, 28:2505–2524, 2007. Imaging Techniques for Biomaterials Characterization.

D. Carter and W. Hayes. The compressive behavior of bone as a two-phase porous structure. *The Journal of Bone & Joint Surgery*, 59(7):954–962, 1977.

M. Castilla Bolaños, J. Buttigieg, and J. Briceño Triana. Development and characterization of a novel porous small intestine submucosa-hydroxyapatite scaffold for bone regeneration. *Materials Science and Engineering: C*, 72:519–525, 2017.

M. Cavalcante and M.-J. Pindera. Generalized fvdam theory for elasticeplastic periodic materials. *International Journal of Plasticity*, 77:90–117, 2016.

H.-A. Cayzac, K. Säi, and L. Laiarinandrasana. Damage based constitutive relationships in semi-crystalline polymer by using multi-mechanisms model. *International Journal of Plasticity*, 51:47–64, 2013.

J. Chaboche, S. Kruch, J. Maire, and T. Pottier. Towards a micromechanics based inelastic and damage modeling of composites. *International Journal of Plasticity*, 17(4):411–439, 2001.

J. Chaboche, P. Kanouté, and A. Roos. On the capabilities of mean-field approaches for the description of plasticity in metal matrix composites. *International Journal of Plasticity*, 21(7):1409–1434, 2005.

B. Chan and K. Leong. Scaffolding in tissue engineering: general approaches and tissue-specific considerations. *European Spine Journal*, 17(4):467–479, 2008.

E. Charrière, S. Terrazzoni, C. Pittet, P. Mordasini, M. Dutoit, J. Lemaître, and P. Zysset. Mechanical characterization of brushite and hydroxyapatite cements. *Biomaterials*, 22(21):2937 – 2945, 2001.

L. Chen and M. Wang. Production and evaluation of biodegradable composites based on PHB–PHV copolymer. *Biomaterials*, 23(13):2631–2639, 2002.

L. Cheng, G. de Saxcé, and D. Kondo. A stress-based variational model for ductile porous materials. *International Journal of Plasticity*, 55:133–151, 2014.

W. Ching, P. Rulis, and A. Misra. Ab initio elastic properties and tensile strength of crystalline hydroxyapatite. *Acta Biomaterialia*, 5(8):3067–3075, 2009.

G. Chinga-Carrasco. Cellulose fibres, nanofibrils and microfibrils: The morphological sequence of mfc components from a plant physiology and fibre technology point of view. *Nanoscale Research Letters*, 6(1):417–423, 2011.

K.-H. Chung, K. Bhadriraju, T. Spurlin, R. Cook, and A. Plant. Nanomechanical properties of thin films of type i collagen fibrils. *Langmuir*, 26(5):3629–3636, 2010.

B. Clarke. Normal bone anatomy and physiology. *Clinical Journal of the American Society of Nephrology*, 3(3):131–139, 2008.

J. Clausen, L. Damkilde, and L. Andersen. An efficient return algorithm for non-associated plasticity with linear yield criteria in principal stress space. *Computers and Structures*, 85(23-24):1795–1807, 2007.

R. Coble and W. Kingery. Effect of porosity on physical properties of alumina. *Journal of the American Ceramic Society*, 39:377–385, 1956.

M. Colak. Physical and mechanical properties of polymer-plaster composites. *Material Letters*, 60(16):1977–1982, 2006.

B. Coleman and W. Noll. The thermodynamics of elastic materials with heat conduction and viscosity. *Archive for Rational Mechanics and Analysis*, 13(1): 167–178, 1963.

A. Cong, J. Op Den Buijs, and D. Dragomir-Daescu. In situ parameter identification of optimal density–elastic modulus relationships in subject-specific finite element models of the proximal femur. *Medical Engineering & Physics*, 33(2): 164–173, 2011.

G. Constantinides and F.-J. Ulm. The effect of two types of c-s-h on the elasticity of cement-based materials: Results from nanoindentation and micromechanical modeling. *Cement and Concrete Research*, 34(1):67–80, 2004.

D. Cooper, A. Turinsky, C. Sensen, and Hallgrímsson. Quantitative 3d analysis of the canal network in cortical bone by micro-computed tomography. *The Anatomical Record*, 4274B(1):169–179, 2003.

D. Cooper, C. Thomas, J. Clement, A. Turinsky, C. Sensen, and B. Hallgrímsson. Age-dependent change in the 3d structure of cortical porosity at the human femoral midshaft. *Bone*, 40:957–965, 2007.

O. Coussy. *Mechanics of porous continua.* Wiley, 1995.

O. Coussy. *Poromechanics.* John Wiley & Sons, 2004.

B. Couteau, M.-C. Hobatho, R. Darmana, J.-C. Brignola, and J.-Y. Arlaud. Finite element modelling of the vibrational behaviour of the human femur using CT-based individualized geometrical and material properties. *Journal of Biomechanics*, 31(4):383–386, 1998.

S. Cowin. A recasting of anisotropic poroelasticity in matrices of tensor components. *Transportation in Porous Media*, 50:35–56, 2003.

S. Cowin. The significance of bone microstructure in mechanotransduction. *Journal of Biomechanics*, 40:105–109, 2007.

S. C. Cowin and M. M. Mehrabadi. The structure of the linear anisotropic elastic symmetries. *Journal of the Mechanics of Physics and Solids*, 40(7):1459–1471, 1992.

H. L. Cox. The elasticity and strength of paper and other fibrous materials. *British Journal of Applied Physics*, 3(3):72–79, 1952.

F. Craciun, C. Galassi, E. Roncari, A. Filippi, and G. Guidarelli. Electro-elastic properties of porous piezoelectric ceramics obtained by tape casting. *Ferroelectrics*, 205:49–67, 1998.

E. Crawley, W. Evans, and G. Owen. A theoretical analysis of the accuracy of single-energy CT bone-mineral measurements. *Physics in Medicine and Biology*, 33(10):1113–1127, 1988.

J. Crolet, B. Aoubiza, and A. Meunier. Compact bone: Numerical simulation of mechanical characteristics. *Journal of Biomechanics*, 26(6):677–687, 1993.

J. Currey. The relationship between the stiffness and the mineral content of bone. *Journal of Biomechanics*, 2:477–480, 1969.

J. Currey. The effect of porosity and mineral content on the young's modulus of elasticity of compact bone. *Journal of Biomechanics*, 21(2):131–139, 1988.

S. Cusack and A. Miller. Determination of the elastic constants of collagen by brillouin light scattering. *Journal of Molecular Biology*, 135(1):39–51, 1979.

A. Czenek, R. Blanchard, A. Dejaco, O. Sigurjónsson, G. Örlygsson, P. Gargiulo, and C. Hellmich. Quantitative intravoxel analyses of microCT-scanned resorbing ceramic biomaterials - perspectives for computer-aided biomaterial design. *Journal of Materials Research*, 29(23):2757–2772, 2014.

R. D'Agostino. Tests for normal distribution. *In: Goodness-of-Fit Techniques, D'Agostino, R., Stepenes, M. (eds.). Marcel Decker, New York*, pages 36–41, 1986.

J. Davies. Bone bonding at natural and biomaterial surfaces. *Biomaterials*, 28 (34):5058–5067, 2007.

F. M. de Sciarra. Nonlocal and gradient rate plasticity. *International Journal of Solids and Structures*, 41(26):7329 – 7349, 2004.

F. M. de Sciarra. A general theory for nonlocal softening plasticity of integral-type. *International Journal of Plasticity*, 24(8):1411 – 1439, 2008a.

F. M. de Sciarra. Variational formulations, convergence and stability properties in nonlocal elastoplasticity. *International Journal of Solids and Structures*, 45 (7-8):2322 – 2354, 2008b.

F. M. de Sciarra. Novel variational formulations for nonlocal plasticity. *International Journal of Plasticity*, 25(2):302 – 331, 2009.

G. de With, H. Van Dijk, N. Hattu, and K. Prijs. Preparation, microstructure and mechanical properties of dense polycrystalline hydroxy apatite. *Journal of Materials Science*, 16(6):1592 – 1598, 1981.

A. Dejaco, V. Komlev, J. Jaroszewicz, W. Swieszkowski, and C. Hellmich. Micro ct-based multi scale elasticity of double-porous (pre-cracked) hydroxyapatite granules for regenerative medicine. *Journal of Biomechanics*, 45(6):1068 — 1075, 2012.

V. Del Grosso and C. Mader. Speed of sound in pure water. *Journal of the Acoustical Society of America*, 52(5B):1442–1446, 1972.

D. Dempster, J. Lian, and S. Goldring. Anatomy and functions of the adult skeleton. *Primer on the metabolic bone diseases and disorders of mineral metabolism*, 6:7–11, 2006.

K. Devendra and V. Tomar. Role of the nanoscale interfacial arrangement in mechanical strength of tropocollagen–hydroxyapatite-based hard biomaterials. *Acta Biomaterialia*, 5(7):2704–2716, 2009.

A. Di Luca, K. Szlazak, I. Lorenzo-Moldero, C. Ghebes, A. Lepedda, W. Swieszkowski, C. Van Blitterswijk, and L. Moroni. Influencing chondrogenic differentiation of human mesenchymal stromal cells in scaffolds displaying a structural gradient in pore size. *Acta Biomaterialia*, 36:210–219, 2016.

A. Díaz and S. Hampshire. Characterisation of porous silicon nitride materials produced with starch. *Journal of the European Ceramic Society*, 24(2):413–419, 2004.

I. Doghri and A. Ouaar. Homogenization of two-phase elasto-plastic composite materials and structures: Study of tangent operators, cyclic plasticity and numerical algorithms. *International Journal of Solids and Structures*, 40(7): 1681–1712, 2003.

P. Dong, S. Haupert, B. Hesse, M. Langer, P.-J. Gouttenoire, V. Bousson, and F. Peyrin. 3d osteocyte lacunar morphometric properties and distributions in human femoral cortical bone using synchrotron radiation micro-ct images. *Bone*, 60:172–185, 2014.

E. Donnelly. Methods for assessing bone quality: A review. *Clinical Orthopaedics and Related Research*, 469(8):2128–2138, 2011.

L. Dormieux, D. Kondo, and F.-J. Ulm. *Microporomechanics*. Wiley, Chichester, U.K., 1st edition edition, 2006a.

L. Dormieux, D. Kondo, and F.-J. Ulm. *Microporomechanics*. John Wiley & Sons, Ltd, Chichester, West Sussex, England, 2006b. ISBN 9780470031889.

L. Dormieux, J. Sanahuja, and Y. Maalej. Résistance d'un polycristal avec interfaces intergranulaires imparfaites. *Comptes Rendus Mécanique*, 335(1):25–31, 2007.

W. Drugan and J. Willis. A micromechanics-based nonlocal constitutive equation and estimates of representative volume element size for elastic composites. *Journal of the Mechanics and Physics of Solids*, 44(4):497–524, 1996.

A. Duerinckx and A. Macovski. Polychromatic streak artifacts in computed tomography images. *Journal of Computer Assisted Tomography*, 2(4):481–487, 1978.

B. Duncker and L. Nordman. Determination of the strength of single fibres. *Paperi ja Puu*, 47(10):539–552, 1965.

G. J. Dvorak. Transformation field analysis of inelastic composite materials. *Proceedings of the Royal Society A: Mathematical, Physical and Engineering Sciences*, 437(1900):311–327, 1992.

G. J. Dvorak and Y. Benveniste. On transformation strains and uniform fields in multiphase elastic media. *Proceedings of the Royal Society A: Mathematical, Physical and Engineering Sciences*, 437(1900):291–310, 1992.

G. J. Dvorak, Y. Bahei-El-Din, and A. Wafa. The modeling of inelastic composite materials with the transformation field analysis. *Modelling and Simulation in Materials Science and Engineering*, 2(3):571–586, 1994.

E. Eanes and a. G. Lundy, D. X-ray diffraction study of the mineralization of turkey leg tendon. *Calcified Tissue International*, 6:239–248, 1970.

J. Eastoe. The amino acid composition of mammalian collagen and gelatin. *Biochemical Journal*, 61(4):589–600, 1955.

L. Eberhardsteiner, C. Hellmich, and S. Scheiner. Layered water in crystal interfaces as source for bone viscoelasticity: arguments from a multiscale approach. *Computer Methods in Biomechanics and Biomedical Engineering*, 17(1):48–63, 2014.

E. M. L. Ehrnrooth and P. Kolseth. The tensile testing of single wood pulp fibers in air and in water. *Wood and Fiber Science*, 16(4):549–566, 1984.

A. Engler, S. Sen, H. Sweeney, and D. Discher. Matrix elasticity directs stem cell lineage specification. *Cell*, 126(4):677–689, 2006.

S. Eppell, B. Smith, H. Kahn, and R. Ballarini. Nano measurements with microdevices: Mechanical properties of hydrated collagen fibrils. *Journal of the Royal Society Interface*, 3(6):117–121, 2006.

M. Epple. Solid-state chemical methods to investigate the nature of calcified deposits. *Zeitschrift für Kardiologie*, 390(3), 2001.

J. Eshelby. The determination of the elastic field of an ellipsoidal inclusion, and related problems. *Proceedings of the Royal Society of London. Series A, Mathematical and Physical Sciences*, 241(1226):376–396, 1957.

A. Every and W. Sachse. Sensitivity of inversion algorithms for recovering elastic constants of anisotropic solids from longitudinal wavespeed data. *Ultrasonics*, 30:43–48, 1992.

P. Fanti, M. Monier-Faugere, Z. Geng, J. Schmidt, P. Morris, D. Cohen, and H. Malluche. The phytoestrogen genistein reduces bone loss in short-term ovariectomized rats. *Osteoporosis International*, 8(3):274–281, 1998.

J. Francisco, Y. Yu, R. Oliver, and W. Walsh. Relationship between age, skeletal site, and time post-ovariectomy on bone mineral and trabecular microarchitecture in rats. *Journal of Orthopaedic Research*, 29(2):189–196, 2011.

P. Fratzl, S. Schreiber, and K. Klaushofer. Bone mineralization as studied by small-angle x-ray scattering. *Connective Tissue Research*, 34(4), 1996.

A. Fritsch and C. Hellmich. Universal microstructural patterns in cortical and trabecular, extracellular and extravascular bone materials: Micromechanics-based prediction of anisotropic elasticity. *Journal of Theoretical Biology*, 244(4):597–620, 2007.

A. Fritsch, L. Dormieux, and C. Hellmich. Porous polycrystals built up by uniformly and axisymmetrically oriented needles: homogenization of elastic properties. *Comptes Rendus Mécanique*, 334(3):151–157, 2006.

A. Fritsch, L. Dormieux, C. Hellmich, and J. Sanahuja. Mechanical behavior of hydroxyapatite biomaterials: an experimentally validated micromechanical model for elasticity and strength. *Journal of Biomedical Materials Research Part A*, 88(1):149–161, 2009a.

A. Fritsch, L. Dormieux, C. Hellmich, and J. Sanahuja. Mechanical behavior of hydroxyapatite biomaterials: An experimentally validated micromechanical model for elasticity and strength. *Journal of Biomedical Materials Research, Part A*, 88A(1):149–161, 2009b.

A. Fritsch, C. Hellmich, and L. Dormieux. Ductile sliding between mineral crystals followed by rupture of collagen crosslinks: Experimentally supported micromechanical explanation of bone strength. *Journal of Theoretical Biology*, 260(2): 230–252, 2009c.

A. Fritsch, C. Hellmich, and L. Dormieux. The role of disc-type crystal shape for micromechanical predictions of elasticity and strength of hydroxyapatite biomaterials. *Philosophical Transactions of the Royal Society A: Mathematical, Physical and Engineering Sciences*, 368(1917):1913–1935, 2010a.

A. Fritsch, C. Hellmich, and L. Dormieux. The role of disc-type crystal shape for micromechanical predictions of elasticity and strength of hydroxyapatite biomaterials. *Philosophical Transactions of the Royal Society of London A: Mathematical, Physical and Engineering Sciences*, 368(1917):1913–1935, 2010b.

A. Fritsch, A. Dejaco, V. Komlev, W. Swieszkowski, J. Jaroszewicz, E. Bongaers, and C. Hellmich. Translation of CT data into voxel-specific micromechanics-based elasticity tensors. *Micro-CT User Meeting, Abstract Book*, SkyScan, 2011: 108–112, 2011.

A. Fritsch, C. Hellmich, and P. Young. Micromechanics-derived scaling relations for poroelasticity and strength of brittle porous polycrystals. *Journal of Applied Mechanics*, 80(2):020905, 2013a.

A. Fritsch, C. Hellmich, and P. Young. Micromechanics-derived scaling relations for poroelasticity and strength of brittle porous polycrystals. *Journal of Applied Mechanics*, 80(2):020905–1–12, 2013b.

F. Fritzen and T. Böhlke. Nonuniform transformation field analysis of materials with morphological anisotropy. *Composites Science and Technology*, 71(4):433—-442, 2011.

H. Frost. Micropetrosis. *Journal of Bone and Joint Surgery*, 42:144–150, 1960.

E. Fukada and Y. Ando. Piezoelectric properties of poly-β-hydroxybutyrate and copolymers of β-hydroxybutyrate and β-hydroxyvalerate. *International Journal of Biological Macromolecules*, 8(6):361–366, 1986.

GE Measurement and Control. Phoenix Nanotom M. 180 kV/20 W X-ray nanoCT system for high-resolution analysis and 3D metrology,

2014. https://www.gemeasurement.com/sites/gemc.dev/files/nanotom_brochure_english_0.pdf.

P. Gentile, V. Chiono, I. Carmagnola, and P. Hatton. An overview of poly(lactic-co-glycolic) acid (plga)-based biomaterials for bone tissue engineering. *International Journal of Molecular Sciences*, 15(3):3640–3659, 2014.

P. Germain. The method of virtual power in continuum mechanics. part 2: Microstructure. *SIAM Journal on Applied Mathematics*, 25(3):556–575, 1973.

L. Gibson and M. Ashby. *Cellular solids: structure and properties*. Cambridge University Press, 1997.

R. Gilmore and J. Katz. Elastic properties of apatites. *Journal of Materials Science*, 17(4):1131–1141, 1982.

J. Gong, J. Arnold, and S. Cohn. Composition of trabecular and cortical bone. *The Anatomical Record*, 149:325–332, 1964.

S. Gould and R. Lewontin. The spandrels of san marco and the panglossian paradigm: a critique of the adaptationist programme. *Proceedings of the Royal Society of London, Series B, Biological Sciences*, 205:581–598, 1979.

P. Govindarajan, W. Böcker, T. El Khassawna, M. Kampschulte, G. Schlewitz, B. Huerter, U. Sommer, L. Dürselen, A. Ignatius, N. Bauer, G. Szalay, S. Wenisch, K. Lips, R. Schnettler, A. Langheinrich, and C. Heiss. Bone matrix, cellularity, and structural changes in a rat model with high-turnover osteoporosis induced by combined ovariectomy and a multiple-deficient diet. *The American Journal of Pathology*, 184(3):765–777, 2014.

Q. Grimal, G. Rus, W. Parnell, and P. Laugier. A two-parameter model of the effective elastic tensor for cortical bone. *Journal of Biomechanics*, 44(8):1621–1625, 2011.

X. Guo and S. Goldstein. Vertebral trabecular bone microscopic tissue elastic modulus and hardness do not change in ovariectomized rats. *Journal of Orthopaedic Research*, 18(2):333–336, 2000.

S. Gupta, R. Kumar, and N. Mishra. Influence of quercetin and nanohydroxyapatite modifications of decellularized goat-lung scaffold for bone regeneration. *Materials Science and Engineering: C*, 71:919–928, 2017.

M. Hahn, M. Vogel, M. Pompesious-Kempa, and G. Delling. Trabecular bone pattern factor—a new parameter for simple quantification of bone microarchitecture. *Bone*, 13(4):327–330, 1992.

B. Halphen and Q. Nguyen. Sur les matériaux standard généralisés. *Journal de Mécanique*, 14:39–63, 1975.

E. Hamed, Y. Lee, and I. Jasiuk. Multiscale modeling of elastic properties of cortical bone. *Acta Mechanica*, 213(1):131–154, 2010.

E. Hamed, E. Novitskaya, J. Li, I. Jasiuk, and J. McKittrick. Experimentally-based multiscale model of the elastic moduli of bovine trabecular bone and its constituents. *Materials Science and Engineering: C*, 54:207–216, 2015.

F. Hammet. A biochemical study of bone growth. I Changes in the ash, organics matter and water during growth (mus norvegicus albinus). *The Journal of Biological Chemistry*, 64:409–428, 1925.

F. Hang and A. Barber. Nano-mechanical properties of individual mineralized collagen fibrils from bone tissue. *Journal of the Royal Society Interface*, 2010.

R. Harley, D. James, A. Miller, and J. White. Phonons and the elastic moduli of collagen and muscle. *Nature*, 267(5608):285–287, 1977.

A. Harrysson and M. Ristinmaa. Large strain elasto-plastic model of paper and corrugated board. *International Journal of Solids and Structures*, 45(11-12): 3334–3352, 2008.

Z. Hashin. Analysis of composite materials - A survey. *Journal of Applied Mechanics*, 50(3):481, 1983.

P. Hasslinger, V. Vass, A. Dejaco, R. Blanchard, G. Örlygsson, P. Gargiulo, and C. Hellmich. Coupling multiscale X-ray physics and micromechanics for bone tissue composition and elasticity determination from micro-ct data, by example of femora from ovx and sham rats. *International Journal for Computational Methods in Engineering Science and Mechanics*, 17(3):222–244, 2016.

K. Helbig. *Foundations of anisotropy for exploration seismics.* Pergamon, New York, 1994.

C. Hellmich. Microelasticity of bone. In L. Dormieux and F.-J.. Ulm, editors, *Applied Micromechanics of Porous Materials - CISM Courses and Lectures No. 480*. 2005.

C. Hellmich and F.-J. Ulm. Micromechanical model for ultrastructural stiffness of mineralized tissues. *Journal of Engineering Mechanics*, 128(8):898–908, 2002a.

C. Hellmich and F.-J. Ulm. Are mineralized tissues open crystal foams reinforced by crosslinked collagen? – some energy arguments. *Journal of Biomechanics*, 535(9):1199–1212, 2002b.

C. Hellmich and F.-J. Ulm. Average hydroxyapatite concentration is uniform in the extracollagenous ultrastructure of mineralized tissues: evidence at the 1-10-micrometer scale. *Biomechanics and Modeling in Mechanobiology*, 2(1):21–36, 2003.

C. Hellmich and F.-J. Ulm. Microporodynamics of bones: Prediction of the "frenkel–biot" slow compressional wave. *Journal of Engineering Mechanics*, 131 (9):918–927, 2005a.

C. Hellmich and F.-J. Ulm. Drained and undrained poroelastic properties of healthy and pathological bone: A poro-micromechanical investigation. *Transport in Porous Media*, 58(3):243–268, 2005b.

C. Hellmich, F.-J. Ulm, and H. Mang. Multisurface chemoplasticity. i: Material model for shotcrete. *Journal of Engineering Mechanics*, 125(6):692–701, 1999.

C. Hellmich, J.-F. Barthélémy, and L. Dormieux. Mineral-collagen interactions in elasticity of bone ultrastructure – a continuum micromechanics approach. *European Journal of Mechanics - A/Solids*, 23(5):783–810, 2004a.

C. Hellmich, F.-J. Ulm, and L. Dormieux. Can the diverse elastic properties of trabecular and cortical bone be attributed to only a few tissue-independent phase properties and their interactions? *Biomechanics and Modeling in Mechanobiology*, 2(4):219–238, 2004b.

C. Hellmich, C. Kober, and B. Erdmann. Micromechanics-based conversion of CT data into anisotropic elasticity tensors, applied to FE simulations of a mandible. *Annals of Biomedical Engineering*, 36(1):108–122, 2008.

C. Hellmich, D. Celundova, and F.-J. Ulm. Multiporoelasticity of hierarchically structured materials: Micromechanical foundations and application to bone. *Journal of Engineering Mechanics*, 135(5):382–394, 2009.

P. Helnwein. Some remarks on the compressed matrix representation of symmetric second-order and fourth-order tensors. *Computer Methods in Applied Mechanics and Engineering*, 190(22-23):2753–2770, 2001.

A. V. Hershey. The elasticity of an isotropic aggregate of anisotropic cubic crystals. *Journal of Applied mechanics - Transactions of the ASME*, 21(3):236–240, 1954.

B. Hesse, P. Varga, M. Langer, A. Pacureanu, S. Schrof, N. Männicke, H. Suhonen, P. Maurer, P. Cloetens, F. Peyrin, and K. Raum. Canalicular network morphology is the major determinant of the spatial distribution of mass density in human bone tissue: evidence by means of synchrotron radiation phase contrast nano-ct. *Journal of Bone and Mineral Research*, 30(2):346–356, 2015.

R. Hill. Elastic properties of reinforced solids: Some theoretical principles. *Journal of the Mechanics and Physics of Solids*, 11(5):357–372, 1963.

R. Hill. A self-consistent mechanics of composite materials. *Journal of the Mechanics and Physics of Solids*, 13(4):213–222, 1965a.

R. Hill. Continuum micro-mechanics of elastoplastic polycrystals. *Journal of the Mechanics and Physics of Solids*, 13(2):89–101, 1965b.

R. Hill. The essential structure of constitutive laws for metal composites and polycrystals. *Journal of the Mechanics and Physics of Solids*, 15(2):79–95, 1967.

A. Hodge and J. Petruska. Recent studies with the electron microscope on ordered aggregates of the tropocollagen molecule. In G. Ramachandran, editor, *Aspects of Protein Structure – Proceedings of a Symposium held in Madras 14 - 18 January 1963 and organized by the University of Madras, India*, pages 289–300. Academic Press, London and New York, 1963.

P. Hoegh-Andersen, L. Tankó, T. Andersen, C. Lundberg, J. Mo, A.-M. Heegaard, J.-M. Delaissé, and S. Christgau. Ovariectomized rats as a model of postmenopausal osteoarthritis: Validation and application. *Arthritis Research & Therapy*, 6(2):R169–R180, 2004.

K. Hofstetter, C. Hellmich, and J. Eberhardsteiner. Development and experimental validation of a continuum micromechanics model for the elasticity of wood. *European Journal of Mechanics-A/Solids*, 24(6):1030–1053, 2005.

H. Hogan, S. Ruhmann, and H. Sampson. The mechanical properties of cancellous bone in the proximal tibia of ovariectomized rats. *Journal of Bone and Mineral Research*, 15(2):284–292, 2000.

S. Hollister. Porous scaffold design for tissue engineering. *Nature Materials*, 4(7): 518–524, 2005.

J. Hubbel and S. Seitzer. Tables of x-ray mass attenuation coefficients and mass energy-absorption coefficients from 1 kev to 20 mev for elements z 1 to 92 and 48 additional substances of dosimetric interest. Technical report, National Institute of Standards and Technology, U.S. Department of Commerce, 2004.

J. Hubbell and S. Seltzer. Tables of X-ray mass attenuation coefficients and mass energy-absorption coefficients from 1 keV to 20 MeV for elements z = 1 to 92 and 48 additional substances of dosimetric interest. U.S. Department of Commerce, National Institute of Standards and Technology (NIST), July 2004, 1996. `http://physics.nist.gov/PhysRefData/XrayMassCoef/cover.html`.

C. Huet. Application of variational concepts to size effects in elastic heterogeneous bodies. *Journal of the Mechanics and Physics of Solids*, 38(6):813–841, 1990.

G. Hunter, P. Hauschka, R. Poole, L. Rosenberg, and H. Goldberg. Nucleation and inhibition of hydroxyapatite formation by mineralized tissue proteins. *Biochemical Journal*, 317(1):59–64, 1996.

D. Hutmacher. Scaffolds in tissue engineering bone and cartilage. *Biomaterials*, 21(24):2529–2543, 2000.

J. Idaszek, M. Zinn, M. Obarzanek-Fojt, V. Zell, W. Swieszkowski, and A. Bruinink. Tailored degradation of biocompatible poly(3-hydroxybutyrate-co-3-hydroxyvalerate)/calcium silicate/poly(lactide-co-glycolide) ternary composites: An in vitro study. *Materials Science and Engineering: C*, 33(7):4352–4360, 2013.

J. Idaszek, A. Bruinink, and W. Swieszkowski. Ternary composite scaffolds with tailorable degradation rate and highly improved colonization by human bone marrow stromal cells. *Journal of Biomedical Materials Research Part A*, 103(7): 2394–2404, 2015a.

J. Idaszek, T. Brynk, J. Jaroszewicz, F. Vanmeert, A. Bruinink, and W. Swieszkowski. Investigation of mechanical properties of porous composite scaffolds with tailorable degradation kinetics after in vitro degradation using digital image correlation. *Polymer Composites*, 2015b.

J. Idaszek, A. Bruinink, and W. Swieszkowski. Delayed degradation of poly(lactide-co-glycolide) accelerates hydrolysis of poly(ε-caprolactone) in ternary composite scaffolds. *Polymer Degradation and Stability*, 124:119–127, 2016.

V. Ievlev, A. Kostyuchenko, E. Belonogov, and S. Barinov. Hardness and the nature of microplasticity of hydroxyapatite. *Inorganic Materials*, 49(4):416–422, 2013.

D. Jackson and D. Hawkes. X-ray attenuation coefficients of elements and mixtures. *Physics Reports*, 70(3):169–233, 1981.

S. Jaecques, H. Van Oosterwyck, L. Muraru, T. Van Cleynenbreugel, E. De Smet, M. Wevers, I. Naert, and J. Vander Sloten. Individualised, micro CT-based finite element modelling as a tool for biomechanical analysis related to tissue engineering of bone. *Biomaterials*, 25(9):1683–1696, 2004.

K. James, H. Levene, J. Parsons, and J. Kohn. Small changes in polymer chemistry have a large effect on the bone–implant interface:: evaluation of a series of degradable tyrosine-derived polycarbonates in bone defects. *Biomaterials*, 20 (23–24):2203–2212, 1999.

T. Jiang, J. Shao, and W. Xu. A non-uniform transformation field analysis for frictional cohesive geomaterials. *European Journal of Mechanics - A/Solids*, 42: 97–111, 2013.

R. Jilka, R. Weinstein, T. Bellido, A. Parfitt, and S. Manolagas. Osteoblast programmed cell death (apoptosis): modulation by growth factors and cytokines. *Journal of Bone and Mineral Research*, 13(5):793–802, 1998.

A. Jones, C. Arns, A. Sheppard, D. Hutmacher, B. Milthorpe, and M. Knackstedt. Assessment of bone ingrowth into porous biomaterials using MICRO-CT. *Biomaterials*, 28(15):2491–2504, 2007. Imaging Techniques for Biomaterials Characterization.

P. Joseph and R. Spital. A method for correcting bone induced artifacts in computed tomography scanners. *Journal of Computer Assisted Tomography*, 2(1): 100–108, 1978.

J. Jowsey. Age changes in human bone. *Clinical Orthopaedics*, 17:210–218, 1960.

D. Kalu. The ovariectomized rat model of postmenopausal bone loss. *Bone and Mineral*, 15(3):175–192, 1991.

E. Katz and S. Li. Structure and function of bone collagen fibrils. *Journal of Molecular Biology*, 80(1):1–15, 1973.

J. Katz and K. Ukraincik. On the anisotropic elastic properties of hydroxyapatite. *Journal of Biomechanics*, 4(3):221–227, 1971.

J. Katz, H. Yoon, S. Lipson, R. Maharidge, A. Meunier, and P. Christel. The effects of remodeling on the elastic properties of bone. *Calcified Tissue International*, 36(1):31 — 36, 1984.

T. Keaveny, E. Wachtel, C. Ford, and W. Hayes. Differences between the tensile and compressive strengths of bovine tibial trabecular bone depend on modulus. *Journal of Biomechanics*, 27(9):1137–1146, 1994.

J. G. Kim, E. Lee, S. H. Kim, K. Y. Whang, S. Oh, and J.-Y. Imm. Effects of a Lactobacillus casei 393 fermented milk product on bone metabolism in ovariectomised rats. *International Dairy Journal*, 19(11):690–695, 2009.

C. Kohlhauser and C. Hellmich. Determination of poisson's ratios in isotropic, transversely isotropic, and orthotropic materials by means of combined ultrasonic-mechanical testing of normal stiffnesses: Application to metals and wood. *European Journal of Mechanics - A/Solids*, 33:82–98, 2012.

C. Kohlhauser and C. Hellmich. Ultrasonic contact pulse transmission for elastic wave velocity and stiffness determination: Influence of specimen geometry and porosity. *Engineering Structures*, 47:115–133, 2013.

W. Koiter. Stress-strain relations, uniqueness and variational theorems for elastic-plastic materials with a singular yield surface. *Quarterly of Applied Mathematics*, 11:350–354, 1953.

T. Kokubo, H. Kushitani, S. Sakka, T. Kitsugi, and T. Yamamuro. Solutions able to reproduce in vivo surface-structure changes in bioactive glass-ceramic a-w3. *Journal of Biomedical Materials Research*, 24(6):721–734, 1990.

R. Kornhuber, R. Krause, O. Sander, P. Deuflhard, and S. Ertel. A monotone multigrid solver for two body contact problems in biomechanics. *Computing and Visualization in Science*, 11(1):3–15, 2008.

G. Kresse and J. Hafner. *Ab initio* molecular dynamics for open-shell transition metals. *Physical Review B*, 48:13115–13118, 1993.

R. Kriz and W. Stinchcomb. Elastic moduli of transversely isotropic graphite fibers and their composites. *Experimental Mechanics*, 19(2):41–49, 1979.

E. Kröner. Berechnung der elastischen konstanten des vielkristalls aus den konstanten des einkristalls. *Zeitschrift für Physik*, 151(4):504–518, 1958.

S. Kruch and J.-L. Chaboche. Multi-scale analysis in elasto-viscoplasticity coupled with damage. *International Journal of Plasticity*, 27:2026–2039, 2011.

Z. Kublik, J. Idaszek, and W. Swieszkowski. Fabrication of porous poly(3-hydroxybutyrate-co-3-hydroxyvalerate) scaffolds using a rapid prototyping technique. *Engineering of Biomaterials*, 15:79–81, 2012.

A. Laib, O. Barou, L. Vico, M. Lafage-Proust, C. Alexandre, and P. Rüegsegger. 3D micro-computed tomography of trabecular and cortical bone architecture with application to a rat model of immobilisation osteoporosis. *Medical and Biological Engineering and Computing*, 38(3):326–332, 2000.

W. Landis. The strength of a calcified tissue depends in part on the molecular structure and organization of its constituent mineral crystals in their organic matrix. *Bone*, 16(5):533–544, 1995.

N. Laws. On the thermostatics of composite materials. *Journal of the Mechanics and Physics of Solids*, 21(1):9–17, 1973.

N. Laws. A note on interaction energies associated with cracks in anisotropic solids. *Philosophical Magazine*, 36(2):367–372, 1977a.

N. Laws. The determination of stress and strain concentrations at an ellipsoidal inclusion in an anisotropic material. *Journal of Elasticity*, 7(1):91–97, 1977b.

N. Laws. A note on penny-shaped cracks in transversely isotropic materials. *Mechanics of Materials*, 4(2):209–212, 1985.

S. Lees. Considerations regarding the structure of the mammalian mineralized osteoid from viewpoint of the generalized packing model. *Connective Tissue Research*, 16(4):281–303, 1987.

S. Lees. Mineralization of type I collagen. *Biophysical Journal*, 85:204–207, 2003.

S. Lees and J. Heeley. Density of a sample bovine cortical bone matrix and its solid constituent in various media. *Calcified Tissue International*, 33:499–504, 1981.

S. Lees and H. Mook. Equatorial diffraction spacing as a function of water content in fully mineralized cow bone determined by neutron diffraction. *Connective Tissue Research*, 39:291–292, 1986.

S. Lees and E. Page. A study of some properties of mineralized turkey leg tendon. *Connective Tissue Research*, 28(4):263–287, 1992.

S. Lees and K. Prostak. The locus of mineral crystallites in bone. *Connective Tissue Research*, 18(1):41–54, 1988.

S. Lees, P. Cleary, J. Heeley, and E. Gariepy. Distribution of sonic plesio-velocity in a compact bone sample. *The Journal of the Acoustical Society of America*, 66(3):641–646, 1979a.

S. Lees, J. Heeley, and P. Cleary. A study of some properties of a sample of bovine cortical bone using ultrasound. *Calcified Tissue International*, 29(1):107–117, 1979b.

S. Lees, J. Ahern, and M. Leonard. Parameters influencing the sonic velocity in compact calcified tissues of various species. *Journal of the Acoustical Society of America*, 74(1):28–33, 1983.

S. Lees, L. Bonar, and H. Mook. A study of dense mineralized tissue by neutron diffraction. *International Journal of Biological Macromolecules*, 6(6):321–326, 1984.

S. Lees, N.-J. Tao, and S. Lindsay. Studies of compact hard tissues and collagen by means of brillouin light scattering. *Connective Tissue Research*, 24(3-4): 187–205, 1990.

S. Lees, D. Hanson, E. Page, and H. Mook. Comparison of dosage-dependent effects of beta-aminopropionitrile, sodium fluoride, and hydrocortisone on selected physical properties of cortical bone. *Journal of Bone and Mineral Research*, 9 (9):1377–1389, 1994a.

S. Lees, K. Prostak, V. Ingle, and K. Kjoller. The loci of mineral in turkey leg tendon as seen by atomic force microscope and electron microscopy. *Calcified Tissue International*, 55(3):180 – 189, 1994b.

S. Lees, D. Hanson, and E. A. Page. Some acoustical properties of the otic bones of a fin whale. *Journal of the Acoustical Society of America*, 99(4):2421–2427, 1995.

V. Lemaire, F. Tobin, L. Greller, C. Cho, and L. Suva. Modeling the interactions between osteoblast and osteoclast activities in bone remodeling. *Journal of Theoretical Biology*, 229:293–309, 2004.

P. Lesclous, D. Guez, B. Baroukh, A. Vignery, and J. Saffar. Histamine participates in the early phase of trabecular bone loss in ovariectomized rats. *Bone*, 34(1):91–99, 2004.

V. Levin. Thermal expansion coefficient of heterogeneous materials. *Inzh. Zh. Mekh. Tverd. Tela*, 2(1):83–94, 1967.

H. Li and J. Chang. Fabrication and characterization of bioactive wollastonite/phbv composite scaffolds. *Biomaterials*, 25(24):5473–5480, 2004.

D.-M. Liu. Preparation and characterisation of porous hydroxyapatite bioceramic via a slip-casting route. *Ceramics International*, 24(6):441–446, 1998.

X. Liu, C. Li, W. Lu, W. Cai, and L. Zheng. Skeletal site-specific response to ovariectomy in a rat model: Change in bone density and microarchitecture. *Clinical Oral Implants Research*, 26(4):392–398, 2015.

H. Lodish, A. Berk, S. L. Zipursky, P. Matsudaira, D. Baltimore, and J. Darnell. *Molecular Cell Biology*, chapter 22.3, Collagen: The Fibrous Proteins of the Matrix. W. H. Freeman, New York, 4th edition edition, 2000. `http://www.ncbi.nlm.nih.gov/books/NBK21582/`.

D. Lowe, N. Lepori-Bui, P. Fomin, L. Sloofman, X. Zhou, M. Farach-Carson, L. Wang, and C. Kirn-Safran. Deficiency in perlecan/hspg2 during bone development enhances osteogenesis and decreases quality of adult bone in mice. *Calcified Tissue International*, 95(1):29–38, 2014.

J. Lubliner. *Plasticity theory.* Courier Corporation, 2008.

K. Luczynski, A. Dejaco, O. Lahayne, J. Jaroszewicz, W. Swieszkowski, and C. Hellmich. Microct/micromechanics-based finite element models and quasi-static unloading tests deliver consistent values for young's modulus of rapid-prototyped polymer-ceramic tissue engineering scaffold. *CMES – Computational Modelling in Engineering & Sciences*, 87(6):505–529, 2012.

K. Luczynski, A. Steiger-Thrirsfeld, J. Bernardi, J. Eberhardsteiner, and C. Hellmich. Extracellular bone matrix exhibits hardening elastoplasticity and more than double cortical strength: Evidence from homogeneous compression of non-tapered single micron-sized pillars welded to a rigid substrate. *Journal of the Mechanical Behavior of Biomedical Materials*, 52:51–62, 2015.

P. Mäkelä and S. Östlund. Orthotropic elastic-plastic material model for paper materials. *International Journal of Solids and Structures*, 40(21):5599–5620, 2003.

J. Mandel. Thermodynamics and plasticity. In *Foundations of continuum thermodynamics*, pages 283–304. Macmillan education uk edition, 1973.

R. W. Mann, G. A. Baum, and C. C. Habeger. Determination of all nine orthotropic elastic constants for machine-made paper. *TAPPI Journal*, 63(2): 163–166, 1980.

R. E. Mark, C. C. Habeger Jr., J. Borch, and M. B. Lyne. *Handbook of physical testing of paper*. Marcel Dekker, New York et al., 2002.

Z. Markov. Elementary micromechanics of heterogeneous media. In *Heterogeneous Media*, pages 1–162. Birkhäuser Boston, 2000.

G. Marotti. A new theory of bone lamellation. *Calcified Tissue International*, 53 (1):47–56, 1993.

G. Marotti, M. Muglia, C. Palumbo, and D. Zaffe. The microscopic determinants of bone mechanical properties. *Italian Journal of Mineral and Electrolyte Metabolism*, 8(4):167–175, 1994.

G. Marotti, M. Ferretti, and C. Palumbo. The problem of bone lamellation: An attempt to explain different proposed models. *Journal of Morphology*, 274(5): 543–550, 2013.

J. Martínez-Reina, J. Domínguez, and J. García-Aznar. Effect of porosity and mineral content on the elastic constants of cortical bone: a multiscale approach. *Biomechanics and Modeling in Mechanobiology*, 210(3):309–322, 2011.

G. Maugin. The principle of virtual power: from eliminating metaphysical forces to providing an efficient modelling tool. *Continuum Mechanics and Thermodynamics*, 5(2):127–146, 2013.

R. McCarthy, L. Jeffcott, and R. McCartney. Ultrasound speed in equine cortical bone: Effects of orientation, density, porosity and temperature. *Journal of Biomechanics*, 23(11):1139–1143, 1990.

E. McNally, H. Schwarcz, G. Botton, and A. Arsenault. A model for the ultrastructure of bone based on electron microscopy of ion-milled sections. *PLoS One*, 7:e29258, 2012.

K. Meek, N. Fullwood, P. Cooke, G. Elliott, D. Maurice, A. Quantock, R. Wall, and C. Worthington. Synchrotron X-ray diffraction studies of the cornea, with implications for stromal hydration. *Biophysical Journal*, 60(2):467–474, 1991.

S. Meille. Etude du comportement méanique du plâtre pris en relation avec sa microstructure (study of the mechanical behaviour of gypsum with regard to its microstructure). *Ph.D thesis, INSA Lyon*, 2001.

E. Melan. Zur plastizität des räumlichen kontinuums. *Ingenieur-Archiv*, 9(5): 116–126, 1938.

T. Metzger, T. Kriepke, T. Vaughan, L. McNamara, and G. Niebur. The in situ mechanics of trabecular bone marrow: The potential for mechanobiological response. *Journal of Biomechanical Engineering*, 137(1):011006, 2015.

J. Michel and P. Suquet. Nonuniform transformation field analysis. *International Journal of Solids and Structures*, 40(2):6937–6955, 2003.

J. Michel and P. Suquet. Computational analysis of nonlinear composite structures using the nonuniform transformation field analysis. *Computer Methods in Applied Mechanics and Engineering*, 193(48-51):5477—-5502, 2004.

C. Miles and M. Ghelashvili. Polymer-in-a-box mechanism for the thermal stabilization of collagen molecules in fibers. *Biophysical Journal*, 76(6):3243–3252, 1999.

A. Miller and S. Parker. The organic matrix of bone. *Philosophical Transactions of the Royal Society B*, 304:455–477, 1984.

MITA. DICOM PS3.3 2013 – Information Object Definitions (2013). Medical Imaging and Technology Alliance (MITA), division of the National Electrical Manufacturers Association (NEMA), 2013. `medical.nema.org/dicom/2013/output/pdf/part03.pdf`.

T. Mori and K. Tanaka. Average stress in matrix and average elastic energy of materials with misfitting inclusions. *Acta Metallurgica*, 21(5):571–574, 1973.

C. Morin and C. Hellmich. Mineralization-driven bone tissue evolution follows from fluid-to-solid phase transformations in closed thermodynamic systems. *Journal of Theoretical Biology*, 335:185–197, 2013.

C. Morin and C. Hellmich. A multiscale poromicromechanical approach to wave propagation and attenuation in bone. *Ultrasonics*, 54(5):1251–1269, 2014.

C. Morin, Z. Moumni, and W. Zaki. A constitutive model for shape memory alloys accounting for thermomechanical coupling. *International Journal of Plasticity*, 27(5):748 – 767, 2011a. ISSN 0749-6419.

C. Morin, Z. Moumni, and W. Zaki. Thermomechanical coupling in shape memory alloys under cyclic loadings: Experimental analysis and constitutive modeling. *International Journal of Plasticity*, 27(12):1959 – 1980, 2011b. ISSN 0749-6419.

C. Morin, C. Hellmich, and P. Henits. Fibrillar structure and elasticity of hydrating collagen: A quantitative multiscale approach. *Journal of Theoretical Biology*, 317:384–393, 2013.

C. Morin, V. Vass, and C. Hellmich. Micromechanics of elastoplastic porous polycrystals: Theory, algorithm, and application to osteonal bone. *International Journal of Plasticity*, 2017.

S. Nemat-Nasser and M. Hori. *Micromechanics: overall properties of heterogeneous materials*. Elsevier, Amsterdam, The Netherlands, 2nd edition edition, 1999.

S. Nikolov and D. Raabe. Hierarchical modeling of the elastic properties of bone at submicron scales: The role of extrafibrillar mineralization. *Biophysical Journal*, 94(11):4220–4232, 2008.

B. Noble. The osteocyte lineage. *Archives of Biochemistry and Biophysics*, 473: 106–111, 2008.

J. Orgel, T. Irving, A. Miller, and T. Wess. Microfibrillar structure of type I collagen in situ. *Proceedings of the National Academy of Sciences of the United States of America*, 103(24):9001–9005, 2006.

M. Ortiz and E. Popov. Accuracy and stability of integration algorithms for elastoplastic constitutive relations. *International Journal for Numerical Methods in Engineering*, 21(9):1561–1576, 1985.

W. Pabst, E. Gregorová, G. Tichá, and E. Týnová. Effective elastic properties of alumina-zirconia composite ceramics-Part 4. Tensile modulus of porous alumina and zirconia. *Ceramics-Silikáty*, 48(4):165–174, 2004.

D. H. Page, F. El-Hosseiny, K. Winkler, and A. P. S. Lancaster. Elastic modulus of single wood pulp fibers. *TAPPI Journal*, 60(4):114–117, 1977.

P. Palacio-Mancheno, A. Larriera, S. Doty, L. Cardoso, and S. Fritton. 3d assessment of cortical bone porosity and tissue mineral density using high-resolution μct: Effects of resolution and threshold method. *Journal of Bone and Mineral Research*, 29(1):142–150, 2012.

E. Papadakis, T. Patton, Y. Tsai, D. Thompson, and R. Thompson. The elastic moduli of a thick composite as measured by ultrasonic bulk wave pulse velocity. *Journal of the Acoustical Society of America*, 89(6):2753–2757, 1991.

A. Parfitt. The physiologic and clinical significance of bone histomorphometric data. In R. Recker, editor, *Histomorphometry, Techniques and Interpretation*, pages 143–223. CRC Press Inc, Boca Raton, FL, USA, 1983.

W. Parnell and Q. Grimal. The influence of mesoscale porosity on cortical bone anisotropy. investigations via asymptotic homogenization. *Journal of the Royal Society Interface*, 6:97–109, 2009.

J. Peelen, B. Rejda, and K. de Groot. Preparation and properties of sintered hydroxylapatite. *Ceramurgia International*, 4(2):71–74, 1978.

V. Pensée, D. Kondo, and L. Dormieux. Micromechanical analysis of anisotropic damage in brittle materials. *Journal of Engineering Mechanics*, 128(8):889–897, 2002.

F. Peters, K. Schwarz, and M. Epple. The structure of bone studied with synchrotron x-ray diffraction, x-ray absorption spectroscopy and thermal analysis. *Thermochimica Acta*, 361(1-2), 2000.

K. Phani. Young's modulus-porosity relation in gypsum systems. *American Ceramic Society Bulletin*, 65:1584–1586, 1986.

B. Pichler and C. Hellmich. Estimation of influence tensors for eigenstressed multiphase elastic media with nonaligned inclusion phases of arbitrary ellipsoidal shape. *Journal of Engineering Mechanics*, 136(8):1043–1053, 2010.

B. Pichler and C. Hellmich. Upscaling quasi-brittle strength of cement paste and mortar: A multi-scale engineering mechanics model. *Cement and Concrete Research*, 41(5):467–476, 2011.

B. Pichler, C. Hellmich, and H. Mang. Impact of rocks onto gravel - design and evaluation of experiments. *International Journal of Impact Engineering*, 31: 559–578, 2005.

B. Pichler, C. Hellmich, and J. Eberhardsteiner. Spherical and acicular representation of hydrates in a micromechanical model for cement paste: prediction of early-age elasticity and strength. *Acta Mechanica*, 203(3):137–162, 2009.

B. Pichler, C. Hellmich, J. Eberhardsteiner, J. Wasserbauer, P. Termkhajornkit, R. Barbarulo, and G. Chanvillard. Effect of gel-space ratio and microstructure on strength of hydrating cementitious materials: An engineering micromechanics approach. *Cement and Concrete Research*, 45:55 – 68, 2013.

R. Pidaparti and D. Burr. Collagen fiber orientation and geometry effects on the mechanical properties of secondary osteons. *Journal of Biomechanics*, 25(8), 1992.

R. Pidaparti, A. Chandran, Y. Takano, and C. Turner. Bone mineral lies mainly outside collagen fibrils: Predictions of a composite model for osternal bone. *Journal of Biomechanics*, 29(7), 1996.

S. Pradhan, D. Katti, and K. Katti. Steered molecular dynamics study of mechanical response of full length and short collagen molecules. *Journal of Nanomechanics and Micromechanics*, 1(3):104–110, 2011.

K. Prostak and S. Lees. Visualization of crystal-matrix structure. In situ demineralization of mineralized turkey leg tendon and bone. *Calcified Tissue International*, 59(6):474 – 479, 1996.

M. Qi, J. Shao, A. Giraud, Q. Zhu, and J. Colliat. Damage and plastic friction in initially anisotropic quasi brittle materials. *International Journal of Plasticity*, 82:260–282, 2016.

T. Qu, A. M. Verma, D., and V. Tomar. Influence of interfacial interactions on deformation mechanism and interface viscosity in α-chitin–calcite interfaces. *Acta Biomaterialia*, 25:325–338, 2015a.

T. Qu, D. Verma, M. Shahidi, B. Pichler, C. Hellmich, and V. Tomar. Mechanics of organic-inorganic biointerfaces - implications for strength and creep properties. *MRS Bulletin*, 40(4):349–358, 2015b.

J. Radon. Über die Bestimmung von Funktionen durch ihre Integralwerte längs gewisser Mannigfaltigkeiten. *Berichte über die Verhandlungen der Königlich-Sächsischen Gesellschaft der Wissenschaften zu Leipzig. Mathematisch-Physische Klasse*, 69:262–277, 1917.

A. Reisinger, D. Pahr, and P. Zysset. Sensitivity analysis and parametric study of elastic properties of an unidirectional mineralized bone fibril-array using mean field methods. *Biomechanics and Modeling in Mechanobiology*, 9(5), 2010.

C. Reynaud, F. Thévenot, T. Chartier, and J.-L. Besson. Mechanical properties and mechanical behaviour of sic dense-porous laminates. *Journal of the European Ceramic Society*, 25(45):589–597, 2005.

K. Rezwan, Q. Chen, J. Blaker, and A. Boccaccini. Biodegradable and bioactive porous polymer/inorganic composite scaffolds for bone tissue engineering. *Biomaterials*, 27(18):3413–3431, 2006.

J. Rho, M. Hobatho, and R. Ashman. Relations of mechanical properties to density and ct numbers in human bone. *Medical Engineering & Physics*, 17(5):347–355, 1995.

J.-Y. Rho, M. Roy, T. Tsui, and G. Pharr. Elastic properties of microstructural components of human bone tissue as measured by nanoindentation. *Journal of Biomedical Materials Research*, 45(1):48–54, 1998.

R. Riedl. A systems-analytical approach to macro-evolutionary phenomena. *The Quarterly Review of Biology*, 52(4):351–370, 1977.

R. Robinson. Chemical analysis and electron microscopy of bone. In K. Rodahl, J. Nicholson, and E. Brown Jr., editors, *Bone as tissue*, pages 186–250. McGraw-Hill, New-York, 1960.

P. Roholl, E. Blauw, C. Zurcher, J. Dormans, and H. Theuns. Evidence for a diminished maturation of preosteoblasts into osteoblasts during aging in rats: an ultrastructural analysis. *Journal of bone and mineral research*, 9(3):355–366, 1994.

P. Roschger, H. Gupta, A. Berzlanovich, G. Ittner, D. Dempster, P. Fratzl, F. Cosman, M. Parisien, R. Lindsay, J. Nieves, and K. Klaushofer. Constant mineralization density distribution in cancellous human bone. *Bone*, 32(3):316–323, 2003.

P. Roschger, E. Paschalis, P. Fratzl, and K. Klaushofer. Bone mineralization density distribution in health and disease. *Bone*, 42(3):456–466, 2008.

M. Rougvie and R. Bear. An X-Ray diffraction investigation of swelling by collagen. *Journal of the American Leather Chemists Association*, 48(12):735–751, 1953.

G. Rousselier and M. Luo. A fully coupled void damage and mohr-coulomb based ductile fracture model in the framework of a reduced texture methodology. *International Journal of Plasticity*, 55:1–24, 2014.

S. Roussette, J. Michel, and P. Suquet. Nonuniform transformation field analysis of elastic-viscoplastic composites. *Composites Science and Technology*, 69(1):22–27, 2009.

M. Saito, A. Shiraishi, M. Ito, S. Sakai, N. Hayakawa, M. Mihara, and K. Marumo. Comparison of effects of alfacalcidol and alendronate on mechanical properties and bone collagen cross-links of callus in the fracture repair rat model. *Bone*, 46:1170–1179, 2009.

H. Saka, D. Goto, and W.-J. Moon. Dislocations in plastically deformed apatite. *Journal of Materials Science*, 43(9):3234–3239, 2008.

J. Salençon. *Handbook of continuum mechanics.* Springer, Heidelberg, Germany, 1st edition edition, 2001.

J. Sanahuja, L. Dormieux, S. Meille, C. Hellmich, and A. Fritsch. Micromechanical explanation of elasticity and strength of gypsum: from elongated anisotropic crystals to isotropic porous polycrystals. *Journal of Engineering Mechanics*, 136(2):239 – 253, 2009.

J. Sanahuja, L. Dormieux, S. Meille, C. Hellmich, and A. Fritsch. Micromechanical explanation of elasticity and strength of gypsum: from elongated anisotropic crystals to isotropic porous polycrystals. *Journal of Engineering Mechanics*, 136(2):239 – 253, 2010.

V. Sansalone, S. Naili, V. Bousson, C. Bergot, F. Peyrin, J. Zarka, J. Laredo, and G. Haiat. Determination of the heterogeneous anisotropic elastic properties of human femoral bone: From nanoscopic to organ scale. *Journal of Biomechanics*, 43(10), 2010.

V. Sansalone, S. Naili, and C. Desceliers. A stochastic homogenization approach to estimate bone elastic properties. *Comptes Rendus Mécanique*, 342(5):326–333, 2014.

N. Sasaki and S. Odajima. Stress-strain curve and young's modulus of a collagen molecule as determined by the x-ray diffraction technique. *Journal of Biomechanics*, 29(5):655–658, 1996.

S. Scheiner, R. Sinibaldi, B. Pichler, V. Komlev, C. Renghini, C. Vitale-Brovarone, F. Rustichelli, and C. Hellmich. Micromechanics of bone tissue-engineering scaffolds, based on resolution error-cleared computer tomography. *Biomaterials*, 30(12):2411–2419, 2009.

S. Scheiner, P. Pivonka, and C. Hellmich. Coupling systems biology with multiscale mechanics, for computer simulations of bone remodeling. *Computer Methods in Applied Mechanics and Engineering*, 254:181–196, 2013.

S. Scheiner, P. Pivonka, and C. Hellmich. Mathematical modeling of postmenopausal osteoporosis and its treatment by the anti-catabolic drug denosumab. *Numerical Methods in Biomedical Engineering*, 30:1–27, 2014.

S. Scheiner, P. Pivonka, and C. Hellmich. Poromicromechanics reveals that physiological bone strains induce osteocyte-stimulating lacunar pressure. *Biomechanics and Modeling in Mechanobiology*, 15(1):9—-28, 2016.

P. Schneider, M. Stauber, R. Voide, M. Stampanoni, L. Donahue, and R. Müller. Ultrastructural properties in cortical bone vary greatly in two inbred strains of mice as assessed by synchrotron light based micro- and nano-ct. *Journal of Bone and Mineral Research*, 22(10):1557–1570, 2007.

P. Schneider, M. Meier, R. Wepf, and R. Müller. Serial fib/sem imaging for quantitative 3d assessment of the osteocyte lacuno-canalicular network. *Bone*, 49(2):304–311, 2011.

K. Schulgasser. On the in-plane elastic constants of paper. *Fibre Science and Technology*, 15(4):257–270, 1981.

H. Schwarcz, E. McNally, and G. Botton. Dark-field transmission electron microscopy of cortical bone reveals details of extrafibrillar crystals. *Journal of Structural Biology*, 188(3):240–248, 2014.

J. Schwiedrzik, R. Raghavan, A. Burki, V. LeNader, U. Wolfram, J. Michler, and P. Zysset. In situ micro pillar compression reveals superior strength and ductility but an absence of damage in lamellar bone. *Nature Materials*, 13:740–747, 2014.

G. Searle. *Experimental Physics. A selection of experiments.* Cambridge University Press, 1st edition edition, 1934. p279.

I. Sevostianov, N. Yilmaz, V. Kushch, and V. Levin. Effective elastic properties of matrix composites with transversely-isotropic phases. *International Journal of Solids and Structures*, 42(2):455–476, 2005.

M. Shahidi, B. Pichler, and C. Hellmich. Viscous interfaces as source for material creep: A continuum micromechanics approach. *European Journal of Mechanics - A/Solids*, 45:41–58, 2014.

M. Shahidi, B. Pichler, and C. Hellmich. How interface size, density, and viscosity affect creep and relaxation functions of matrix-interface composites: a micromechanical study. *Acta Mechanica*, 227:229 – 252, 2016a.

M. Shahidi, B. Pichler, and C. Hellmich. Interfacial micromechanics assessment of classical rheological models. i: Single interface size and viscosity. *Journal of Engineering Mechanics*, 142(3), 2016b.

M. Shahidi, B. Pichler, and C. Hellmich. Interfacial micromechanics assessment of classical rheological models. ii: Multiple interface sizes and viscosities. *Journal of Engineering Mechanics*, 142(3), 2016c.

M. Shareef, P. Messer, and R. van Noort. Fabrication, characterization and fracture study of a machinable hydroxyapatite ceramic. *Biomaterials*, 14(1):69–75, 1993.

S. Shefelbine, U. Simon, L. Claes, A. Gold, Y. Gabet, I. Bab, R. Müller, and P. Augat. Prediction of fracture callus mechanical properties using micro-CT images and voxel-based finite element analysis. *Bone*, 36(3):480–488, 2005.

W. Shen and J. Shao. An incremental micro-macro model for porous geomaterials with double porosity and inclusion. *International Journal of Plasticity*, 83:37–54, 2016.

W. Shen, J. Shao, D. Kondo, and B. Gatmiri. A micro-macro model for clayey rocks with a plastic compressible porous matrix. *International Journal of Plasticity*, 36:64–85, 2012.

W. Shen, A. Oueslati, and G. de Saxcé. Macroscopic criterion for ductile porous materials based on a statically admissible microscopic stress field. *International Journal of Plasticity*, 70:60–76, 2015.

Z. Shen, M. Dodge, H. Kahn, R. Ballarini, and S. Eppell. Stress-strain experiments on individual collagen fibrils. *Biophysical Journal*, 95(8):3956–3963, 2008.

A. Shojaei and G. Li. Viscoplasticity analysis of semicrystalline polymers: A multiscale approach within micromechanics framework. *International Journal of Plasticity*, 42:31–49, 2013.

W. Sietsema. Animal models of cortical porosity. *Bone*, 17(4):297–305, 1995.

M. Silva, M. Brodt, Z. Fan, and J.-Y. Rho. Nanoindentation and whole-bone bending estimates of material properties in bones from the senescence accelerated mouse SAMP6. *Journal of Biomechanics*, 37(11):1639–1646, 2004.

M. Simbara, R. Carbonari, and S. Malmonge. Scaffold prototype for heart valve tissue engineering: Design and material analyses. In D. Jaffray, editor, *World Congress on Medical Physics and Biomedical Engineering, Toronto, Canada*, volume 51 of *IFMBE Proceedings*, 2015.

J.-C. Simo and T. J.-R. Hughes. *Computational Inelasticity.* Springer, Heidelberg, Germany, 1st edition edition, 1998.

J.-C. Simo and R.-L. Taylor. Consistent tangent operators for rate-independent elastoplasticity. *Computer Methods in Applied Mechanics and Engineering*, 48 (1):101–118, 1985.

J. Skedros, J. Holmes, E. Vajda, and R. Bloebaum. Cement lines of secondary osteons in human bone are not mineral-deficient: new data in a historical perspective. *The Anatomical Record A*, 286(1):781–803, 2005.

L. Sokoloff. A note on the histology of cement lines. In *Perspectives in Biomedical Engineering*, pages 135–138. Springer, 1973.

A. Stroud. Approximate calculation of multiple integrals. *Prentice Hall, Englewood Cliffs, NJ*, 1971.

X. Su, K. Sun, F. Cui, and W. Landis. Organization of apatite crystals in human woven bone. *Bone*, 32(2):150 – 162, 2003.

P. Suquet, editor. *Continuum micromechanics.* Springer-Verlag, Wien, 1997a.

P. Suquet. *Continuum micromechanics.* Springer, Wien, 1997b.

K. Szlazak, J. Jaroszewicz, B. Ostrowska, T. Jaroszewicz, M. Nabialek, M. Szota, and W. Swieszkowski. Characterization of three-dimensional printed composite scaffolds prepared with different fabrication methods. *Archives of Metallurgy and Materials*, 61(2A):645–649, 2016.

K. Tai, F.-J. Ulm, and C. Ortiz. Nanogranular origins of the strength of bone. *Nanoletters*, 6(11):2520–2525, 2006.

K. Tai, G. Pelled, D. Sheyn, A. Bershteyn, L. Han, I. Kallai, Y. Zilberman, C. Ortiz, and D. Gazit. Nanobiomechanics of repair bone regenerated by genetically modified mesenchymal stem cells. *Tissue Engineering Part A*, 14(10):1709—-1720, 2008.

Q. Tao, D. Verma, M. Shahidi, B. Pichler, C. Hellmich, and V. Tomar. Mechanics of organic-inorganic biointerfaces—implications for strength and creep properties. *MRS Bulletin*, 40(04):349–358, 2015.

E. Tazawa. Effect of self stress on flexural strength of gypsum-polymer composites. *Advanced Cement Based Materials*, 7(1):1–7, 1998.

S. Teitelbaum. Bone resorption by osteoclasts. *Science*, 2000.

D. Thompson, H. Simmons, C. Pirie, and H. Ke. FDA Guidelines and animal models for osteoporosis. *Bone*, 17(4):125–133, 1995.

S. Tommasini, A. Trinward, A. Acerbo, F. De Carlo, L. Miller, and S. Judex. Changes in intracortical microporosities induced by pharmaceutical treatment of osteoporosis as detected by high resolution micro-ct. *Bone*, 50:596–604, 2012.

J. Tryding. *In-plane fracture of paper*. PhD thesis, Division of Structural Mechanics, Lund University, Lund, Sweden, 1996.

C. Turner, S. Cowin, J. Rho, R. Ashman, and J. Rice. The fabric dependence of the orthotropic elastic constants of cancellous bone. *Journal of Biomechanics*, 23(6):549–561, 1990.

T. Uesaka, K. Murakami, and R. Imamura. Two-dimensional linear viscoelasticity of paper. *Wood Science and Technology*, 14(2):131–141, 1980.

M. Urist, R. DeLange, and G. Finerman. Bone cell differentiation and growth factors. *Science*, 1983.

B. Van Rietbergen, H. Weinans, R. Huiskes, and A. Odgaard. A new method to determine trabecular bone elastic properties and loading using micromechanical finite-element models. *Journal of Biomechanics*, 28(1):69–81, 1995.

B. Van Rietbergen, R. Müller, D. Ulrich, P. Rüegsegger, and R. Huiskes. Tissue stresses and strain in trabeculae of a canine proximal femur can be quantified from computer reconstructions. *Journal of Biomechanics*, 32(2):165–173, 1999.

P. Vena, D. Gastaldi, and R. Contro. Determination of the effective elastic-plastic response of metal-ceramic composites. *International Journal of Plasticity*, 24 (3):483–508, 2007.

B. Viswanath, R. Raghavan, U. Ramamurty, and N. Ravishankar. Mechanical properties and anisotropy in hydroxyapatite single crystals. *Scripta Materialia*, 57(4):361–364, 2007.

J. Vuong and C. Hellmich. Bone fibrillogenesis and mineralization: Quantitative analysis and implications for tissue elasticity. *Journal of Theoretical Biology*, 287:115–130, 2011.

C. Wang, H. Chen, X. Zhu, Z. Xiao, K. Zhang, and X. Zhang. An improved polymeric sponge replication method for biomedical porous titanium scaffolds. *Materials Science and Engineering: C*, 70, Part 2:1192–1199, 2017.

L. Wang, P. Orhii, J. Banu, and D. Kalu. Effects of separate and combined therapy with growth hormone and parathyroid hormone on lumbar vertebral bone in aged ovariectomized osteopenic rats. *Bone*, 28(2):202–207, 2001.

B. E. Warren. X-ray diffraction methods. *Journal of Applied Physics*, 12(5):375 –384, 1941.

B. E. Warren and B. L. Averbach. The effect of cold-work distortion on X-ray patterns. *Journal of Applied Physics*, 21(6):595–599, 1950.

F. Weidenreich. Das knochengewebe. In *Handbuch der mikroskopischen Anatomie des Menschen*, pages 391–520. Springer, 1930.

S. Weiner and H. Wagner. The material bone: structure-mechanical function relations. *Annual Review of Materials Science*, 48:271–298, 1998.

S. Weiner, T. Arad, I. Sabanay, and W. Traub. Rotated plywood structure of primary lamellar bone in the rat: Orientations of the collagen fibril arrays. *Bone*, 20:509–514, 1997.

J. Weinmann and H. Sicher. *Bone and bones.* Mosby, St. Louis, 1955.

H.-R. Wenk and P. Van Houtte. Texture and anisotropy. *Report on Progress in Physics*, 67:1367–1428, 2004.

H.-R. Wenk, M. Voltolini, M. Mazurek, L. R. Van Loon, and A. Vinsot. Preferred orientations and anisotropy in shales: Callovo-oxfordian shale (france) and opalinus clay (switzerland). *Clays and Clay Minerals*, 56(3):285 – 306, 2008.

J. Wergedal and Baylink. Electron microprobe measurements of bone mineralization rate in vivo. *American Journal of Physiology*, 226(2):345–352, 1974.

H. Wiesmann, U. Meyer, U. Plate, and H. Höhling. Aspects of collagen mineralization in hard tissue formation. *International Review of Cytology*, 242:121–156, 2005.

D. Williams. On the mechanisms of biocompatibility. *Biomaterials*, 29(20):2941–2953, 2008.

D. Wirtz, N. Schiffers, T. Pandorf, K. Radermacher, D. Weichert, and R. Forst. Critical evaluation of known bone material properties to realize anisotropic FE-simulation of the proximal femur. *Journal of Biomechanics*, 33(10):1325–1330, 2000.

X.-F. Wu and Y. A. Dzenis. Elasticity of planar fiber networks. *Journal of Applied Physics*, 98(9):093501, 2005.

B. Wysocki, J. Idaszek, S. K., K. Strzelczyk, T. Brynk, K. Kurzydlowski, and W. Swieszkowski. Post-processing and biological evaluation of the titanium scaffolds for bone tissue engineering. *Materials*, 9(197), 2016.

Q. Xia, M. Boyce, and D. Parks. A constitutive model for the anisotropic elastic–plastic deformation of paper and paperboard. *International journal of solids and structures*, 39(15):4053–4071, 2002.

Y. Yang, X. Zheng, B. Li, S. Jiang, and L. Jiang. Increased activity of osteocyte autophagy in ovariectomized rats and its correlation with oxidative stress status and bone loss. *Biochemical and Biophysical Research Communications*, 451(1): 86–92, 2014.

M. Yazdimamaghani, M. Razavi, D. Vashaee, K. Moharamzadeh, A. Boccaccini, and L. Tayebi. Porous magnesium-based scaffolds for tissue engineering. *Materials Science and Engineering: C*, 71:1253–1266, 2017.

Y. Yoon and S. Cowin. The estimated elastic constants for a single bone osteonal lamella. *Biomechanics and Modeling in Mechanobiology*, 7(1), 2008.

Z. Yosibash, N. Trabelsi, and C. Hellmich. Subject-specific p-FE analysis of the proximal femur utilizing micromechanics-based material properties. *International Journal for Multiscale Computational Engineering*, 6(5):483–498, 2008.

D. Zahn and O. Hochrein. Computational study of interfaces between hydroxyapatite and water. *Physical Chemistry Chemical Physics*, 5(18):4004–4007, 2003.

A. Zajac and D. Discher. Cell differentiation through tissue elasticity-coupled, myosin-driven remodeling. *Current Opinion in Cell Biology*, 20(6):609–615, 2008.

A. Zaoui. Structural morphology and constitutive behavior of microheterogeneous materials. In *Continuum Micromechanics*, pages 291–347. 1997.

A. Zaoui. Continuum micromechanics: Survey. *Journal of Engineering Mechanics*, 128(8):808–816, 2002.

T. Zeng, J. Shao, and W. Xu. Multiscale modeling of cohesive geomaterials with a polycrystalline approach. *Mechanics of Materials*, 69(1):132 – 145, 2014.

J.-X. Zhu, Y. Sasano, I. Takahashi, I. Mizogushi, and M. Kagayama. Temporal and spatial gene expression of major bone extracellular matrix molecules during embryonic mandibular osteogenesis in rats. *The Histochemical Journal*, 33:25–35, 2001.

Q. Zhu, D. Kondo, J. Shao, and Pensée. Micromechanical modelling of anisotropic damage in brittle rocks and application. *International Journal of Rock Mechanics and Mining Sciences*, 45(4):467–477, 2008.

O. C. Zienkiewicz and R. L. Taylor. *The finite element method.* McGraw-Hill, London et al., 4th edition, 1994. ISBN 0-07-084174-8.

M. Zinn, B. Witholt, and T. Egli. Occurrence, synthesis and medical application of bacterial polyhydroxyalkanoate. *Advanced Drug Delivery Reviews*, 53(1):5–21, 2001.

L. Zylberberg, W. Traub, V. de Buffrenil, F. Allizard, A. T., and S. Weiner. Rostrum of a toothed whale: ultrastructural study of a very dense bone. *Bone*, 23:241–247, 1998.